FORMATION MECHANISM, DEFECT ENGINEERING AND APPLICATIONS OF POROUS ORGANIC CAGES

A Dissertation
Presented to
The Academic Faculty

by

Guanghui Zhu

In Partial Fulfillment
of the Requirements for the Degree
Doctor of Philosophy in the
School of Chemical & Biomolecular Engineering

Georgia Institute of Technology
December 2018

FORMATION MECHANISM, DEFECT ENGINEERING AND APPLICATIONS OF POROUS ORGANIC CAGES

Approved by:

Dr. Ryan P. Lively, Advisor
School of Chemical & Biomolecular Engineering
Georgia Institute of Technology

Dr. Christopher W. Jones, Advisor
School of Chemical & Biomolecular Engineering
Georgia Institute of Technology

Dr. David S. Sholl
School of Chemical & Biomolecular Engineering
Georgia Institute of Technology

Dr. J. Carson Meredith
School of Chemical & Biomolecular Engineering
Georgia Institute of Technology

Dr. M. G. Finn
School of Chemistry & Biochemistry
Georgia Institute of Technology

Date Approved: October 22nd, 2018

To my supporting and loving family

ACKNOWLEDGEMENTS

Ph.D. dissertation is a choice that become part of one's life, without the supports from other people, it would not be possible. I want to acknowledge people and organizations, without whom I would not be able to finish and enjoy the journey.

I have the special privilege of working with two brilliant advisors, Professor Ryan Lively and Professor Christopher Jones. First I want to thank them for trusting me and admitting me as part of their groups. I think that I have performed up to their expectations and maybe exceeded them. Of course I did not mature as a better person on myself, I indeed am aware of and appreciate the efforts they made on improving and polishing me. They are enlightening and sage, and prudent in mentoring young researchers. I am thankful for the relationship that I have developed with both of them, which I think is the best relationship one can hold in the academic world. They allowed, encouraged, and guided me to follow my heart and realize my potentials. They are definitely the pivot during my Ph.D. research. I would also like to thank my committee members, Professor David Sholl, Professor Carson Meredith, and Professor M. G. Finn, for their insights, suggestions, and time.

I enjoyed working with the Lively group and Jones group members. I want to thank Dr. Melinda Jue, Dr. Brian Pimentel, and Erkang Zhou for their initial guidance and continuous mentoring, helping, and discussions. I want to give special thanks to Dr. Simon Pang for all technical and non-technical advises and his endless support for me. We have the same mind. I want to thank Dr. Melinda Jue, Dr. Richelle Lyndon, Dr. Achintya Sujan, Yao Ma, Fengyi Zhang, Ronita Mathias, Matt Rivera, Nathan Ellebracht, Claudia

Okonkwo, Sang Jae Park, Christopher D Hoffman, Avery Agles, and Jacob Lee for their valuable collaborations. I want to thank Dr. Dong-Yeun Koh, Dr. Tianmiao Lai, Dr. Eric Moschetta, Dr. Shaowei Yang, Dr. Yun-Ho Ahn, Dr. Caroline Hoyt, Dr. Taylor Sulmonetti, Dr. Grace Chen, Dr. Kiwon Eum, Dr. Micaela Taborga Claure, Dr. Miles Sakwa-Novak, Dr. Steph Didas, Dr. Kristina Golub, Dr. Michele Sarazen, Dr. Lalit Durante, Chunjae Yoo, Jason Lee, Stephen DeWitt, Leo Chiang, Hye Youn Jang, Conrad Roos, Qandeel Almas, Akshay Korde, Byunghyun Min for the helpful discussions. I realized that the list is absurdly long. But they are all important portions of my research.

I want to acknowledge my funding source from UNCAGE-ME EFRC center sponsored by Department of Energy. This nationwide research center give me tremendous learning and collaboration opportunities. All my works have been highly collaborative. In addition to the collaborations mentioned in last part, I also want to thank researchers from groups in GT, national labs, and other universities. Among all the collaborators I want to specially thank Yang Liu. We worked together from my first project to her last project. Our complementary skill sets and personalities have made the collaboration enjoyable and delightful. In terms of this thesis, Yang Liu has contributed to the computational studies that accompany Chapter 2, 3, and 4. I want to thank Dr. David Bostwick in School of Chemistry and Biochemistry for the assistance and discussion in mass spectrometry analysis in Chapter 2 and 3. I want to thank Dr. Melinda L Jue for measuring water isotherms, Dr. Souryadeep Bhattacharyya for conducting humid acid gas exposure experiments, and Dr. Uma Tumuluri for helping in the *in situ* IR measurement in Chapter 4. I want to thank Claudia Okonkwo with the acid gas uptake instrumentation in Chapter 5. I want to thank Xunxiang Hu for measuring positron annihilation lifetime spectroscopy

in Chapter 6. I also want to thank collaborators in other projects during my PhD study: Dr. Luis Flores, Prof. David A Dixon, Prof. David Sholl, Prof. Zili Wu, Prof. Sankar Nair, Dr. Jan Michael Y Carrillo, Prof. Bobby G Sumpter, Dr. Akshita Dutta, Dr. Nina Tyminska, Dr. James Collins, Prof. JR Schmidt, Prof. Sergey Vasenkov.

The friends I have made in Atlanta helped me stay motivated throughout my PhD study. In addition to the people already mentioned, I want to thank Yang Jiao, Zihao Qu, Xu Du, Weize Hu, Siwei Guo, Zhibo Yuan, Lu Jiang, Songcheng Wang, Haotian Wang, Yi Liu, Wenqin You, Zewei Wang, Weicheng Bai.

TABLE OF CONTENTS

LIST OF TABLES

LIST OF FIGURES

SUMMARY

Porous organic cages (POCs) are a class of discrete porous molecules with unique properties and potential for various applications. This thesis work focuses on fundamental as well as applied aspects of POCs. This thesis will start with detailed investigation of the formation mechanisms of imine-based POCs and implying new design strategies for POCs (Chapter 2). Then various defect behavior of POC molecules and solids are studied that showed improved physical properties (Chapter 3&4). One particular type of amorphous POC named amorphous scrambled porous organic cages (ASPOCs) is tested as adsorbent support and membrane additives as proof-of-concept studies of potential applications of POCs (Chapter 5&6).

The syntheses of POCs represent an important synthetic puzzle in dynamic covalent chemistry based self-sorting. Improved understanding of the formation mechanisms of POCs can lead to control and rational design of cages with desired functionality. In the first study (Chapter 2), I explore the formation mechanisms of imine-based POCs using time-resolved electrospray mass spectrometry. Upon mixing of the linkers, localized random assembly immediately occurs between the linkers to form a wide range of intermediates. These intermediates transform into several species with specific metastable geometries in a short time period. The metastable species then act as a reservoir for simultaneous dissolution and assembly towards the desired cages, with a small amount of incomplete cages or undesired byproducts coexisting in the final product. Electronic structure calculations at the density functional theory and correlated molecular orbital theory levels are used to validate the formation mechanism. Based on our observations from both

experiments and calculations, I propose a comprehensive method for designing and predicting new POC species.

The observation of stable incomplete cages during CC3-R synthesis inspired us to design intentionally defective cages (Chapter 3). These “missing-linker” type molecular defects are installed into CC3-R via non-solvent induced crystallization. The defective CC3-R materials are found to have enhanced CO_2 interaction and improved CO_2 uptake capacity due to the additional functional groups present within the CC3 crystals. In addition to molecular defects, defect at the crystal level is also studied (Chapter 4). Both known and new CC3-based porous organic cages are prepared and exposed to acidic SO2 in vapor and liquid conditions. Distinct differences in the stability of the CC3 cages exist depending on the chirality of the diamine linkers used. The acid catalyzed CC3 degradation mechanism is probed via in-situ IR and a degradation pathway is proposed and supported with computational results. CC3 crystals synthesized with racemic mixtures of diaminocyclohexane exhibited enhanced stability compared to CC3-R and CC3-S. Confocal fluorescent microscope images reveal that the stability difference in CC3 species originates from an abundance of mesoporous grain boundaries in CC3-R and CC3-S, allowing facile access of aqueous SO_2 throughout the crystal, promoting decomposition. These grain boundaries are absent from CC3 crystals made with racemic linkers.

In Chapter 5, I explore the applicability of POCs as molecular porous supports for polymeric amines. I find that primary amines in poly(ethylenimine) (PEI) can undergo metathesis with the imine bonds present in POCs, resulting in non-porous products. This problem can be overcome by transforming the primary amines in PEI to tertiary amines via methylation. The methylated PEI (mPEI) forms homogeneous composites with ASPOCs

without undesired reactions or phase separation. The microscopic structure of the composites is studied using molecular dynamics simulations. These composite materials are evaluated as adsorbents for low concentration SO_2 (200 ppm) adsorption and show good thermal and cyclic stability.

Finally, I investigate performance of ASPOC containing mixed-matrix membranes. When fabricated into mixed matrix membranes, the soluble POC molecules have the potential to exhibit molecular-level intimate mixing with matrix polymer. However, the incorporation of POCs into mixed matrix membrane is still in its infancy and lacks demonstration of comprehensive improvement of membrane performance. In chapter 6, I utilized vertex functionalized amorphous scrambled porous organic cages (ASPOCs) in mixed matrix membranes to study a series of key questions in this field. The dispersion of ASPOC mixtures possessing different crystallization tendencies within a polymer matrix are probed using Raman imaging and Energy Dispersive X-Ray (EDX) mapping. Gas permeation experiments of N_2, CO_2, CH_4 and SF_6 were carried out as a function of ASPOC loading and crystallization tendency. A 4 fold of permeability increase was observed for N_2, CO_2 and CH_4 compared to pure polymer membrane. Moreover, a clear molecular sieving effect was observed for SF_6, resulting in 2-4 fold of increase of N2/SF6 selectivity compared to the pure polymer membrane. The membranes were further examined in organic solvent nanofiltration experiments using a cross-flow permeation approach. The Molecular Weight Cut-off (MWCO) of the membranes were calculated based on the polystyrene permeation tests. Overall, these membranes demonstrated homogeneous mixing between the POC molecules and the polymer matrix, and showed potential to be used in molecular separation processes.

CHAPTER 1. INTRODUCTION

1.1 Porous Material in Separation Applications

Energy security and climate change are major societal and technological concerns in recent years. The industrial sector accounts for 24 % of global CO_2 emissions and 38 % of global total energy use.[1] Half of the energy consumption in US industrial sector is associated with separation and purifications of gases and liquids streams.[2] Traditional separation methods are usually based on differentiating matters from their phase change temperature, which are energy-intensive. Alternative technologies such as adsorption or membrane-based separation methods can be 10 times more efficient. A critical element of these emerging technologies is the development of novel materials possessing the structural and functional features necessary to realize the potential of advanced separations.

Porous solid materials that contain cavities inside the particles are of particular interest because of the void spaces interact with atoms, ions, and molecules. The interaction of guest molecules with porous material can take place in different manners. The guest molecules can be selectively adsorbed into the pore space, which can be used in adsorption applications. Porous material with uniform pore structure can differentiate molecules based on their size, known as molecular-sieving, which can be used in membrane separations. Recently, the difference of diffusivities of molecules in porous materials have also been exploited, as illustrated in Pimentel's work on kinetic separations.[3] Depending on the pore diameter, porous materials can be further divided into three categories: microporous materials (pore diameter < 2 nm), mesoporous materials (2 nm < pore diameter < 50 nm), and macroporous materials (pore diameter > 50 nm).

Based on the relevance to separation sciences, several classes of materials and their recent advances will be reviewed in this chapter. The materials include zeolites, metal-organic frameworks (MOFs), polymers of intrinsic microporosity (PIMs), and carbon molecular sieves (CMS). One particular material, porous organic cages (POCs), is the focus of this dissertation and will be thoroughly reviewed from its discovery, properties, to applications. Some other novel porous materials that have been developed in recent years and showed promising adsorptive properties, such as porous aromatic frameworks (PAFs) and covalent organic frameworks (COFs), will not be discussed here because of their current limitations in synthetic scale-up.

1.1.1 Recent Advances of Zeolites in Separation Applications

Zeolites are crystalline aluminosilicates with well-defined pore structures. The uniform pore characteristics have rendered zeolites massive applications in shape-selective separations and catalytic reactions.[4-7] Zeolite has been used historically as adsorbents for moistures.[8-10] Their ability to adsorb water molecules down to ppm level makes it suitable for liquefaction pretreatment. Storage/adsorptive separation of other gas molecules in zeolites have also been explored.[11-16] Notably, the separation of O_2 from N_2 in air using lithium-exchanged zeolite-Y.[17-19]

1.1.1.1 Additive Manufacturing of Zeolite Monolith as Adsorbents

Despite the wide commercialization of zeolites in industrial catalysis and adsorptive applications, recent research has been emerging in the field of additive manufacturing to develop structured zeolite contactors. Computational fluid dynamics

simulations can be used to optimize the geometries of contactors which can then be precisely fabricated by additive manufacturing.

Recently, Thakkar et al. reported the first example of 3D printed zeolite (13X and 5A) monoliths, for CO_2 adsorption from 5000 ppm CO_2/N_2 mixture (not air capture as they claimed).[20] Although no optimization on the geometry was carried out, less mass transfer resistance was observed in monolithic beds compared to powder beds during CO_2 breakthrough experiments. However, the development of extrusion of a zeolite/binder paste suggests that 3D printing allows an alternative approach to adsorbent material fabrication, with a capability to fine-tune structural, chemical and mechanical properties for use in gas separation processes. Inspired by these results, they were also able to 3D print aminosilica adsorbents into 3D monoliths, which exhibited CO_2 adsorptive characteristics comparable to their corresponding powders.[21]

Zeolite 13X and carbon were fabricated into monoliths and compared to the normal shape form of beads in adsorption of H_2S and CO_2. [22] 13X beads exhibited the highest adsorption capacity and longest breakthrough, followed by the printed 13X structures. The adsorption and desorption rates of the 3D printed structures were found to be significantly faster than that of beads. More complex gas mixtures separation (CO_2, CH_4, and N_2) was carried out with 3D-printed ZSM-5 monolith.[23] Though no technical innovation was involved. Inspired by direct 3D-printing of polymers with phase inversion developed in our group[24], the 3D-printing of polymer-zeolite composite was also reported.[25]

The current research of zeolite additive manufacturing has been mainly focused on experimental techniques such as formulation and extrusion method. Significant effort is

needed in the computational optimization of geometries is needed in order to truly demonstrate the advantages of additive manufacturing in adsorption applications.

1.1.1.2 Zeolitic Membranes

Zeolitic membranes have attracted research interest since the early 1990s. Early works include silicalite membrane grown on ceramic discs for n-butane/i-butane separation[26] and CH_3OH/H_2, CH_3OH/CH_4 separations[27].

A series of studies have been carried out in Japan that developed NaA pervaporation membranes, which eventually lead to large-scale commercialization.[28-30] The NaA membranes were prepared on the surfaces of porous tubular supports composed of mullite, α-alumina and/or cristobalite using the hydrothermal synthesis. The membrane showed very high water-selective permeation through all the ethanol concentrations with a separation factor at 5 wt% water/95 wt% ethanol mixture greater than 5000. The excellent performance of the membrane module led to the first large-scale pervaporation plant that produces solvents with very low water content. The plant is equipped with 16 modules, each of which consists of 125 pieces of NaA zeolite membrane tubes (12 mm outer diameter, 80 cm length and 1 μm average pore size).

MFI-type zeolite membranes were continuously developed in Michael Tsapatsis' group.[31-39] Deep understanding of the microstructure optimization and orientation control was accumulated over the years and bred membranes from seeded and epitaxial growth with outstanding performance.

Despite the continuous research in zeolitic membranes, the intrinsic limitations such as repeatability, reproducibility, defect-rich, hard-to-scale-up limited the commercialization of zeolite membranes. Despite the success example of the pervaporation membranes, which does not require a fully defect-free membrane, but based on the hydrophilicity of zeolite materials, gas and liquid separations that largely depends on the defect concentration in the membranes are still far from commercialization. With techno-economics analysis of the zeolite membranes, the commercial potential of zeolitic membranes will become favorable for other gas- and liquid-phase separations with continued R&D efforts.[40] Compared to other types of membranes, zeolite membrane might find a better suit in high-temperature membrane reactors or other niche areas.

Recent studies of MFI membranes have been focused on ultra-thin morphology for xylene isomers separation.[41-43] The MFI membrane was fabricated using seeded nanosheet growth followed by gel-free secondary growth with a final membrane thickness of 0.5 - 1.5 μm. The best performing membrane showed *p*-xylene permeance of 2.9×10^{-7} mol m^{-2} s^{-1} Pa^{-1} and a separation factor over 10,000 between *p*-xylene and *o*-xylene.[43]

The brittleness of the thin selective zeolite layer also required careful selection and matching of support, often ceramic materials.[44-45] The properties of porous support play a crucial role in successful membrane preparation. Rigid inorganic supports are usually necessary to ensure mechanical stability of the thin membrane layer. The selection of the support is limited by their stability in hydrothermal and alkaline synthesis conditions, surface morphology, and permeance. Highly porous ceramic supports are commonly used in the literature. Zhang et al. reported deposition of melt compound exfoliated MFI nanosheets on porous polymer supports via filtration assisted deposition.[46] The resulting

membrane showed *n*-butane/isobutane selectivity of 5.4, with *n*-butane permeance of 3.5×10^{-7} mol m^{-2} s^{-1} Pa^{-1}. This approach opens more possibility for support selection and is promising in scaling up compared to traditional hydrothermal synthesis.

1.1.1.3 Zeolite Containing Mixed Matrix Membranes

Inorganic zeolitic membranes surpass the trade-off between permeability and selectivity in polymeric membranes and have shown extraordinary separation performances in challenging molecular pairs.[42, 47-48] However, the preparation of large-scale, defect-free inorganic membranes suitable for industrial applications remains a challenge. Mixed matrix membranes (MMM) incorporate inorganic filler materials (i.e., the "discrete" phase) into a polymer (i.e., the continuous phase or the "matrix") to boost the performance of the membranes while retaining the intrinsic scalability of polymer processing. These materials have long been proposed to address the orthogonal issues associated with polymer membranes and inorganic membranes.[49-50]

The zeolite containing MMMs were practiced as early as zeolitic membranes.[51] A thorough review on different kinds of zeolite–polymer MMMs, with corresponding separation tasks, operating conditions, and the performance of zeolite–polymer MMMs are done by Bastani et al. in 2018.[52] Material selection for both matrix and sieve phases and dope formulation are key aspects in the development of MMMs. Although rubbery and glassy polymers have both been practiced to form the MMMs[53-54], rubbery polymer usually exhibits high permeability and low selectivity. As a result, glassy polymers as matrix with relatively lower permeability and considerably higher selectivity are more promising towards commercial applications.

During the fabrication of a MMM, one factor of great importance is particle agglomeration due to sedimentation or surface pattern (migration to the surface). Due to the very different physical properties and the difference in density between zeolite and polymers, precipitation of zeolite may occur during the MMM preparation.[50] In contrast to sedimentation, particles may move to the membrane surface and agglomerate. It is believed that surface pattern is the result of convection cells that form during casting of films. The formation of convection cells in liquids that are heated or cooled can be due to instabilities driven by buoyancy or surface tension.[55]

Another complexity is adhesion between polymer and zeolite fillers during solidification of the membranes, especially in case of glassy polymers since they are less conforming to zeolite crystals. The balance of three interactions, polymer−solvent, polymer−sieve, and solvent−sieve determines the polymer sieve adhesion.[56] A polymer molecule is more solvated in a good solvent and has a larger coil size than if it is in a poor solvent. Therefore, as the solvent power decreases, the dimension of the polymer molecule in solution decreases and the amount adsorbed increases, because the coil surface area occupied decreases.[57] The solvent−sieve interaction is important because it is desirable for the solvent to desorb from the sieve surface when the polymer segments approach. Thus, an ideal system would be one where the sieve has a stronger affinity for the polymer than the solvent, while the polymer has a stronger affinity for the zeolite surface than the solvent. These relations can be quantified with the help of Hildebrand solubility parameters for the polymer−solvent interaction, and using the liquid−solid interaction strength parameter ε^o for alumina and silica for the solvent−sieve interaction, the higher the parameter, the stronger the interaction.[58]

Problems with particle dispersion, stress accumulation, and the polymer-filler interface give rise to many defects reported in the literature. Four major defect cases that affect membrane performance are described as follows.[59]

Case 1: Voids. This phenomenon generally occurs if the polymer and filler phases are incompatible, but may also be caused by surface delamination during the formation process. MMMs that bear void defects will show an increase in permeability, but no gain in selectivity relative to the matrix polymer as a result of the preferred non-selective pathway around the filler. Successful solutions include sieve surface modification, polymer–sieve grafting, and chemical functionalization of the sieve surface.[60]

Case 2: Dilated Interfaces. Low chain density shells may form around filler particles as a result of poor "matching" of the polymer–filler interfacial chemistry or undesirable stress relief mechanisms during membrane formation. This is one instance of a phenomenon commonly known as the zone-of-influence. In this case, the polymer phase around the filler material is less densely packed than the bulk polymer phase. Dilated interfacial polymer can have desirable effects on MMM transport[61], but more often is an undesired defect[62]. Figure 1.1 illustrates the typical negative consequence of dilated interfaces.

Case 3: Densely Packed Interfaces. Alternatively, a high resistance zone-of-influence may occur when the polymer chains pack more densely around the sieve relative to the bulk, thereby restricting access to the filler phase. Excessively dense chain adsorption at the filler interface will produce a barrier-like zone-of-influence compared to the bulk phase, which leads to a decrease in membrane productivity.

Case 4: Plugged Sieves. An additional post-formation nonideality in hybrid membranes is related to the sieve itself. Depending on the size of the sieve's pore window and the kinetic diameters of the other system components, it is possible to create a dispersion of plugged sieves. In this regard, the filler phase will behave like a barrier, with a depression in the membrane. Plugged sieves are generally a result of solvent or other processing component entering into the sieves and/or polymer chains' sorption on the sieves.

1.1.2 Recent Advances of MOFs in Separation Applications

MOFs are coordination networks of metal ions or clusters and organic linkers. The coordination chemistry and materials have a long history, such as transition metal cyanide compounds (early examples are Hofmann-type clathrates, Prussian-Blue type structures, and Werner complexes).[63] Porous frameworks gained interest when the search for novel materials suitable for separation science went beyond zeolites, but the materials usually cannot maintain permanent porosity upon guest molecule removal. MOFs that exhibit permanent porosity have been prepared in Yaghi's group in the late 1990s and early 2000s.[64-66] The methodology of isoreticular synthesis has also been brought forth.[67] The diversity of the secondary building units (SBUs) gives a large family of MOFs and their distinct interactions with guest molecules have garnered significant research in the areas of separation, storage, and catalysis.[5, 68-70]

The lower thermal and structural stability of MOFs compared to zeolites limited their applications in traditional high-temperature catalysis applications. However, the diversity of MOFs and their large pore size and high pore volumes allows application

possibilities in adsorption area. The rich interactions between the guest and the pore environment that can be originated from pore decoration of both metal and linker aspect can result in unexpected properties. MOF research originated primarily from material science and chemistry groups have been mainly focused on adsorptive properties.[71-74] Indeed, the adsorption capacities of guest molecules exceed the values reported for zeolites. Some noteworthy MOF types are discussed in the following sections.

1.1.2.1 MOF-74 and Amine-appended Expanded MOF-74

Jeffery Long's group developed a series MOFs with 1D hexagonal pore system (MOF analog of SBA-15).[75-81] Mg-MOF-74 ($Mg(dobdc)_2$, CPO-27-Mg)), composed of Mg and 2,5-dioxido-1,4-benzenedicarboxylate, is notable for its high CO2 uptakes at a low pressure under dry conditions (5.28 mmol/g at 40°C and 0.15 bar), which stem primarily from the high density of open metal sites (OMSs).[75] However, the difficulty in regeneration associated with its high heat of adsorption and relatively low stability under humid conditions prevent the use of MOF-74 in CO_2 capture applications.[82-83] It was discovered that amines could attach to the OMSs in both parent MOF-74 and expanded MOF-74 with dopbdc (4,4′-dihydroxy-3,3′-biphenyldicarboxylic acid) linker.[76, 82] The CO_2 sorption isotherm for amine-appended $Mg(dopbdc)_2$ exhibited a step change, which is desirable for maximized working capacity with minimal change between adsorption and regeneration conditions.[77] The step isotherm was then elucidated by various experimental and computational investigations to be caused by cascade CO_2 insertion between the amine and the metal atom.[77-78, 80]

The adsorption of guest molecules was probed beyond CO_2 in MOF-74 type materials. Adsorption of CO, CH_4, N_2, O_2, Ar, and P_4 in Co_2(dobdc) was investigated using *in situ* single crystal X-ray diffraction. All these molecules exhibit weak interactions with the high-spin cobalt(II) sites in the framework.[80] The uniqueness of isolated metal sites was further exploited for cooperative CO adsorption.[79] Two metal-organic frameworks, Fe_2Cl_2(bbta) (H_2bbta = 1*H*,5*H*-benzo(1,2-*d*:4,5-*d*′)bistriazole) and Fe_2Cl_2(btdd) (H_2btdd = bis(1*H*-1,2,3-triazolo[4,5-*b*],[4′,5′-*i*])dibenzo[1,4]dioxin) were discovered to have cooperative spin-transition upon increase in CO partial pressure as a result of the chain arrangement of the iron atoms. Mn_2(*m*-dobdc) was identified as an outstanding adsorbent for separating ethylene from a mixture of oxidative coupling of methane product.[81]

1.1.2.2 SIFSIX MOFs

Another major class of MOFs explored in various adsorption processes are SIFSIX MOFs, which are isoreticular structures based on hexafluorosilicate (SIFSIX) pillars. This class of material dates back to one of the earliest MOFs.[84] Later on they have been explored in CO_2 separation and resulted in optimal kinetics and thermodynamics of CO_2 adsorption.[85] Several variants of SIFSIX-1-Cu ($[Cu(4,4'\text{-bipyridine})_2(SiF_6)]_n$) were synthesized by isoreticular chemistry, including SIFSIX-2-Cu ($[Cu(4,4'\text{-dipyridylacetylene})_2(SiF_6)]_n$), interpenetrated version SIFSIX-2-Cu-i, SIFSIX-3-Zn ($[Zn(pyrazine)_2(SiF_6)]_n$), and tested in low-pressure CO_2, CH_4 and N_2 sorption. It was found that the interpenetrated SIFSIX-2-Cu-i exhibited substantially high adsorption values of 121.2 $cm^3\ g^{-1}$ (5.41 mmol g^{-1}, 238 mg g^{-1}). CO_2 breakthrough experiments were conducted in CO_2/CH_4, CO_2/N_2, and CO_2/H_2 mixtures under both dry/humid conditions.

SIFSIX-2-Cu-i showed good CO_2 adsorption performance under different conditions with remarkable cyclability. In another set of studies, SIFSIX-3-Cu ($[Cu(pyrazine)_2(SiF_6)]_n$) exhibited enhanced adsorption energetics and subsequently displayed carbon dioxide uptake and selectivity at very low partial pressures relevant to air capture and trace carbon dioxide removal.[86] By changing the metal center from Cu to Ni, SIFSIX-3-Ni was developed for practical CO2 capture in a wide range of CO_2 concentrations with the presence of H_2S.[87]

The SIFSIX MOFs are not only limited to CO_2 adsorption. Reserve selectivity can be achieved in close-related materials. SIFSIX-3-Ni sets a benchmark for CO_2/C_2H_2 selectivity at low partial pressures, whereas TIFSIX-2-Cu-i ranks among the best porous materials in the context of C_2H_2/CO_2 selectivity.[88] The affinity of C_2H_2 to the pore environment led to investigations of C_2H_2/C_2H_4 separation.[89] SIFSIX-2-Cu-i and SIFSIX-1-Cu exhibited exceptional C_2H_2 capture performance because the geometric disposition of SiF_6^{2-} moieties enables preferential binding of C_2H_2 molecules. Both materials have pore spaces that enable extremely high C_2H_2 capture under low pressures, and they unexpectedly represent new benchmarks for the highly efficient removal of minor amounts of $C_2H_2$from C_2H_4 gas (SIFSIX-2-Cu-i) and mass separation of C_2H_2/C_2H_4 mixtures under ambient conditions (SIFSIX-1-Cu).

Replacing $(SiF_6)^{2-}$ pillar with $(NbOF_5)^{2-}$ pillar results in NbOFFIVE type MOFs.[90] A full molecular exclusion of propane from propylene at standard ambient temperature and pressure was achieved in NbOFFIVE-1-Ni, while SIFSIX-3-Ni was found to adsorb both propylene and propane.

1.1.2.3 MOF Membranes

Since certain MOFs show a permanent porosity and reasonable stability such as zeolitic imidazolate frameworks (ZIFs), the potential application fields of MOFs are similar to the applications of zeolites. These include gas storage, separation by adsorption and heterogeneous catalysis. Consequently, MOFs have also been evaluated as a supported μm-sized membrane layer in gas separation, as highlighted in a recent review by Qiu et al.137 Due to the similarity of MOFs and zeolites, supported MOF membranes could be synthesized successfully by using the whole tool box developed for the preparation of supported zeolite membranes: seeding of macroporous ceramics, microwave heating and of surface charges (zeta potential) and covalent bonds between ceramic support and MOF layer.[91] Compared to zeolite membranes, although supported MOF membranes can have reduced thermal/chemical stability, their easier synthesis routes, abundant variations, and possibility of post-synthetic modification still make MOF membranes are attractive research area.

Similar to zeolite membrane fabrication, the seeded-growth method was adopted for polycrystalline MOF membrane synthesis[92]. MMOF seeds were synthesized and crushed into submicrometer sized crystals. Seed layers of these particles were deposited on PEI coated α-alumina supports. Secondary growth was done using the same gel composition used for seed crystal synthesis. The membrane exhibits ideal selectivity for H_2/N_2 of 23.

A dramatic emphasize have been placed on ZIF membrane fabrication because of their higher stability, relevant pore sizes, and facile synthesis.[93-94] Microwave-assisted

solvothermal synthesis and using porous substrate as Zn source as versatile synthesis routes.[95-96] In pursue of uniform and thin ZIF membranes, interfacial synthesis was developed as a self-limiting formation method for ZIF membranes.[97-99] In this method, Zn source and 2-methylimidazole are dissolved separately in either miscible or immiscible solvents. The two stock solution are supplied to two sides of the membrane (in case of hollow fiber supports, bore and shell sides), respectively. The ions then diffuse through the support and form a thin membrane on the support. By using the immiscible solvent system, one can control the side where the membrane is grown and achieve better thickness control.

The introduction of linkers can also be in the vapor phase. In a recent study done by Tsapatsis et al., ZnO was deposited onto porous support by atomic layer deposition (ALD).[100] Exposing the ZnO layer with ligand vapor resulted in the partial transformation of ZnO into ZIF membranes. It was shown that 10 and 20 cycles of ALD could yield membranes with high selectivity (~100) for propylene over propane and good propylene permeance ($>10^{-8}$ mol Pa^{-1} m^{-2} s^{-1}).

In additional to direct synthesis of supported MOF membranes, alternative fabrication methods have been explored that could be potentially easier to scale up.[101-102] A modified soft-physical exfoliation method was used to disintegrate a lamellar amphiprotic MOF into nanosheets with a high aspect ratio. Consequently, sub-10 nm-thick ultrathin membranes were successfully prepared, and these demonstrated a remarkable H_2/CO_2 separation performance, with a separation factor of up to 166 and H_2 permeance of up to 8×10^{-7} mol m^{-2} s^{-1} Pa^{-1} at elevated testing temperatures owing to a well-defined size-exclusion effect.[102]

1.1.2.4 MOF Containing MMMs

As mentioned in Section 1.1.1.3, zeolite-based MMMs are limited due to the incompatibility between inorganic zeolite and the organic polymer. The "half-organic" nature of MOFs that potentially could offer a higher affinity to polymer matrix resulted in a considerable activity in revisiting this concept with MOF-based MMMs. Regarding the fillers, HKUST-1, ZIF-8, and MIL-50(Al) with and without amino groups have been the most studied MOFs. In several recent papers, an improved separation behavior of MMMs with nano-particulate fillers is reported.[103-107] In a large percentage of the reported results, improvements in flux at constant selectivities with respect to the bare polymer have been reported and only in circa 10% of the cases improvements in both flux and selectivity were achieved.[91]

Similar to supported MOF membranes, the MOF containing MMMs gathered an early interest in gas separations.[108-109] Presently investigated MOFs for MMMs include $[Cu(SiF_6)(4,4'\text{-BIPY})_2]$, $[Cu_3(BTC)_2(H_2O)_3]$ (HKUST-1, Cu-BTC), [Cu(BDC)(DMF)], $[Zn_4O(BDC)_3]$ (MOF-5), [Zn(2-methylimidazolate)$_2$] (ZIF-8), [Zn(purinate)$_2$] (ZIF-20), [Zn(2-carboxyaldehyde imidazolate)$_2$] (ZIF-90), $Mn(HCOO)_2$, [Al(BDC)(μ-OH)] (MIL-53(Al)), $[Al(NH_2\text{-BDC})(\mu\text{-OH})]$ (NH_2-MIL-53(Al)) and $[Cr_3O(BDC)_3(F,OH)(H_2O)_2]$ (MIL-101) (4,4′-BIPY = 4,4′-bipyridine, BTC = benzene-1,3,5-tricarboxylate, BDC = benzene-1,4-dicarboxylate, terephthalate). MOF-polymer MMMs are investigated for the permeability of the single gases H_2, N_2, O_2, CH_4, CO_2 and of the gas mixtures O_2/N_2, H_2/CH_4, CO_2/CH_4, H_2/CO_2, CH_4/N_2 and CO_2/N_2.[108]

Diamine-appended Mg_2(dobpdc) discussed in Section 1.1.2.1 was incorporated into 6FDA-DAM polymer matrix for CO_2/N_2 separation.[110] A novel synthesis of Mg_2(dobpdc) nanorods was developed to produce defect-free membranes. A 2-fold increase in the CO_2 permeability with similar CO_2/N_2 selectivity to 6FDA-DAM was observed. The importance of the matching between MOF and polymer properties was demonstrated recently.[111] Sub-micron sized face-centered cubic (fcu)-MOF crystals were produced by ultralow temperature grinding and solvent sedimentation. These 100-400 nm particles were then incorporated into 6FDA-DAM hollow fiber MMMs with a selective skin layer of ~5 μm. The membranes together with some other benchmarking combinations were tested in simultaneous removal of CO_2 and H_2S from CH_4, an important separation in natural gas sweetening, and showed performance improvement upon the polymer upper bound. The membranes were also shown to improve both selectivity and permeability of butane isomer separations as a function of loading up to 30 wt %.

1.2 Porous Organic Cages

Porous organic cages (POCs) are individual molecules with an intrinsic cavity; i.e., they are microporous molecules.[112-115] They can be dissolved in common organic solvents without altering the porosity of an individual cage and can be packed into solid form upon solvent removal to give a 3-dimensional pore network. This connected pore network results from openings between adjacent porous molecules and, depending on the solvent removal rate, from inefficient packing of the POC molecules.[116-118] POCs have many appealing properties relative to crystalline framework microporous materials, such as ease of modification, mobility, and importantly, solution processability, as highlighted in a recent review from Cooper and co-workers.[119]

Primarily due to the allure of solution processable microporous crystals and the interesting applications such a feature enables, POCs have recently been studied for gas separation, adsorption, molecular recognition, and sensing.[120-124] More recently, the concept of porous liquids (PLs) utilizing POCs was experimentally discovered. These are liquids that have permanent, well-defined cavities. This idea was first put forward in a theoretical paper[125] and was recently demonstrated experimentally with several imine-based POCs.[126-129] The concept of porous liquids combines the permanent pores found in conventional porous materials with liquid-like properties, which introduces the possibility of enhancing existing liquid-based chemical processes such as scrubbing and liquid-liquid extraction.

In this section, I will discuss the discovery and synthesis of porous organic cages, then the unique properties that result from the nature and structure of the cages, and finally discuss the difference between POCs and conventional porous materials and several outlooks.

1.2.1 Synthesis of Porous Organic Cages

As mentioned in Section 1.1, zeolites and MOFs are established extended porous materials. Zeolites have an annual global market of several million tonnes and have made a huge impact on society. MOFs are in active research and produces thousands of papers every year. Together with some other emerging porous materials, such as COFs and PIMs, they maintain a porous structure as a result of their rigid connections between atoms, either covalent or coordination bonds. It is usually uncommon to observe molecular solids to be porous since molecules tend to pack in a way that maximizes intermolecular interactions

and minimizes distance. The quest for porous molecular solids has seen some examples, including tris(o-phenylenedioxy)cyclophosphazene (TPP)[130], Dianin's compound[131], calixarenes[132], cucurbiturils[133], Noria[134], phthalocyanines[135], triptycenetrisbenzimidazolone (TTBI)[136] and a triptycene-based organic molecule of intrinsic microporosity (OMIM)[137]. Most of the solids are extrinsically porous, i.e., pores originated form the inefficient packing. And fewer intrinsic porous solids are reported, i.e., the molecule has a cavity inside.

The discovery of intrinsically porous molecules are impeded by the difficulty of synthesis. Early stage cage compounds have been designed in a stepwise synthetic manner with irreversible reaction. In 1993, Williams et al. reported a 4-step synthesis towards cage-type structures from hexabromobenzene and furan.[138] However, the low yield as a result of multiple steps and isomer formation limited the further studies of this molecule. Later on, the dynamic covalent chemistry (DCC) including imine chemistry[139], disulfide exchange[140], boronic acid condensation[141], and olefin/alkyne metathesis[142] have made the synthesis of cage compound more viable. The imine chemistry has been dominating the early pioneer works since the facile reaction condition and readily available reactants.[143-145]

The most noteworthy POC family is imine-based cage compounds developed by Andrew Cooper in University of Liverpool.[119, 146-151] The cages are formed from imine condensation (Schiff-base formation) between simple multivalent aldehyde and amine molecules. Most cages are built from triformylbenzene and different types of diamines and later other stoichiometries have also been explored.[152] The Cooper cages will also be the

focus of this dissertation due to its relevant pore sizes to small guest molecules of separation interests.

Michael Mastalerz in Ruprecht-Karls-Universität Heidelberg developed a slightly more complex imine condensation system with triaminotriptycene and 4-tert-butyl salicyldialdehyde.[153-154] The larger reactant resulted in larger pore sizes as well as higher surface areas.[121] The concept was extended to other imine-based cages of different geometry and size. For instance, a [4 + 4] cubic structure from triptycene trissalicylaldehyde and triptycene triamine were accessible as an amorphous insoluble solid, able to adsorb 18.2 wt % CO2 at ambient conditions.[155] Besides imine condensation, they also explored the reversible formation of boronic esters from boronic acids and diols. Condensation between Triptycene tetraol and benzene triboronic acid yield a large cuboctahedral [12 + 8] cage with pore dimensions of 2 nm and a BET surface area of 3758 m^2/g which hold the records for porous molecular materials.[141] Smaller tetrahedral [4 + 6] boronic ester cages were synthesized too. These cages show selective gas sorption with the preference of saturated hydrocarbon ethane over ethylene and acetylene.[156]

Other dynamic covalent chemistries used for cage compound synthesis are alkene metathesis and alkyne metathesis. Compared to cages connected by imine and boronic ester bonds, alkene and alkyne bonded cages are more rigid and chemically stable. Alkene based cages usually involve porphyrin compounds. Inomata et al. reported a gold nanocluster templated synthesis of a hexaporphyrin cage through alkene end-group metathesis.[157] A large flexible double porphyrin cage was synthesized via DABCO-templated olefin metathesis reaction.[158] The first alkyne based cage was synthesized from alkyne functionalized porphyrin and a special multidentate molybdenum catalyst.[122] The reaction

was carried out without a template and the yield is pretty high (56%). The same group reported a permanently interlocked alkyne cage from simple triyne monomers.[159]

Reversible bond formation allows error correction for the cages to self-assemble as the thermodynamic product. This can give higher yields than for irreversible carbon-carbon bond formation and avoids purification steps. However, in some cases, reversibility can also lead to the formation of interlocked, catenated cages.[160-163] Catenation can occur if there is sufficient space, and the correct geometry, for one or more cages to penetrate through the windows of another. A thermodynamic driving force for this interlocking may be provided by favourable interactions such as π–π stacking.

All reactions discussed so far are batch processes, but the soluble nature of cages also allows them to be synthesized in continuous flow reactions, either irreversibly to produce carbon-carbon bonded cages[164] or using reversible imine condensation[165]. Flow chemistry is attractive in terms of both scalability and safety.

1.2.2 Properties of Porous Organic Cages

1.2.2.1 Porosity

The origin of porosity in zeolites and MOFs can be considered as all intrinsic, as the pores are created by the rigid framework and confined within the bulk structure. Porous solids from non-porous molecules can be considered only have extrinsic porosity. When it comes to POCs, both intrinsic and extrinsic porosity can exist in the solid state. The intrinsic porosity comes from single cage molecules by the cavity that created by rigid cage exterior atoms. And extrinsic porosity arises from intermolecular voids, which might be

due to inefficient packing or even crystalline packing. While the intrinsic porosity are "permanent" to the cage structure, extrinsic porosity can be tuned by changing the packing efficiency via freeze-drying of the solvent.[118]

The extrinsic porosity can also be tuned by changing the vertex functionality. In a homogeneous cage system (only one type of cage are present), bulky aryl groups are attached to the vertices of the cage and reached a BET surface area of 854 m^2/g, which is higher than that of an unfunctionalized cage with the same internal dimension.[166] Another strategy to create extrinsic porosity is introducing heterogeneous cage mixtures.[117] The incompatibility of the different vertex functionalities frustrated the crystallization and resulted in an amorphous solid.

1.2.2.2 Solubility

POCs share some similarities with MOFs, COFs, and porous polymer networks, but because of their discrete molecular nature, they are usually solution processable. The direct impact of solubility on POCs is that traditional solution characterization (e.g., solution NMR, HPLC), purification (e.g., recrystallization, preparative chromatography), and modification (homogeneous organic reaction) techniques can be applied to them that are unavailable for insoluble, extended frameworks.

Solution NMR, MS, and HPLC are most commonly used characterization techniques for POCs as a first step to check the structure and purity of synthesized product. Post-synthetic modifications have been carried out on dissolved cage species.[167] Imines can be readily reduced to amines, which is more chemically stable and can provide extra functionality for guest interaction (CO_2). However, due to more rotational flexibility of the

amine bond, reduced cages usually collapse upon solvent removal and lose permanent porosity.[168-169] The shape persistence can be resumed by tying the amine bond with acetone or formaldehyde.[170] The resulting solid are found to be stable over a large range of pH values (2-12). Cage solubility in common solvents has also allowed them to be used as components in the synthesis of macromolecular porous materials such as cage polymers[171] and cage MOFs[172].

Another material genesis that uniquely resulted from the solubility of POCs are intrinsically porous liquids.[173-177] The working theory of these materials was based on concentrated solutions of organic cages in solvents that are too large to enter the cage pores. The fluidity of the porous liquid offers the potential to be processed as common industrial liquids. For examples, porous liquid can be adopted in a setup similar to CO_2 scrubbing system and use for different gas adsorption applications.

To exploit the solubility of POCs, the underlying implication is not to use POCs in their powder form. So far there have been emerging applications that utilize the solubility of POCs that would be otherwise not accessible with traditional porous materials.[148, 150, 178-179] And we envision the POCs in membranes are promising fields of this material. Further utilizing the solubility will be one the main focus of this dissertation in developing materials for separation applications with POCs.

1.2.2.3 Stability

The stability of POC materials is intrinsically inherent with the formation chemistry. In cages that are formed from reversible reactions such as imine and boronic ester condensation reactions, the week point is the condensation bond, which under

catalytic conditions might go through hydrolysis. Surprisingly, imine-based cages have been found to be stable under boiling water.[180] The water stability of POCs surpass most of MOFs.[181] The acid/base stability has not been studied in the cage materials, but it is intuitive to infer that acid conditions will break the imine bond fairly easy.

In realistic applications, the exposure to acid/base streams is inevitable. The stability of POCs in such conditions need to be considered and proper mitigation routes such as using irreversible bond or converting week reversible bond to more stable bonds are desired. For example. Doonan et al. has demonstrated the alkyne-linked intrinsically porous cages.[164, 182]

Converting vulnerable imine bonds into more stable bonds have also been reported. The tied amine cage mentioned in Section 1.2.2.2 is an example on acid/base stable POC.[170] Likewise, Banerjee has shown that porous organic cages can be stable under both acidic and basic conditions because of keto-enol tautomerism.[183] Few MOFs or COFs are stable over such broad pH ranges; indeed, most zeolites are unstable under either acidic or basic conditions.

1.2.2.4 Structural Flexibility

The flexibility in POC materials has two sources. The first source is the packing flexibility as a result of non-covalent packing interactions that allow crystal phase transition and amorphization. The second source is the bond flexibility within the single cage.

CC1 is among one of the first reported [4+6] imine cages.[139] The cage crystal was reported as a non-porous solid during discovery. However, it was found later that upon exposure to different solvent vapors, crystal-to-crystal transformations occur between a non-porous polymorph (CC1α'), a selectively-porous polymorph (CC1β'), and a non-selectively porous polymorph (CC1γ').[184] The transformation was further elucidated from the conformational changes in the cage molecule itself.[185] The CC1 cage has three conformers as a result of free rotation from its 12 imine bonds-1^{T}-R, 1^{T}-S, and 1^{C3}. The non-porous polymorph, CC1α′, comprises as a racemate of both of the tetrahedral conformers 1^{T}-R and 1^{T}-S. The transformation to the CC1β′ polymorph involves half of the tetrahedral conformers converting to a non-tetrahedral conformer with C_3 symmetry (1^{C3}).

The solvent induced phase transition was demonstrated on several other cage systems.[186] 1,4-dioxane was found to direct CC1, CC2, and CC13 into isoreticular structural with 3-dimensional diamondoid pore channels. For CC13, a dual, interpenetrating pore structure is formed that doubles the gas uptake and the surface area in the resulting dioxane-directed crystals.

1.2.2.5 Crystallinity

POCs are packed in solid state with week non-covalent interactions. This feature leads to the crystal structural flexibility mentioned in Section 1.2.2.4. Not only the crystalline phase will depend on its solvent history,[184] the crystallinity is also dependent on the removal method of the solvent. As mentioned in Section 1.2.2.1, the loss of crystallinity can result in increased surface area and pore volume.[116] However, this is not always true,

the surface area and pore volume also depend on the connectivity of the intrinsic pores. It was also observed that lower surface area could result from the amorphization.[118, 187]

The molecular nature and solubility also allow mixing and crystallization between different cages with similar topology. The first porous co-crystal was constructed from two organic cages: cage 1 and cage 3-R.[188] This is attributed to the favourable interactions between cages of opposite chirality. A solution of CC3-R were added to a solution of CC1, which is racemic in solution but has sufficient molecular flexibility to convert between enantiomers. As the cages crystallize, the chirality of CC1 is directed into the S configuration in the solid state. This design strategy can be extended to ternary cage co-crystals (tercrystals) with three molecular components.[189]

The mixing between hetero-cages usually results in frustration of the crystal packing with the lack of shape or chiral recognition. The cage mixture can be produced by either *de novo* synthesis from linker mixture or by linker exchange of pure cages.[147] The synthesis and isolation of single component mixed-linker cages have not been reported yet.

The crystallization between cages with different topology has been only reported recently. [190-191] In the first example, cavities within a CC3-R solvate that will collapse upon solvent removal were stabilized by introducing a second [3+2] cage molecule that matches the size and shape of the unstable voids.[190] In the second example, a series of tubular cage structures (TCC) were synthesized.[191] The racemic co-crystal was first explored with TCC2-R/TCC2-S cage pairs. The chiral pair recognition was further extended to co-crystals of tubular and tetrahedral cages, i.e., TCC3-R and CC3-S. scXRD revealed that

the structure comprises homochiral, window-to-window CC3-S layers pillared by heterochiral CC3-S/TCC2-R window-to-window interactions.

1.2.3 Design of Porous Organic Cages

The current discovery of new porous organic cage species largely depends on experimentally screening new combinations of linkers.[149, 192] Moreover, the synthetic conditions and activation methods have to be carefully designed and executed to yield the desired pure product.[193] Computational methods can accelerate the design of new porous molecular crystals *in silico*, although there are challenges associated with this approach.[194] The complexity involved in the prediction of solid porous organic cage materials' topologies and properties arises from two aspects: (1) the assembly of linkers into a cage in solution; and (2) the packing of cages into the solid state upon crystallization and desolvation. The latter has been addressed by crystal structure prediction methods employed by Cooper and co-workers[152], in which they utilized crystal structure prediction (CSP) methods to forecast new porous polymorphs of a known molecule.[195] However, the use of energy-structure-function (ESF) maps for crystal structure predictions of solid POC materials requires *a priori* knowledge of the single cage structures. To this end, *in silico* prediction of the single cage structures is still problematic because of a lack of accurate methods for predicting the topology of these cage species.

There are several families of POCs based on different dynamic covalent chemistries (DCC).[196-199] One of the earliest discovered and most intriguing classes of POCs is built from reversible iminization reactions.[115, 146] Understanding the formation of POCs and the selection between different cycloimination stoichiometries (topologies) is important to the

design of new POC materials bearing different cage cavities and functionalities. For example, reactions between trialdehydes and diamines can take place via [2+3], [4+6] or [8+12] cycloiminations.[149, 200-201] Reversible imination reaction enables product selection towards thermodynamically stable topologies. Thus, prediction methods have been proposed based on the energy difference between possible topologies. Prior to this dissertation, there were several attempts to assess the energies of the cage species.[149, 192, 202] For example, Zhang and co-workers calculated the relative energies of several covalent organic polyhedrons (COPs) and their intermediates based on the reactions of triamines and dialdehydes using molecular mechanics.[192] Their computed energies, however, were not consistent with experimental results, which the authors attributed to kinetic effects. Jelfs et al. have shown that the diamine length affects the reaction thermodynamics towards either [2+3] or [4+6] cycloimination.[149] Their density functional theory (DFT) calculations at the PBE-D3/TZVP level were implemented in periodic models where the crystal structure was predetermined by single crystal analysis. Unfortunately, the crystal structure required for periodic calculations is usually unknown during the design process. These observations suggest that to determine the size and the shape of the cages, high-accuracy calculations of formation energies on single cage species are required, especially in the case of imine-based POCs whose electron-rich structures contain many weak van der Waals interactions.

1.2.4 Applications of Porous Organic Cages

1.2.4.1 Adsorption

Cages bearing permanent porosity are good candidates for storage and adsorptive separations of small molecules. Cage systems have shown selectivity in common industrial gases between CO_2/CH_4[121], CO_2/N_2[203-205], H_2/N_2[118], and SF_6/N_2[206]. Current selectivity data are usually calculated from isotherms and lacks breakthrough demonstration.

Due to the large cage size and pore opening, POCs are also investigated in larger molecule separations such as noble gases and organic molecules. The separation between noble gases remains a challenge as their small size difference (Kr (diameter = 3.69 Å;), Xe (4.10 Å) and Rn (4.17 Å)). CC3-R have a cavity of 4.4 Å and a flexible pore opening of around 3.6 Å. These dimensions are potential to be able to separate Kr and Xe molecules. Breakthrough measurements show a clean separation of Krypton (40 ppm) from Xenon (400 ppm) when present as low-concentration impurities diluted in air.[207] The same study also looks into selective adsorption of chiral molecules into CC3.

Building on the latter, there were multiple reports recently in which soluble molecular cages were deposited directly into gas chromatography columns.[208-211] These cage-coated capillary columns showed good selectivity for the separation of a series of organic mixtures and structural isomers, such as n-alkanes, n-alcohols and aromatic hydrocarbons, and enhanced resolution for the separation of chiral molecules. Specific adsorption properties can also be built into porous molecular solids. For example, stable, water-tolerant non-covalent organic frameworks based on electron-rich pyrazoles showed

good adsorption properties for both hydrocarbons and ozone-depleting substances, such as CFCs and fluorocarbons.[212]

Another area in adsorption to exploit the porosity and solubility of POCs is use amorphous POCs for porous molecular composite supports. There is just one report of this so far[178], in which non-porous materials were blended into scrambled porous imine cage materials. Synergistic CO_2 uptake was observed for a PEI/POC composite (17 wt % PEI), with the material delivering a higher CO_2 uptake than either of the two isolated organic components. There are multiple opportunities here. For example, a cheap commercial polymer, such as polystyrene, might be rendered porous-or at least permeable-by simply blending it with molecular pores. In addition, membranes with homogenously distributed fillers can be developed with the amorphous and molecular nature of the cage mixtures.

1.2.4.2 Membranes

The solution processability offers more possibility of fabricating POCs into membrane devices. Song et al. demonstrate a supported POC thin film deposited by spin-coating.[150] This work showed the potential for POCs to be used in membrane separation with easier processability and good gas selectivity. The use of POCs as fillers in MMMs are also promising because of their solution processability and the promise to form homogeneous dispersion within the polymer matrix.

Bushell et al. reported the first synthesis of a POC composite membrane, whereby the cage molecules were induced to crystallize within the membrane matrix.[148] Starting from a solution of PIM-1 and CC3-R, a dispersed but phase-separated composite was generated by in situ crystallization. The study showed that the incorporation of POCs

significantly enhances the permeability with increasing weight percent of the porous cage. The selectivity of gases in this study remains unaffected.

In a computational study, Evans et al. assessed how POCs act as soluble additives that could ameliorate nonselective gas transport pathways in MMMs.[213] Five POCs were investigated, comprising three different families of materials, including the tetrahedral imine cages (CC1, CC2, CC3) reported by Cooper and co-workers, an adamantoid cage from the group of Mastalerz, and the elongated, all-carbon-bonded, triangular dipyramidal cage. The PIM-1/cage MMM composites were generated in silico and benchmarked against experimental data reported by Bushell et al. The power of this approach was to allow analysis of numerous polymer/POC compositions, thereby generating the permeabilities and selectivities for 40 % volume compositions of MMMs comprised of POCs and the polymer hosts Matrimid, Ultem, PIM-1, and PIM-7. This revealed that larger cage structures in the MMMs significantly improve the permeability for H_2/N_2 and H_2/CO_2 separations and is concomitant with a minor increase in the selectivity for H_2.

Mao and Zhang investigated MMM composites incorporating the waterwheel-shaped POC Noria.[214] MMMs were prepared by incorporating Noria as well as its derivatives Noria-Boc and Noria-COtBu as the fillers in the polyimide 6FDA-DAM. The substituted derivatives achieved better integration, giving a homogeneous dispersion of the nanoaggregates and close interfacial mixing of the phases, particularly in the cases where hydrophobic substituents were used. The separation performance of the resulting composites was strongly related to the chemical structures of the additives. Noria/6FDA-DAM composites gave a minor improvement in CO_2/CH_4 selectivity (15 % increase) concomitant with a 53 % decrease in permeability for CH_4. In contrast, the introduction of

Noria-COtBu tends to increase the free volume and gas permeability of the MMMs (e.g., methane permeability increases by nearly 40 %).

1.2.4.3 Catalysis

Cage immobilized catalyst offers the potential for solubilizing heterogeneous catalyst particles. The uniformity of the metal nanoparticles can be well controlled within the cage. The confinement of metal nanoparticles in cage cavities also raise the possibility of size-selective catalysis by controlling guest access through the cage window.

CC3-R was used as a support for Rh nanoparticles with a size of ~ 1.1 nm.[215] The nanoparticles confined in CC3-R can be dissolved in the reaction mixture and used as a homogeneous catalyst. The segregation of the nanoparticles also reduced the aggregation between the nanoparticles. The obtained homogenized heterogeneous catalyst Rh/CC3-R-homo exhibits significantly enhanced catalytic performance toward various liquid-phase catalytic reactions (methanolysis of ammonia borane), as compared with the heterogeneous counterpart Rh/CC3-R-hetero. Moreover, Rh/CC3-R-homo shows excellent durability and recyclability.

Cages synthesized from triphenyl amine-based trialdehydes and cyclohexane diamine were used to immobilize palladium nanoparticles.[216] The well-dispersed cage-embedded NPs exhibit efficient catalytic performance in the cyanation of aryl halides under heterogeneous, additive-free condition. Moreover, these materials have excellent stability and recyclability without any agglomeration of PdNPs after several cycles.

1.3 Research Objectives

The use of traditional porous materials in separation science has been explored extensively. However, technical difficulties associated with their processability pose large impedance in the material and process development. On the other side, POCs are emerging materials with promising features and properties that could potentially advance the field of separations. Before this material can fully exhibit its potential, several key questions are to be answered, which will also serve as the objectives of this thesis.

1. Design and synthesis of POCs with proper structure and properties

The first question is the design and synthesis of POCs with proper structure and properties. There are a number of challenges involved in the design and synthesis of POCs. First, suitable cage precursors must be chosen with the correct geometry to form a cage. Nevertheless, any cage precursor combination can, in principle, form an amorphous polymer network instead of a cage. So the product prediction is also very important. The modeling of cage assemble into the solid state are essential to the prediction of POC solids properties. While the cage crystal prediction method has been explored in the literature, the assembly of linkers into cages and product selection are not fully explored. This will be the first objective of the thesis.

2. Defect engineering of POCs for modified properties

The second question is the modification of POCs with the assistant of computational simulation. As demonstrated in the MOF research area, defects in MOFs can profoundly affect the properties of MOFs. For POCs, the defect existence and effect

on their properties is essentially unexplored. Defect engineering will be the second objective aiming at modifying POC properties towards better performance or stability.

3. Proof of concept applications of POCs in adsorption and membranes

The third question is the applicability of POCs in separation applications. Many researchers as well as our group have envisioned the potential benefits that can be resulted from the solubility and processability of the POC molecules. However, there lacks true demonstration of the benefits other than the simple reproduction of current techniques from extended porous materials. In the last objective, I aim at developing proof-of-concept application examples that truly unlock the potential of POCs.

1.4 Dissertation Organization

This thesis will focus on both fundamental and applied aspects of POCs as mentioned in the Research Objectives. This thesis will start with detailed investigation of the formation mechanisms of imine-based POCs and implying new design strategies for POCs (Chapter 2). Then various defect behavior of POC molecules and solids are studied that showed improved physical properties (Chapter 3&4). One particular type of amorphous POC named amorphous scrambled porous organic cages (ASPOCs) is tested as adsorbent support and membrane additives as proof-of-concept studies of potential applications of POCs (Chapter 5&6).

1.5 References

(1) Energy Technology Perspectives 2017 - Catalysing Energy Technology Transformations. International Energy Agency: France, 2017.

(2) Sholl, D. S.; Lively, R. P. Seven chemical separations: to change the world. *Nature* **2016,** *532*, 435-437.

(3) Pimentel, B. R.; Lively, R. P. Enabling Kinetic Light Hydrocarbon Separation via Crystal Size Engineering of ZIF-8. *Industrial & Engineering Chemistry Research* **2016,** *55*, 12467-12476.

(4) Jacobs, P.; Flanigen, E.; Jansen, J.; van Bekkum, H. *Introduction to zeolite science and practice*. Elsevier: 2001.

(5) Davis, M. E. Ordered porous materials for emerging applications. *Nature* **2002,** *417*, 813-821.

(6) Cejka, J.; Corma, A.; Zones, S. *Zeolites and catalysis: synthesis, reactions and applications*. John Wiley & Sons: 2010.

(7) Martínez, C.; Corma, A. Inorganic molecular sieves: Preparation, modification and industrial application in catalytic processes. *Coordination Chemistry Reviews* **2011,** *255*, 1558-1580.

(8) Gustav, W.; Fritz, S. Production of dry gases. Google Patents: 1928.

(9) Matyear, J. C. Drying of gases. Google Patents: 1959.

(10) Milton, R. M. Molecular sieve adsorbents. Google Patents: 1959.

(11) Langmi, H. W.; McGrady, G. S. Non-hydride systems of the main group elements as hydrogen storage materials. *Coordination Chemistry Reviews* **2007,** *251*, 925-935.

(12) Menon, V. C.; Komarneni, S. Porous Adsorbents for Vehicular Natural Gas Storage: A Review. *Journal of Porous Materials* **1998,** *5*, 43-58.

(13) Wheatley, P. S.; Butler, A. R.; Crane, M. S.; Fox, S.; Xiao, B.; Rossi, A. G.; Megson, I. L.; Morris, R. E. NO-Releasing Zeolites and Their Antithrombotic Properties. *Journal of the American Chemical Society* **2006,** *128*, 502-509.

(14) Yong, Z.; Mata, V.; Rodrigues, A. r. E. Adsorption of carbon dioxide at high temperature—a review. *Separation and Purification Technology* **2002,** *26*, 195-205.

(15) Gollakota, S. V.; Chriswell, C. D. Study of an adsorption process using silicalite for sulfur dioxide removal from combustion gases. *Industrial & Engineering Chemistry Research* **1988,** *27*, 139-143.

(16) Liu, C. Y.; Aika, K.-i. Ammonia Adsorption on Ion Exchanged Y-zeolites as Ammonia Storage Material. *Journal of the Japan Petroleum Institute* **2003,** *46*, 301-307.

(17) Batta, L. Selective adsorption process for air separation. Google Patents: 1973.

(18) Kazuo, K. Adsorption separation process. Google Patents: 1965.

(19) Mckee, D. W. Separation of an oxygen-nitrogen mixture. Google Patents: 1964.

(20) Thakkar, H.; Eastman, S.; Hajari, A.; Rownaghi, A. A.; Knox, J. C.; Rezaei, F. 3D-Printed Zeolite Monoliths for CO2 Removal from Enclosed Environments. *ACS Applied Materials & Interfaces* **2016,** *8*, 27753-27761.

(21) Thakkar, H.; Eastman, S.; Al-Mamoori, A.; Hajari, A.; Rownaghi, A. A.; Rezaei, F. Formulation of Aminosilica Adsorbents into 3D-Printed Monoliths and Evaluation of Their CO2 Capture Performance. *ACS Applied Materials & Interfaces* **2017,** *9*, 7489-7498.

(22) Middelkoop, V.; Coenen, K.; Schalck, J.; Van Sint Annaland, M.; Gallucci, F. 3D printed versus spherical adsorbents for gas sweetening. *Chemical Engineering Journal* **2018**.

(23) Couck, S.; Lefevere, J.; Mullens, S.; Protasova, L.; Meynen, V.; Desmet, G.; Baron, G. V.; Denayer, J. F. M. CO2, CH4 and N2 separation with a 3DFD-printed ZSM-5 monolith. *Chemical Engineering Journal* **2017,** *308*, 719-726.

(24) Zhang, F.; Ma, Y.; Liao, J.; Breedveld, V.; Lively, R. P. Solution-Based 3D Printing of Polymers of Intrinsic Microporosity. *Macromolecular Rapid Communications* **2018,** *39*, 1800274.

(25) Thakkar, H.; Lawson, S.; Rownaghi, A. A.; Rezaei, F. Development of 3D-printed polymer-zeolite composite monoliths for gas separation. *Chemical Engineering Journal* **2018,** *348*, 109-116.

(26) Jia, M.-D.; Peinemann, K.-V.; Behling, R.-D. Ceramic zeolite composite membranes.: Preparation, characterization and gas permeation. *Journal of Membrane Science* **1993,** *82*, 15-26.

(27) Jia, M.-D.; Chen, B.; Noble, R. D.; Falconer, J. L. Ceramic-zeolite composite membranes and their application for separation of vapor/gas mixtures. *Journal of Membrane Science* **1994,** *90*, 1-10.

(28) Kita, H.; Horii, K.; Ohtoshi, Y.; Tanaka, K.; Okamoto, K.-I. Synthesis of a zeolite NaA membrane for pervaporation of water/organic liquid mixtures. *Journal of Materials Science Letters* **1995,** *14*, 206-208.

(29) Kondo, M.; Komori, M.; Kita, H.; Okamoto, K.-i. Tubular-type pervaporation module with zeolite NaA membrane. *Journal of Membrane Science* **1997,** *133*, 133-141.

(30) Morigami, Y.; Kondo, M.; Abe, J.; Kita, H.; Okamoto, K. The first large-scale pervaporation plant using tubular-type module with zeolite NaA membrane. *Separation and Purification Technology* **2001,** *25*, 251-260.

(31) Lai, Z.; Bonilla, G.; Diaz, I.; Nery, J. G.; Sujaoti, K.; Amat, M. A.; Kokkoli, E.; Terasaki, O.; Thompson, R. W.; Tsapatsis, M.; Vlachos, D. G. Microstructural

Optimization of a Zeolite Membrane for Organic Vapor Separation. *Science* **2003,** *300*, 456.

(32) Lai, Z.; Tsapatsis, M. Gas and Organic Vapor Permeation through b-Oriented MFI Membranes. *Industrial & Engineering Chemistry Research* **2004,** *43*, 3000-3007.

(33) Lai, Z.; Tsapatsis, M.; Nicolich, J. P. Siliceous ZSM-5 Membranes by Secondary Growth of b-Oriented Seed Layers. *Advanced Functional Materials* **2004,** *14*, 716-729.

(34) Choi, J.; Ghosh, S.; King, L.; Tsapatsis, M. MFI zeolite membranes from a- and randomly oriented monolayers. *Adsorption* **2006,** *12*, 339-360.

(35) Choi, J.; Jeong, H.-K.; Snyder, M. A.; Stoeger, J. A.; Masel, R. I.; Tsapatsis, M. Grain Boundary Defect Elimination in a Zeolite Membrane by Rapid Thermal Processing. *Science* **2009,** *325*, 590.

(36) Yoo, W. C.; Stoeger, J. A.; Lee, P.-S.; Tsapatsis, M.; Stein, A. High-Performance Randomly Oriented Zeolite Membranes Using Brittle Seeds and Rapid Thermal Processing. *Angewandte Chemie* **2010,** *122*, 8881-8885.

(37) Stoeger, J. A.; Choi, J.; Tsapatsis, M. Rapid thermal processing and separation performance of columnar MFI membranes on porous stainless steel tubes. *Energy & Environmental Science* **2011,** *4*, 3479-3486.

(38) Varoon, K.; Zhang, X.; Elyassi, B.; Brewer, D. D.; Gettel, M.; Kumar, S.; Lee, J. A.; Maheshwari, S.; Mittal, A.; Sung, C.-Y.; Cococcioni, M.; Francis, L. F.; McCormick, A. V.; Mkhoyan, K. A.; Tsapatsis, M. Dispersible Exfoliated Zeolite Nanosheets and Their Application as a Selective Membrane. *Science* **2011,** *334*, 72.

(39) Lee, T.; Choi, J.; Tsapatsis, M. On the performance of c-oriented MFI zeolite Membranes treated by rapid thermal processing. *Journal of Membrane Science* **2013,** *436*, 79-89.

(40) Bedard, R.; Liu, C. Recent Advances in Zeolitic Membranes. *Annual Review of Materials Research* **2018,** *48*, 83-110.

(41) Agrawal, K. V.; Topuz, B.; Pham, T. C. T.; Nguyen, T. H.; Sauer, N.; Rangnekar, N.; Zhang, H.; Narasimharao, K.; Basahel, S. N.; Francis, L. F.; Macosko, C. W.; Al-Thabaiti, S.; Tsapatsis, M.; Yoon, K. B. Oriented MFI Membranes by Gel-Less Secondary Growth of Sub-100 nm MFI-Nanosheet Seed Layers. *Advanced Materials* **2015,** *27*, 3243-3249.

(42) Jeon, M. Y.; Kim, D.; Kumar, P.; Lee, P. S.; Rangnekar, N.; Bai, P.; Shete, M.; Elyassi, B.; Lee, H. S.; Narasimharao, K.; Basahel, S. N.; Al-Thabaiti, S.; Xu, W.; Cho, H. J.; Fetisov, E. O.; Thyagarajan, R.; DeJaco, R. F.; Fan, W.; Mkhoyan, K. A.; Siepmann, J. I.; Tsapatsis, M. Ultra-selective high-flux membranes from directly synthesized zeolite nanosheets. *Nature* **2017,** *543*, 690.

(43) Kim, D.; Jeon, M. Y.; Stottrup, B. L.; Tsapatsis, M. para-Xylene Ultra-selective Zeolite MFI Membranes Fabricated from Nanosheet Monolayers at the Air–Water Interface. *Angewandte Chemie International Edition* **2018,** *57*, 480-485.

(44) Tsapatsis, M.; Kumar, V. A.; Francis, L. *Silica support structure for a zeolite membrane*; Regents of the University of Minnesota, Minneapolis, MN (United States): 2018.

(45) Kosinov, N.; Gascon, J.; Kapteijn, F.; Hensen, E. J. M. Recent developments in zeolite membranes for gas separation. *Journal of Membrane Science* **2016,** *499*, 65-79.

(46) Zhang, H.; Xiao, Q.; Guo, X.; Li, N.; Kumar, P.; Rangnekar, N.; Jeon, M. Y.; Al-Thabaiti, S.; Narasimharao, K.; Basahel, S. N.; Topuz, B.; Onorato, F. J.; Macosko, C. W.; Mkhoyan, K. A.; Tsapatsis, M. Open-Pore Two-Dimensional MFI Zeolite Nanosheets for the Fabrication of Hydrocarbon-Isomer-Selective Membranes on Porous Polymer Supports. *Angewandte Chemie International Edition* **2016,** *55*, 7184-7187.

(47) Lai, Z.; Bonilla, G.; Diaz, I.; Nery, J. G.; Sujaoti, K.; Amat, M. A.; Kokkoli, E.; Terasaki, O.; Thompson, R. W.; Tsapatsis, M.; Vlachos, D. G. Microstructural Optimization of a Zeolite Membrane for Organic Vapor Separation. *Science* **2003,** *300*, 456-460.

(48) Brown, A. J.; Brunelli, N. A.; Eum, K.; Rashidi, F.; Johnson, J. R.; Koros, W. J.; Jones, C. W.; Nair, S. Interfacial microfluidic processing of metal-organic framework hollow fiber membranes. *Science* **2014,** *345*, 72-75.

(49) Kulprathipanja, S.; Neuzil, R. W.; Li, N. N. Separation of fluids by means of mixed matrix membranes. US4740219A, 1988.

(50) Chung, T.-S.; Jiang, L. Y.; Li, Y.; Kulprathipanja, S. Mixed matrix membranes (MMMs) comprising organic polymers with dispersed inorganic fillers for gas separation. *Progress in Polymer Science* **2007,** *32*, 483-507.

(51) Kulprathipanja, S.; Neuzil, R. W.; Li, N. N. Separation of fluids by means of mixed matrix membranes. Google Patents: 1988.

(52) Bastani, D.; Esmaeili, N.; Asadollahi, M. Polymeric mixed matrix membranes containing zeolites as a filler for gas separation applications: A review. *Journal of Industrial and Engineering Chemistry* **2013,** *19*, 375-393.

(53) Duval, J.-M.; Kemperman, A. J. B.; Folkers, B.; Mulder, M. H. V.; Desgrandchamps, G.; Smolders, C. A. Preparation of zeolite filled glassy polymer membranes. *Journal of Applied Polymer Science* **1994,** *54*, 409-418.

(54) Jia, M.; Peinemann, K.-V.; Behling, R.-D. Molecular sieving effect of the zeolite-filled silicone rubber membranes in gas permeation. *Journal of Membrane Science* **1991,** *57*, 289-292.

(55) V G Levich, a.; Krylov, V. S. Surface-Tension-Driven Phenomena. *Annual Review of Fluid Mechanics* **1969,** *1*, 293-316.

(56) Mahajan, R.; Koros, W. J. Factors Controlling Successful Formation of Mixed-Matrix Gas Separation Materials. *Industrial & Engineering Chemistry Research* **2000,** *39*, 2692-2696.

(57) Zecha, H. Stabilization of colloidal dispersions by polymer adsorption. Von TATSUO SATO und RICHARD RUCH. Surfactant Science Series. New York/Basel: Marcel Dekker Inc. 1980. 155 S., 46 Abb., 302 Lit. SFr. 58.—. *Acta Polymerica* **1981,** *32*, 582-582.

(58) Barton, A. F. *CRC handbook of solubility parameters and other cohesion parameters*. Routledge: 2017.

(59) Tarabara, E. M. V. H. V. *Encyclopedia of Membrane Science and Technology*. Wiley: 2013.

(60) Li, Y.; Guan, H.-M.; Chung, T.-S.; Kulprathipanja, S. Effects of novel silane modification of zeolite surface on polymer chain rigidification and partial pore blockage in polyethersulfone (PES)–zeolite A mixed matrix membranes. *Journal of Membrane Science* **2006,** *275*, 17-28.

(61) Merkel, T. C.; Toy, L. G.; Andrady, A. L.; Gracz, H.; Stejskal, E. O. Investigation of Enhanced Free Volume in Nanosilica-Filled Poly(1-trimethylsilyl-1-propyne) by 129Xe NMR Spectroscopy. *Macromolecules* **2003,** *36*, 353-358.

(62) Moore, T. T.; Koros, W. J. Non-ideal effects in organic–inorganic materials for gas separation membranes. *Journal of Molecular Structure* **2005,** *739*, 87-98.

(63) Dunbar, K. R.; Heintz, R. A. Chemistry of transition metal cyanide compounds: Modern perspectives. *Progress in Inorganic Chemistry* **1996**, 283-391.

(64) Chen, B.; Eddaoudi, M.; Hyde, S. T.; Keeffe, M.; Yaghi, O. M. Interwoven Metal-Organic Framework on a Periodic Minimal Surface with Extra-Large Pores. *Science* **2001,** *291*, 1021.

(65) Eddaoudi, M.; Kim, J.; Rosi, N.; Vodak, D.; Wachter, J.; Keeffe, M.; Yaghi, O. M. Systematic Design of Pore Size and Functionality in Isoreticular MOFs and Their Application in Methane Storage. *Science* **2002,** *295*, 469.

(66) Li, H.; Eddaoudi, M.; O'Keeffe, M.; Yaghi, O. M. Design and synthesis of an exceptionally stable and highly porous metal-organic framework. *Nature* **1999,** *402*, 276.

(67) Furukawa, H.; Cordova, K. E.; O'Keeffe, M.; Yaghi, O. M. The Chemistry and Applications of Metal-Organic Frameworks. *Science* **2013,** *341*.

(68) Rosi, N. L.; Eckert, J.; Eddaoudi, M.; Vodak, D. T.; Kim, J.; O'Keeffe, M.; Yaghi, O. M. Hydrogen storage in microporous metal-organic frameworks. *Science* **2003,** *300*, 1127-1129.

(69) Lee, J.; Farha, O. K.; Roberts, J.; Scheidt, K. A.; Nguyen, S. T.; Hupp, J. T. Metal-organic framework materials as catalysts. *Chemical Society Reviews* **2009,** *38*, 1450-1459.

(70) Li, J. R.; Kuppler, R. J.; Zhou, H. C. Selective gas adsorption and separation in metal-organic frameworks. *Chemical Society Reviews* **2009,** *38*, 1477-1504.

(71) Collins, D. J.; Zhou, H.-C. Hydrogen storage in metal–organic frameworks. *Journal of Materials Chemistry* **2007,** *17*, 3154-3160.

(72) He, Y.; Zhou, W.; Qian, G.; Chen, B. Methane storage in metal–organic frameworks. *Chemical Society Reviews* **2014,** *43*, 5657-5678.

(73) Matsuda, R.; Kitaura, R.; Kitagawa, S.; Kubota, Y.; Belosludov, R. V.; Kobayashi, T. C.; Sakamoto, H.; Chiba, T.; Takata, M.; Kawazoe, Y.; Mita, Y. Highly controlled acetylene accommodation in a metal–organic microporous material. *Nature* **2005,** *436*, 238.

(74) Sumida, K.; Rogow, D. L.; Mason, J. A.; McDonald, T. M.; Bloch, E. D.; Herm, Z. R.; Bae, T.-H.; Long, J. R. Carbon Dioxide Capture in Metal–Organic Frameworks. *Chemical Reviews* **2012,** *112*, 724-781.

(75) Mason, J. A.; Sumida, K.; Herm, Z. R.; Krishna, R.; Long, J. R. Evaluating metal–organic frameworks for post-combustion carbon dioxide capture via temperature swing adsorption. *Energy & Environmental Science* **2011,** *4*, 3030-3040.

(76) McDonald, T. M.; Lee, W. R.; Mason, J. A.; Wiers, B. M.; Hong, C. S.; Long, J. R. Capture of Carbon Dioxide from Air and Flue Gas in the Alkylamine-Appended Metal–Organic Framework mmen-Mg2(dobpdc). *Journal of the American Chemical Society* **2012,** *134*, 7056-7065.

(77) McDonald, T. M.; Mason, J. A.; Kong, X.; Bloch, E. D.; Gygi, D.; Dani, A.; Crocellà, V.; Giordanino, F.; Odoh, S. O.; Drisdell, W. S.; Vlaisavljevich, B.; Dzubak, A. L.; Poloni, R.; Schnell, S. K.; Planas, N.; Lee, K.; Pascal, T.; Wan, L. F.; Prendergast, D.; Neaton, J. B.; Smit, B.; Kortright, J. B.; Gagliardi, L.; Bordiga, S.; Reimer, J. A.; Long, J. R. Cooperative insertion of CO2 in diamine-appended metal-organic frameworks. *Nature* **2015,** *519*, 303.

(78) Drisdell, W. S.; Poloni, R.; McDonald, T. M.; Pascal, T. A.; Wan, L. F.; Pemmaraju, C. D.; Vlaisavljevich, B.; Odoh, S. O.; Neaton, J. B.; Long, J. R.; Prendergast, D.; Kortright, J. B. Probing the mechanism of CO2 capture in diamine-appended metal–organic frameworks using measured and simulated X-ray spectroscopy. *Physical Chemistry Chemical Physics* **2015,** *17*, 21448-21457.

(79) Reed, D. A.; Keitz, B. K.; Oktawiec, J.; Mason, J. A.; Runčevski, T.; Xiao, D. J.; Darago, L. E.; Crocellà, V.; Bordiga, S.; Long, J. R. A spin transition mechanism for cooperative adsorption in metal–organic frameworks. *Nature* **2017,** *550*, 96.

(80) Gonzalez, M. I.; Mason, J. A.; Bloch, E. D.; Teat, S. J.; Gagnon, K. J.; Morrison, G. Y.; Queen, W. L.; Long, J. R. Structural characterization of framework–gas interactions in the metal–organic framework Co2(dobdc) by in situ single-crystal X-ray diffraction. *Chemical Science* **2017,** *8*, 4387-4398.

(81) Bachman, J. E.; Reed, D. A.; Kapelewski, M. T.; Chachra, G.; Jonnavittula, D.; Radaelli, G.; Long, J. R. Enabling alternative ethylene production through its selective adsorption in the metal–organic framework Mn2(m-dobdc). *Energy & Environmental Science* **2018,** *11*, 2423-2431.

(82) Choi, S.; Watanabe, T.; Bae, T.-H.; Sholl, D. S.; Jones, C. W. Modification of the Mg/DOBDC MOF with Amines to Enhance CO2 Adsorption from Ultradilute Gases. *The Journal of Physical Chemistry Letters* **2012,** *3*, 1136-1141.

(83) Jiao, Y.; Morelock, C. R.; Burtch, N. C.; Mounfield, W. P.; Hungerford, J. T.; Walton, K. S. Tuning the Kinetic Water Stability and Adsorption Interactions of Mg-MOF-74 by Partial Substitution with Co or Ni. *Industrial & Engineering Chemistry Research* **2015,** *54*, 12408-12414.

(84) Subramanian, S.; Zaworotko, M. J. Porous Solids by Design: [Zn(4,4′-bpy)2(SiF6)]n • xDMF, a Single Framework Octahedral Coordination Polymer with Large Square Channels. *Angewandte Chemie International Edition in English* **1995,** *34*, 2127-2129.

(85) Nugent, P.; Belmabkhout, Y.; Burd, S. D.; Cairns, A. J.; Luebke, R.; Forrest, K.; Pham, T.; Ma, S.; Space, B.; Wojtas, L.; Eddaoudi, M.; Zaworotko, M. J. Porous materials with optimal adsorption thermodynamics and kinetics for CO2 separation. *Nature* **2013,** *495*, 80.

(86) Shekhah, O.; Belmabkhout, Y.; Chen, Z.; Guillerm, V.; Cairns, A.; Adil, K.; Eddaoudi, M. Made-to-order metal-organic frameworks for trace carbon dioxide removal and air capture. *Nature Communications* **2014,** *5*, 4228.

(87) Shekhah, O.; Belmabkhout, Y.; Adil, K.; Bhatt, P. M.; Cairns, A. J.; Eddaoudi, M. A facile solvent-free synthesis route for the assembly of a highly CO2 selective and H2S tolerant NiSIFSIX metal–organic framework. *Chemical Communications* **2015,** *51*, 13595-13598.

(88) Chen, K.-J.; Scott, Hayley S.; Madden, David G.; Pham, T.; Kumar, A.; Bajpai, A.; Lusi, M.; Forrest, Katherine A.; Space, B.; Perry, John J.; Zaworotko, Michael J. Benchmark C2H2/CO2 and CO2/C2H2 Separation by Two Closely Related Hybrid Ultramicroporous Materials. *Chem* **2016,** *1*, 753-765.

(89) Cui, X.; Chen, K.; Xing, H.; Yang, Q.; Krishna, R.; Bao, Z.; Wu, H.; Zhou, W.; Dong, X.; Han, Y.; Li, B.; Ren, Q.; Zaworotko, M. J.; Chen, B. Pore chemistry and size control in hybrid porous materials for acetylene capture from ethylene. *Science* **2016,** *353*, 141.

(90) Cadiau, A.; Adil, K.; Bhatt, P. M.; Belmabkhout, Y.; Eddaoudi, M. A metal-organic framework–based splitter for separating propylene from propane. *Science* **2016,** *353*, 137.

(91) Rangnekar, N.; Mittal, N.; Elyassi, B.; Caro, J.; Tsapatsis, M. Zeolite membranes – a review and comparison with MOFs. *Chemical Society Reviews* **2015,** *44*, 7128-7154.

(92) Ranjan, R.; Tsapatsis, M. Microporous Metal Organic Framework Membrane on Porous Support Using the Seeded Growth Method. *Chemistry of Materials* **2009,** *21*, 4920-4924.

(93) Li, Y.-S.; Liang, F.-Y.; Bux, H.; Feldhoff, A.; Yang, W.-S.; Caro, J. Molecular Sieve Membrane: Supported Metal–Organic Framework with High Hydrogen Selectivity. *Angewandte Chemie* **2010,** *122*, 558-561.

(94) Bux, H.; Chmelik, C.; Krishna, R.; Caro, J. Ethene/ethane separation by the MOF membrane ZIF-8: Molecular correlation of permeation, adsorption, diffusion. *Journal of Membrane Science* **2011,** *369*, 284-289.

(95) Bux, H.; Liang, F.; Li, Y.; Cravillon, J.; Wiebcke, M.; Caro, J. Zeolitic Imidazolate Framework Membrane with Molecular Sieving Properties by Microwave-Assisted Solvothermal Synthesis. *Journal of the American Chemical Society* **2009,** *131*, 16000-16001.

(96) Wang, X.; Sun, M.; Meng, B.; Tan, X.; Liu, J.; Wang, S.; Liu, S. Formation of continuous and highly permeable ZIF-8 membranes on porous alumina and zinc oxide hollow fibers. *Chemical Communications* **2016,** *52*, 13448-13451.

(97) Kwon, H. T.; Jeong, H.-K. In Situ Synthesis of Thin Zeolitic–Imidazolate Framework ZIF-8 Membranes Exhibiting Exceptionally High Propylene/Propane Separation. *Journal of the American Chemical Society* **2013,** *135*, 10763-10768.

(98) Brown, A. J.; Brunelli, N. A.; Eum, K.; Rashidi, F.; Johnson, J. R.; Koros, W. J.; Jones, C. W.; Nair, S. Interfacial microfluidic processing of metal-organic framework hollow fiber membranes. *Science* **2014,** *345*, 72.

(99) Eum, K.; Ma, C.; Koh, D.-Y.; Rashidi, F.; Li, Z.; Jones, C. W.; Lively, R. P.; Nair, S. Zeolitic Imidazolate Framework Membranes Supported on Macroporous Carbon Hollow Fibers by Fluidic Processing Techniques. *Advanced Materials Interfaces* **2017,** *4*, 1700080.

(100) Ma, X.; Kumar, P.; Mittal, N.; Khlyustova, A.; Daoutidis, P.; Mkhoyan, K. A.; Tsapatsis, M. Zeolitic imidazolate framework membranes made by ligand-induced permselectivation. *Science* **2018,** *361*, 1008.

(101) Peng, Y.; Li, Y.; Ban, Y.; Jin, H.; Jiao, W.; Liu, X.; Yang, W. Metal-organic framework nanosheets as building blocks for molecular sieving membranes. *Science* **2014,** *346*, 1356.

(102) Peng, Y.; Li, Y.; Ban, Y.; Yang, W. Two-Dimensional Metal–Organic Framework Nanosheets for Membrane-Based Gas Separation. *Angewandte Chemie International Edition* **2017,** *56*, 9757-9761.

(103) Li, T.; Pan, Y.; Peinemann, K.-V.; Lai, Z. Carbon dioxide selective mixed matrix composite membrane containing ZIF-7 nano-fillers. *Journal of Membrane Science* **2013,** *425-426*, 235-242.

(104) Zornoza, B.; Martinez-Joaristi, A.; Serra-Crespo, P.; Tellez, C.; Coronas, J.; Gascon, J.; Kapteijn, F. Functionalized flexible MOFs as fillers in mixed matrix membranes for highly selective separation of CO2 from CH4 at elevated pressures. *Chemical Communications* **2011,** *47*, 9522-9524.

(105) Liu, X.-L.; Li, Y.-S.; Zhu, G.-Q.; Ban, Y.-J.; Xu, L.-Y.; Yang, W.-S. An Organophilic Pervaporation Membrane Derived from Metal–Organic Framework Nanoparticles for Efficient Recovery of Bio-Alcohols. *Angewandte Chemie International Edition* **2011,** *50*, 10636-10639.

(106) Rodenas, T.; van Dalen, M.; García-Pérez, E.; Serra-Crespo, P.; Zornoza, B.; Kapteijn, F.; Gascon, J. Visualizing MOF Mixed Matrix Membranes at the Nanoscale: Towards Structure-Performance Relationships in CO2/CH4 Separation Over NH2-MIL-53(Al)@PI. *Advanced Functional Materials* **2014,** *24*, 249-256.

(107) Yang, T.; Xiao, Y.; Chung, T.-S. Poly-/metal-benzimidazole nano-composite membranes for hydrogen purification. *Energy & Environmental Science* **2011,** *4*, 4171-4180.

(108) Tanh Jeazet, H. B.; Staudt, C.; Janiak, C. Metal–organic frameworks in mixed-matrix membranes for gas separation. *Dalton Transactions* **2012,** *41*, 14003-14027.

(109) Galizia, M.; Chi, W. S.; Smith, Z. P.; Merkel, T. C.; Baker, R. W.; Freeman, B. D. 50th Anniversary Perspective: Polymers and Mixed Matrix Membranes for Gas and Vapor Separation: A Review and Prospective Opportunities. *Macromolecules* **2017,** *50*, 7809-7843.

(110) Maserati, L.; Meckler, S. M.; Bachman, J. E.; Long, J. R.; Helms, B. A. Diamine-Appended Mg2(dobpdc) Nanorods as Phase-Change Fillers in Mixed-Matrix Membranes for Efficient CO2/N2 Separations. *Nano Letters* **2017,** *17*, 6828-6832.

(111) Liu, G.; Chernikova, V.; Liu, Y.; Zhang, K.; Belmabkhout, Y.; Shekhah, O.; Zhang, C.; Yi, S.; Eddaoudi, M.; Koros, W. J. Mixed matrix formulations with MOF molecular sieving for key energy-intensive separations. *Nature Materials* **2018,** *17*, 283-289.

(112) Tozawa, T.; Swamy, S.; Jiang, S.; Adams, D. J.; Shakespeare, S.; Jones, J. T. A.; Clowes, R.; Bradshaw, D.; Hasell, T.; Bacsa, J.; Trewin, A.; Slawin, A. M.; Steiner, A.; Cooper, A. I. Porous organic cages. *Abstracts of Papers of the American Chemical Society* **2009,** *238*.

(113) Mastalerz, M. Shape-Persistent Organic Cage Compounds by Dynamic Covalent Bond Formation. *Angewandte Chemie-International Edition* **2010,** *49*, 5042-5053.

(114) Jin, Y.; Voss, B. A.; Noble, R. D.; Zhang, W. A Shape-Persistent Organic Molecular Cage with High Selectivity for the Adsorption of CO2 over N-2. *Angewandte Chemie-International Edition* **2010,** *49*, 6348-6351.

(115) Cooper, A. I. Nanoporous Organics Enter the Cage Age. *Angewandte Chemie-International Edition* **2011,** *50*, 996-998.

(116) Hasell, T.; Chong, S. Y.; Jelfs, K. E.; Adams, D. J.; Cooper, A. I. Porous Organic Cage Nanocrystals by Solution Mixing. *Journal of the American Chemical Society* **2012,** *134*, 588-598.

(117) Jiang, S.; Jones, J. T. A.; Hasell, T.; Blythe, C. E.; Adams, D. J.; Trewin, A.; Cooper, A. I. Porous organic molecular solids by dynamic covalent scrambling. *Nature Communications* **2011,** *2*.

(118) Jiang, S.; Jelfs, K. E.; Holden, D.; Hasell, T.; Chong, S. Y.; Haranczyk, M.; Trewin, A.; Cooper, A. I. Molecular dynamics simulations of gas selectivity in amorphous porous molecular solids. *Journal of the American Chemical Society* **2013,** *135*, 17818-17830.

(119) Holst, J. R.; Trewin, A.; Cooper, A. I. Porous organic molecules. *Nature Chemistry* **2010,** *2*, 915-920.

(120) Jin, Y.; Voss, B. A.; Jin, A.; Long, H.; Noble, R. D.; Zhang, W. Highly CO_2-selective organic molecular cages: what determines the CO_2 selectivity. *Journal of the American Chemical Society* **2011,** *133*, 6650-6658.

(121) Mastalerz, M.; Schneider, M. W.; Oppel, I. M.; Presly, O. A Salicylbisimine Cage Compound with High Surface Area and Selective CO2/CH4 Adsorption. *Angewandte Chemie International Edition* **2011,** *50*, 1046-1051.

(122) Zhang, C.; Wang, Q.; Long, H.; Zhang, W. A Highly C70 Selective Shape-Persistent Rectangular Prism Constructed through One-Step Alkyne Metathesis. *Journal of the American Chemical Society* **2011,** *133*, 20995-21001.

(123) Brutschy, M.; Schneider, M. W.; Mastalerz, M.; Waldvogel, S. R. Porous organic cage compounds as highly potent affinity materials for sensing by quartz crystal microbalances. *Advanced Materials* **2012,** *24*, 6049-6052.

(124) Chen, L.; Reiss, P. S.; Chong, S. Y.; Holden, D.; Jelfs, K. E.; Hasell, T.; Little, M. A.; Kewley, A.; Briggs, M. E.; Stephenson, A. Separation of rare gases and chiral

molecules by selective binding in porous organic cages. *Nature materials* **2014,** *13*, 954-960.

(125) O'Reilly, N.; Giri, N.; James, S. L. Porous Liquids. *Chemistry – A European Journal* **2007,** *13*, 3020-3025.

(126) Giri, N.; Davidson, C. E.; Melaugh, G.; Del Popolo, M. G.; Jones, J. T. A.; Hasell, T.; Cooper, A. I.; Horton, P. N.; Hursthouse, M. B.; James, S. L. Alkylated organic cages: from porous crystals to neat liquids. *Chemical Science* **2012,** *3*, 2153-2157.

(127) Melaugh, G.; Giri, N.; Davidson, C. E.; James, S. L.; Del Popolo, M. G. Designing and understanding permanent microporosity in liquids. *Physical Chemistry Chemical Physics* **2014,** *16*, 9422-9431.

(128) Giri, N.; Del Pópolo, M. G.; Melaugh, G.; Greenaway, R. L.; Rätzke, K.; Koschine, T.; Pison, L.; Gomes, M. F. C.; Cooper, A. I.; James, S. L. Liquids with permanent porosity. *Nature* **2015,** *527*, 216-220.

(129) James, S. L. The Dam Bursts for Porous Liquids. *Advanced Materials* **2016**, n/a-n/a.

(130) Allcock, H.; Siegel, L. Phosphonitrilic compounds. III. 1 Molecular inclusion compounds of tris (o-phenylenedioxy) phosphonitrile trimer. *Journal of the American Chemical Society* **1964,** *86*, 5140-5144.

(131) Barrer, R. M.; Shanson, V. H. Dianin's compound as a zeolitic sorbent. *Journal of the Chemical Society, Chemical Communications* **1976**, 333-334.

(132) Atwood, J. L.; Barbour, L. J.; Jerga, A.; Schottel, B. L. Guest transport in a nonporous organic solid via dynamic van der Waals cooperativity. *Science* **2002,** *298*, 1000-1002.

(133) Freeman, W.; Mock, W.; Shih, N. Cucurbituril. *Journal of the American Chemical Society* **1981,** *103*, 7367-7368.

(134) Kudo, H.; Hayashi, R.; Mitani, K.; Yokozawa, T.; Kasuga, N. C.; Nishikubo, T. Molecular waterwheel (Noria) from a simple condensation of resorcinol and an alkanedial. *Angewandte Chemie* **2006,** *118*, 8116-8120.

(135) Bezzu, C. G.; Helliwell, M.; Warren, J. E.; Allan, D. R.; McKeown, N. B. Heme-like coordination chemistry within nanoporous molecular crystals. *Science* **2010,** *327*, 1627-1630.

(136) Mastalerz, M.; Oppel, I. M. Rational construction of an extrinsic porous molecular crystal with an extraordinary high specific surface area. *Angewandte Chemie International Edition* **2012,** *51*, 5252-5255.

(137) Kohl, B.; Rominger, F.; Mastalerz, M. Crystal structures of a molecule designed not to pack tightly. *Chemistry–A European Journal* **2015,** *21*, 17308-17313.

(138) Ashton, P. R.; Girreser, U.; Giuffrida, D.; Kohnke, F. H.; Mathias, J. P.; Raymo, F. M.; Slawin, A. M. Z.; Stoddart, J. F.; Williams, D. J. Molecular belts. 2. Substrate-directed syntheses of belt-type and cage-type structures. *Journal of the American Chemical Society* **1993,** *115*, 5422-5429.

(139) Tozawa, T.; Jones, J. T.; Swamy, S. I.; Jiang, S.; Adams, D. J.; Shakespeare, S.; Clowes, R.; Bradshaw, D.; Hasell, T.; Chong, S. Y. Porous organic cages. *Nature materials* **2009,** *8*, 973.

(140) Horng, Y. C.; Lin, T. L.; Tu, C. Y.; Sung, T. J.; Hsieh, C. C.; Hu, C. H.; Lee, H. M.; Kuo, T. S. Preparation of a Reversible Redox‐Controlled Cage‐Type Molecule Linked by Disulfide Bonds. *European Journal of Organic Chemistry* **2009,** *2009*, 1511-1514.

(141) Zhang, G.; Presly, O.; White, F.; Oppel, I. M.; Mastalerz, M. A permanent mesoporous organic cage with an exceptionally high surface area. *Angewandte Chemie International Edition* **2014,** *53*, 1516-1520.

(142) Wang, Q.; Zhang, C.; Noll, B. C.; Long, H.; Jin, Y.; Zhang, W. A tetrameric cage with D2h symmetry through alkyne metathesis. *Angewandte Chemie International Edition* **2014,** *53*, 10663-10667.

(143) MacDowell, D.; Nelson, J. Facile synthesis of a new family of cage molecules. *Tetrahedron Letters* **1988,** *29*, 385-386.

(144) Liu, X.; Liu, Y.; Li, G.; Warmuth, R. One-Pot, 18-Component Synthesis of an Octahedral Nanocontainer Molecule. *Angewandte Chemie International Edition* **2006,** *45*, 901-904.

(145) Quan, M. L. C.; Cram, D. J. Constrictive binding of large guests by a hemicarcerand containing four portals. *Journal of the American Chemical Society* **1991,** *113*, 2754-2755.

(146) Tozawa, T.; Jones, J. T. A.; Swamy, S. I.; Jiang, S.; Adams, D. J.; Shakespeare, S.; Clowes, R.; Bradshaw, D.; Hasell, T.; Chong, S. Y.; Tang, C.; Thompson, S.; Parker, J.; Trewin, A.; Bacsa, J.; Slawin, A. M. Z.; Steiner, A.; Cooper, A. I. Porous organic cages. *Nature Materials* **2009,** *8*, 973-978.

(147) Jiang, S.; Jones, J. T. A.; Hasell, T.; Blythe, C. E.; Adams, D. J.; Trewin, A.; Cooper, A. I. Porous organic molecular solids by dynamic covalent scrambling. *Nature Communications* **2011,** *2*, 207.

(148) Bushell, A. F.; Budd, P. M.; Attfield, M. P.; Jones, J. T. A.; Hasell, T.; Cooper, A. I.; Bernardo, P.; Bazzarelli, F.; Clarizia, G.; Jansen, J. C. Nanoporous Organic Polymer/Cage Composite Membranes. *Angewandte Chemie-International Edition* **2013,** *52*, 1253-1256.

(149) Jelfs, K. E.; Eden, E. G. B.; Culshaw, J. L.; Shakespeare, S.; Pyzer-Knapp, E. O.; Thompson, H. P. G.; Bacsa, J.; Day, G. M.; Adams, D. J.; Cooper, A. I. In silico Design of

Supramolecules from Their Precursors: Odd-Even Effects in Cage-Forming Reactions. *Journal of the American Chemical Society* **2013,** *135*, 9307-9310.

(150) Song, Q.; Jiang, S.; Hasell, T.; Liu, M.; Sun, S.; Cheetham, A. K.; Sivaniah, E.; Cooper, A. I. Porous Organic Cage Thin Films and Molecular-Sieving Membranes. *Advanced Materials* **2016**, n/a-n/a.

(151) Giri, N.; Del Popolo, M. G.; Melaugh, G.; Greenaway, R. L.; Ratzke, K.; Koschine, T.; Pison, L.; Gomes, M. F. C.; Cooper, A. I.; James, S. L. Liquids with permanent porosity. *Nature* **2015,** *527*, 216-+.

(152) Slater, A. G.; Little, M. A.; Pulido, A.; Chong, S. Y.; Holden, D.; Chen, L.; Morgan, C.; Wu, X.; Cheng, G.; Clowes, R.; Briggs, M. E.; Hasell, T.; Jelfs, K. E.; Day, G. M.; Cooper, A. I. Reticular synthesis of porous molecular 1D nanotubes and 3D networks. *Nat. Chem.* **2017,** *9*, 17-25.

(153) Mastalerz, M. One-pot synthesis of a shape-persistent endo-functionalised nano-sized adamantoid compound. *Chemical Communications* **2008**, 4756-4758.

(154) Mastalerz, M. Porous Shape-Persistent Organic Cage Compounds of Different Size, Geometry, and Function. *Accounts of Chemical Research* **2018**.

(155) Elbert, S. M.; Rominger, F.; Mastalerz, M. Synthesis of a Rigid C3v-Symmetric Tris-salicylaldehyde as a Precursor for a Highly Porous Molecular Cube. *Chemistry – A European Journal* **2014,** *20*, 16707-16720.

(156) Elbert, S. M.; Regenauer, N. I.; Schindler, D.; Zhang, W.-S.; Rominger, F.; Schröder, R. R.; Mastalerz, M. Shape-Persistent Tetrahedral [4+6] Boronic Ester Cages with Different Degrees of Fluoride Substitution. *Chemistry – A European Journal* **2018,** *24*, 11438-11443.

(157) Inomata, T.; Konishi, K. Gold nanocluster confined within a cage: template-directed formation of a hexaporphyrin cage and its confinement capability. *Chemical Communications* **2003**, 1282-1283.

(158) Taesch, J.; Heitz, V.; Topić, F.; Rissanen, K. Templated synthesis of a large and flexible covalent porphyrinic cage bearing orthogonal recognition sites. *Chemical Communications* **2012,** *48*, 5118-5120.

(159) Wang, Q.; Yu, C.; Long, H.; Du, Y.; Jin, Y.; Zhang, W. Solution-Phase Dynamic Assembly of Permanently Interlocked Aryleneethynylene Cages through Alkyne Metathesis. *Angewandte Chemie International Edition* **2015,** *54*, 7550-7554.

(160) Gil‐Ramírez, G.; Leigh, D. A.; Stephens, A. J. Catenanes: fifty years of molecular links. *Angewandte Chemie International Edition* **2015,** *54*, 6110-6150.

(161) Hasell, T.; Wu, X.; Jones, J. T.; Bacsa, J.; Steiner, A.; Mitra, T.; Trewin, A.; Adams, D. J.; Cooper, A. I. Triply interlocked covalent organic cages. *Nature chemistry* **2010,** *2*, 750.

(162) Wang, Q.; Yu, C.; Long, H.; Du, Y.; Jin, Y.; Zhang, W. Solution‐Phase Dynamic Assembly of Permanently Interlocked Aryleneethynylene Cages through Alkyne Metathesis. *Angewandte Chemie* **2015,** *127*, 7660-7664.

(163) Zhang, G.; Presly, O.; White, F.; Oppel, I. M.; Mastalerz, M. A Shape‐Persistent Quadruply Interlocked Giant Cage Catenane with Two Distinct Pores in the Solid State. *Angewandte Chemie* **2014,** *126*, 5226-5230.

(164) Kitchin, M.; Konstas, K.; Sumby, C. J.; Czyz, M. L.; Valente, P.; Hill, M. R.; Polyzos, A.; Doonan, C. J. Continuous flow synthesis of a carbon-based molecular cage macrocycle via a three-fold homocoupling reaction. *Chemical Communications* **2015,** *51*, 14231-14234.

(165) Briggs, M. E.; Slater, A. G.; Lunt, N.; Jiang, S.; Little, M. A.; Greenaway, R. L.; Hasell, T.; Battilocchio, C.; Ley, S. V.; Cooper, A. I. Dynamic flow synthesis of porous organic cages. *Chemical Communications* **2015,** *51*, 17390-17393.

(166) Bojdys, M. J.; Briggs, M. E.; Jones, J. T. A.; Adams, D. J.; Chong, S. Y.; Schmidtmann, M.; Cooper, A. I. Supramolecular Engineering of Intrinsic and Extrinsic Porosity in Covalent Organic Cages. *Journal of the American Chemical Society* **2011,** *133*, 16566-16571.

(167) Schneider, M. W.; Oppel, I. M.; Griffin, A.; Mastalerz, M. Post-Modification of the Interior of Porous Shape-Persistent Organic Cage Compounds. *Angewandte Chemie International Edition* **2013,** *52*, 3611-3615.

(168) Culshaw, J. L.; Cheng, G.; Schmidtmann, M.; Hasell, T.; Liu, M.; Adams, D. J.; Cooper, A. I. Dodecaamide Cages: Organic 12-Arm Building Blocks for Supramolecular Chemistry. *Journal of the American Chemical Society* **2013,** *135*, 10007-10010.

(169) Jin, Y.; Voss, B. A.; Noble, R. D.; Zhang, W. A Shape-Persistent Organic Molecular Cage with High Selectivity for the Adsorption of CO2 over N2. *Angewandte Chemie International Edition* **2010,** *49*, 6348-6351.

(170) Liu, M.; Little, M. A.; Jelfs, K. E.; Jones, J. T. A.; Schmidtmann, M.; Chong, S. Y.; Hasell, T.; Cooper, A. I. Acid- and Base-Stable Porous Organic Cages: Shape Persistence and pH Stability via Post-synthetic "Tying" of a Flexible Amine Cage. *Journal of the American Chemical Society* **2014,** *136*, 7583-7586.

(171) Buyukcakir, O.; Seo, Y.; Coskun, A. Thinking outside the cage: controlling the extrinsic porosity and gas uptake properties of shape-persistent molecular cages in nanoporous polymers. *Chemistry of Materials* **2015,** *27*, 4149-4155.

(172) Swamy, S. I.; Bacsa, J.; Jones, J. T.; Stylianou, K. C.; Steiner, A.; Ritchie, L. K.; Hasell, T.; Gould, J. A.; Laybourn, A.; Khimyak, Y. Z. A metal− organic framework with a covalently prefabricated porous organic linker. *Journal of the American Chemical Society* **2010,** *132*, 12773-12775.

(173) Giri, N.; Del Pópolo, M. G.; Melaugh, G.; Greenaway, R. L.; Rätzke, K.; Koschine, T.; Pison, L.; Gomes, M. F. C.; Cooper, A. I.; James, S. L. Liquids with permanent porosity. *Nature* **2015,** *527*, 216.

(174) Giri, N.; Davidson, C. E.; Melaugh, G.; Del Pópolo, M. G.; Jones, J. T.; Hasell, T.; Cooper, A. I.; Horton, P. N.; Hursthouse, M. B.; James, S. L. Alkylated organic cages: from porous crystals to neat liquids. *Chemical Science* **2012,** *3*, 2153-2157.

(175) Mastalerz, M. Materials chemistry: Liquefied molecular holes. *Nature* **2015,** *527*, 174.

(176) Melaugh, G.; Giri, N.; Davidson, C. E.; James, S. L.; Del Pópolo, M. G. Designing and understanding permanent microporosity in liquids. *Physical Chemistry Chemical Physics* **2014,** *16*, 9422-9431.

(177) O'Reilly, N.; Giri, N.; James, S. L. Porous liquids. *Chemistry–A European Journal* **2007,** *13*, 3020-3025.

(178) Jiang, S.; Chen, L.; Briggs, M. E.; Hasell, T.; Cooper, A. I. Functional porous composites by blending with solution-processable molecular pores. *Chemical Communications* **2016,** *52*, 6895-6898.

(179) Hasell, T.; Zhang, H.; Cooper, A. I. Solution-Processable Molecular Cage Micropores for Hierarchically Porous Materials. *Advanced Materials* **2012,** *24*, 5732-5737.

(180) Hasell, T.; Schmidtmann, M.; Stone, C. A.; Smith, M. W.; Cooper, A. I. Reversible water uptake by a stable imine-based porous organic cage. *Chemical Communications* **2012,** *48*, 4689-4691.

(181) Burtch, N. C.; Jasuja, H.; Walton, K. S. Water stability and adsorption in metal–organic frameworks. *Chemical reviews* **2014,** *114*, 10575-10612.

(182) Avellaneda, A.; Valente, P.; Burgun, A.; Evans, J. D.; Markwell-Heys, A. W.; Rankine, D.; Nielsen, D. J.; Hill, M. R.; Sumby, C. J.; Doonan, C. J. Kinetically Controlled Porosity in a Robust Organic Cage Material. *Angewandte Chemie International Edition* **2013,** *52*, 3746-3749.

(183) Bera, S.; Basu, A.; Tothadi, S.; Garai, B.; Banerjee, S.; Vanka, K.; Banerjee, R. Odd–Even Alternation in Tautomeric Porous Organic Cages with Exceptional Chemical Stability. *Angewandte Chemie International Edition* **2017,** *56*, 2123-2126.

(184) Jones, J. T. A.; Holden, D.; Mitra, T.; Hasell, T.; Adams, D. J.; Jelfs, K. E.; Trewin, A.; Willock, D. J.; Day, G. M.; Bacsa, J.; Steiner, A.; Cooper, A. I. On-Off Porosity

Switching in a Molecular Organic Solid. *Angewandte Chemie-International Edition* **2011,** *50*, 749-753.

(185) Jelfs, K. E.; Schiffmann, F.; Jones, J. T. A.; Slater, B.; Cora, F.; Cooper, A. I. Conformer interconversion in a switchable porous organic cage. *Physical Chemistry Chemical Physics* **2011,** *13*, 20081-20085.

(186) Hasell, T.; Culshaw, J. L.; Chong, S. Y.; Schmidtmann, M.; Little, M. A.; Jelfs, K. E.; Pyzer-Knapp, E. O.; Shepherd, H.; Adams, D. J.; Day, G. M.; Cooper, A. I. Controlling the Crystallization of Porous Organic Cages: Molecular Analogs of Isoreticular Frameworks Using Shape-Specific Directing Solvents. *Journal of the American Chemical Society* **2014,** *136*, 1438-1448.

(187) Schneider, M. W.; Oppel, I. M.; Ott, H.; Lechner, L. G.; Hauswald, H. J. S.; Stoll, R.; Mastalerz, M. Periphery‐Substituted [4+ 6] Salicylbisimine Cage Compounds with Exceptionally High Surface Areas: Influence of the Molecular Structure on Nitrogen Sorption Properties. *Chemistry–A European Journal* **2012,** *18*, 836-847.

(188) Jones, J. T. A.; Hasell, T.; Wu, X.; Bacsa, J.; Jelfs, K. E.; Schmidtmann, M.; Chong, S. Y.; Adams, D. J.; Trewin, A.; Schiffman, F.; Cora, F.; Slater, B.; Steiner, A.; Day, G. M.; Cooper, A. I. Modular and predictable assembly of porous organic molecular crystals. *Nature* **2011,** *474*, 367.

(189) Hasell, T.; Chong, S. Y.; Schmidtmann, M.; Adams, D. J.; Cooper, A. I. Porous organic alloys. *Angewandte Chemie* **2012,** *124*, 7266-7269.

(190) Little, M. A.; Briggs, M. E.; Jones, J. T. A.; Schmidtmann, M.; Hasell, T.; Chong, S. Y.; Jelfs, K. E.; Chen, L.; Cooper, A. I. Trapping virtual pores by crystal retro-engineering. *Nature Chemistry* **2015,** *7*, 153.

(191) Slater, A. G.; Little, M. A.; Pulido, A.; Chong, S. Y.; Holden, D.; Chen, L.; Morgan, C.; Wu, X.; Cheng, G.; Clowes, R.; Briggs, M. E.; Hasell, T.; Jelfs, K. E.; Day, G. M.; Cooper, A. I. Reticular synthesis of porous molecular 1D nanotubes and 3D networks. *Nature Chemistry* **2016,** *9*, 17.

(192) Jin, Y.; Jin, A.; McCaffrey, R.; Long, H.; Zhang, W. Design Strategies for Shape-Persistent Covalent Organic Polyhedrons (COPs) through Imine Condensation/Metathesis. *Journal of Organic Chemistry* **2012,** *77*, 7392-7400.

(193) Briggs, M. E.; Cooper, A. I. A Perspective on the Synthesis, Purification, and Characterization of Porous Organic Cages. *Chemistry of Materials* **2017,** *29*, 149-157.

(194) Evans, J. D.; Jelfs, K. E.; Day, G. M.; Doonan, C. J. Application of computational methods to the design and characterisation of porous molecular materials. *Chemical Society Reviews* **2017,** *46*, 3286-3301.

(195) Pulido, A.; Chen, L.; Kaczorowski, T.; Holden, D.; Little, M. A.; Chong, S. Y.; Slater, B. J.; McMahon, D. P.; Bonillo, B.; Stackhouse, C. J.; Stephenson, A.; Kane, C. M.;

Clowes, R.; Hasell, T.; Cooper, A. I.; Day, G. M. Functional materials discovery using energy–structure–function maps. *Nature* **2017,** *543*, 657-664.

(196) Jin, Y.; Zhu, Y.; Zhang, W. Development of organic porous materials through Schiff-base chemistry. *CrystEngComm* **2013,** *15*, 1484-1499.

(197) Jin, Y.; Wang, Q.; Taynton, P.; Zhang, W. Dynamic Covalent Chemistry Approaches Toward Macrocycles, Molecular Cages, and Polymers. *Acc. Chem. Res.* **2014,** *47*, 1575-1586.

(198) Zhang, G.; Mastalerz, M. Organic cage compounds - from shape-persistency to function. *Chem. Soc. Rev.* **2014,** *43*, 1934-1947.

(199) Hasell, T.; Cooper, A. I. Porous organic cages: soluble, modular and molecular pores. *Nature Reviews Materials* **2016,** *1*, 16053.

(200) Jiang, S.; Bacsa, J.; Wu, X.; Jones, J. T. A.; Dawson, R.; Trewin, A.; Adams, D. J.; Cooper, A. I. Selective gas sorption in a 2+3 'propeller' cage crystal. *Chemical Communications* **2011,** *47*, 8919-8921.

(201) Jelfs, K. E.; Wu, X.; Schmidtmann, M.; Jones, J. T. A.; Warren, J. E.; Adams, D. J.; Cooper, A. I. Large Self-Assembled Chiral Organic Cages: Synthesis, Structure, and Shape Persistence. *Angewandte Chemie-International Edition* **2011,** *50*, 10653-10656.

(202) Santolini, V.; Miklitz, M.; Berardo, E.; Jelfs, K. E. Topological landscapes of porous organic cages. *Nanoscale* **2017,** *9*, 5280-5298.

(203) Ding, H.; Yang, Y.; Li, B.; Pan, F.; Zhu, G.; Zeller, M.; Yuan, D.; Wang, C. Targeted synthesis of a large triazine-based [4+ 6] organic molecular cage: structure, porosity and gas separation. *Chemical Communications* **2015,** *51*, 1976-1979.

(204) Hong, S.; Rohman, M. R.; Jia, J.; Kim, Y.; Moon, D.; Kim, Y.; Ko, Y. H.; Lee, E.; Kim, K. Porphyrin boxes: rationally designed porous organic cages. *Angewandte Chemie International Edition* **2015,** *54*, 13241-13244.

(205) Jiang, S.; Bacsa, J.; Wu, X.; Jones, J. T.; Dawson, R.; Trewin, A.; Adams, D. J.; Cooper, A. I. Selective gas sorption in a [2+ 3]'propeller'cage crystal. *Chemical Communications* **2011,** *47*, 8919-8921.

(206) Hasell, T.; Miklitz, M.; Stephenson, A.; Little, M. A.; Chong, S. Y.; Clowes, R.; Chen, L.; Holden, D.; Tribello, G. A.; Jelfs, K. E. Porous organic cages for sulfur hexafluoride separation. *Journal of the American Chemical Society* **2016,** *138*, 1653-1659.

(207) Chen, L.; Reiss, P. S.; Chong, S. Y.; Holden, D.; Jelfs, K. E.; Hasell, T.; Little, M. A.; Kewley, A.; Briggs, M. E.; Stephenson, A.; Thomas, K. M.; Armstrong, J. A.; Bell, J.; Busto, J.; Noel, R.; Liu, J.; Strachan, D. M.; Thallapally, P. K.; Cooper, A. I. Separation of rare gases and chiral molecules by selective binding in porous organic cages. *Nature Materials* **2014,** *13*, 954.

(208) Kewley, A.; Stephenson, A.; Chen, L.; Briggs, M. E.; Hasell, T.; Cooper, A. I. Porous organic cages for gas chromatography separations. *Chemistry of Materials* **2015,** *27*, 3207-3210.

(209) Xie, S.-M.; Zhang, J.-H.; Fu, N.; Wang, B.-J.; Chen, L.; Yuan, L.-M. A chiral porous organic cage for molecular recognition using gas chromatography. *Analytica chimica acta* **2016,** *903*, 156-163.

(210) Zhang, J.-H.; Xie, S.-M.; Chen, L.; Wang, B.-J.; He, P.-G.; Yuan, L.-M. Homochiral porous organic cage with high selectivity for the separation of racemates in gas chromatography. *Analytical chemistry* **2015,** *87*, 7817-7824.

(211) Zhang, J.-H.; Xie, S.-M.; Wang, B.-J.; He, P.-G.; Yuan, L.-M. Highly selective separation of enantiomers using a chiral porous organic cage. *Journal of Chromatography A* **2015,** *1426*, 174-182.

(212) Chen, T.-H.; Popov, I.; Kaveevivitchai, W.; Chuang, Y.-C.; Chen, Y.-S.; Daugulis, O.; Jacobson, A. J.; Miljanić, O. Š. Thermally robust and porous noncovalent organic framework with high affinity for fluorocarbons and CFCs. *Nature communications* **2014,** *5*, 5131.

(213) Evans, J. D.; Huang, D. M.; Hill, M. R.; Sumby, C. J.; Thornton, A. W.; Doonan, C. J. Feasibility of Mixed Matrix Membrane Gas Separations Employing Porous Organic Cages. *The Journal of Physical Chemistry C* **2013,** *118*, 1523-1529.

(214) Mao, H.; Zhang, S. Mixed-matrix membranes incorporated with porous shape-persistent organic cages for gas separation. *Journal of Colloid and Interface Science* **2017,** *490*, 29-36.

(215) Sun, J.-K.; Zhan, W.-W.; Akita, T.; Xu, Q. Toward Homogenization of Heterogeneous Metal Nanoparticle Catalysts with Enhanced Catalytic Performance: Soluble Porous Organic Cage as a Stabilizer and Homogenizer. *Journal of the American Chemical Society* **2015,** *137*, 7063-7066.

(216) Mondal, B.; Acharyya, K.; Howlader, P.; Mukherjee, P. S. Molecular Cage Impregnated Palladium Nanoparticles: Efficient, Additive-Free Heterogeneous Catalysts for Cyanation of Aryl Halides. *Journal of the American Chemical Society* **2016,** *138*, 1709-1716.

CHAPTER 2. FORMATION MECHANISMS OF IMINE BASED POROUS ORGANIC CAGES

The syntheses of porous organic cages (POCs) represent an important synthetic puzzle in dynamic covalent chemistry based self-sorting. Improved understanding of the formation mechanisms of POCs can lead to control and rational design of cages with desired functionalities. In Chapter 2, the formation mechanisms of imine-based POCs using time-resolved electrospray mass spectrometry is being explored. It is found that the synthesis of the [4+6] cycloimine cage CC3-R and the [2+3] cycloimine cage CC-pentane both proceed through similar intermediates via a series of consecutive reactions. This chapter is published as part of a research article.[1]

2.1 Introduction

While the POCs show promising properties and initial examples of applications, the design of functional POCs for targeted applications are lacking demonstration. The design of functional porous cage solids for specific applications raises several difficult questions. The first consideration is whether a given set of precursors will form a cage molecule at all and, if so, what is the most favorable stoichiometry (for example, [2 + 3], [4 + 6] or [8 + 12]). If a cage does form, will it maintain its void cavity or collapse to a denser structure upon solvent removal or exchange, and how will it pack in the solid state? Finally, what will the physical properties of that porous cage crystal be in terms of its adsorption selectivity? If we want to design new functional porous organic crystals ‘on

paper' (or rather, in silico), then we need to have the capability to compute answers to all of these questions.

The first part of the question is essential for further modeling of the cages. Current studies do not present a systematic study on the accuracy and applicability of different computational methods in determining the final product of the condensation reaction. In addition, in the studies mentioned in Section 1.2.3, it was hypothesized that, in the synthesis of POCs from dynamic imination reactions, the product would be dominated by the most thermodynamically stable cage. While the structural energy difference calculations indicate the relative thermodynamic stability of cages with different topologies, these calculations generally do not consider the formation energies of reaction intermediates.[2] It is possible that some intermediates have lower energies compared to cage species. Indeed, small intermediates might be excluded from the most thermodynamically stable, larger species during the product purification process. Furthermore, the intermediates that are often ignored in the reactions and calculations may contain hidden information on the shape selection. Gaining insights into such intermediates is essential to fully understand the formation mechanisms of POCs and will lead to more informed structural predictions.

One promising set of tools to probe discrete molecules are mass spectrometry (MS) techniques such as electrospray- (ESI-) and matrix-assisted laser desorption/ionization- (MALDI-) MS. These soft ionization methods have already been used in identifying the molecular masses of POCs.[3] This approach is particularly useful in characterizing mixed-linker cages sharing similar physical and chemical properties, such as in amorphous scrambled porous organic cages (ASPOCs).[4] In addition to product determination, MS can also provide time-resolved "snapshots" of a reactive system when the reaction is monitored

over time, thus providing insights into the assembly of organic linkers to cages. The synthesis of POCs usually takes place at mild solution conditions, which are well-suited for time-resolved ESI-MS analysis.

2.2 Experimental

2.2.1 Materials

Triformylbenzene was purchased from Manchester Organics (UK) or self-synthesized.1 (1R,2R)-(-)-1,2-diaminocyclohexane, isophthalaldehyde, trifluoroacetic acid, anhydrous dichloromethane were purchased from Sigma Aldrich (US). Pentane-1,5-diamine was purchased from TCI Chemicals (US). Ultra-pure grade N_2 and CO_2 used in physisorption measurements were purchased from Airgas (US). All solvents and chemicals were used upon receive without any purification.

2.2.2 Synthesis of CC3-R

In a typical synthesis, 243 mg triformylbenzene and 255 mg (1R,2R)-(-)-1,2-diaminocyclohexane was dissolved in 10 mL anhydrous dichloromethane. To the mixture, 10 µL trifluoroacetic acid was added as the catalyst. The reaction mixture was left at room temperature for 3 days, and the white crystals were recovered by washing with ethanol.

2.2.3 Synthesis of CC-pentane

In a typical synthesis, 90 mg triformylbenzene and 97.36 µL pentane-1,5-diamine was dissolved in 18 mL anhydrous dichloromethane. The reaction mixture was left at room temperature for 5 days. The solvent was removed by rotary evaporation and the pale-yellow

solid was re-dissolved in dichloromethane and filtered off any insoluble content. The final product was obtained by removing the solvent with rotary-evaporation. The yield of the solid product was quantitative and re-dissolving the solid resulted in 8.8 wt% undissolved solids.

2.2.4 Traditional and Time-resolved Mass Spectrometry Methods

2.2.4.1 ESI- and MALDI-MS

ESI-MS of samples were taken on a Waters Quattro LC system. MALDI-MS of samples were taken on a Bruker AutoFlex III instrument.

2.2.4.2 Time-resolved MS

For CC3-R, 20.3 mg triformylbenzene was dissolved in 0.75 mL anhydrous dichloromethane. 21.3 mg (1R,2R)-(-)-1,2-diaminocyclohexane was dissolved in 0.75 mL anhydrous dichloromethane in separate vials. Upon mixing, the first injection was taken with an Agilent 1100 binary HPLC and diluted with a continuous flow of methanol and injected into the ionization chamber of the Quattro system.

The same reaction for CC3-R was carried out in chloroform to study the effect of solvent on the formation of CC3-R cages. Solutions of triformylbenzene (6.8 mg) and (R,R)-1,2-diaminocyclohexane (7.1 mg) were separately prepared with 0.75 mL of chloroform. The two solutions were mixed right before the first MS injection.

For CC-pentane, 3.8 mg triformylbenzene was dissolved in 0.75 mL anhydrous dichloromethane. 4.11 μL pentane-1,5-diamine was dissolved in 0.75 mL anhydrous

dichloromethane in a separate vial. Upon mixing, the first injection was taken by diluting the reaction mixture with a continuous flow of methanol and injected into the ionization chamber.

2.2.5 Supplemental characterization method

2.2.5.1 NMR

Solution ^{1}H NMR spectra were recorded at 400.13 MHz using a Bruker Avance III 400 NMR spectrometer.

2.2.5.2 Powder X-ray Diffraction (PXRD)

Powder X-ray diffraction data were collected on a PANalytical Empyrean X-ray diffraction system in reflection Bragg-Brentano geometry operating at 45 kV and 40 mA. PXRD patterns were collected with a step size of 0.0131 degrees 2θ and a scan time of 80 s/step over 2-50 degrees 2θ.

2.3 Results and Discussion

2.3.1 Syntheses of CC3-R and CC-pentane

Two imine-based POCs with different topologies were selected for this study focusing on cage formation of triformylbenzene with different diamines (Figure 2.1). One topology is the [4+6] cycloimination between triformylbenzene and (1R,2R)-(-)-1,2-diaminocyclohexane to form a structure called CC3-R.[5] Another topology is the [2+3] cycloimination between triformylbenzene and 1,5-pentane-diamine to form a structure called CC-pentane.[6]

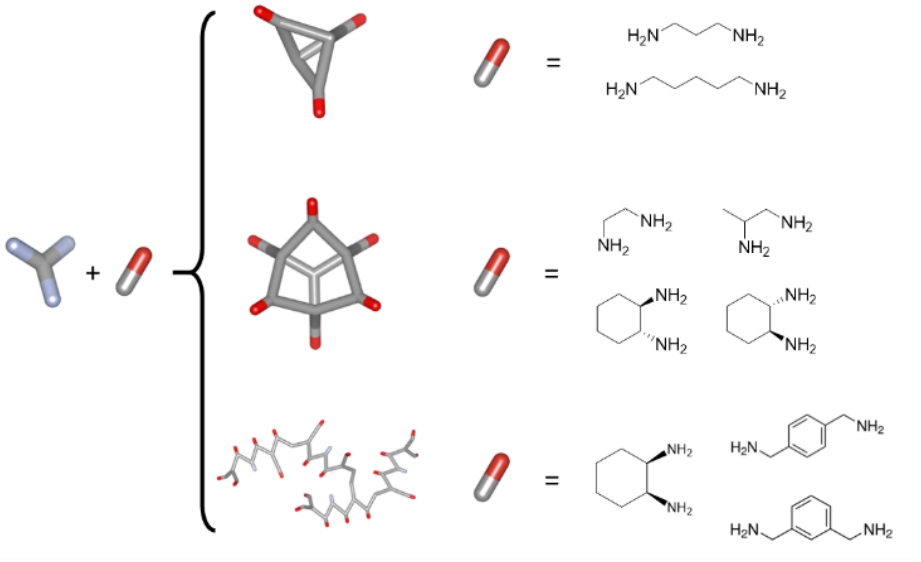

Figure 2.1 Schematic of different geometries of molecules formed when different diamines are used in the reaction with triformylbenzene

* This list is not intended to be comprehensive. A blue "tail" signifies an unreacted carboxaldehyde group. Both of the amine groups in diaminocyclohexane are omitted for clarity, and the connectivity can be determined by totaling the gray cylinders connected to red dots.

The synthesis of the two aforementioned compounds was carried out prior to the time-resolved MS experiments. ^{1}H solution NMR was carried out and showed completion of the imination condensation (Figure 2.2 and Figure 2.3). The cages are further characterized via ESI-MS to determine their topology (Figure 2.4 and Figure 2.5). CC3-R has a molecular weight of 1117 Da, indicating a [4+6] cycloimination reaction between triformylbenzene and cyclohexanediamine to form an octahedral cage with four windows arranged in a tetrahedral geometry. CC-pentane has a molecular weight of 523 Da, indicating a [2+3] cycloimination reaction between triformylbenzene and pentanediamine with a petal-wheel geometry.

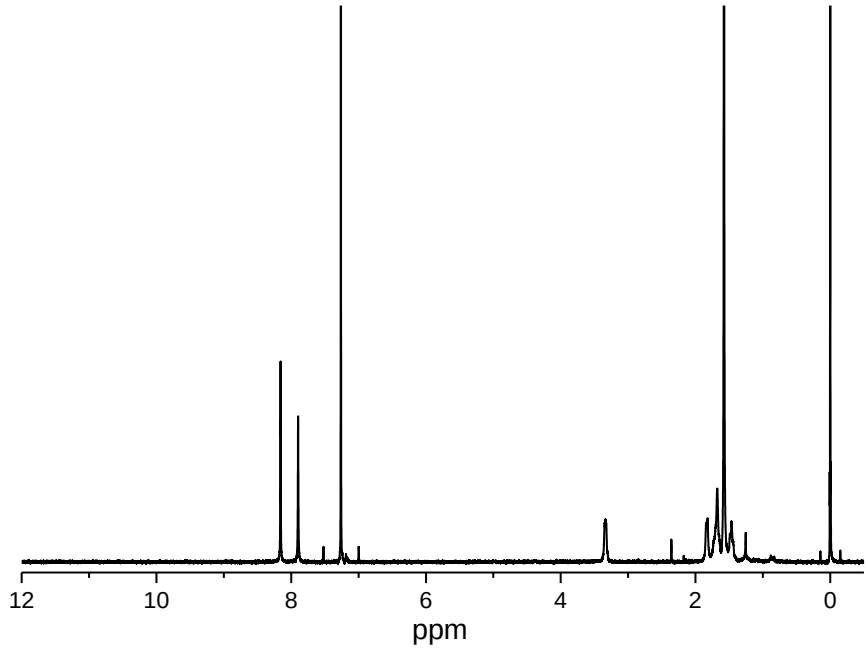

Figure 2.2 ^{1}H-NMR data of CC3-R, as-synthesized. ^{1}H NMR ($CDCl_3$) δ 8.15 (s, CH=N, 12H), 7.89 (s, ArH, 12H), 3.33 (m, CHN, 12H), 1.9 – 1.4 (m, CH_2, 48H) ppm

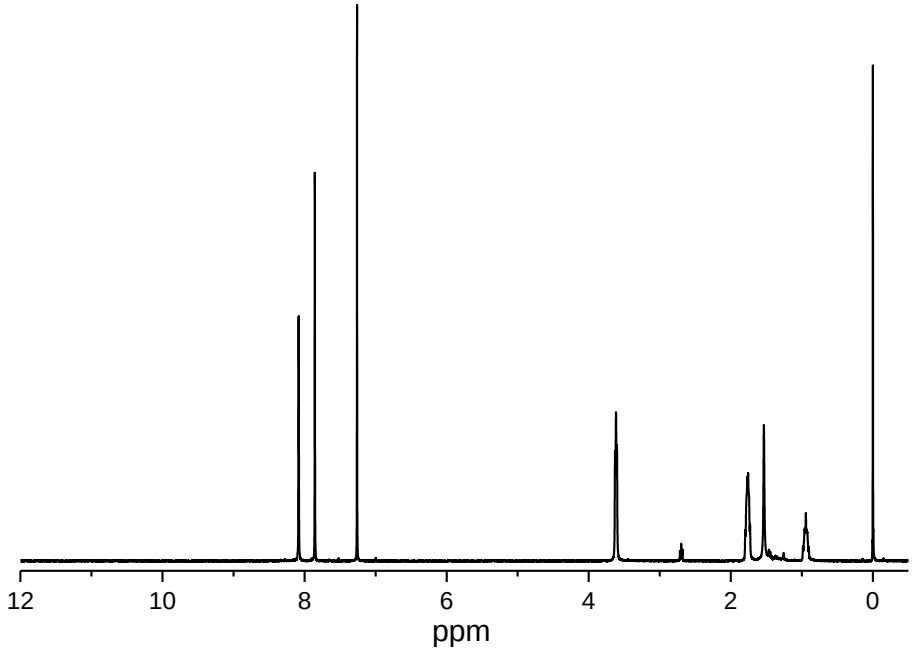

Figure 2.3 ^{1}H-NMR data of CC-pentane, as-synthesized. ^{1}H NMR: ($CDCl_3$) δ 8.09 (s, CH=N, 6H) 7.86 (s, ArH, 6H) 3.61 (t, CH2, 12H) 1.77 (tt, CH_2, 12H) 0.88 (m, CH_2, 6H) ppm

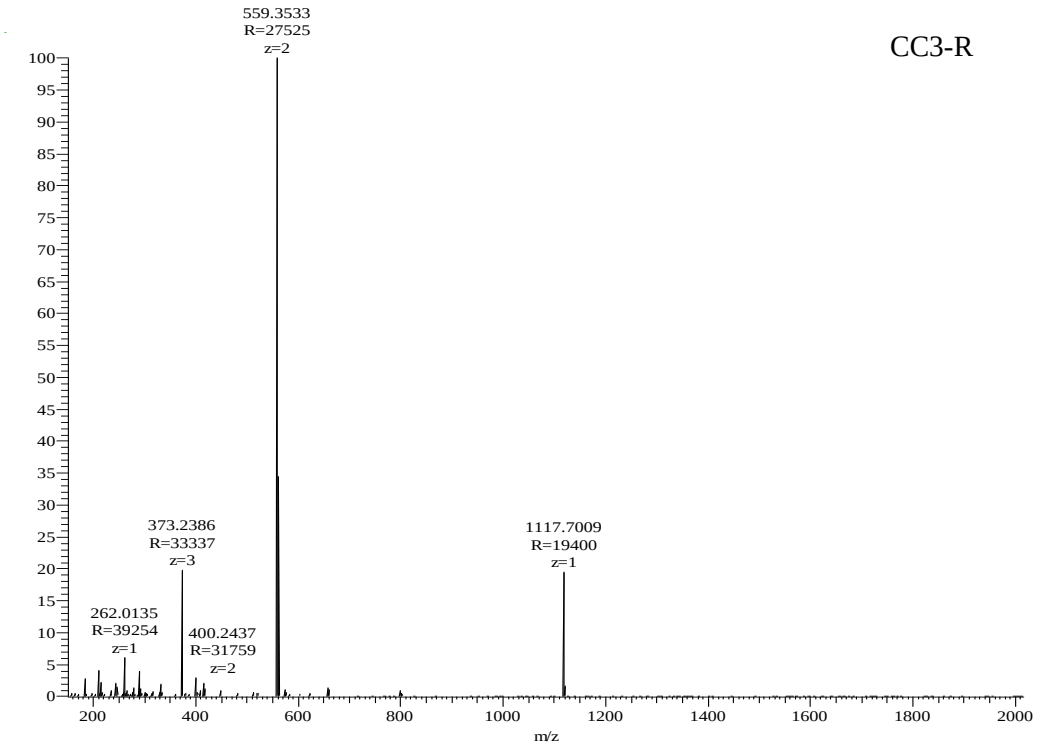

Figure 2.4 ESI-MS data of CC3-R, as-synthesized. m/z: 1117 ($[M+H]^+$)

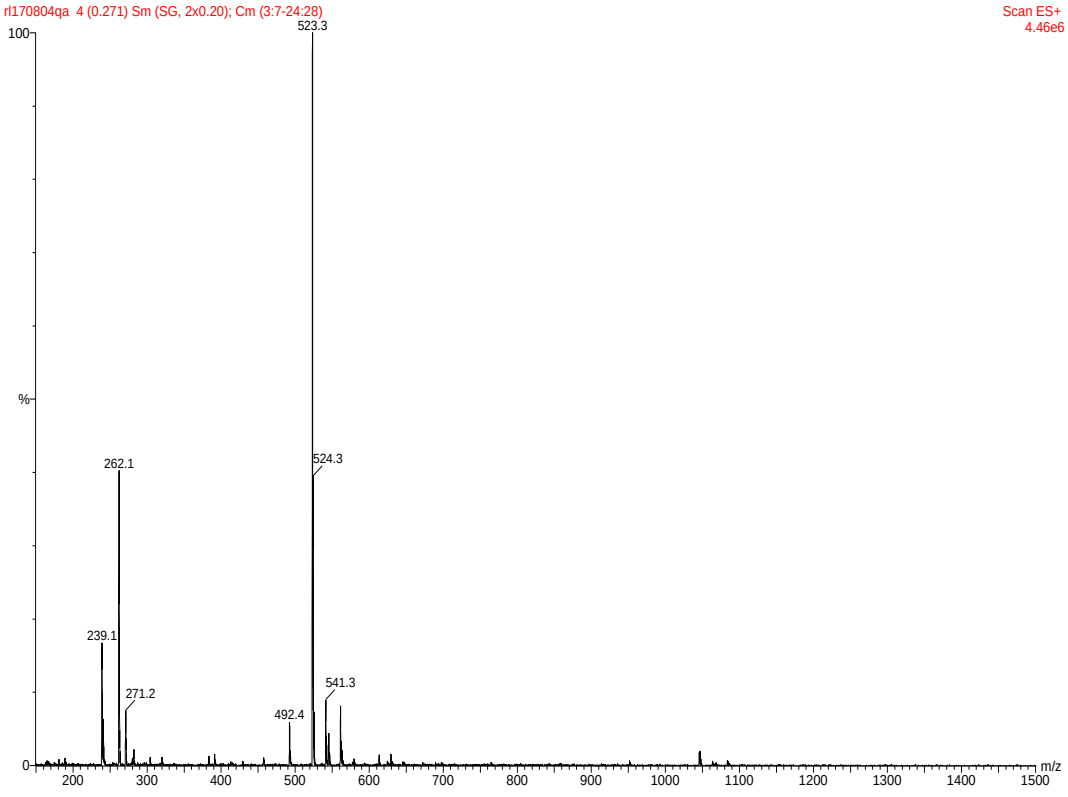

Figure 2.5 ESI-MS data of CC-pentane, as-synthesized. m/z: 523 ($[M+H]^+$)

2.3.2 Time-resolved ESI-MS Evaluation of the CC3-R Synthesis

Time-resolved electrospray ionization mass spectrometry (ESI-MS) was employed to measure the transformation of triformylbenzene and diaminocyclohexane to CC3-R. To ensure the consistency of the measurements, a specific procedure for tracking POC reactions was developed. Two dilute solutions of reactants in dichloromethane (DCM) were individually prepared and mixed immediately before the time-resolved measurement. To enable closer monitoring of the initiation of the reaction, no acid catalysts were added to the system. Five microliter aliquots of the reaction mixture were sampled through a liquid chromatography auto-sampler at predetermined time intervals. The samples were then diluted with a constant flow of methanol before being injected into the ionization chamber to ensure proper ionization of the species in the gas phase. The whole process was programmed and automated to minimize operational error. Even though the procedure was designed to be consistent between sample intervals, the ESI-MS data were determined to be semi-quantitative. However, the qualitative trends of species emerging from the measurements give clear information on the reaction kinetics.

After initial mixing of triformylbenzene and diaminocyclohexane solutions, subsequent samples were taken every 11 min over the first 6 h. After that, samples were taken every 1 h. The spectra showed no changes after 8 h (Figure 2.6). CC3-R was not observed in the spectra throughout the measurement, which might be due to precipitation of CC3-R cages when the small volume fraction of sample aliquots mixed with the constant methanol flow. This hypothesis is supported by CC3-R solubility tests in DCM/methanol mixtures with methanol volume fractions ranging from 10% to 90%. The results (Figure

2.7) showed that in methanol-rich solution mixtures, the solubility of CC3-R would drop precipitously.

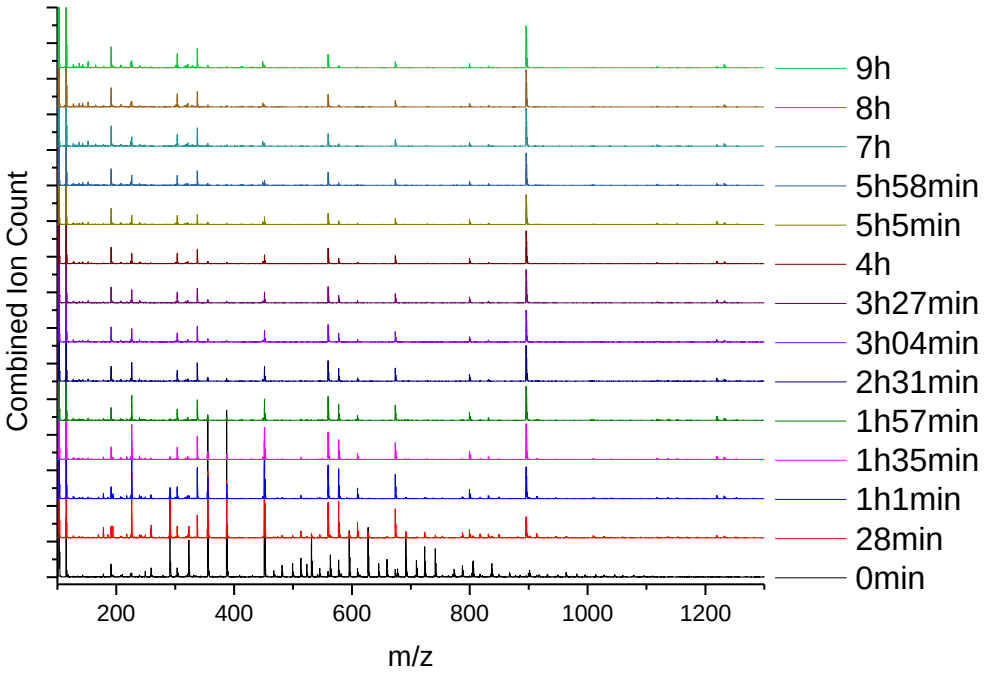

Figure 2.6 Time-resolved ESI-MS spectra of samples taken from the CC3-R synthesis in the first 9 h

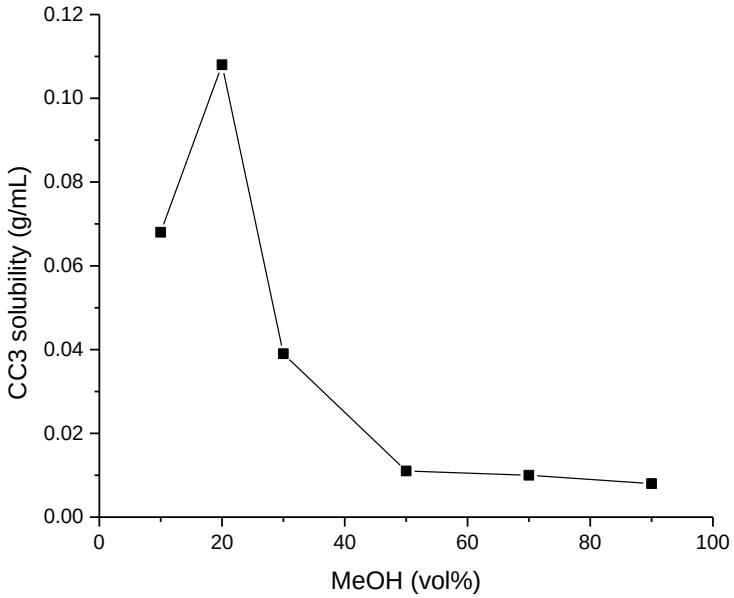

Figure 2.7 CC3-R solubility in DCM/MeOH solvent mixture

The precipitated solid resulting from mixing with methanol during the reaction was also isolated and confirmed to be CC3-R cages by ESI-MS. It is thus important to emphasize that the gas phase fragments observed in ESI-MS spectra may not be a quantitative reflection of the solution composition, as suggested by the absence of CC3-R cage detection. The ESI-MS spectra over the first two hours are plotted in Figure 2.8.

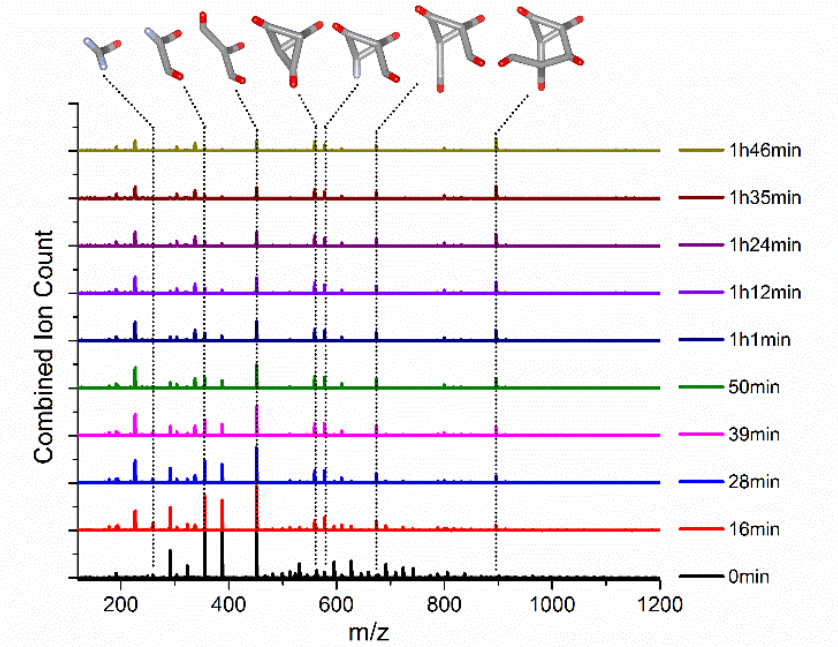

Figure 2.8 Time-resolved ESI-MS spectra of samples taken from the CC3-R synthesis in the first 2 h

One advantage of mass spectrometry is the measurement of discrete signals from a mixture of species with similar physical/chemical properties that would be otherwise hard to separate or distinguish, which allows us to track the intermediate species independently. The spectra contain ionization fragments and higher charged species that pose analytical challenges. To facilitate peak identification, a list of all possible reaction products with up to four triformylbenzene molecules was formulated prior to the monitoring of the reaction, as listed in Table 2.1. Cage-like molecules, as well as short chains, were considered.

Table 2.1 Possible Intermediates during the synthesis of CC3-R

Entry	# of Triformylbenzene	# of Diaminocyclohexane	# of Imine Bonds	Mass (calculated)
1	1	1	1	258.31
2	1	2	2	354.48
3	1	3	3	450.65
4	2	1	2	402.43
5	2	2	3	498.6
6	2	2	4	480.58
7	2	3	4	594.77
8	2	3	5	576.75
9([2+3])	2	3	6	558.73
10	2	4	5	690.94
11	2	4	6	672.92
12	2	5	6	787.11
13	3	2	4	642.72
14	3	3	5	738.89
15	3	3	6	720.87
16	3	4	6	835.06
17	3	4	7	817.04
18	3	4	8	799.02
19	3	5	7	931.23
20	3	5	8	913.21
21	3	5	9	895.19
22	3	6	8	1027.4
23	3	6	9	1009.38
24	3	7	9	1123.57
25	4	3	6	883.01
26	4	4	7	979.18
27	4	4	8	961.16
28	4	5	8	1075.35
29	4	5	9	1057.33
30	4	5	10	1039.31
31	4	6	9	1171.52
32	4	6	10	1153.5
33	4	6	11	1135.48
34 ([4+6])	4	6	12	1117.46
35	4	7	10	1267.69
36	4	7	11	1249.67
37	4	7	12	1231.65
38	4	8	11	1363.86
39	4	8	12	1345.84
40	4	9	12	1460.03

The peaks from the mass spectrometry were compared against the list, and key intermediate species were identified and listed in Table 2.2. Only peak envelopes that have a combined ion counts (CIC) larger than $2x10^5$ were considered for clarity. The relative stability was determined by the long-term behavior inferred from Figure 2.9 Time-resolved ESI-MS spectra of samples taken from the CC3-R synthesis in the first 9 h.

Table 2.2 Assignment of the key species identified during the time-resolved ESI-MS measurements of CC3-R synthesis

Entry in Table 2.1	m/z (obs)	z	Formula*	Assign ment	Stable?	m/z (calcd)
	191.1	1+	N/A	N/A	Yes	N/A
3	226.3	2+	$(TFB)_1(DACH)_3(H_2O)_{-3}$	[1+3]	Yes	227.4
1	259.2	1+	$(TFB)_1(DACH)_1(H_2O)_{-1}$	[1+1]	Yes	259.3
	291.2	1+	N/A	N/A	No	N/A
	323.3	1+	N/A	N/A	No	N/A
11	337.5	2+	$(TFB)_2(DACH)_4(H_2O)_{-6}$	[2+4]	Yes	338.5
2	355.1	1+	$(TFB)_1(DACH)_2(H_2O)_{-2}$	[1+2]	Yes	355.5
	387.4	1+	N/A	N/A	No	N/A
3	451.5	1+	$(TFB)_1(DACH)_3(H_2O)_{-3}$	[1+3]	Yes	451.7
	531.4	1+	N/A	N/A	No	N/A
9	559.5	1+	$(TFB)_2(DACH)_3(H_2O)_{-6}$	[2+3]	Yes	559.7
8	577.5	1+	$(TFB)_2(DACH)_3(H_2O)_{-5}$	[2+3]	Yes	577.8
7	595.4	1+	$(TFB)_2(DACH)_3(H_2O)_{-4}$	[2+3]	No	595.8
	627.4	1+	N/A	N/A	No	N/A
11	673.5	1+	$(TFB)_2(DACH)_4(H_2O)_{-6}$	[2+4]	Yes	673.9
10	691.5	1+	$(TFB)_2(DACH)_4(H_2O)_{-5}$	[2+4]	No	691.9
15	723.4	1+	$(TFB)_3(DACH)_3(H_2O)_{-6}$	[3+3]	No	721.9
14	741.5	1+	$(TFB)_3(DACH)_3(H_2O)_{-5}$	[3+3]	No	739.9
21	895.6	1+	$(TFB)_3(DACH)_5(H_2O)_{-9}$	[3+5]	Yes	896.2

*The formulas were listed as the number of triformylbenzene (TFB) molecule and diaminocyclohexane (DACH) molecule in the structure minus the dehydration number.

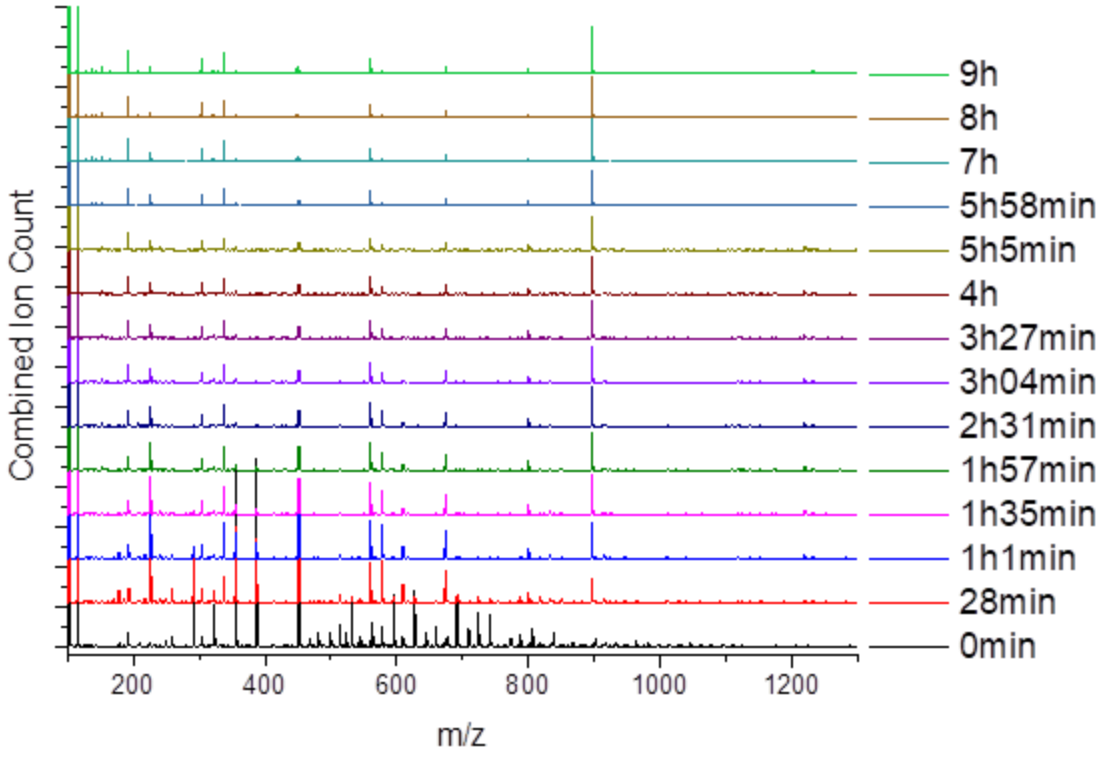

Figure 2.9 Time-resolved ESI-MS spectra of samples taken from the CC3-R synthesis in the first 9 h

It can be observed in Figure 2.8 that the first time point in the data series showed distinct peaks compared to later time points. Several m/z peaks appeared between 500 and 800, which rapidly converted to other species and could not be observed in later spectra. The m/z peaks at 191.1, 291.2, 323.3, 531.4, and 627.4 could not be assigned to an intermediate relevant to the reaction between triformylbenzene and diaminocyclohexane and seem likely to be ionization products of the intermediates. Throughout the measurement, several stable intermediates were observed, as indicated in Table 2.2. Although the intensities of the m/z envelopes of the spectra were not quantitative, the CIC

of the seven assigned stable intermediates is plotted against reaction time in Figure 2.10 as a reflection of the transformations happening in the liquid phase.

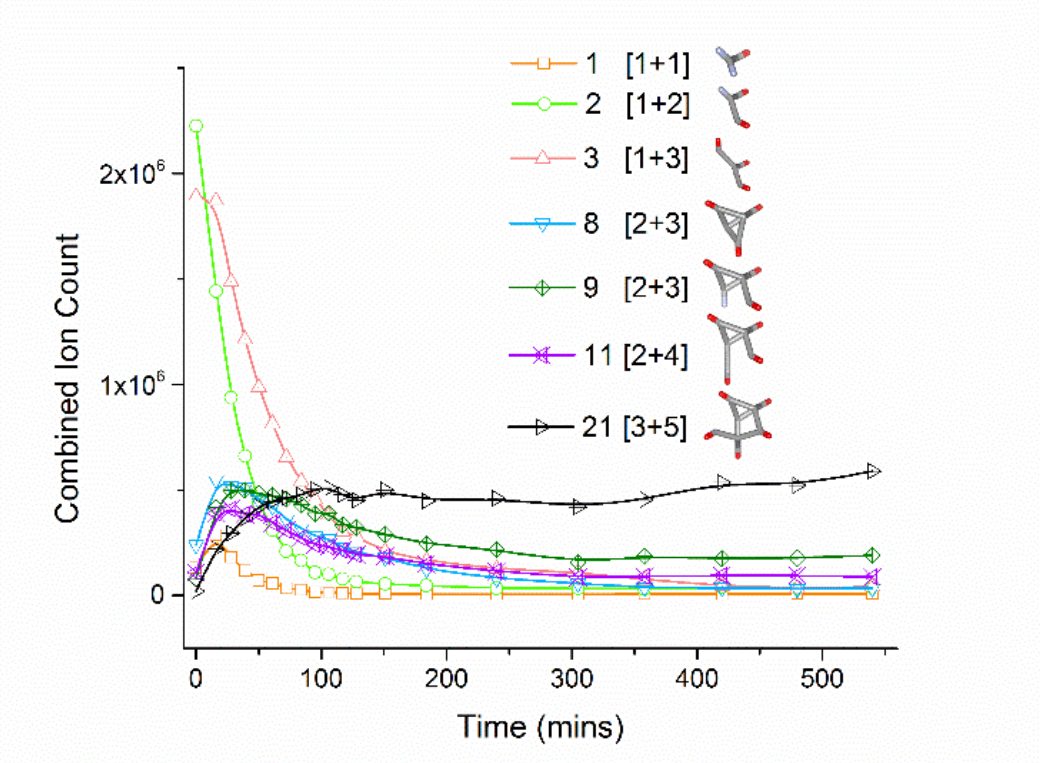

Figure 2.10 Time-resolved combined ion counts of stable intermediates during ESI-MS measurement of CC3-R synthesis

The seven species can be grouped into three categories: small intermediates (entries 1, 2, and 3 in Table 2.1), medium intermediates (entries 8, 9, and 11), and a large intermediate (entry 21). In general, small intermediates started with high relative abundance and dropped to low levels within a timeframe of two hours. The relative abundance of medium intermediates slightly increased over the first 30 minutes of the reaction and then gradually decreased to a plateau. The large intermediate increased slowly over time. The reaction pathway of CC3-R formation can be inferred from these observations. The linkers (triformylbenzene and diaminocyclohexane) assemble into small imination fragments upon mixing in a very short period (between the mixing of the solvent

and the first measurement). The smaller fragments then go through a self-conformational search towards large intermediates and complete [4+6] cages via a series of consecutive reactions. Although CC3-R cages are usually considered as the thermodynamically stable product in this reaction,[7-8] it was observed in this measurement that several stable intermediates could coexist with the CC3-R cages. Interestingly, a [2+3] cycloimination byproduct (small cage) that is an undesirable product when aiming to produce CC3-R was observed throughout the reaction showed in Figure 2.11.

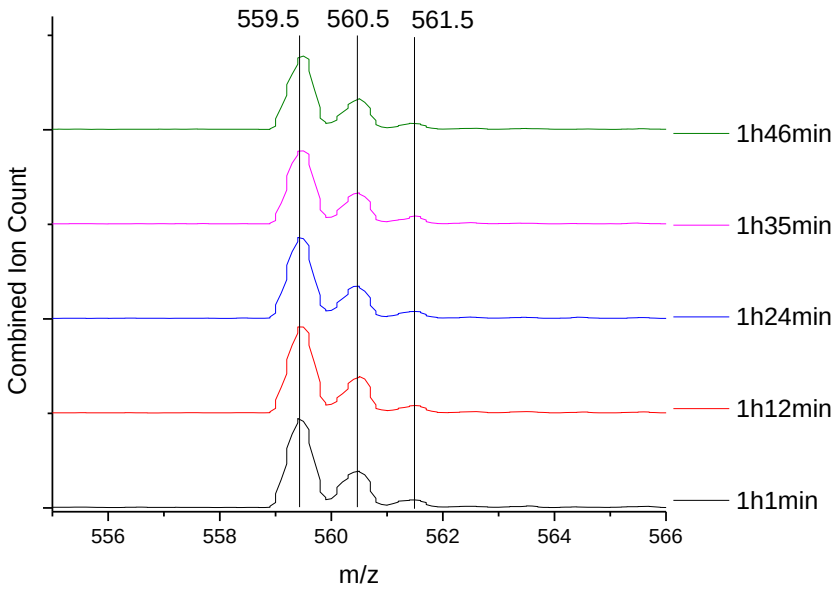

Figure 2.11 [2+3] cage observed during CC3-R synthesis. The separation of 1 m/z in the peaks indicates a single charged [2+3] cage

Previous work has shown that the choice of synthesis solvent can play a role in the cage formation process.[2, 9-10] For example, Warmuth and co-workers have shown that three different imine cages can be formed from the same starting materials by varying the synthesis solvent.[10] Considering this, the formation of CC3-R in chloroform was also monitored to evaluate the effects of solvents on imine cage formation. The time-resolved

ESI-MS spectra are shown in Figure 2.12. In this case, a more dilute concentration of reactants was used and the spectra in the first 3 hours of the reaction resembled the first 30 minutes of the reaction in DCM. Importantly, the species observed agreed uniformly with those shown in Table 2.2, and no obvious deviation from the reaction in DCM was observed. Solvent effects were also considered in detail using theoretical calculations, as discussed in later sections.

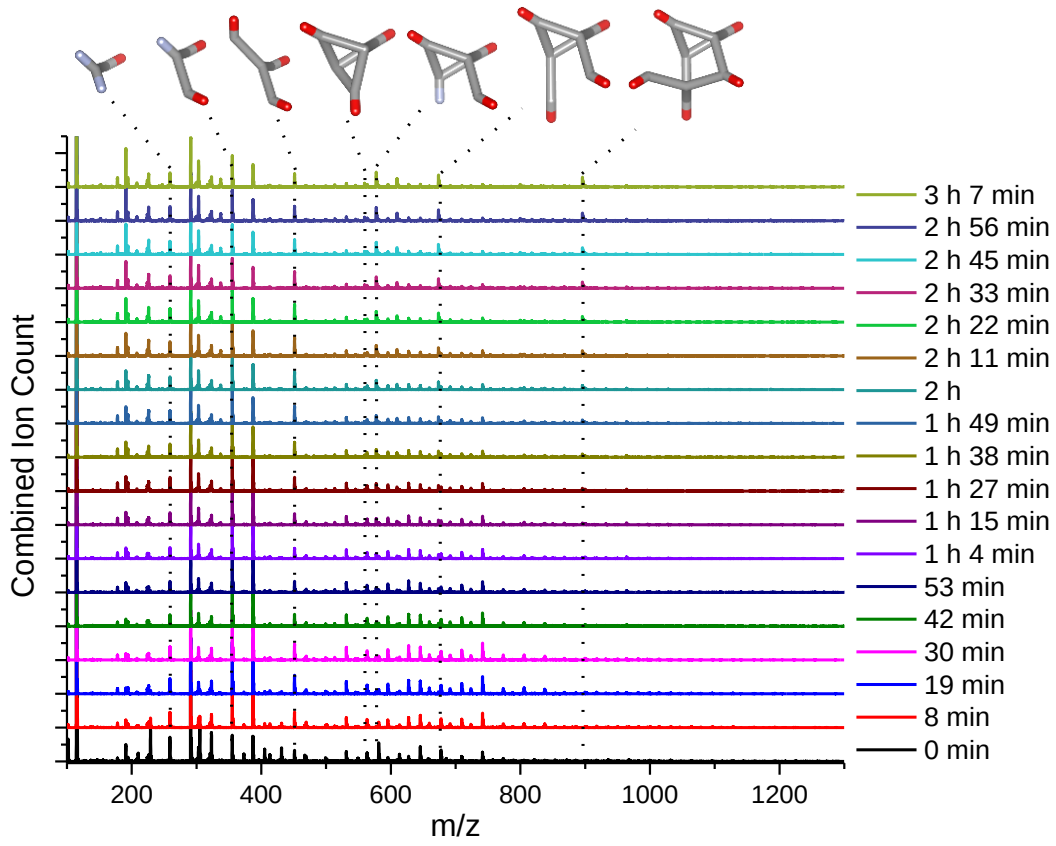

Figure 2.12 Time-resolved ESI-MS spectra of samples taken from the CC3-R synthesis in $CHCl_3$

2.3.3 Time-resolved ESI-MS Study during CC-pentane Synthesis

During the initial synthesis of CC-pentane it was found that upon mixing of triformylbenzene and 1,5-pentanediamine, the reaction mixture became cloudy, indicating

the formation of precipitation. The undisturbed cloudy solution turned clear after several hours. To further investigate this observation, the solid content was isolated by filtration with a PVDF membrane of 100 nm pore size. The isolated solid is not soluble in common solvents. The infrared spectrum of the solid showed very similar peaks with isolated CC-pentane. Powder X-ray diffraction showed a broad peak. An attempt to obtain the molecular weight using Time-of-Flight Secondary Ion Mass Spectrometry (ToF-SIMS) failed to give any m/z peak under 2000. Compared to the rigid (R,R)-diaminocyclohexane linker in CC3-R, 1,5-pentanediamine involved in CC-pentane synthesis is more flexible. Our results suggest that the flexibility of the linker leads to the formation of polymeric species in the initial stage of the reaction that is subsequently consumed by the cage formation process via dynamic equilibrium. The final clear solution was rotation-evaporated to yield a white solid. However, the solid could not be fully re-dissolved in dichloromethane or chloroform, which has also been observed in the literature.[6]

The same time-resolved mass spectrometry methodology used for CC3-R was applied to the CC-pentane synthesis. The CC-pentane was pre-determined not to precipitate out in a methanol/DCM solution. Surprisingly, other than the undetectable polymeric species, the time-resolved ESI-MS spectra (Figure 2.13) of samples taken from the CC-pentane synthesis were analogous to CC3-R. The predicted geometries of the various intermediates resemble the species found during CC3-R synthesis.

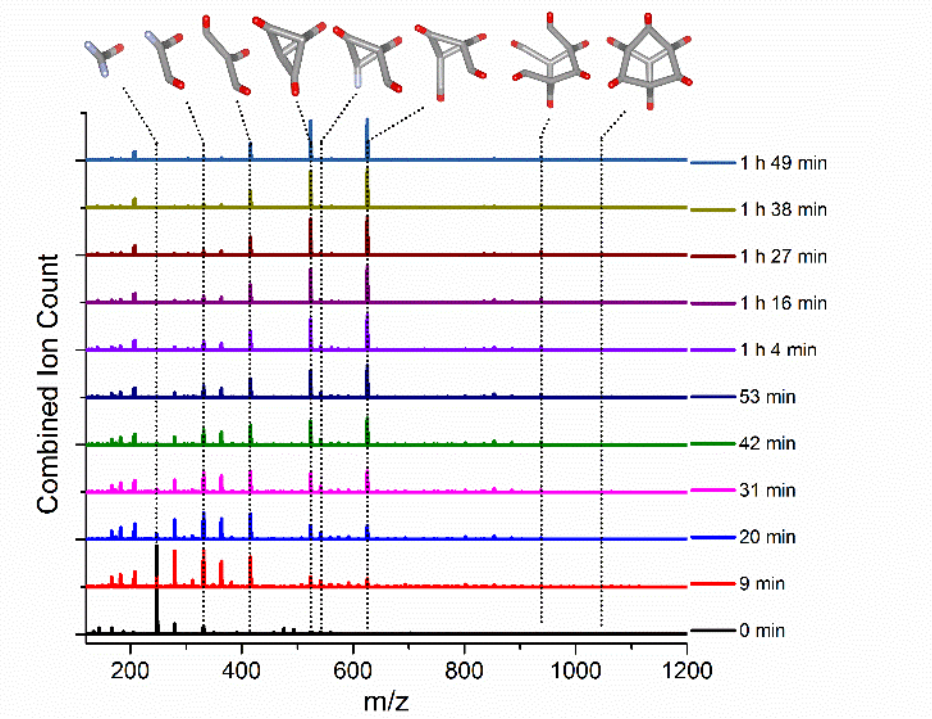

Figure 2.13 Time-resolved ESI-MS spectra of samples taken from the CC-pentane synthesis in the first 2 h

The initiation of CC-pentane synthesis occurred over a short period, similar to the CC3-R synthesis. The linkers in the reaction mixture assemble into several stable intermediates in less than 30 min. Similar to the process described in the CC3-R analysis, the list of all possible reaction products with up to four triformylbenzene molecules was formulated prior to the monitoring of the reaction, as listed in Table 2.3. The species found from the MS experiments are listed in Table 2.4. The species in the lower m/z region (up to 625.6 m/z) matched well with the intermediates observed in the CC3-R synthesis. In the higher m/z region, a [3+6] intermediate was observed, in contrast with the [3+5] intermediate observed in CC3-R synthesis.

Table 2.3 Possible intermediates during the synthesis of CC-pentane

Entry	# of Triformylbenzene	# of Diaminocyclohexane	# of Imine Bonds	Mass (calculated)
1	1	1	1	246.3
2	1	2	2	330.46
3	1	3	3	414.62
4	2	1	2	390.42
5	2	2	3	474.58
6	2	2	4	456.56
7	2	3	4	558.74
8	2	3	5	540.72
9([2+3])	2	3	6	522.7
10	2	4	5	642.9
11	2	4	6	624.88
12	2	5	6	727.06
13	3	2	4	618.7
14	3	3	5	702.86
15	3	3	6	684.84
16	3	4	6	787.02
17	3	4	7	769
18	3	4	8	750.98
19	3	5	7	871.18
20	3	5	8	853.16
21	3	5	9	835.14
22	3	6	8	955.34
23	3	6	9	937.32
24	3	7	9	1039.5
25	4	3	6	846.98
26	4	4	7	931.14
27	4	4	8	913.12
28	4	5	8	1015.3
29	4	5	9	997.28
30	4	5	10	979.26
31	4	6	9	1099.46
32	4	6	10	1081.44
33	4	6	11	1063.42
34 ([4+6])	4	6	12	1045.4
35	4	7	10	1183.62
36	4	7	11	1165.6
37	4	7	12	1147.58
38	4	8	11	1267.78
39	4	8	12	1249.76
40	4	9	12	1351.94

Table 2.4 Assignments of the key intermediate species identified during the time-resolved ESI-MS measurements of CC-pentane synthesis

Entry in Table 2.3	m/z (obs)	z	Formula*	Assignment	Stable?	m/z (calcd)
	205.2	1+	N/A	N/A	Yes	N/A
3	208.1	2+	$(TFB)_1(PDA)_3(H_2O)_{-3}$	[1+3]	Yes	208.3
1	247.1	1+	$(TFB)_1(PDA)_1(H_2O)_{-1}$	[1+1]	Yes	246.3
	279.1	1+	N/A	N/A	No	N/A
	303.3	1+	N/A	N/A	No	N/A
2	331.3	1+	$(TFB)_1(PDA)_2(H_2O)_{-2}$	[1+2]	Yes	331.5
	363.4	1+	N/A	N/A	No	N/A
3	415.4	1+	$(TFB)_1(PDA)_3(H_2O)_{-3}$	[1+3]	Yes	415.6
9	523.4	1+	$(TFB)_2(PDA)_3(H_2O)_{-6}$	[2+3]	Yes	523.7
8	541.5	1+	$(TFB)_2(PDA)_3(H_2O)_{-5}$	[2+3]	Yes	541.7
7	559.4	1+	$(TFB)_2(PDA)_3(H_2O)_{-4}$	[2+3]	No	559.7
	591.4	1+	N/A	N/A	No	N/A
11	625.5	1+	$(TFB)_2(PDA)_4(H_2O)_{-6}$	[2+4]	Yes	625.9
23	937.7	1+	$(TFB)_3(PDA)_6(H_2O)_{-9}$	[3+6]	Yes	938.3
34	1045.6	1+	$(TFB)_4(PDA)_6(H_2O)_{-12}$	[4+6]	Yes	1046.4

*The formulas were listed as the number of triformylbenzene (TFB) molecule and 1,5-pentanediamine (PDA) molecule in the structure minus the dehydration number.

In a similar fashion to CC3-R, the time-dependent CIC of stable CC-pentane intermediates are shown in Figure 2.14, which highlights the transformations happening in the liquid phase reaction mixture. Importantly, similar behavior to CC3-R was observed for small intermediates (entries 1, 2, and 3 in Table 2.3), that is, high relative abundance at short times that reduce to low levels within two hours of reaction initiation. However, unlike CC3-R, the medium-sized CC-pentane intermediates (entries 8, 9, and 11) dominate the final product.

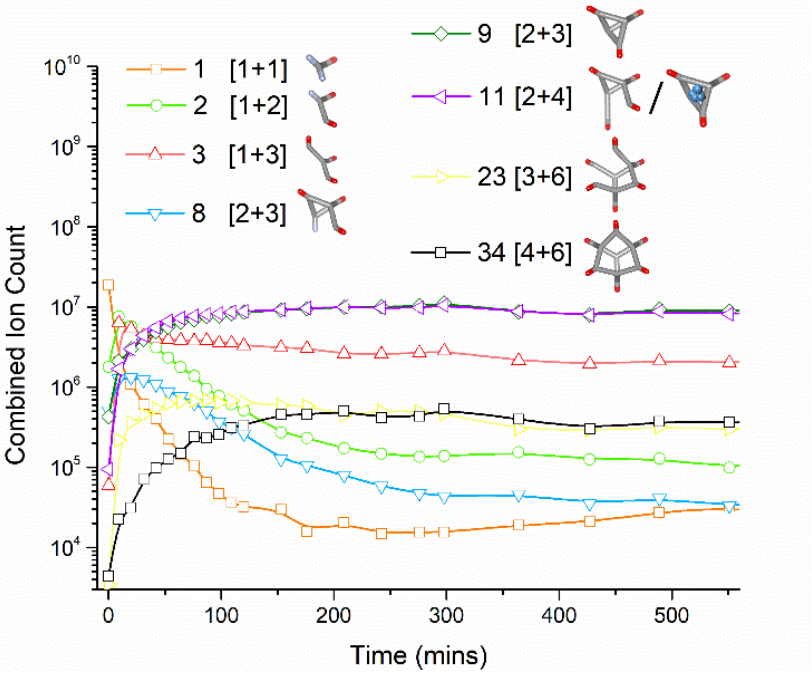

Figure 2.14 Time-resolved combined ion counts of stable intermediates during ESI-MS measurement of CC-pentane synthesis

In addition, species 9 ([2+3] cage) and 11 ([2+4] intermediate) exist at similar concentrations in the CC-pentane reaction mixture. This close matching of concentration led us to speculate that the 625.5 peak observed in the MS was related to the [2+3] cage rather than the [2+4] intermediate's peak. A close inspection of their molecular mass revealed that the difference between them was 102.1, and indeed a 102.1 m/z species was also observed in the spectra, which corresponds to a $(MeOH)_2(H_2O)_2$ cluster that is commonly observed in ESI-MS spectra.[11] This suggests the existence of a [2+3] cage with a solvent cluster trapped inside. However, an isotope analysis between the [2+4] intermediate and the trapped cluster was indistinguishable (Figure 2.15). Nevertheless, electronic structure models strongly suggest that the presence of a solvent cluster within the [2+3] is likely (Figure 2.16).

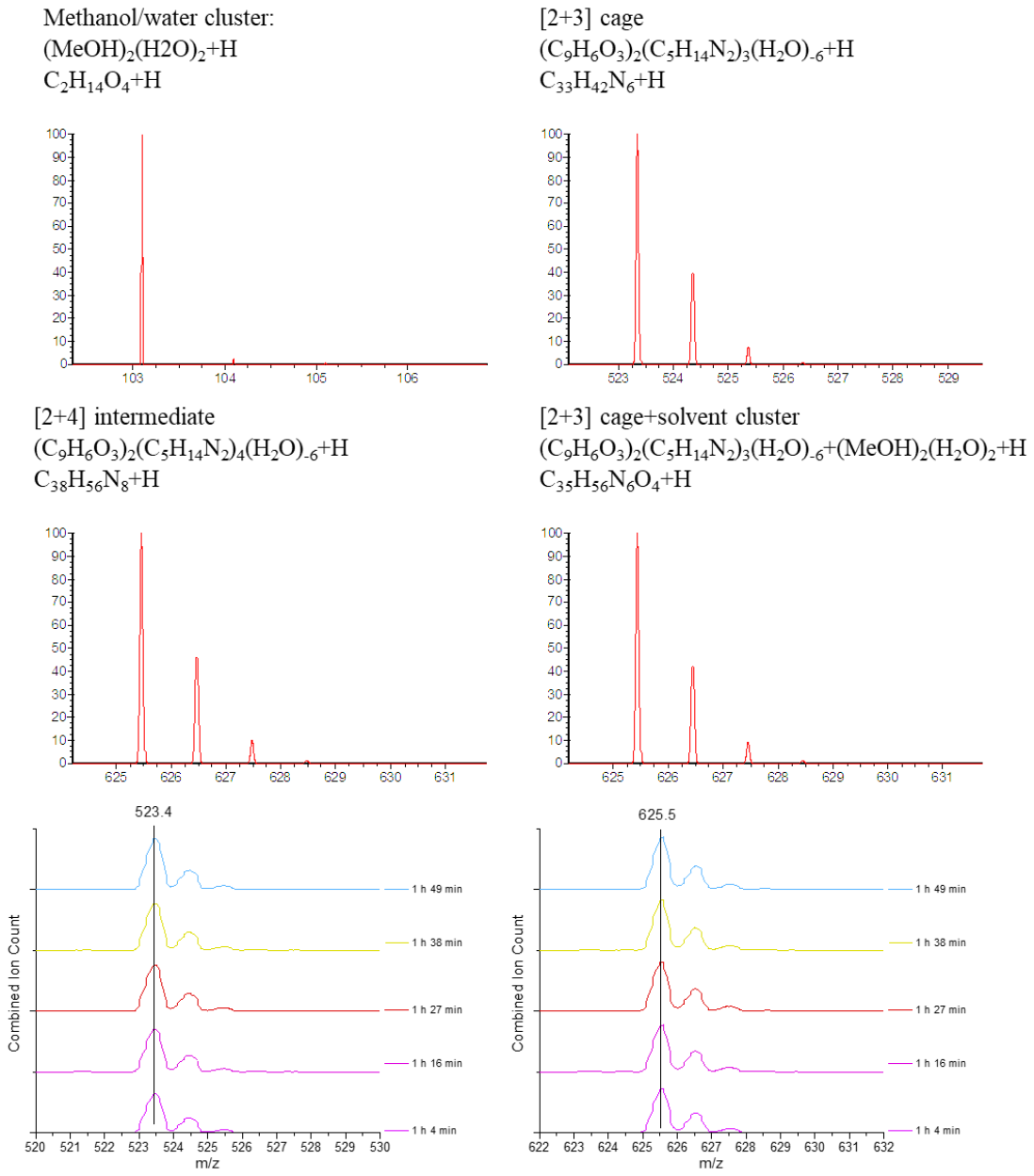

Figure 2.15 Isotope comparison of [2+3] cage with trapped cluster and [2+4] intermediate between experiment and prediction in CC-pentane

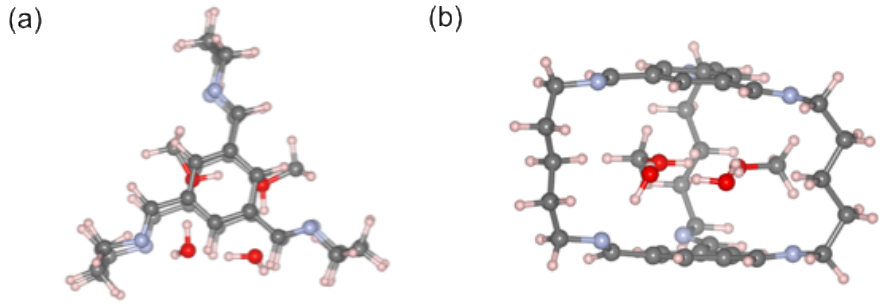

Figure 2.16 (a) Top view and (b) Side view of [2+3] cage with a $(MeOH)_2(H_2O)_2$ cluster trapped inside

The similarity between the reaction courses of CC3-R and CC-pentane suggests a generalization of the imine based POC formation mechanism: upon mixing of the linkers, localized random assembly immediately occurs between the linkers to form a wide range of intermediates. These intermediates are transformed into several species with certain stable geometries over a short period. The stable species are then slowly converted to the desired cages, while a small amount incomplete cages or undesired byproducts will continue to coexist at any given time.

2.4 Conclusions and Remarks

2.4.1 Conclusions

In summary, time-resolved mass spectrometry was utilized to study the reaction pathways of imine-based POCs with two representative POC species, CC3-R and CC-pentane. It was observed that both systems adopt a similar reaction pathway through a series of consecutive reactions, suggesting a general reaction mechanism for such POCs. Upon mixing of the linkers, localized random assembly immediately occurs between the

linkers to form a wide range of intermediates. These intermediates are transformed into several species with certain metastable geometries in a short period. The metastable species are then slowly converted to the desired cages, while a small amount of incomplete cages or undesired byproducts remain in the final product. The observation of the [2+3] cage species in CC3-R synthesis is very important in understanding the formation of a series of keto-enamine POCs reported in the literature. The knowledge of reaction mechanism through a [2+3] cage can direct the synthesis of thermodynamically unfavorable cages.

This study served as a starting point and basis for a computational study that utilized *ab initio* and DFT calculations to verify the observed mechanisms. These computational results are presented in Yang Liu's Ph.D. Dissertation. From the combination of the two studies, we demonstrated that the APFD/DZVP2 basis set is suitable for qualitative evaluation of the size and permanent porosity of cage products backed by both experimental observations and higher level calculations. Based on our findings, we proposed a methodology for the design of imine-based POC species that could also be applied to other POCs described in section 2.4.4.

2.4.2 Enal-to-keto Tautomerization

It is important to note that the formation of imine based POCs through a [2+3] cage is essential in explaining several experimentally observed phenomena in the literature. It has been shown in covalent organic frameworks (COFs) that, if the imine bond has an adjacent hydroxyl group (i.e., *ortho*-phenols), they will undergo an irreversible transformation through keto-enamine bond formation and form a tied-in stable framework.[12-13] Similar research aimed at increasing stability of imine-based POCs has

been done by Kieryk et al., in which they used 2,4,6-trihydroxy-1,3,5-benzenetricarboxalde hyde to react with diaminocyclohexane.[14] However, only [2+3] keto-enamine cages were formed in this case, suggesting that as the reaction goes through a [2+3] intermediate, the irreversible keto-enamine bond formation prevents the cage from breaking and forming larger products. In similar work, triformylphenol was used to derive salen-type organic cages.[15] With all three diamine linkers used (ethylenediamine, trans-(1R,2R)-1,2-diaminocyclohexane and (1R,2R)-diphenylethylenediamine), only [4+6] cages were observed, which suggest the single keto bond does not alter the reversibility of the cage and the thermodynamic preference of [4+6] cages. 2,4,6-trihydroxy-1,3,5-benzenetricarboxaldehyde was also used to react with a series of alkanediamines with increasing chain length.[16] In contrast to the odd-even alternation with chain length between [2+3] and [4+6] cages observed with triformylbenzene,[6] only [2+3] cages were observed with odd-even alternation on the cage conformation (gauche vs. eclipsed). This again can be explained by the formation mechanism discussed here and the enal-to-keto tautomerization. Our general finding can thus be used to direct the synthesis of thermodynamically unfavorable cages with linkers that will otherwise form other cages or even polymers.

2.4.3 Diaza-Cope Rearrangement

The Diaza-Cope rearrangement has been previously reported to impede the synthesis of CC9 and CC10 via competition with the cage formation reaction.[17] It is therefore critically necessary to consider the formation of the rearrangement product during the design of new POCs. The thermodynamic stability and equilibrium constant for the rearrangement reaction can be determined by calculating the energy values of the reactants

and the rearrangement product.[18-19] As the Diaza-Cope rearrangement requires vicinal diamines, we only considered CC3-R in this calculation. We selected a pair of clusters composed of one (R,R)-1,2-diaminocyclohexane and two triformylbenzene molecules, which was the smallest cluster needed for the Diazo-Cope rearrangement reaction to take place, as shown in Figure 2.17. The formation energies of these two clusters were calculated at APFD/DZVP2 level, and the Diaza-Cope product energy was predicted to be 38.9 kJ/mol higher than reactant energy, thus indicating a thermodynamically unfavorable reaction at these conditions. The corresponding reaction equilibrium constant was 2×10^{-26} at room temperature, which is considerably less than 10^2, the minimum equilibrium constants required for completing rearrangement reactions.[20] Similar calculations can be performed to rule out the possibility of the Diaza-Cope rearrangement in designing other imine-based POCs.

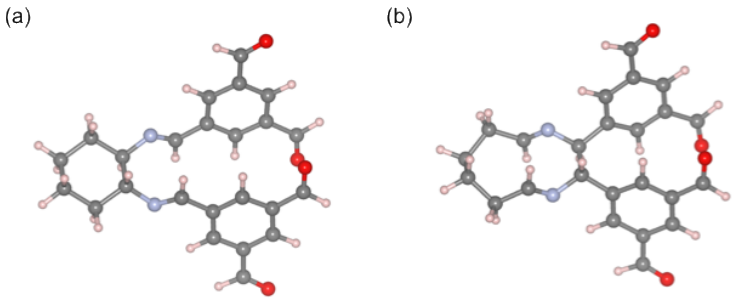

Figure 2.17 (a) Reactant and (b) Product for hypothetical Diaza-Cope rearrangement reaction during CC3-R synthesis

2.4.4 New Approach to the in silico Design of POCs

Based on our experimental and computational findings, we propose a more comprehensive method for *in silico* design of new cage species. First, the energy calculation methods need to be carefully chosen for the selected dynamic covalent

chemistry. For imine based POCs, one can use dispersion corrected functionals with either DZVP2. For other POC systems, it will be necessary to benchmark DFT functionals with higher-level calculations before selecting a calculation approach. Second, structures for energy calculations should be prepared with consideration of both complete cages and intermediates, and possible competing reactions. From our above conclusions, a direct comparison between different cages only yields limited information. The structures that are neighbors of the cages should also be included in the calculations, for example, [1+3] intermediates and the open [2+3] intermediates around the [2+3] cage. Lastly, the structures should be geometry optimized and their energy values calculated with the appropriate computational methods. If the relative energy values of the structures indicate the likelihood of coexistence of cages and intermediates in the equilibrium product, extra synthetic and/or purification precautions need to be considered to acquire pure cage products.

2.5 References

(1) Zhu, G.; Liu, Y.; Flores, L.; Lee, Z. R.; Jones, C. W.; Dixon, D. A.; Sholl, D. S.; Lively, R. P. Formation Mechanisms and Defect Engineering of Imine-Based Porous Organic Cages. *Chemistry of Materials* **2018,** *30*, 262-272.

(2) Santolini, V.; Miklitz, M.; Berardo, E.; Jelfs, K. E. Topological landscapes of porous organic cages. *Nanoscale* **2017,** *9*, 5280-5298.

(3) Jin, Y.; Jin, A.; McCaffrey, R.; Long, H.; Zhang, W. Design Strategies for Shape-Persistent Covalent Organic Polyhedrons (COPs) through Imine Condensation/Metathesis. *Journal of Organic Chemistry* **2012,** *77*, 7392-7400.

(4) Jiang, S.; Jones, J. T. A.; Hasell, T.; Blythe, C. E.; Adams, D. J.; Trewin, A.; Cooper, A. I. Porous organic molecular solids by dynamic covalent scrambling. *Nature Communications* **2011,** *2*, 207.

(5) Tozawa, T.; Jones, J. T. A.; Swamy, S. I.; Jiang, S.; Adams, D. J.; Shakespeare, S.; Clowes, R.; Bradshaw, D.; Hasell, T.; Chong, S. Y.; Tang, C.; Thompson, S.; Parker, J.;

Trewin, A.; Bacsa, J.; Slawin, A. M. Z.; Steiner, A.; Cooper, A. I. Porous organic cages. *Nature Materials* **2009,** *8*, 973-978.

(6) Jelfs, K. E.; Eden, E. G. B.; Culshaw, J. L.; Shakespeare, S.; Pyzer-Knapp, E. O.; Thompson, H. P. G.; Bacsa, J.; Day, G. M.; Adams, D. J.; Cooper, A. I. In silico Design of Supramolecules from Their Precursors: Odd-Even Effects in Cage-Forming Reactions. *Journal of the American Chemical Society* **2013,** *135*, 9307-9310.

(7) Briggs, M. E.; Slater, A. G.; Lunt, N.; Jiang, S.; Little, M. A.; Greenaway, R. L.; Hasell, T.; Battilocchio, C.; Ley, S. V.; Cooper, A. I. Dynamic flow synthesis of porous organic cages. *Chemical Communications* **2015,** *51*, 17390-17393.

(8) Belowich, M. E.; Stoddart, J. F. Dynamic imine chemistry. *Chemical Society Reviews* **2012,** *41*, 2003-2024.

(9) Lee, S.; Yang, A.; Moneypenny, T. P.; Moore, J. S. Kinetically Trapped Tetrahedral Cages via Alkyne Metathesis. *Journal of the American Chemical Society* **2016,** *138*, 2182-2185.

(10) Liu, X.; Warmuth, R. Solvent Effects in Thermodynamically Controlled Multicomponent Nanocage Syntheses. *J. Am. Chem. Soc.* **2006,** *128*, 14120-14127.

(11) Keller, B. O.; Sui, J.; Young, A. B.; Whittal, R. M. Interferences and contaminants encountered in modern mass spectrometry. *Analytica Chimica Acta* **2008,** *627*, 71-81.

(12) DeBlase, C. R.; Silberstein, K. E.; Truong, T.-T.; Abruña, H. D.; Dichtel, W. R. β-Ketoenamine-Linked Covalent Organic Frameworks Capable of Pseudocapacitive Energy Storage. *Journal of the American Chemical Society* **2013,** *135*, 16821-16824.

(13) Kandambeth, S.; Mallick, A.; Lukose, B.; Mane, M. V.; Heine, T.; Banerjee, R. Construction of Crystalline 2D Covalent Organic Frameworks with Remarkable Chemical (Acid/Base) Stability via a Combined Reversible and Irreversible Route. *Journal of the American Chemical Society* **2012,** *134*, 19524-19527.

(14) Kieryk, P.; Janczak, J.; Panek, J.; Miklitz, M.; Lisowski, J. Chiral 2+3 Keto-Enamine Pseudocyclophanes Derived from 1,3,5-Triformylphloroglucinol. *Organic Letters* **2016,** *18*, 12-15.

(15) Petryk, M.; Szymkowiak, J.; Gierczyk, B.; Spolnik, G.; Popenda, L.; Janiak, A.; Kwit, M. Chiral, triformylphenol-derived salen-type 4+6 organic cages. *Organic & Biomolecular Chemistry* **2016,** *14*, 7495-7499.

(16) Bera, S.; Basu, A.; Tothadi, S.; Garai, B.; Banerjee, S.; Vanka, K.; Banerjee, R. Odd–Even Alternation in Tautomeric Porous Organic Cages with Exceptional Chemical Stability. *Angewandte Chemie International Edition* **2017,** *56*, 2123-2126.

(17) Bojdys, M. J.; Briggs, M. E.; Jones, J. T. A.; Adams, D. J.; Chong, S. Y.; Schmidtmann, M.; Cooper, A. I. Supramolecular Engineering of Intrinsic and Extrinsic

Porosity in Covalent Organic Cages. *Journal of the American Chemical Society* **2011,** *133*, 16566-16571.

(18) Kim, H.; Staikova, M.; Lough, A. J.; Chin, J. Stereospecific Synthesis of Alkyl-Substituted Vicinal Diamines from the Mother Diamine: Overcoming the "Intrinsic Barrier" to the Diaza-Cope Rearrangement Reaction. *Organic Letters* **2009,** *11*, 157-160.

(19) Kim, H.; Nguyen, Y.; Yen, C. P.-H.; Chagal, L.; Lough, A. J.; Kim, B. M.; Chin, J. Stereospecific Synthesis of C2 Symmetric Diamines from the Mother Diamine by Resonance-Assisted Hydrogen-Bond Directed Diaza-Cope Rearrangement. *Journal of the American Chemical Society* **2008,** *130*, 12184-12191.

(20) Kim, H.; Nguyen, Y.; Lough, A. J.; Chin, J. Stereospecific Diaza-Cope Rearrangement Driven by Steric Strain. *Angewandte Chemie International Edition* **2008,** *47*, 8678-8681.

CHAPTER 3. MICRO-SCALE DEFECTS IN POROUS ORGANIC CAGES

Despite significant research in porous organic cages (POCs), little is known about molecular-scale defects in these materials. Here, point defects within an imine-based cage are designed using unbalanced linker nodes. Building on the formation pathway illustrated in Chapter 2 and using a computational prediction method, rapid non-solvent induced crystallization is utilized to "freeze" defective cage molecules within POC crystals. The defect structure is deduced via solution NMR, FTIR, electrospray ionization and matrix-assisted laser desorption/ionization mass spectroscopy. Gas uptake experiments show that the cage defects facilitate CO_2 adsorption. This chapter is published as part of a research article.[1]

3.1 Introduction

Since their introduction in 2009, porous organic cages (POCs) have been explored in a variety of applications including separations, adsorption, molecular recognition, and catalysis.[2-7] These porous molecules are generally used in the form of solid particles containing individual cages packed together by weak van der Waals interactions, usually resulting in a crystalline material.

As pointed out by Briggs and Cooper, the complexity involved in the synthesis and purification in POC materials can be more challenging compared to conventional MOF materials.[8] While the cage molecules are the thermodynamically stable products for carefully selected linker pairs, deliberate isolation, purification, and activation is required

to acquire the desired *de novo* product. Characterization techniques such as SEM, PXRD, and NMR are typically used to demonstrate the phase and chemical purity of the product. These techniques, however, do not readily distinguish impurities from the product, especially if the impurity shares similar linkage and symmetry with the desired product. As a result, little is known about the formation or existence of incomplete cages or other related defects in POCs.

There has been a recent emphasis on defects and disorder in the study of metal-organic frameworks (MOFs),[9-10] as the mechanical and chemical properties resulting from defects have the potential to broaden the utility of these materials.[11-13] In the area of POCs, however, current studies often assume phase and chemical purity of the cage crystal. Little is known about the formation or existence of incomplete cages or other related defects in POCs. It can be expected that analogous "missing-linker" type defects that were found in MOFs could also exist at a molecular level (i.e., a cage level) in POCs based on the observation in Chapter 2 of the [3+5] intermediate in CC3-R and the [2+4] intermediate in CC-pentane.[14-15] Indeed, CC3-R synthesized and purified according to literature procedures may also possess these incomplete cages, as shown in Figure 3.1, which motivated us to explore the possibility of intentionally creating defective CC3-R materials.

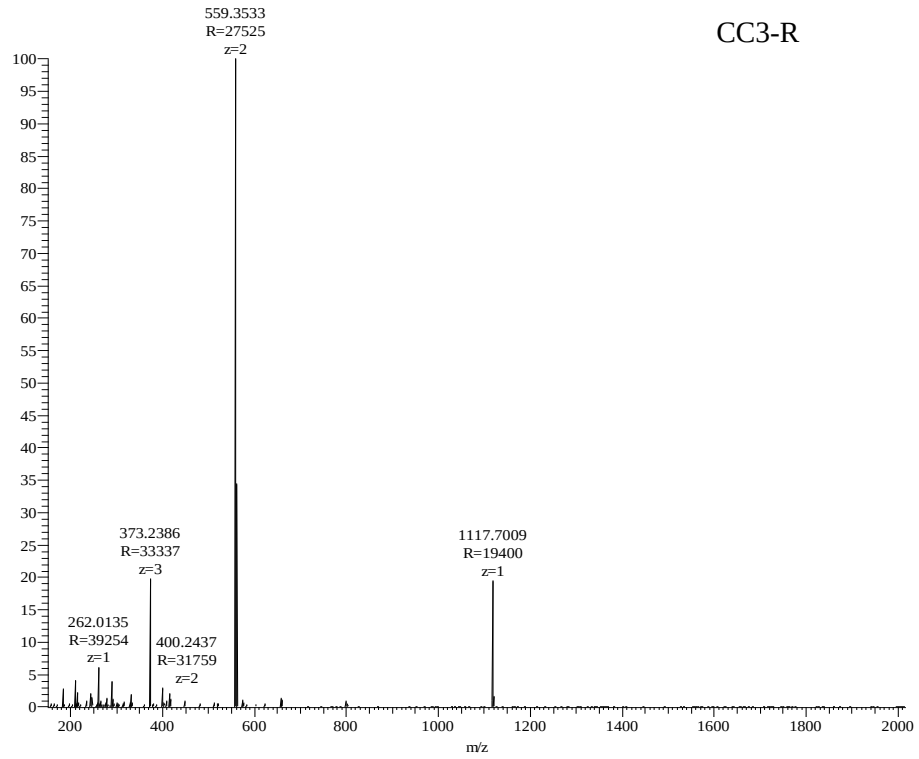

Figure 3.1 ESI-MS data of CC3-R, as-synthesized. m/z: 1117 ($[M+H]^+$)

As incomplete cages are potentially a part of "as-synthesized" materials and can also be derived from contacting acid or base species in aggressive applications, it is important to understand the influence of the broken cage bonds on the POC samples as those bonds may result in changes in their performance-related properties: (1) the incomplete cages may change the host-guest interaction properties; (2) a broken bond in the cage molecule may accelerate the decomposition of the cage. In this chapter, I used the well-studied CC3 cage as an example to demonstrate the coexistence of defective species along with pristine CC3-R cages and studied the effect these defects have on gas sorption properties. As the CC3-R cage molecule is the thermodynamically stable product of the cycloimination between triformylbenzene (TFB) and (R,R)-diaminocyclohexane, *de novo* synthesis is required for generating defects in the cage crystals. In this work, I designed two defective cage systems. So-called "Type-1" defective CC3-R molecules incorporate

isophthalaldehyde (IPA) into the structure shown in Figure 3.2. These Type-1 molecules contain free amine groups that do not have a corresponding aldehyde group to form an imine bond, analogous to "missing-linker" defects in MOFs. The so-called "Type-2" defective CC3-R molecules were also devised that contain only kinetic defects with no other reagents added to the system.

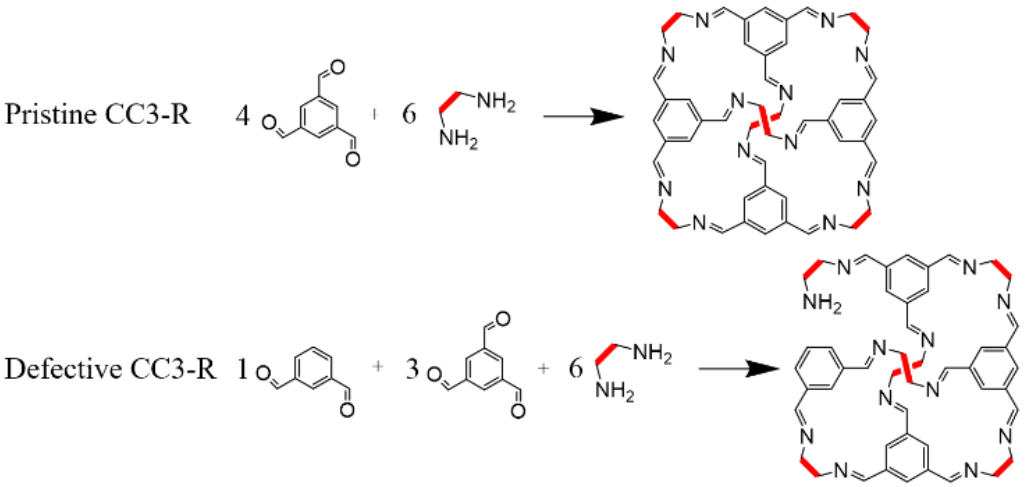

Figure 3.2 Synthesis scheme of CC3-R and one possible structure of defective CC3-R molecules

3.2 Experimental

3.2.1 Materials

Triformylbenzene was purchased from Manchester Organics (UK) or self-synthesized.[16] (1R,2R)-(-)-1,2-diaminocyclohexane, isophthalaldehyde, trifluoroacetic acid, anhydrous dichloromethane were purchased from Sigma Aldrich (US). Pentane-1,5-diamine was purchased from TCI Chemicals (US). Ultra-pure grade N_2 and CO_2 used in physisorption measurements were purchased from Airgas (US). All solvents and chemicals were used upon receive without any purification.

3.2.2 Synthesis of CC3-R

In a typical synthesis, 243 mg triformylbenzene and 255 mg (1R,2R)-(-)-1,2-diaminocyclohexane was dissolved in 10 mL anhydrous dichloromethane. To the mixture, 10 μL trifluoroacetic acid was added as a catalyst. The reaction mixture was left at room temperature for 3 days, and the white crystals were recovered by washing with ethanol.

3.2.3 Synthesis of Defective CC3-R

Different amounts of isophthalaldehyde were mixed with triformylbenzene with mass ratios of 1:2, and 1:10. In CC3-R-IPA-a, 53.9 mg triformylbenzene and 27 mg isophthalaldehyde were used. In CC3-R-IPA-b, 73.7 mg triformylbenzene and 7.5 mg isophthalaldehyde were used. To the solution of the aldehyde mixture, a solution of (1R,2R)-(-)-1,2-diaminocyclohexane (85 mg) in anhydrous dichloromethane (6 mL). 5 μL trifluoroacetic acid was added as a catalyst. The reaction was allowed to react for 1 hours at room temperature. 10 mL acetone was added to the reaction mixture, and a white precipitate formed simultaneously. The product was isolated by centrifuge and washed with ethanol. Yield: CC3-R-IPA-a, 31.1 mg, 34% based on triformylbenzene and 22% based on diaminocyclohexane; CC3-R-IPA-b, 45.2 mg, 36% based on triformylbenzene and 33% based on diaminocyclohexane.

For comparison purposes, CC3-R crystals were also prepared by fast crystallization and used in PXRD and gas sorption measurements. To a solution of CC3-R (60 mg) in DCM (20 mL) acetone was added to form a suspension. The crystals were separated by centrifugation.

3.2.4 Characterization

3.2.4.1 Scanning Electron Microscopy (SEM)

High-resolution imaging of the crystal morphology was achieved using a Hitachi SU8230 Cold Field Emission Scanning Electron Microscope (CFE-SEM). The dry samples were attached to aluminum stubs using copper tape. The samples were then coated with a 20 nm layer of gold/palladium using a Hummer 6 Gold/Palladium Sputterer. Imaging was taken at a working distance of 8 mm and a working voltage of 3 kV using a mix of upper and lower secondary electron detectors.

3.2.4.2 Powder X-ray Diffraction (PXRD)

Powder X-ray diffraction data were collected on a PANalytical Empyrean X-Ray diffraction system in reflection Bragg-Brentano geometry operating at 45 kV and 40 mA. Samples were activated at 80ºC under dynamic vacuum for 12 h and then packed onto a flat silica sample holder. The sample was then loaded in an Anton Paar HTK 1200 High-Temperature Oven Chamber connected to a vacuum pump and a CO_2 cylinder. Z adjustment and Omega correction were performed on each sample to ensure maximum signal-to-noise ratio and to minimize zero shift. The sample was evacuated in situ with dynamic vacuum and heating. PXRD patterns were taken at 80ºC and 25ºC. CO_2 was introduced into the chamber and allowed to flow for 30 min before a PXRD pattern was taken with the post sorption sample. PXRD patterns were collected with a step size of 0.0131 degrees 2θ and a scan time of 80 s/step over 2-50 degrees 2θ.

3.2.4.3 Fourier Transform Infrared Spectroscopy (FTIR)

FTIR spectroscopy was recorded by a Thermo Scientific Nicolet iS50 FT-IR equipped with an iS50 ATR module. Samples were analyzed in powder form with 128 scans with a resolution of 4 cm^{-1}.

3.2.4.4 Gas Sorption Analysis

Surface area analysis was conducted with nitrogen at 77 K using a Brunauer–Emmett–Teller surface area analyzer (BET, Micromeritics ASAP2020HD). CO_2 isotherms were collected from the same equipment at 308 K.

3.2.4.5 NMR

Solution ^1H NMR spectra were recorded at 400.13 MHz using a Bruker Avance III 400 NMR spectrometer.

3.2.4.6 ESI- and MALDI-MS

ESI-MS of samples were taken on a Waters Quattro LC system. MALDI-MS of samples were taken on a Bruker AutoFlex III instrument.

3.2.4.7 High-pressure Liquid Chromatography Mass-spectroscopy (HPLC-MS)

HPLC-MS analysis was conducted using an Agilent 1100 HPLC system connected to a Micromass Quattro LC triple mass spectrometer. Separation was achieved using an Ascentis Phenyl column, 50x2.1 mm, with 3 um particles with a 100 % methanol mobile phase at a flow rate of 0.3 mL/min. The column temperature was set to 30 °C, and 10 µL of a 0.1 mg/mL concentration sample was injected for each analysis. Spectra were acquired

in positive ion ESI mode, and the instrument was scanned from m/z 275-1500 at 3 sec/scan. The capillary was held at 3.5 kV, and the cone voltage was 20 V.

3.3 Results and Discussions

3.3.1 Synthesis of Defective CC3-R

Here, defective CC3-R cages with pre-installed defects were designed exploiting the knowledge of the formation pathway. To mimic the missing linker defects in MOFs, isophthalaldehyde (IPA) was introduced into the CC3-R synthesis, which would result in free amine groups that do not have a corresponding aldehyde group to form an imine bond. Figure 3.2 shows one possible structure of IPA incorporated into CC3-R, as compared to pristine CC3-R.

The first trial of a direct synthesis from a mixture of TFB, IPA, and DACH gave only pristine CC3-R species. To investigate the likelihood of the existence of the defective structures in the final product, my collaborator Yang Liu calculated the reaction formation energy of the defective structure shown in Figure 3.2 at the MP2/aug-cc-pVDZ level and compared it to pristine CC3-R. The calculated reaction formation energies of the defective structure in Scheme 1 are -437.3 kJ/mol, compared to -528.9 kJ/mol of CC3-R. Although the reaction formation energy of CC3-R is lower than the defective species, the energy differences are small enough to indicate that defective cages may be present at low concentrations after synthesis of CC3-R if complete thermodynamic equilibrium is not attained.

Our energetic calculations suggest that the synthesis reaction involving IPA needs to be stopped before full equilibrium is reached to yield defective CC3-R with free amine groups, whose impact can then be assessed. To this end, I used a non-solvent induced crystallization method to "freeze" potential defective structures during the CC3-R synthesis. In the normal crystallization of POCs, solvents or solvent mixtures are slowly removed to allow the cage molecules to crystallize.[8] In contrast, upon quick addition of non-solvents (i.e., acetone) to the reaction mixture, the clear synthesis solution immediately becomes cloudy, and the product can be subsequently separated by centrifugation. Different amounts of the "defective" ligand IPA were added as reactant (mass ratio of TFB to IPA is 2:1, and 10:1) and allowed to react for 1 h before rapid crystallization. These two samples were denoted as samples CC3-R-IPA-a and CC3-R-IPA-b, respectively. A CC3-R sample was also prepared by solvent-induced fast crystallization to enable comparison to the defective samples in XRD and physisorption measurements.

3.3.2 Defect Characterization

Mass spectrometry was used to characterize the composition of the samples. In the ESI-MS, several incomplete cage species were observed for CC3-R-IPA-a and CC3-R-IPA-b (Figure 3.3, Figure 3.4, and Figure 3.5). The compositions and m/z ratios of these incomplete cages are listed in Table 3.1 as IC (incomplete cage) 1-6. All the incomplete cages share a similar geometry with the parent cage. No cages or intermediates larger (regarding m/z) than CC3-R were observed.

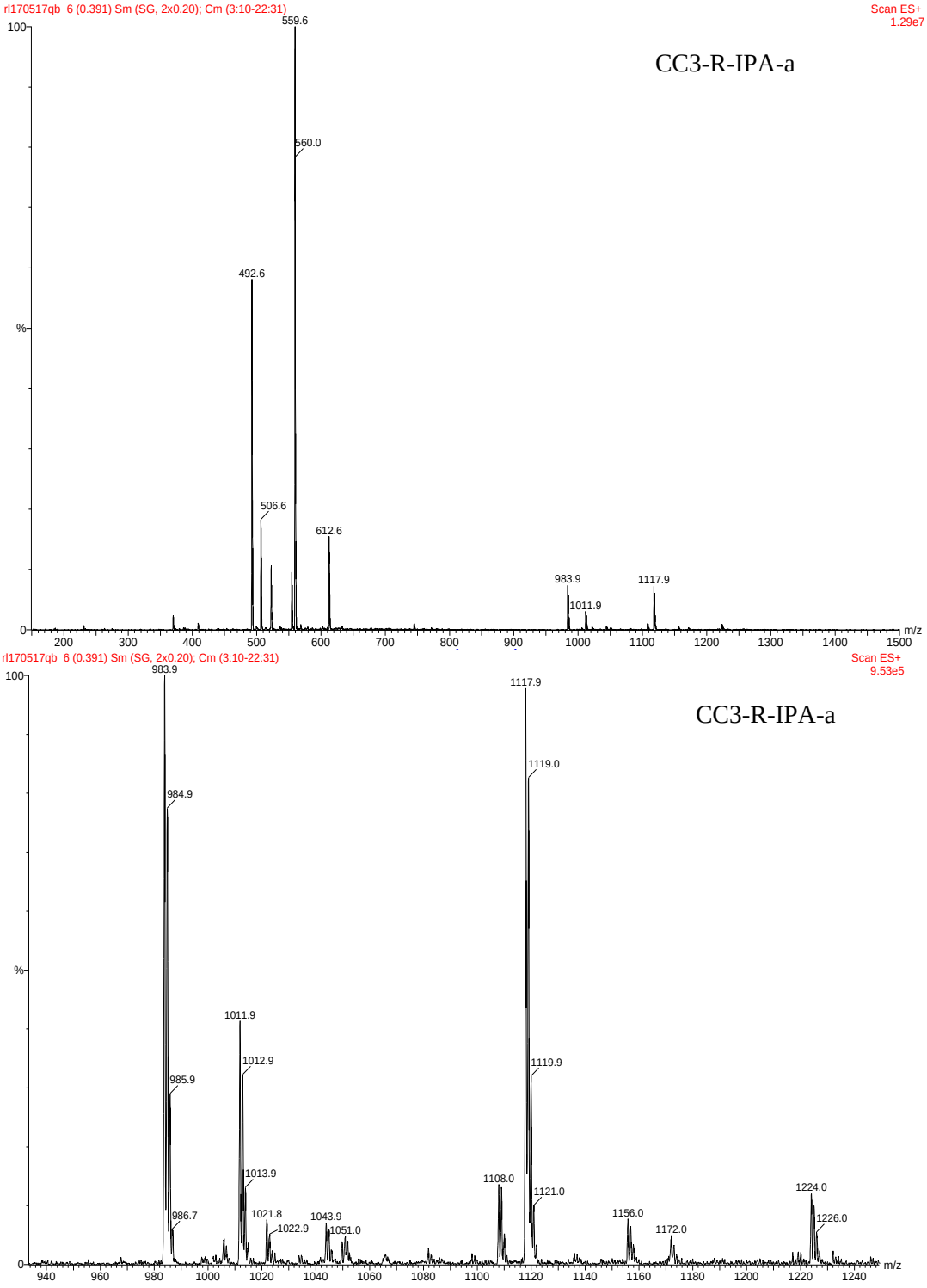

Figure 3.3 ESI-MS of defective CC3-R-IPA-a (full range and magnified)

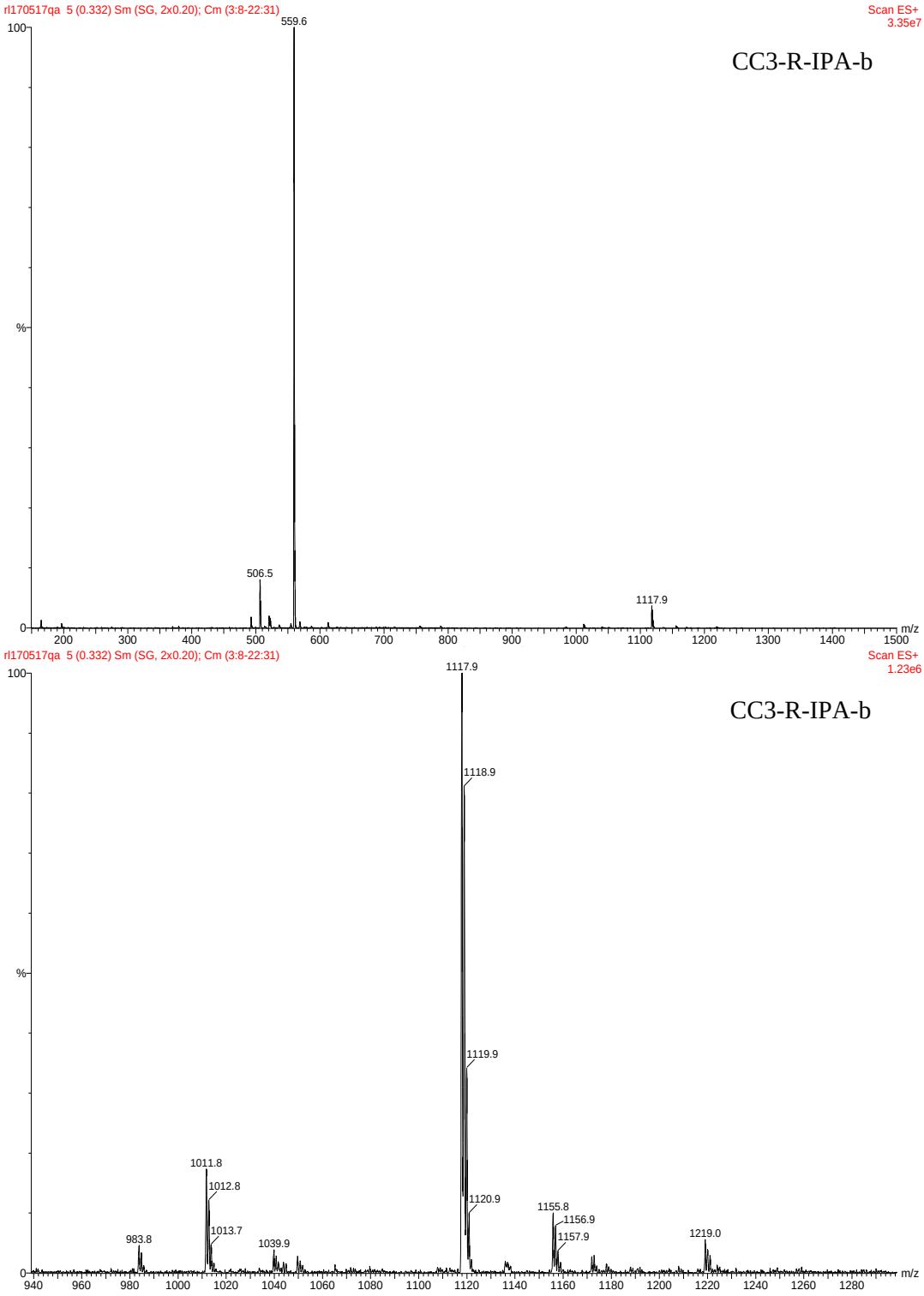

Figure 3.4 ESI-MS of defective CC3-R-IPA-b

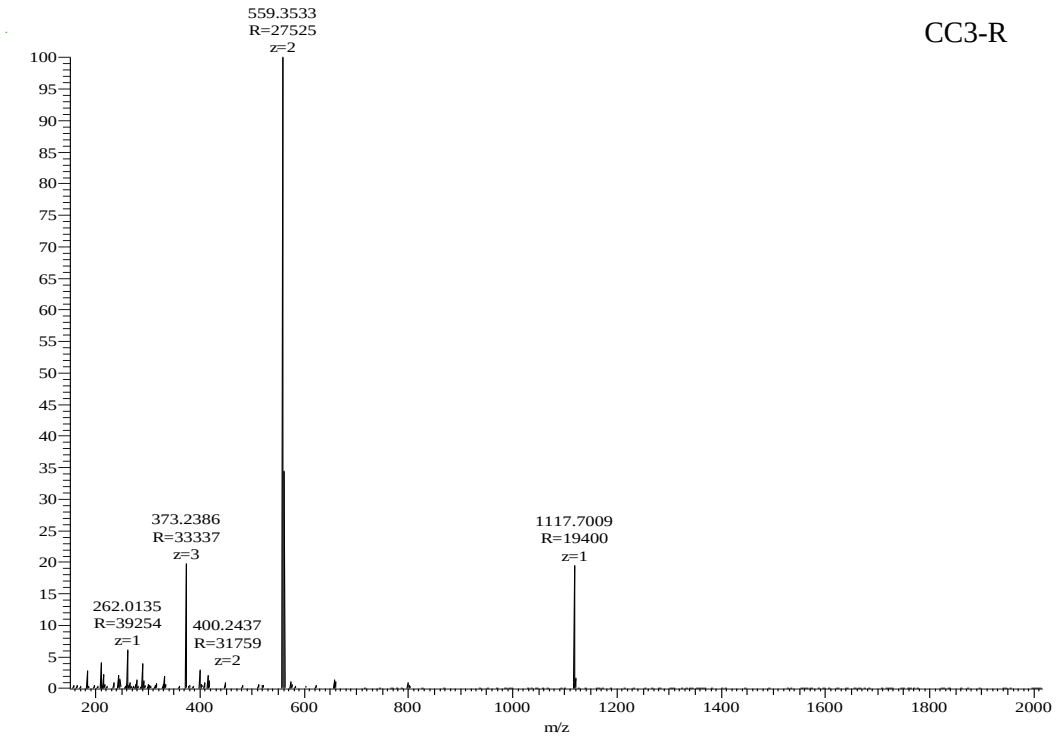

Figure 3.5 ESI-MS of defective CC3-R and pristine CC3-R

Table 3.1 List of species in defective CC3-R

	# of Triformylbenzene	# of Isophthalaldehyde	# of Diaminocyclohexane	Bonds	Mw [Da]
IC1	2	1	4	8	771.01
IC2	2	2	5	10	983.29
IC3	3	0	5	9	895.19
IC4	3	1	5	10	1011.3
IC5	3	1	6	11	1107.47
IC6	3	1	7	11	1221.66
CC3-R	4	0	6	12	1117.46

The composition and presence of the defective species in CC3-R-IPA-a were further analyzed using high-pressure liquid chromatography-mass spectrometry (HPLC-MS). The chromatograms shown in Figure 3.6 highlight clear separation between incomplete cages and the defect-free cages around 10 min and 20 min, respectively. Importantly, the HPLC-MS data suggest that the majority of the products are defect-free

CC3-R cages and IC4 species (Figure 3.7). Integration of non-trivial quantities of the identified defective species noticeably influenced the macroscopic properties of the samples (e.g., guest molecule uptake).

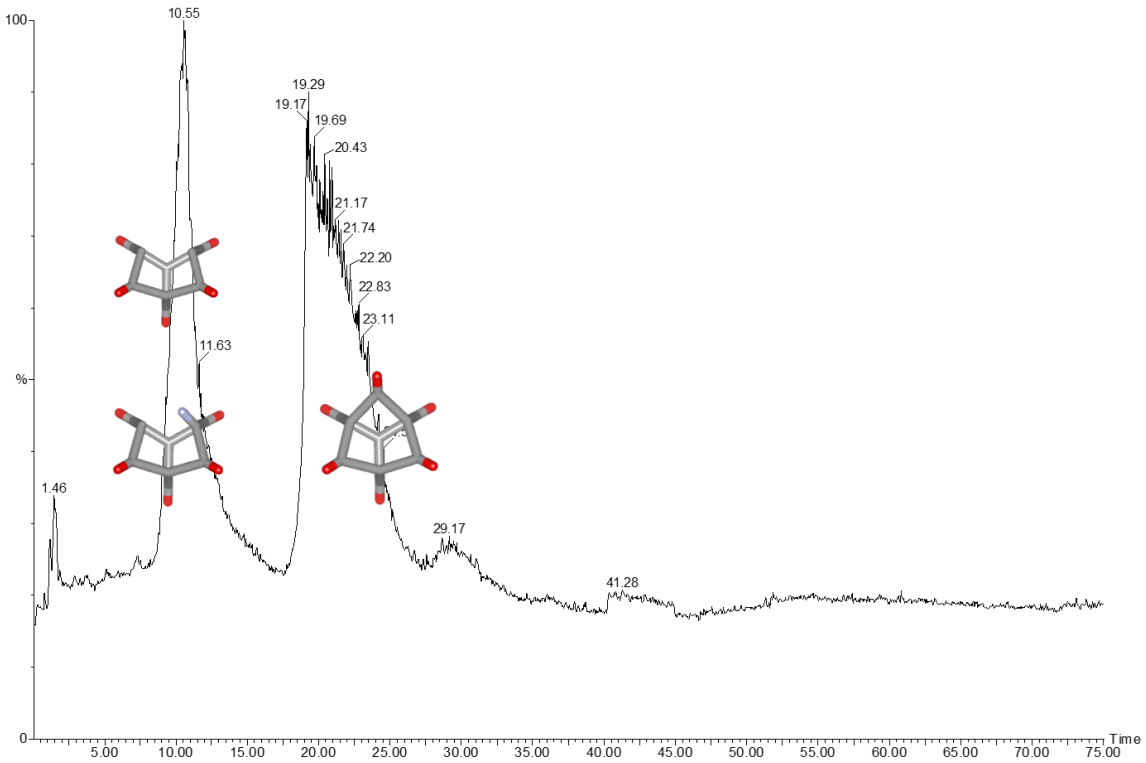

Figure 3.6 Chromatogram of CC3-R-IPA-a in HPLC-MS

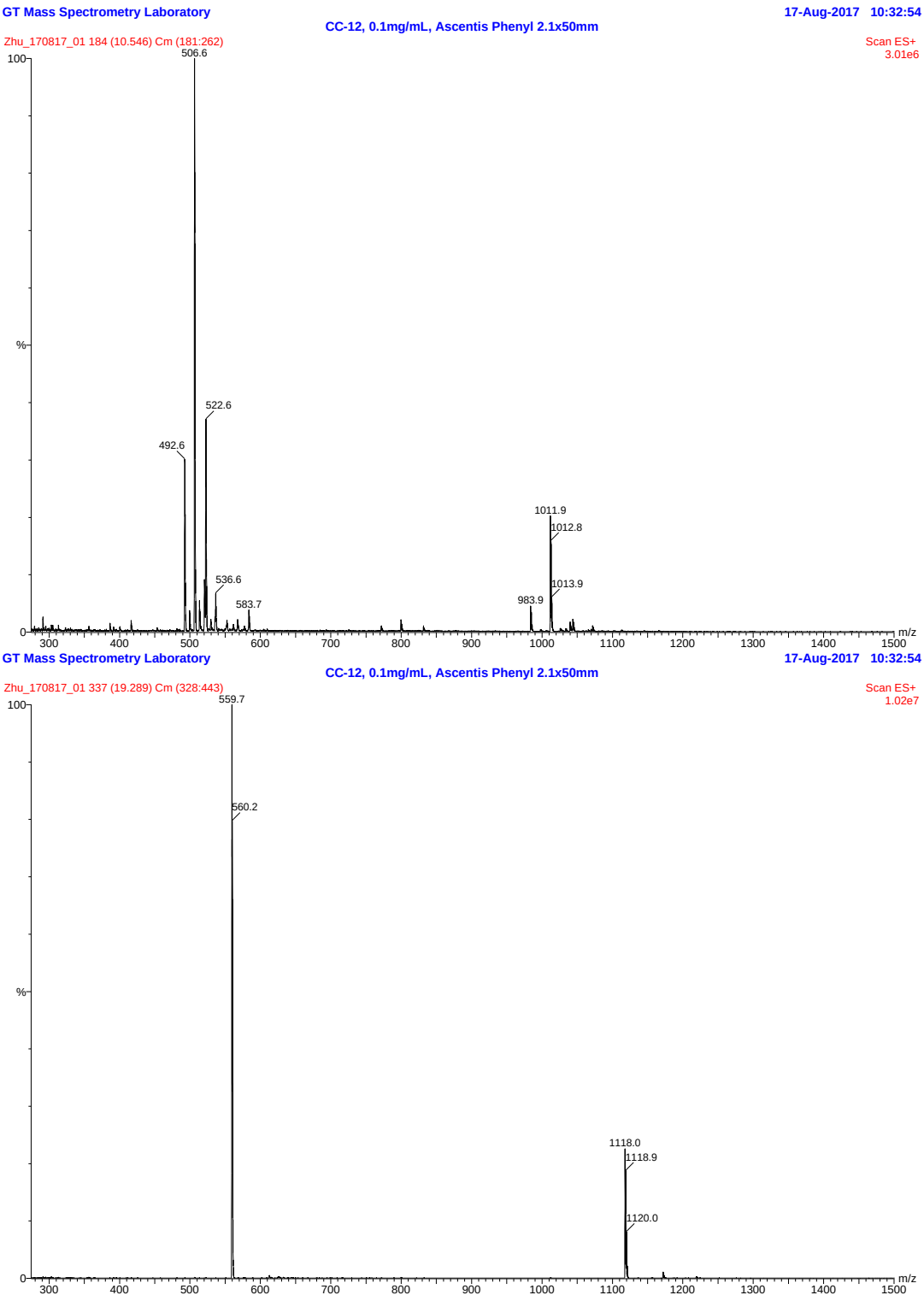

Figure 3.7 Integration of combined ion counts of the peak around 10 min and 20 min in the chromatogram of CC3-R-IPA-a in HPLC-MS

The higher concentration of defects in defective CC3-R can be detected by IR and ^{1}H NMR. Figure 3.8 shows the IR spectra of the powder samples. The free aldehyde and amine peaks were highlighted in the defective samples. The vibrational modes of primary N-H around 1600 cm^{-1} cannot be distinguished as it overlaps with existing C=N (1645 cm^{-1}) and C=C (1600 cm^{-1}) bonds. Indeed, the free aldehyde group might be coming from the reactant trapped in the crystal as a result of quenching.

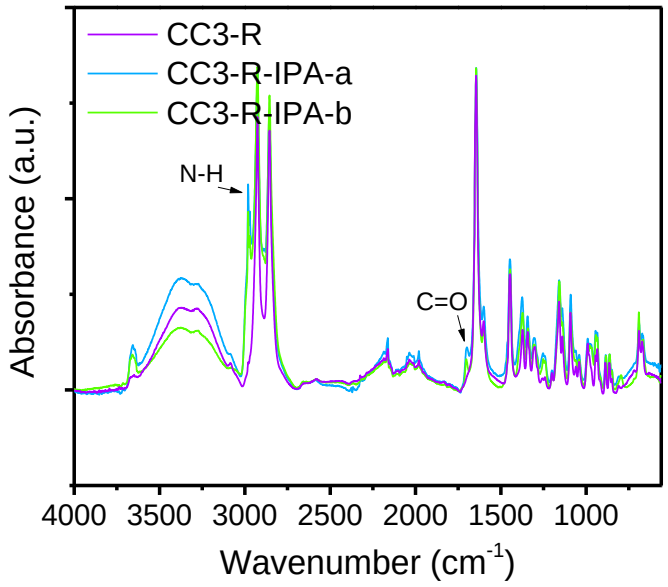

Figure 3.8 FTIR spectra of sample CC3-R-IPA-a and CC3-R-IPA-b compared to pristine CC3-R. The fingerprint vibrational bands of C=O moieties at 1700 cm^{-1} and N-H stretch at 3000 cm^{-1} was observed in two defective CC3-R samples

The presence of free and bonded isophthalaldehyde was further probed by solution ^{1}H NMR. As shown in Figure 3.9, the three samples all showed similar ^{1}H shift compared to CC3-R. No signal for triformylbenzene and isophthalaldehyde was observed, indicating no reactant was trapped during the fast crystallization of the defective samples. This confirms that the C=O bond observed in IR is from defective cages. A closer inspection of the ^{1}H NMR spectra between chemical shift 10.5 ppm and 7.6 ppm reveals that the *meta*-

H on benzene ring was not affected by the iminization and can be detected in the defective samples (Figure 3.10).

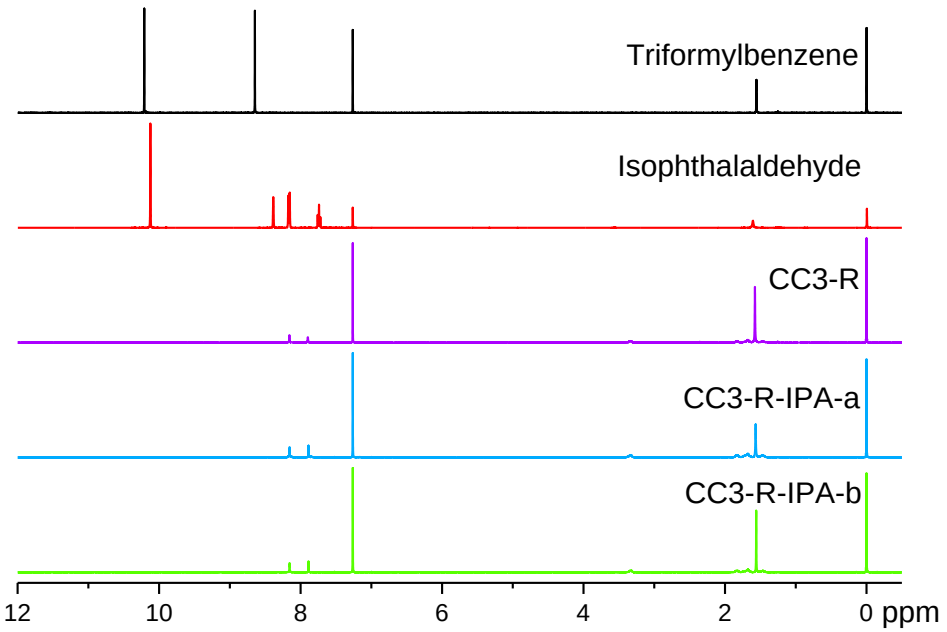

Figure 3.9 ^{1}H NMR spectra of triformylbenzene, isophthalaldehyde, CC3-R, and two defective CC3-R samples

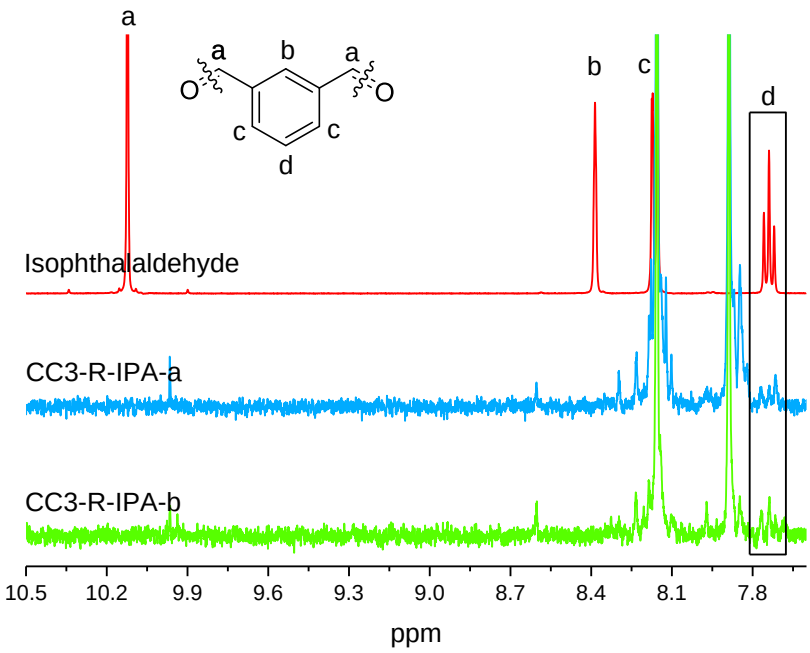

Figure 3.10 Detailed ^{1}H NMR spectra of isophthalaldehyde, and three Type-1 defective CC3-R samples. For easier comparison, the spectra of the latter three samples were amplified and normalized by CH=N (δ=8.15 ppm). The *meta* position aromatic H with respect to carboxaldehyde was highlighted in a frame

From the integration of the ^{1}H NMR spectra, the concentration of the incorporated isophthalaldehyde can be induced. As shown in Figure 3.11, 12 imine hydrogens at 8.15 ppm chemical shift can be found from the integration that resulted from 12 imine linkages between 4 triformylbenzene and 6 cyclohexane diamine molecules. Another 12 aromatic hydrogens at 7.89 ppm chemical shift result from 4 triformylbenzene molecules each with 3 hydrogens. Another 12 aliphatic hydrogen at 3.33 ppm chemical shift on the α-carbon of the imine bond comes from 6 cyclohexane molecules. 48 aliphatic hydrogen on the 6 cyclohexane molecules sits between 1.3 and 1.9 ppm chemical shift.

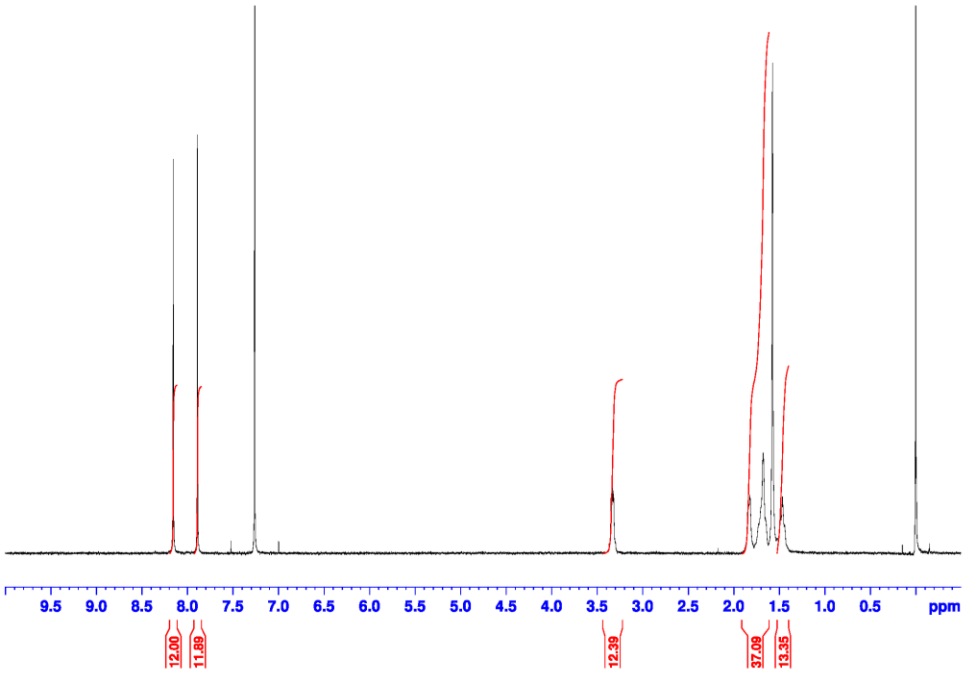

Figure 3.11 Integral of ^{1}H NMR spectra of CC3-R: ^{1}H NMR ($CDCl_3$) δ 8.15 (s, C*H*=N, 12H), 7.89 (s, ArH, 12H), 3.33 (m, C*H*N, 12H), 1.9 – 1.4 (m, CH2, 48H) ppm

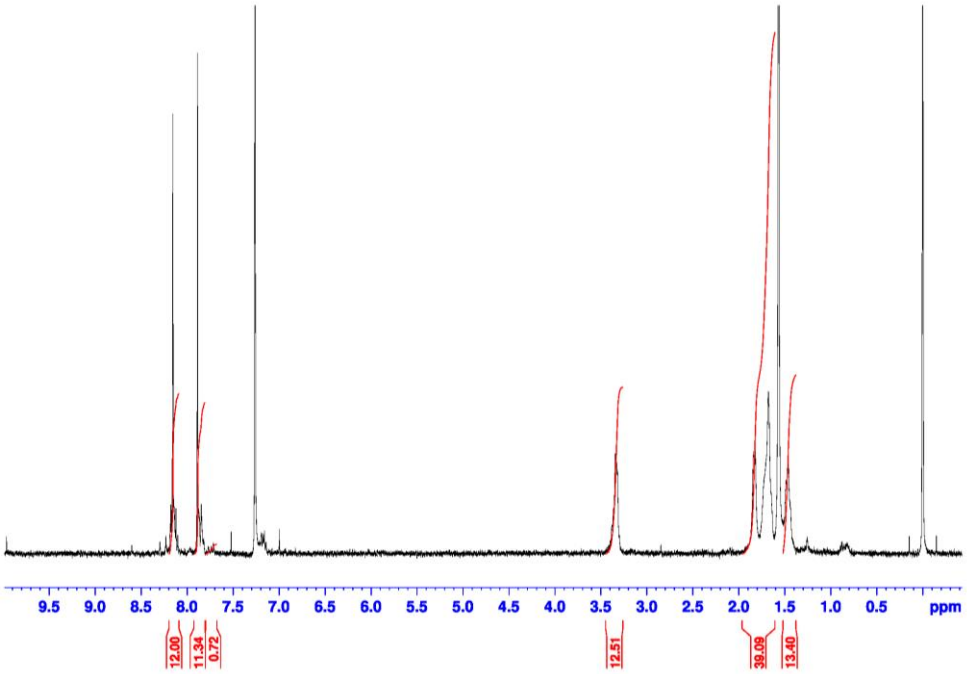

Figure 3.12 Integral of ^{1}H NMR spectra of CC3-R-IPA-a: ^{1}H NMR ($CDCl_3$) δ 8.15 (s, C*H*=N, 12H), 7.89 (s, ArH, 11H), 7.75 (t, *m*-ArH, 0.72H), 3.33 (m, C*H*N, 12H), 1.9 – 1.4 (m, CH2, 48H) ppm

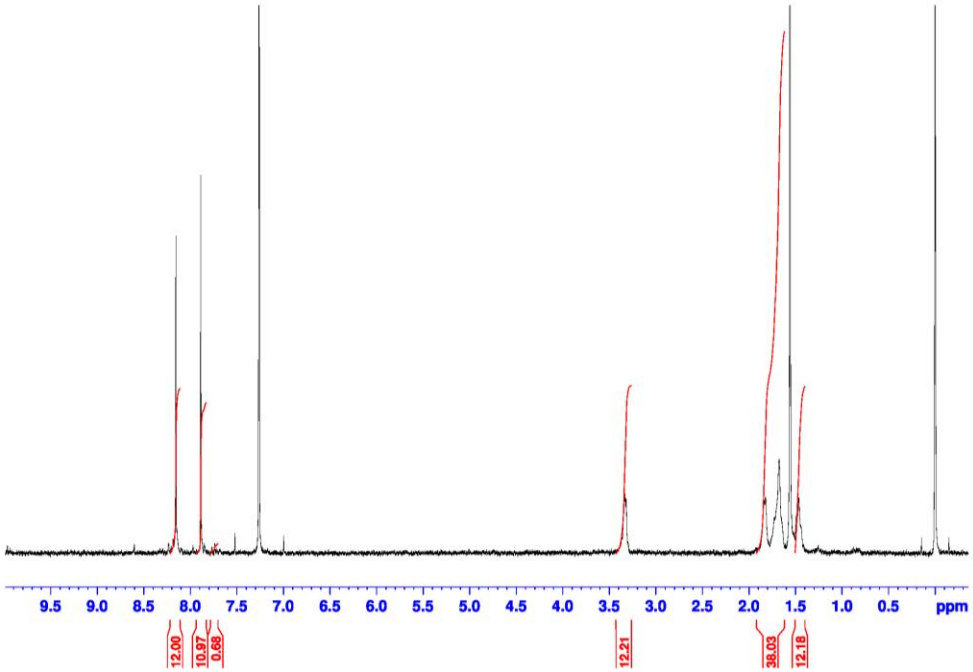

Figure 3.13 Integral of ^{1}H NMR spectra of CC3-R-IPA-b: ^{1}H NMR ($CDCl_3$) δ 8.15 (s, C*H*=N, 12H), 7.89 (s, ArH, 11H), 7.75 (t, *m*-ArH, 0.68H), 3.33 (m, C*H*N, 12H), 1.9 – 1.4 (m, CH2, 48H) ppm

In the CC3-R-IPA-a and -b samples (Figure 3.12 and Figure 3.13), hydrogen from isophthalaldehyde can be observed at 7.75 ppm chemical shift. From CC3-R-IPA-a, this peak integrated to 0.72 relative to 12 imine hydrogens. This indicates on average less than one isophthalaldehyde molecule was incorporated in the defective cages, which also corroborated the LC-MS results that the cage crystal is a mixture of CC3-R and IC4 cages.

3.3.3 Macroscopic Properties Affected by Defects

The effect of incomplete cages inside the crystal on guest interactions was evaluated using N_2 and CO_2 physisorption (Figure 3.14 and

Table 3.2). While the interaction of sorbate molecules in CC3-R crystals only happens in the form of physisorption, the defective cages possess more functional groups that have additional electronic interactions with the sorbates. In both samples, a decrease

in the surface area was observed from 469 m^2/g of CC3-R to 397 m^2/g in CC3-R-IPA-a and 438 m^2/g in CC3-R-IPA-b. In contrast, the CO_2 uptake increased from 1.11 mmol/g of CC3-R to 1.41 mmol/g in CC3-R-IPA-a and 1.48 mmol/g in CC3-R-IPA-b.

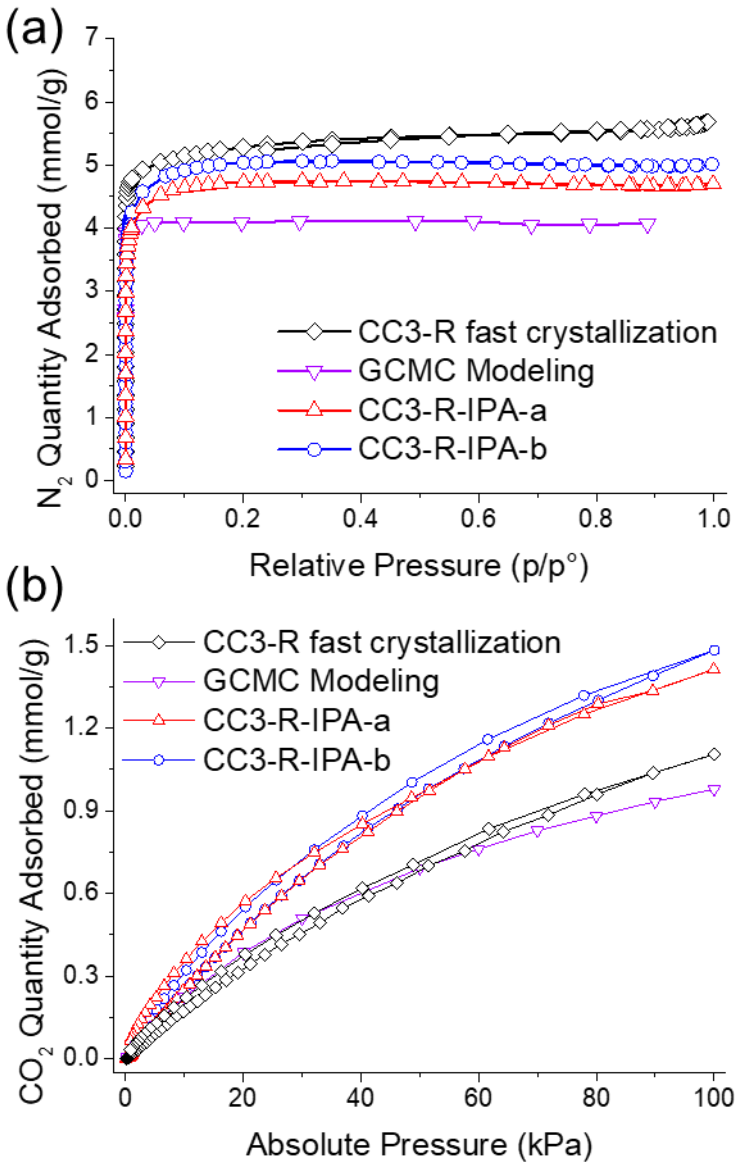

Figure 3.14 (a) N_2 isotherms at 77 K for "defect-free" CC3-R and two defective samples. (b) CO_2 isotherms at 308 K for "defect-free" CC3-R and 2 defective samples. GCMC isotherm modeling of CC3-R is shown in black.

Table 3.2 Textural properties of samples in this study

Sample	V_{micro}[a] [$cm^3\ g^{-1}$]	S_{micro}[a] [$m^2\ g^{-1}$]	S_{ext}[a] [$m^2\ g^{-1}$]	V_t[b] [$cm^3\ g^{-1}$]	S_{BET}[c] [$m^2\ g^{-1}$]	CO_2 uptake 1bar, 308 K
CC3-R, fast crystallization	0.150	380	75	0.19	469	1.11
CC3-R-IPA-a	0.132	345	52	0.159	397	1.41
CC3-R-IPA-b	0.151	384	53	0.173	438	1.48

a Determined from the t-plot method.
b Determined at p/p0 = 0.95.
c Determined from Brunauer, Emmett, and Teller (BET) method.

Powder X-ray diffraction experiments were conducted on *in situ* evacuated and CO_2 saturated samples (Figure 3.15). Unit cell refinement of the powder patterns for CC3-R-IPA-b (TFB:IPA=10:1) and CC3-R-IPA-a (TFB:IPA=2:1) reveal that the lattice parameter α at 25 ºC under vacuum changed from 24.80(1) Å to 24.76(2) Å (compared to CC3-R with 24.856(3) Å). The small change in lattice parameter is attributed to different shapes of the incomplete cages in the crystals based on the following: in defective CC3-R, defect modalities IC1 – IC4 all have a smaller size compared to a complete CC3-R cage. We hypothesize the random packing of these species in the crystals will result in a reduction in crystal lattice parameter.

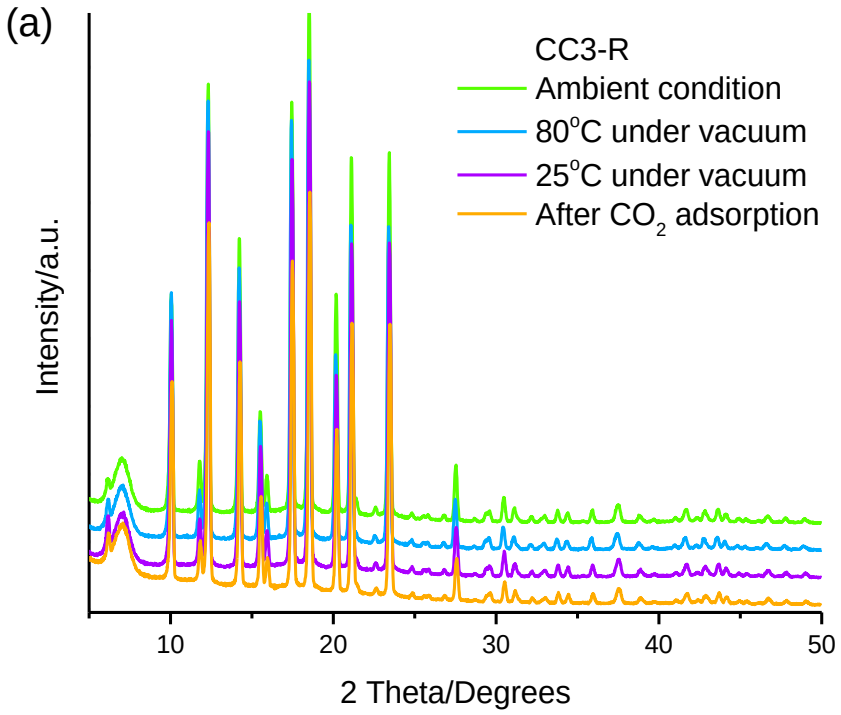
(a)
CC3-R
Ambient condition
80°C under vacuum
25°C under vacuum
After CO2 adsorption
Intensity/a.u.
10
20
30
40
50
2 Theta/Degrees

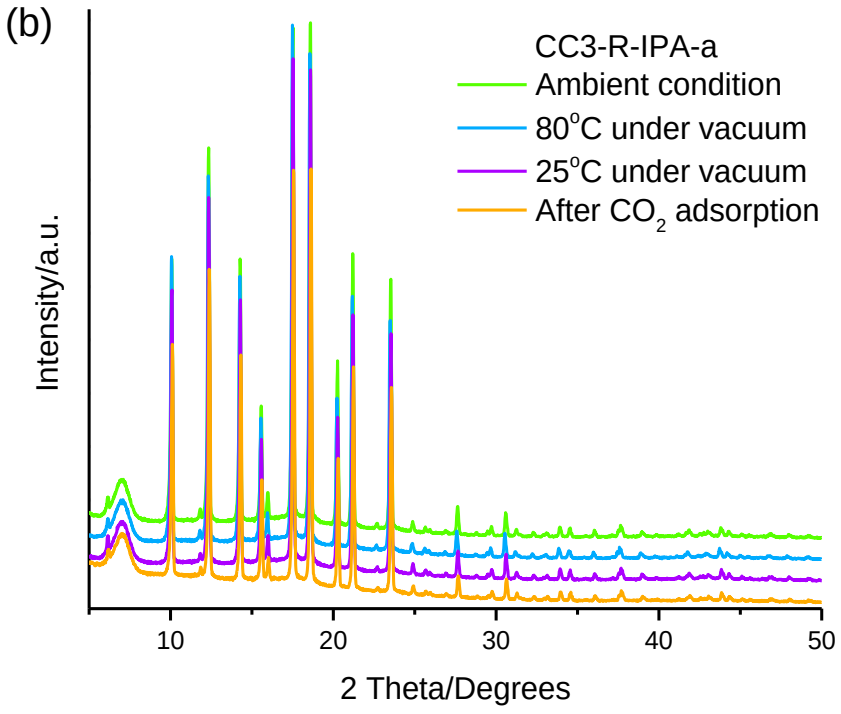
(b)
CC3-R-IPA-a
Ambient condition
80°C under vacuum
25°C under vacuum
After CO2 adsorption
Intensity/a.u.
10
20
30
40
50
2 Theta/Degrees

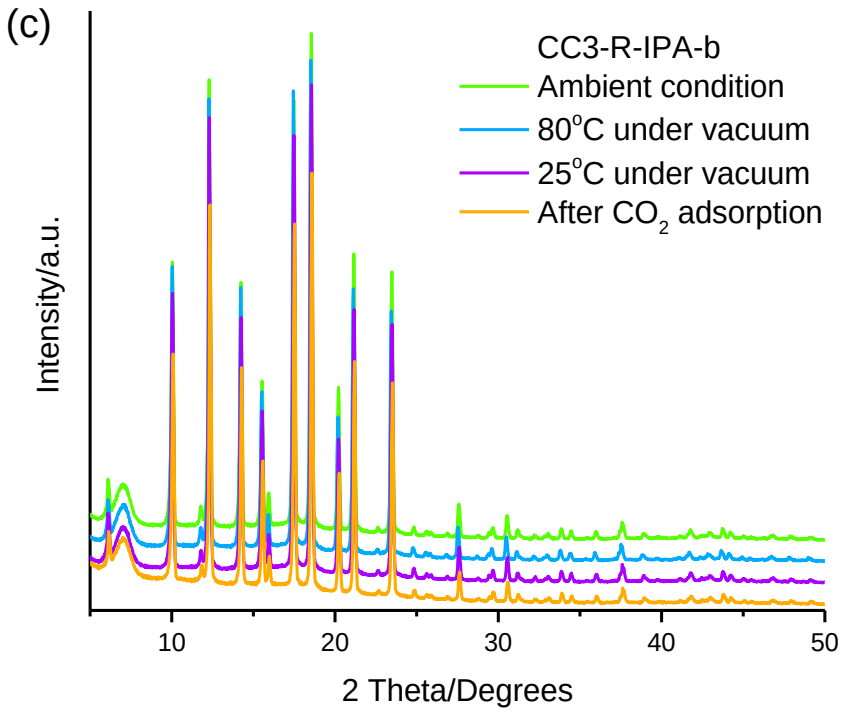

Figure 3.15 *in situ* X-ray diffraction of (a) pristine and (b,c) defective CC3-R samples produced from non-solvent induced crystallization. The patterns were collected at the following conditions: at ambient conditions, after being held at 80 ºC for 30 min, after being cooled down to 25 ºC, and after equilibration with CO_2 for 30 min

Unit cell refinement was performed on each diffraction pattern to determine the lattice parameter of the samples at different conditions. The refinement was carried out using the built-in unit cell refinement function in HighScore Plus, which is performed by a least squares fit through the angular differences between measured peaks and indexed reflections (from the published CC3 structure file), and also by adjusting the sample displacement. The refinement was carried out from 8.5 to 50 degree 2θ to minimize the effect from the amorphous peak around 7 degrees 2θ that is from the background of the XRD system. The lattice parameters (α) are summarized in Table 3.3. The last digits in

parenthesis are estimated standard deviations (ESDs) from the peak refining. The fitting was evaluated by Snyder's figure of merit (FOM).[17]

Table 3.3 List of lattice parameters (a, Å) in defective and pristine CC3-R samples under ambient condition, held at 80 ºC for 30 min, cooled down to 25 ºC, and equilibrate with CO_2 for 30 min, respectively

	CC3-R		CC3-R-IPA-a		CC3-R-IPA-b	
	a, Å	FOM	a, Å	FOM	a, Å	FOM
Ambient condition	24.89(1)#	29	24.75(1)	32	24.77(2)	20
80 ºC vacuum	24.82(4)*	9	24.82(1)	31	24.84(1)	30
25ºC vacuum	24.856(3)	118	24.76(2)	25	24.80(1)	35
Equilibrate with CO_2	24.95(4)*	10	24.84(3)*	12	24.81(1)	33

The last digits in parenthesis are estimated standard deviations (ESDs) from the peak refining.
* Numbers with an asterisk indicate a FOM<20.

The SEM images of the defective samples are shown in Figure 3.16. It can be observed that in CC3-R-IPA-a, in which more IPA is incorporated into the structure, there is more intergrowth between the octahedral crystals and surface deformation. The incorporation of IPA into the crystal likely changed the cage packing motif and resulted in such disturbed morphology.

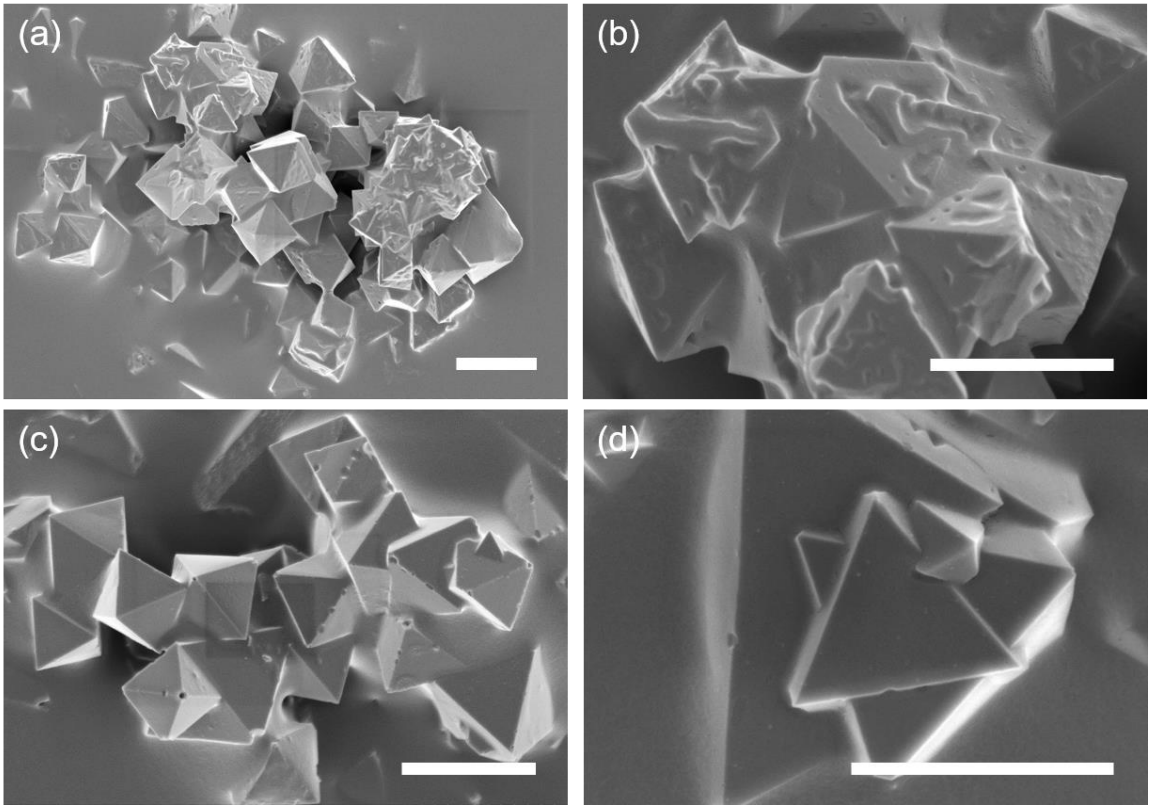

Figure 3.16 SEM of defective CC3-R crystals. (a) and (b) CC3-R-IPA-a crystals, (c) and (d) CC3-R-IPA-b crystals.

* The scale bars in (a) and (c) represent 5 μm. The scale bars in (b) and (d) represent 3 μm

3.4 Conclusions

In summary, we used nonsolvent-induced crystallization guided by theoretical calculations to successfully introduce a non-trivial amount of incomplete cages into CC3-R samples as a means to study the effects of defective species on porous organic cage materials' properties and performance metrics. Theoretical calculation methods were developed based on the knowledge learned in Chapter 2. The incomplete cages trapped in CC3 crystals were identified by various mass spectrometry techniques. The effects of the incomplete cages on the parent materials were evaluated with an emphasis on the physisorption of guest molecules and the potential stability of the cage molecules. In this

case, all selected defective samples have large affinity towards CO_2 (as shown by experimental and computational results), and all defective cages are more unstable than the pristine CC3-R cage.

3.5 References

(1) Zhu, G.; Liu, Y.; Flores, L.; Lee, Z. R.; Jones, C. W.; Dixon, D. A.; Sholl, D. S.; Lively, R. P. Formation Mechanisms and Defect Engineering of Imine-Based Porous Organic Cages. *Chemistry of Materials* **2018,** *30*, 262-272.

(2) Tozawa, T.; Jones, J. T. A.; Swamy, S. I.; Jiang, S.; Adams, D. J.; Shakespeare, S.; Clowes, R.; Bradshaw, D.; Hasell, T.; Chong, S. Y.; Tang, C.; Thompson, S.; Parker, J.; Trewin, A.; Bacsa, J.; Slawin, A. M. Z.; Steiner, A.; Cooper, A. I. Porous organic cages. *Nature Materials* **2009,** *8*, 973-978.

(3) Zwijnenburg, M. A.; Berardo, E.; Peveler, W. J.; Jelfs, K. E. Amine Molecular Cages as Supramolecular Fluorescent Explosive Sensors: A Computational Perspective. *Journal of Physical Chemistry B* **2016,** *120*, 5063-5072.

(4) Xie, S. M.; Zhang, J. H.; Fu, N.; Wang, B. J.; Chen, L.; Yuan, L. M. A chiral porous organic cage for molecular recognition using gas chromatography. *Analytica Chimica Acta* **2016,** *903*, 156-163.

(5) Song, Q. L.; Jiang, S.; Hasell, T.; Liu, M.; Sun, S. J.; Cheetham, A. K.; Sivaniah, E.; Cooper, A. I. Porous Organic Cage Thin Films and Molecular-Sieving Membranes. *Advanced Materials* **2016,** *28*, 2629-2637.

(6) Uemura, T.; Nakanishi, R.; Mochizuki, S.; Kitagawa, S.; Mizuno, M. Radical Polymerization of Vinyl Monomers in Porous Organic Cages. *Angewandte Chemie International Edition* **2016,** *55*, 6443-6447.

(7) Sun, J. K.; Zhan, W. W.; Akita, T.; Xu, Q. Toward Homogenization of Heterogeneous Metal Nanoparticle Catalysts with Enhanced Catalytic Performance: Soluble Porous Organic Cage as a Stabilizer and Homogenizer. *Journal of the American Chemical Society* **2015,** *137*, 7063-7066.

(8) Briggs, M. E.; Cooper, A. I. A Perspective on the Synthesis, Purification, and Characterization of Porous Organic Cages. *Chemistry of Materials* **2017,** *29*, 149-157.

(9) Bennett, T. D.; Cheetham, A. K.; Fuchs, A. H.; Coudert, F.-X. Interplay between defects, disorder and flexibility in metal-organic frameworks. *Nat. Chem.* **2017,** *9*, 11-16.

(10) Sholl, D. S.; Lively, R. P. Defects in Metal–Organic Frameworks: Challenge or Opportunity? *The Journal of Physical Chemistry Letters* **2015,** *6*, 3437-3444.

(11) Thornton, A. W.; Babarao, R.; Jain, A.; Trousselet, F.; Coudert, F. X. Defects in metal-organic frameworks: a compromise between adsorption and stability? *Dalton Transactions* **2016,** *45*, 4352-4359.

(12) Bennett, T. D.; Yue, Y.; Li, P.; Qiao, A.; Tao, H.; Greaves, N. G.; Richards, T.; Lampronti, G. I.; Redfern, S. A. T.; Blanc, F.; Farha, O. K.; Hupp, J. T.; Cheetham, A. K.; Keen, D. A. Melt-Quenched Glasses of Metal–Organic Frameworks. *Journal of the American Chemical Society* **2016,** *138*, 3484-3492.

(13) Fukushima, T.; Horike, S.; Inubushi, Y.; Nakagawa, K.; Kubota, Y.; Takata, M.; Kitagawa, S. Solid Solutions of Soft Porous Coordination Polymers: Fine-Tuning of Gas Adsorption Properties. *Angewandte Chemie* **2010,** *122*, 4930-4934.

(14) Zhang, C.; Han, C.; Sholl, D. S.; Schmidt, J. R. Computational Characterization of Defects in Metal–Organic Frameworks: Spontaneous and Water-Induced Point Defects in ZIF-8. *The Journal of Physical Chemistry Letters* **2016,** *7*, 459-464.

(15) Fang, Z.; Bueken, B.; De Vos, D. E.; Fischer, R. A. Defect-Engineered Metal–Organic Frameworks. *Angewandte Chemie International Edition* **2015,** *54*, 7234-7254.

(16) Zhu, G.; Hoffman, C. D.; Liu, Y.; Bhattacharyya, S.; Tumuluri, U.; Jue, M. L.; Wu, Z.; Sholl, D. S.; Nair, S.; Jones, C. W.; Lively, R. P. Engineering Porous Organic Cage Crystals with Increased Acid Gas Resistance. *Chemistry – A European Journal* **2016,** *22*, 10743-10747.

(17) Smith, G. S.; Snyder, R. L. FN: A criterion for rating powder diffraction patterns and evaluating the reliability of powder-pattern indexing. *Journal of Applied Crystallography* **1979,** *12*, 60-65.

CHAPTER 4. MESO-SCALE DEFECTS IN POROUS ORGANIC CAGES AND THEIR ACID GAS STABILITY

In this chapter, defects at a larger scale compared to those discussed in Chapter 3 are considered. Specifically, defects at the mesoscale are found to affect the stability of the cage crystals, and a new synthesis route is proposed to mitigate the formation of these defects. This chapter is published as part of a research article.[1]

Both known and new CC3-based porous organic cages are prepared and exposed to acidic SO_2 in vapor and liquid conditions. Distinct differences in the stability of the CC3 cages exist depending on the chirality of the diamine linkers used. The acid-catalyzed CC3 degradation mechanism is probed via *in situ* IR and a degradation pathway is proposed. CC3 crystals synthesized with racemic mixtures of diaminocyclohexane exhibited enhanced stability compared to CC3-R and CC3-S. Confocal fluorescent microscope images reveal that the stability difference in CC3 species originates from an abundance of mesoporous grain boundaries in CC3-R and CC3-S, allowing facile access of aqueous SO_2 throughout the crystal, promoting decomposition. These grain boundaries are absent from CC3 crystals made with racemic linkers.

4.1 Introduction

After the exploration of the formation mechanisms of imine-based POCs that opens the door to customize design towards targeted applications in Chapter 2, and the attempt in Chapter 3 to improve the performance of the POC materials via defect enrichment, in this chapter, some practical issues are considered.

Two issues that any new material must certainly face in separation applications are (i) the stability of the material in the face of aggressive contaminants such as H_2S, SO_X, NO_X, and water,[2-3] and (ii) the scalability of the production of the material. Here, the stability of imine-based cages was investigated using CC3 as a model compound for investigating SO_2 contamination, as SO_2 is usually present in significant concentrations in industrial gases such as flue gas from coal-fired power stations. The chemical and physical degradation mechanism of CC3-R exposed to dilute SO_2 conditions is thus developed. We also describe a reduced cost method for the synthesis of CC3-like molecules. This method is shown to enhance acid stability relative to the chiral CC3-R or CC3-S. This increased stability is attributed to the reduction in mesoporous planar defects in POC crystals; an effect visualized by confocal fluorescent microscopy.

4.2 Experimental

4.2.1 Materials

1,3,5-Triformylbenzene was purchased from Manchester Organics or synthesized by oxidizing 1,3,5-benzenetrimethanol with PCC. All other chemicals were purchased from Sigma-Aldrich and used without further purification.

4.2.2 Synthesis of CC3-R

CC3-R was synthesized according to the literature report.[1] In a typical synthesis, 243 mg triformylbenzene was added to a conical flask. A solution of 255 mg (1*R*,2*R*)-1,2-diaminocyclohexane in 10 mL anhydrous DCM was added slowly to the flask so that the triformylbenzene powder was not disturbed. 10 μL trifluoroacetic acid was added to the

mixture as the iminization catalyst. The flask was capped and kept still at room temperature for 3 days. The yellow reaction mixture was filtered and washed to white using a 95% ethanol / 5% DCM mixture. The product was dried in a conventional oven at 80 °C and then in a vacuum oven at 80 °C overnight.

4.2.3 Synthesis of CC3-S, CC3-trans and CC3-mix

The synthesis of CC3-S, CC3-trans, and CC3-mix was identical to CC3-R, except that different enantiomer/diastereomers were used. In the CC3-S synthesis, (1*S*,2*S*)-1,2-diaminocyclohexane was used instead of (1*R*,2*R*)-1,2-diaminocyclohexane. In the CC3-trans synthesis, a racemic mixture of (1*R*,2*R*)-1,2-diaminocyclohexane and (1*S*,2*S*)-1,2-diaminocyclohexane was used. In the CC3-mix synthesis, a mixture of *cis*-diaminocyclohexane, (1*R*,2*R*)-1,2-diaminocyclohexane and (1*S*,2*S*)-1,2-diaminocyclohexane was used.

4.2.4 Humid SO_2 Exposure Procedure

Samples were exposed to 50 ppm SO_2 in air with relative humidity of 80% for 2 days or 4 days at room temperature (24 °C). The acid gas mixture was prepared according to the previous literature reports with slight modifications.[2]

Briefly, the SO_2 gas was generated from a 400 mL aqueous solution of 0.5 mg/mL $NaHSO_3$ at a pH of 3.7 at 45 °C. The temperature of the solution was maintained with a water bath(VWR). Air at 60 mL/min was bubbled through the solution and carried humid SO_2 gas stream to the exposure unit (Secador mini-desiccator). Gas concentration inside the exposure unit was continuously monitored with the portable PAC 7000 SO_2 detector

purchased from Dräger. Data from the detector was transferred to a computer after the exposure run was finished. The relative humidity was continuously monitored by a commercially available humidity sensor (Ambient Weather). A second SO_2 sensor was kept running outside the exposure unit for leak detection. Steady-state levels of SO_2 and relative humidity were achieved within a few hours. The $NaHSO_3$ solution was refilled to maintain SO_2 level after every 2 days. The water bath, acid gas generator unit and exposure unit were all placed inside a fume hood with high exhaust rates and handled with caution at all times.

4.2.5 Solution Phase SO_2 Exposure Procedure

”Accelerated” acid stability tests were performed using aqueous acid solutions in addition to humid acid gases. Aqueous solutions of SO_2 at differing concentrations were diluted from concentrated SO_2 solutions. The final pH was measured with a pH meter and the approximate corresponding dry SO_2 concentration was calculated based on Henry’s law. The cage crystals (~70 mg) were soaked in 20 mL of SO_2 solution at each concentration in a sealed acid reactor for 4 days at room temperature. The acid reactors were mounted in a rotating oven to ensure homogeneous mixing. The resulting solid was filtered and washed with DI water and ethanol to remove sulfur anions and decomposed linkers.

The corresponding SO_2 concentration was calculated as follows:

For a solution with pH=3.20 as an example, $[H^+]=10^{-3.2}$ mol/L$=6.31\times10^{-4}$ mol/L. SO_2 has a dissociation constant pK_a of 1.81. $[SO_2]_{solution}=[H^+]^2/K_a=2.58\times10^{-5}$ mol/L$\approx2.58\times10^{-5}$ mol/kg. Henry’s constant of SO_2 at room temperature is $K_{H,SO2}^{o}=1.3$

mol/kg·bar. For gas phase SO_2 in equilibrium with the solution calculated above, the partial pressure of SO_2 would be $p_{SO2}=[SO_2]_{solution}/ K_{H,SO2}^{o}=20\times10^{-6}$ bar, which is 20 ppm.

4.2.6 Characterization

4.2.6.1 Scanning Electron Microscopy (SEM)

High-resolution imaging of the crystal morphology was achieved using a Hitachi SU8230 Cold Field Emission Scanning Electron Microscope (CFE-SEM). The dry samples were attached to aluminum stubs using copper tape. The samples were then coated with a 2 nm layer of gold/palladium using a Hummer 6 Gold/Palladium Sputterer. Imaging was taken at a working distance of 8 mm and a working voltage of 3 kV using a mix of upper and lower secondary electron detectors.

4.2.6.2 Powder X-ray Diffraction (PXRD)

Normal powder X-ray diffraction data were collected on a Panalytical X'pert PRO Multi-Purpose Diffractometer (MPD) in reflection Bragg-Brentano geometry operating with a Cu anode at 45 kV and 40 mA. Samples were mounted as a loose powder onto a silicon zero background holder. PXRD patterns were collected with a step size of 0.02 degrees 2θ and a scan time of 10 s/step over 2-50 degrees 2θ. High-resolution XRD patterns were collected on a PANalytical X'Pert PRO Alpha-1. The patterns were collected with a step size of 0.002 degrees 2θ and a scan time of 250 s/step over 2-50 degrees 2θ on a sample stage rotating at 4 rotation/s.

4.2.6.3 Fourier Transform Infrared Spectroscopy (FTIR)

FTIR spectroscopy was recorded by a Thermo Scientific Nicolet iS50 FT-IR equipped with an iS50 ATR module. Samples were analyzed in powder form with 128 scans with a resolution of 4 cm^{-1}.

4.2.6.4 Gas Sorption Analysis

The surface area analysis was conducted with nitrogen at 77 K using a Brunauer–Emmett–Teller surface area analyzer (BET, Micromeritics ASAP2020HD). CO_2 isotherms were collected from the same equipment at 308 K.

4.2.6.5 NMR

Solution ^{1}H NMR spectra were recorded at 400.13 MHz using a Bruker Avance III 400 NMR spectrometer. DP-MAS solid-state ^{13}C NMR spectra were recorded at 100.6 MHz using Bruker DSX 300.

4.2.6.6 Confocal Microscopy

Fluorescent images were taken using a Zeiss LSM 700-405 Confocal Microscope. The crystals were placed on an Eppendorf imaging dish with a thickness of 170 μm. 1 mg/mL fluorescence sodium salt in NMP was dropped onto the sample and left for 10 min before imaging. A 485 nm laser was used for excitation and z-stack images with slices of 0.35 μm were taken.

4.2.7 in situ IR Experimental Setup

CC3-R was pretreated at 110°C for 1 h with 25 cm^3/min He in the DRIFTS cell (diffuse reflectance Fourier transform infrared spectroscopy, Pike Technologies HC-900). The temperature was cooled down to 25°C, after temperature equilibrium was reached, 210 ppm SO_2 in He was supplied to the cell at 25 cm^3/min for 60 min. The residual gas was purged with He flow at 25 cm^3/min for 10 min. A temperature programmed desorption was followed after the purge. CC3-R sample was heated to 120°C with a ramping rate of 10°C/min; the temperature of the sample was held at 120°C for 15 min, and was then cooled down to 25°C at a ramping rate of 10°C/min.

Single beam IR spectra were collected continuously during the SO_2 adsorption step using a Thermo Nicolet Nexus 670 spectrometer in diffuse reflectance mode. The outlet gases from the DRIFTS reactor were analyzed using a quadrupole mass spectrometer (Omnistar GSD-301 O2, Pfeiffer Vacuum).

4.3 Results and Discussions

CC3-R was synthesized according to literature as shown in Figure 4.1 from [4+6] cycloimination between triformylbenzene and (1R,2R)-cyclohexanediamine.[4] After isolation from the synthesize solution, octahedron crystals are obtained with the size ranging from 20-50 μm (Figure 4.2). The diffraction patterns of the crystals matched the calculated powder pattern as shown in Figure 4.3.

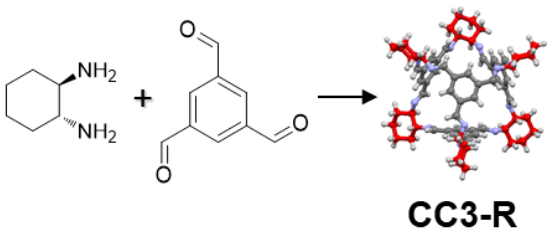

Figure 4.1 Synthetic route of CC3-R from 1,3,5-triformylbenzene and (*R*,*R*)-1,2-diaminocyclohexane

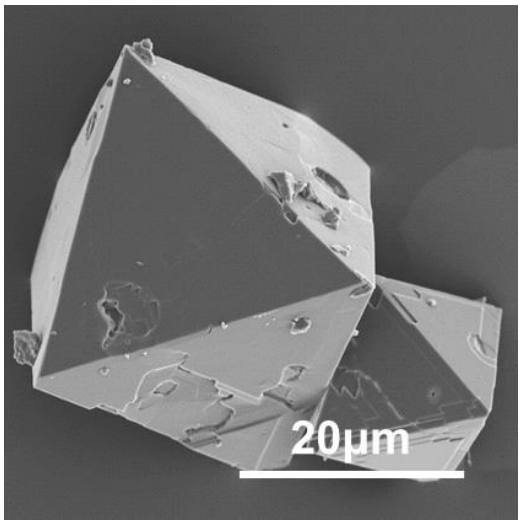

Figure 4.2 SEM image of octahedral CC3-R crystals

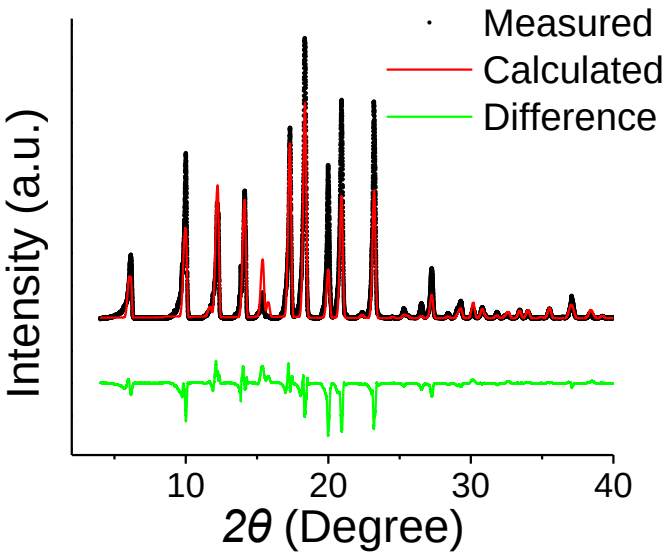

Figure 4.3 Rietveld refinement of powder X-ray diffraction pattern of CC3-R

4.3.1 CC3-R Decomposition Pathway Probed with in situ IR

To assess the interaction between CC3-R and SO_2, the sample was loaded in an *in situ* DRIFTS-IR cell and exposed to dilute SO_2 gas. The differential spectra in Figure 4.4 (i.e., the SO_2-exposed spectra relative to the neat CC3-R spectra) at different times during the exposure reveal chemical bond evolution during the interaction with the humid acid gas. Positive peaks indicate the occurrence of new species and negative peaks indicate diminishing species. From the figure, several positive peaks are identified. This includes major peaks at 3174 cm^{-1}, 3385 cm^{-1} that can be attributed to N-H stretching, peaks at 715 cm^{-1}, 1050 cm^{-1}, 1228 cm^{-1} that can be attributed to S=O/S-O stretching.

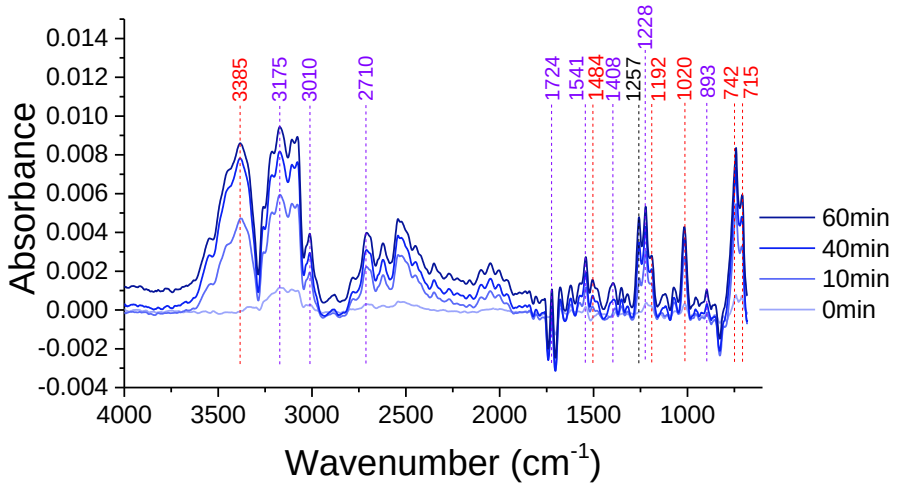

Figure 4.4 IR spectra obtained during different time intervals of SO_2 adsorption on CC3-R, major peaks are labeled with the corresponding color of the structures in Figure 4.5

A comprehensive peak assignment is tabulated in Table 4.1 with the help of DFT calculations. Major peaks can be assigned to either an H_2SO_3 insertion intermediate or a -NH_2--SO_2 adduct.

Table 4.1 Assignment summary for peaks in the differential spectra under SO_2 exposure based on DFT calculations

Wavenumbers [cm^{-1}]	Assignment
715	S-O stretch in intermediate structure
742	C-O stretch (C-O-S) in intermediate structure
893, 922, 952	N-H bend in amine-SO_2 complex
1020	C-N stretch (C-NH_2) in intermediate structure
1050	S=O symmetric stretch in amine-SO_2 complex
1072	O-H bend/S=O stretch in intermediate structure
1192	C-N stretch (C-N(H)) in intermediate structure
1228	S=O asymmetric stretch in amine-SO_2 complex
1257	Gas phase SO_2
1353, 1387, 1408	C-H bend (H-C=O) in amine-SO_2 complex
1484	N-H bend in intermediate structure
1541	N-H bend in amine-SO_2 complex
1724	C=O stretch in amine-SO_2 complex
2710	C-H stretch (H-C=O) in amine-SO_2 complex
3010	O···H in amine-SO_2 complex
3175, 3214	N-H stretch in amine-SO_2 complex
3385	N-H asymmetric stretch in amine-SO_2 complex N-H stretch in intermediate structure
3550	O-H stretch in intermediate structure

A potential chemical degradation mechanism was developed utilizing these *in situ* IR experiments and both the vibrational modes and corresponding IR frequencies of various species that are formed during degradation. First, the imine bond in pristine CC3-R is attacked by HSO_3^- and H^+, forming a decomposition intermediate shown in Figure 4.5b. This intermediate structure becomes a broken cage with a dangling amine group and aldehyde group as shown in Figure 4.5c. Finally, SO_2 can easily interact with the newly-generated amine groups to form -NH_2--SO_2 complexes (Figure 4.5d). The imine hydrolysis

pathway was not explicitly considered here as the cages have been found to be stable in boiling water for at least 4 h.[5]. In general, good agreement between the calculated and experimental results was observed.

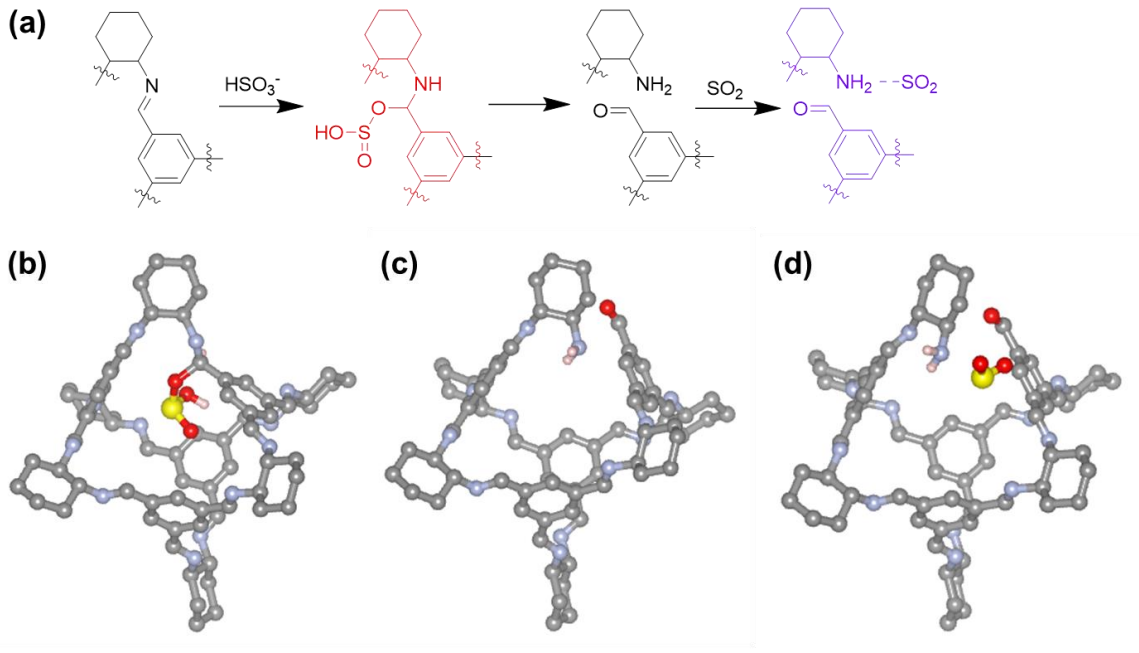

Figure 4.5 (a) Proposed degradation pathway—imine bond cleavage facilitated by HSO_3^-, (b) Relaxed structure of decomposition intermediate of CC3-R, and (c) Relaxed structure of broken cage and $–NH_2$--SO_2 complex

From the proposed degradation pathway it is noted that the first step involved insertion of H_2SO_3 into the imine bond, which required gas phase SO_2 to react with a water molecule. The MS signal during the whole analysis for SO_2 and H_2O was shown in Figure 4.6. The water content has a high count during the process. This amount of water is essential in the decomposition reaction and was from the physisorbed water in CC3-R (Figure 4.7).

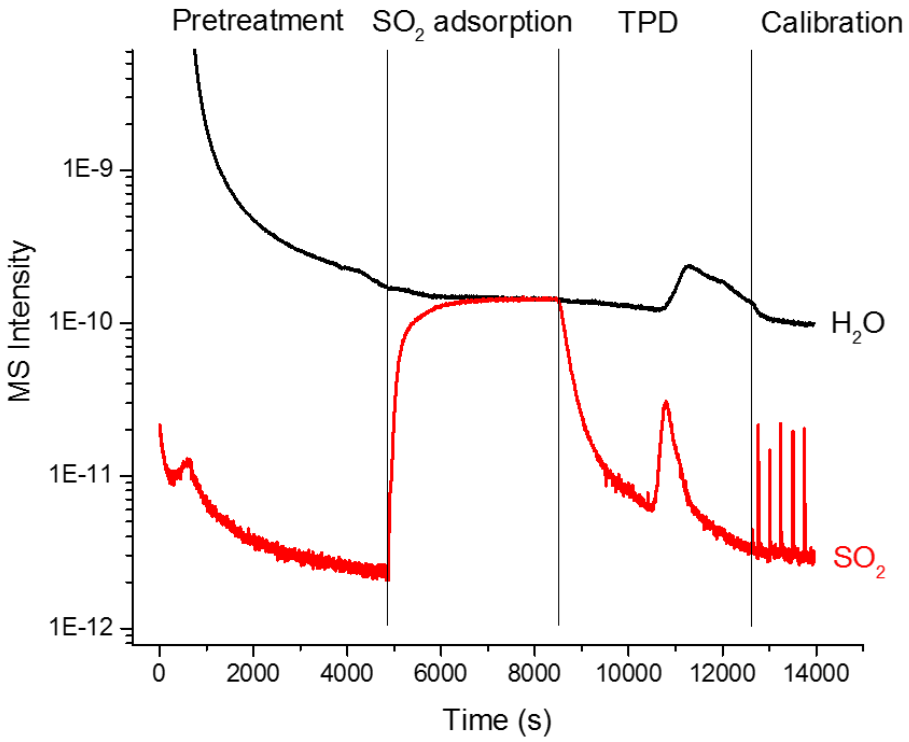

Figure 4.6 MS signal intensity of H_2O and SO_2 during in situ IR analysis

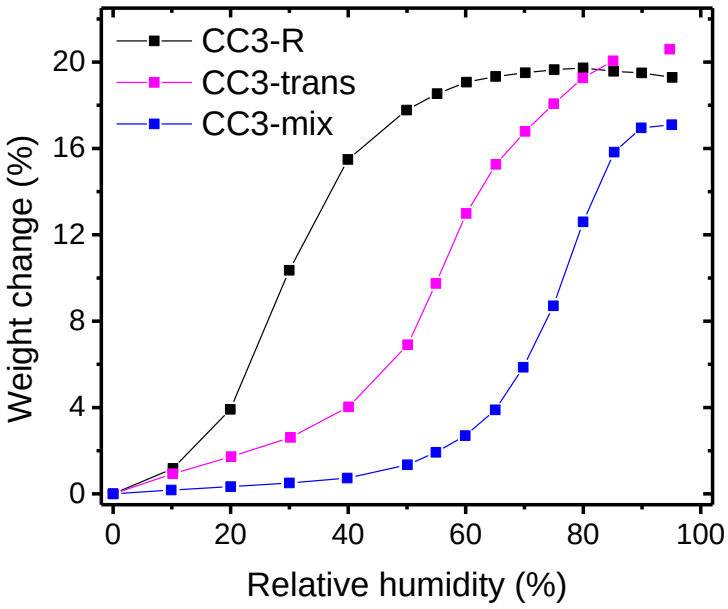

Figure 4.7 Water sorption isotherms of CC3-R, CC3-trans, and CC3-mix

4.3.2 Humid SO_2 Stability Test in Homochiral CC3 Crystals

The samples recovered from the *in situ* IR experiments exhibited minimal deviations in crystallinity and morphology relative to the pristine samples. To further understand the chemical and physical degradation mechanisms of CC3 crystals, larger crystals and extended exposure times in humid vapor and aqueous liquid acid conditions were investigated. The SO_2 stability of both CC3-R and CC3-S were first investigated under humid vapor conditions. Samples were exposed to 50 ppm SO_2 for 2 and 4 days at 80% relative humidity at room temperature.[6] The morphology of the samples exposed to these conditions was examined by SEM (Figure 4.8). After the 2-day exposure, the octahedral shapes of both CC3-R and CC3-S were maintained; however, irregular thin cracks were formed inside the crystal (Figure 4.8 1a, 1b). A higher number density of acid-induced cracks was observed at longer exposure times (Figure 4.8 2a, 2b).

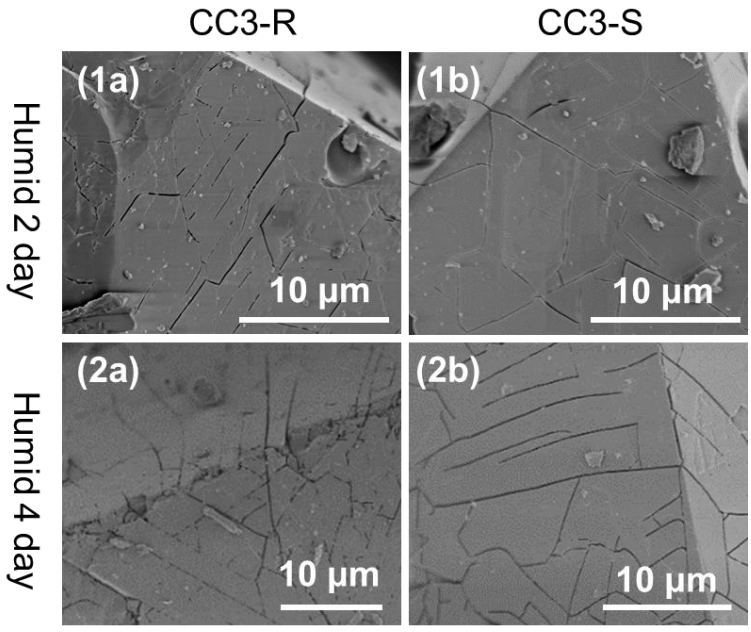

Figure 4.8 Morphological changes of (a) CC3-R and (b) CC3-S after humid SO_2 exposure for 2 and 4 days (rows 1 and 2, respectively)

The crystallinity of both 2-day and 4-day exposed samples were estimated using PXRD and no loss of crystallinity was observed (Figure 4.9). FTIR spectra were taken after the acid gas exposure as well as after the samples were washed with ethanol. For the samples exposed to humid SO_2 for 2 days, no apparent difference in the spectra was found (Figure 4.10). However, for the samples exposed for 4 days, new absorption peaks corresponding to C=O and N-H bonds were observed, in excellent agreement with the in situ IR experiments. Those signature vibrations diminished after the samples were washed with ethanol, indicating that free linkers formed during cage decomposition were mobile.

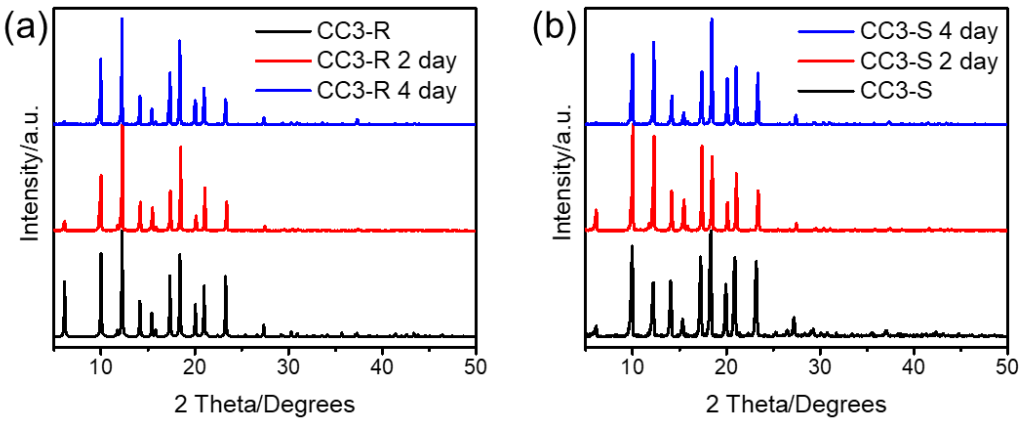

Figure 4.9 XRD of (a) CC3-R (b) CC3-S after humid SO_2 exposure for 2 and 4 days showed no crystallinity change in the materials

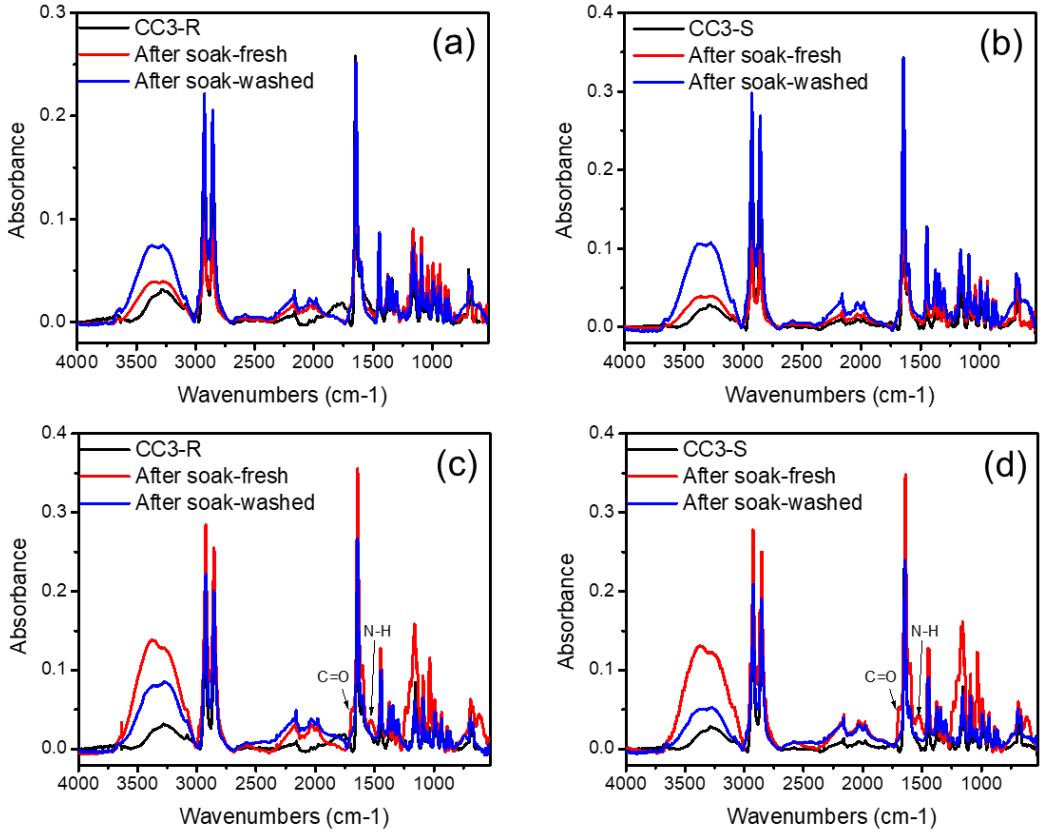

Figure 4.10 FTIR of CC3-R and CC3-S after humid SO_2 exposure for 2 days (a) & (b) and 4 days (c) & (d) and after washed with ethanol and dried

A comparison of the water sorption isotherms and the pore volume of CC3 derived from N_2 physisorption (Figure 4.7) indicates that relative humidity greater than 80% resulted in pore filling with liquid-like water within the pores of CC3. This "liquid-like" adsorbed water creates a similar chemical environment in high humidity and aqueous experiments.

4.3.3 Aqueous SO_2 Stability Test in Homochiral CC3 Crystals

The SO_2 stability of the materials was then studied in aqueous conditions as an extension to the humid SO_2 vapor exposure experiments. The liquid phase SO_2 concentrations correspond to approximately (A) 20 ppm, (B) 1000 ppm and (C) 10000 ppm

of gas-phase concentrations. CC3-R soaked in a 20 ppm equivalent solution was eroded on the surface, and small holes and cracks were visible under SEM (Figure 4.11 1a, 1b). At a higher acid concentration (1000 ppm), all the CC3-R crystals exhibited broadened cracks compared to the humid exposure result (Figure 4.11 1a).

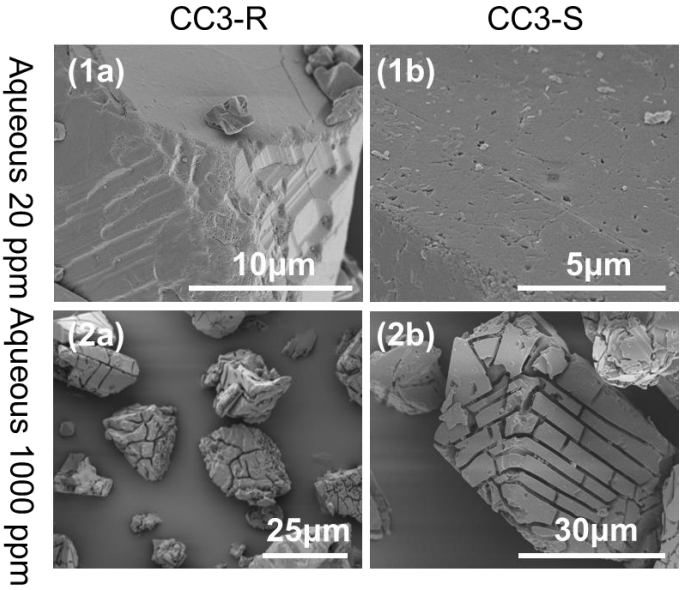

Figure 4.11 Morphological changes of (a) CC3-R and (b) CC3-S after aqueous phase SO_2 exposure at 20 and 1000 ppm equivalent (rows 1 and 2, respectively).

These cracks were also observed using fluorescent confocal microscopy (Figure 4.12). Images at different depths of the crystal showed interlinked cracks throughout the crystal, which likely originated from grain boundaries in the CC3-R and CC3-S crystals (the effect of these grain boundaries will be discussed in detail later in the chapter). The 10000 ppm equivalent solution dissolved the cages. CC3-S exhibited identical morphological changes to CC3-R under all acid concentrations, as expected.

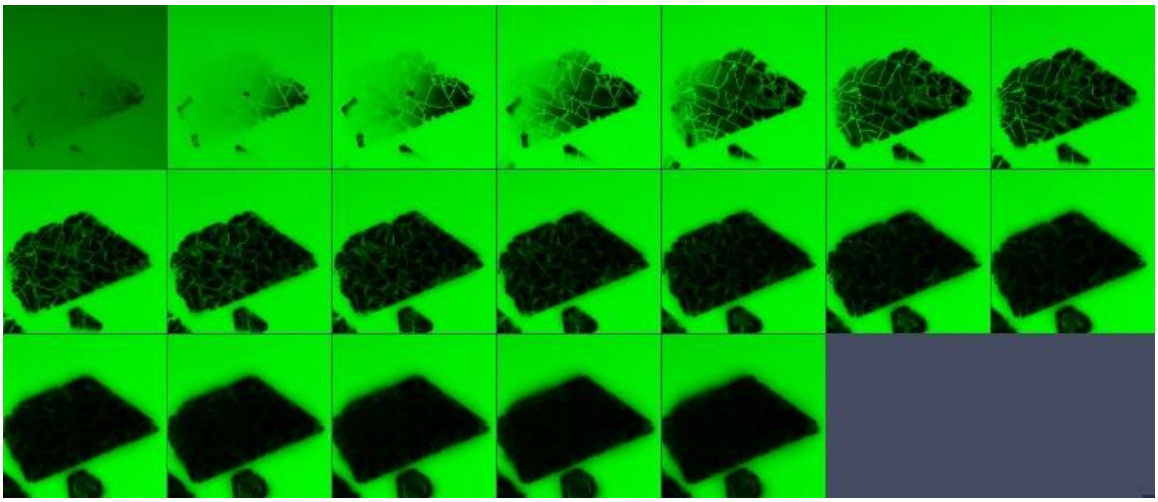

Figure 4.12 Fluorescent confocal microscope slices with 0.35 µm thickness of a CC3-R crystal with cracks from SO_2 attack

CC3-R was washed with ethanol after aqueous SO_2 exposure and showed C=O and N-H bond vibrations in the FTIR spectrum (Figure 4.13). The broken or damaged cages on the surface were likely washed off during the collection of the crystals from the SO_2 solution. Therefore, the C=O and N-H vibrations observable in the FTIR spectra should originate from damaged cages inside the crystal that cannot diffuse out through the pores of the CC3 crystals and be thus left inside.

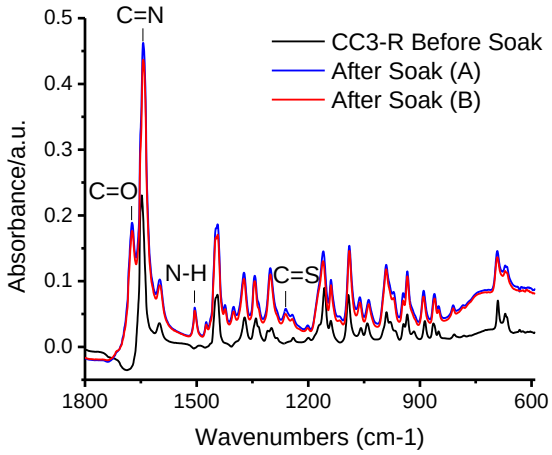

Figure 4.13 FTIR of CC3-R after aqueous SO_2 exposure for 4 days

The crystallinity of aqueous SO_2 treated CC3-R was examined by PXRD (Figure 4.14). The reflection at 6.1° 2θ ([111] crystal face) becomes more pronounced while the relative intensity of other reflections remains unchanged. The most significant change is that the reflections at 15.42° 2θ and 15.82° 2θ disappeared. These two reflections correspond to the [3 3 1] and [4 2 0] crystal faces, respectively. Their disappearance is consistent with imine bond cleavage, which was also suggested by FTIR measurements.

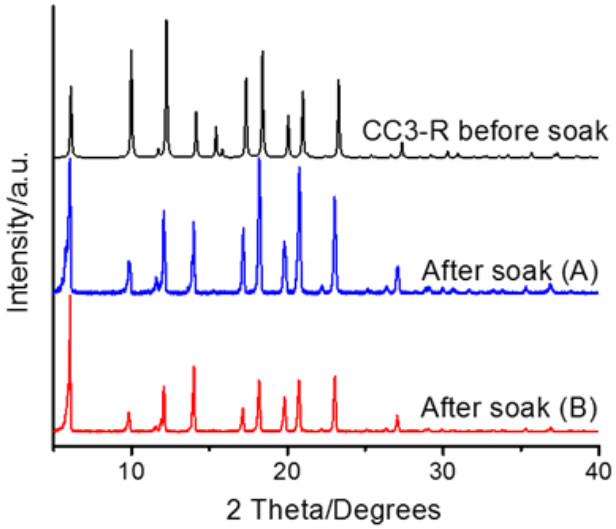

Figure 4.14 XRD of aqueous SO_2 treated CC3-R

4.3.4 Synthesis of Heterochiral CC3 Cages

As noted by Cooper and co-workers, CC3-R and CC3-S cages can efficiently pack together by chiral recognition and instantaneously precipitate from the mixing of CC3-R and CC3-S solutions (crystals samples resulting from precipitation are denoted as CC3-RS in this chapter).[4] This observation was explained by the high packing energy between cages containing (*R*,*R*)- and (*S*,*S*)- 1,2-diaminocyclohexane. Although the shape and size of the

CC3-RS crystals can be controlled by varying the temperature and mixing rate, the resulting crystals tend to be quite small (< 500 nm).

Here, we attempt to enhance the stability of CC3-R crystals by using a low-cost racemic mixture of diaminocyclohexane during the synthesis of CC3. Instead of mixing pre-formed CC3-R and CC3-S cages, mixed linker CC3 cages were synthesized from racemic mixtures of diaminocyclohexane, as shown in Figure 4.15. This molecule has two stereocenters and thus has three stereoisomers: two trans enantiomers and one cis diastereomer. CC3-trans and CC3-mix were synthesized as described in the experimental section.

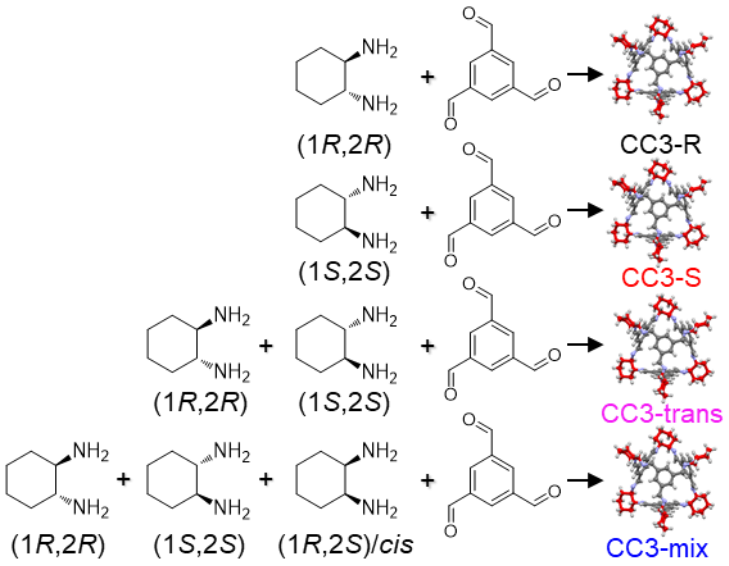

Figure 4.15 Synthesis routes of various CC3 species, the different cages are color coded in this paper when multiple cages are presented. (CC3-R: black, CC3-S: red, CC3-trans: magenta, CC3-mix: blue)

The morphology of CC3-R, CC3-S, CC3-trans, and CC3-mix is shown in Figure 4.16. In general, all samples have the same octahedral shape with different sizes. Because of the faster nucleation and growth in CC3-trans and CC3-mix, these two samples tend to

grow with a smaller size. Powder X-ray diffraction patterns of the samples are shown in Figure 4.17. Reflections for CC3-trans and CC3-mix shift to higher 2θ positions relative to CC3-R. Rietveld refinement indicated that CC3-mix cage molecules pack more densely than CC3-R (Figure 4.18). Despite this tighter packing, CC3-trans and CC3-mix showed higher N_2 and CO_2 uptake relative to CC3-R/CC3-S (Figure 4.19).

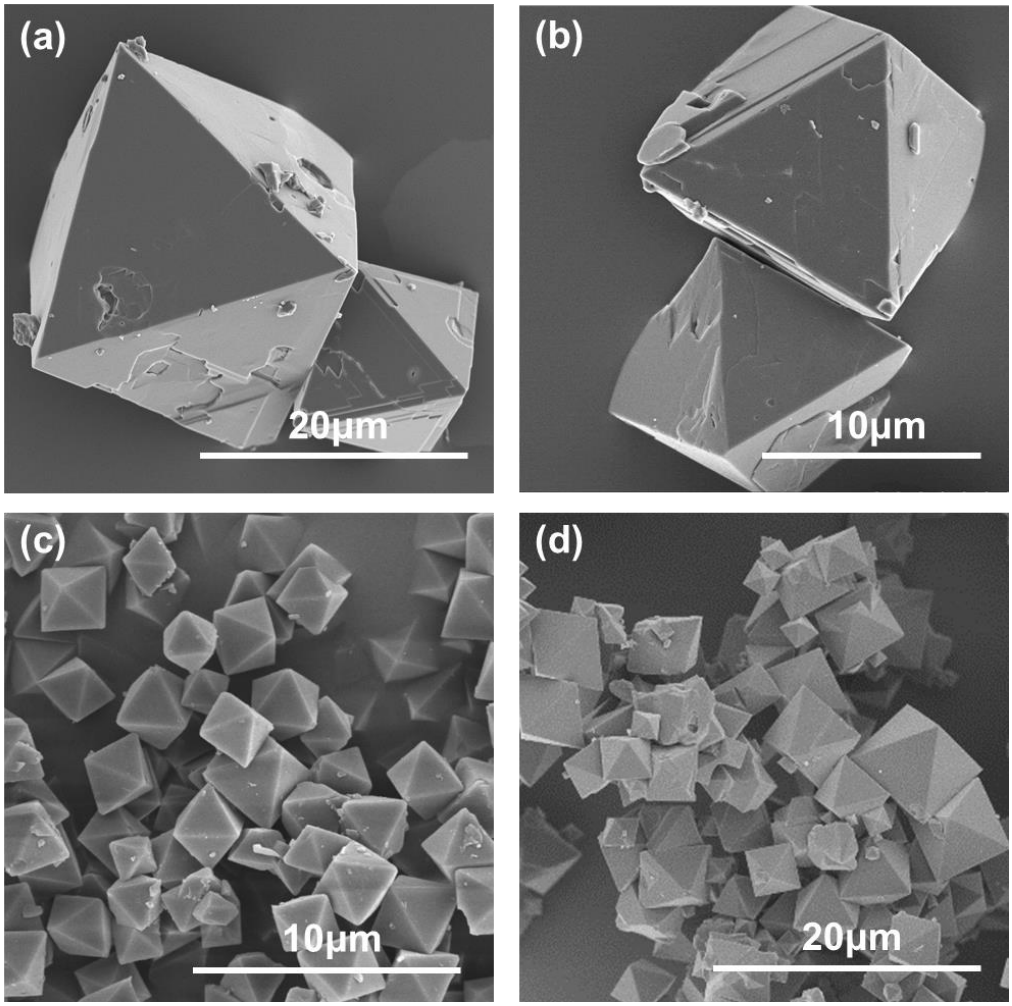

Figure 4.16 SEM of (a) CC3-R, (b) CC3-S, (c) CC3-trans, and (d) CC3-mix

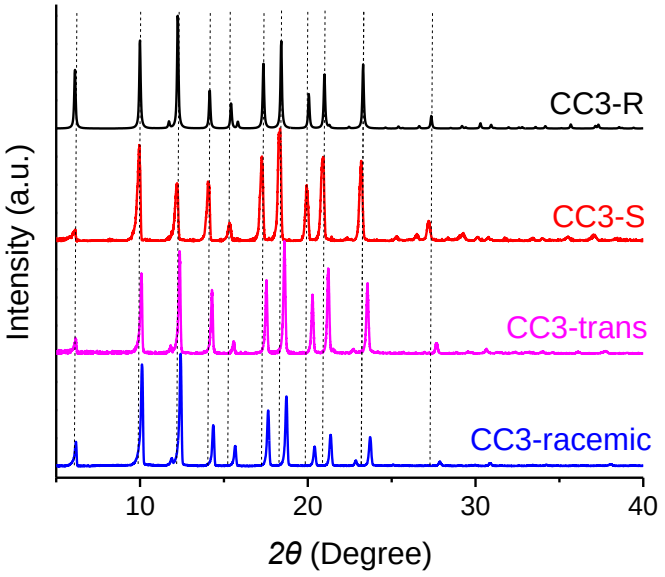

Figure 4.17 Powder diffraction patterns of various CC3 species

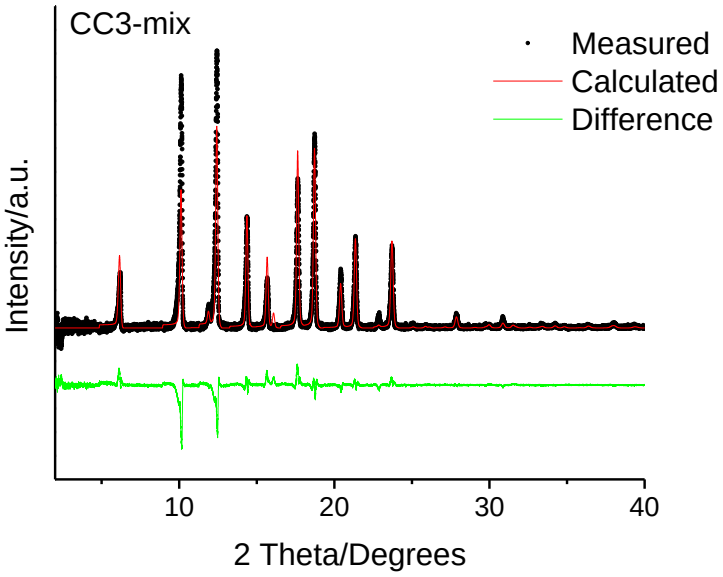

Figure 4.18 Rietveld refinement of CC3-mix. The resolved structure showed that CC3-mix has a lattice parameter of 24.5093 Å while CC3-R has a lattice parameter of 25.1642 Å

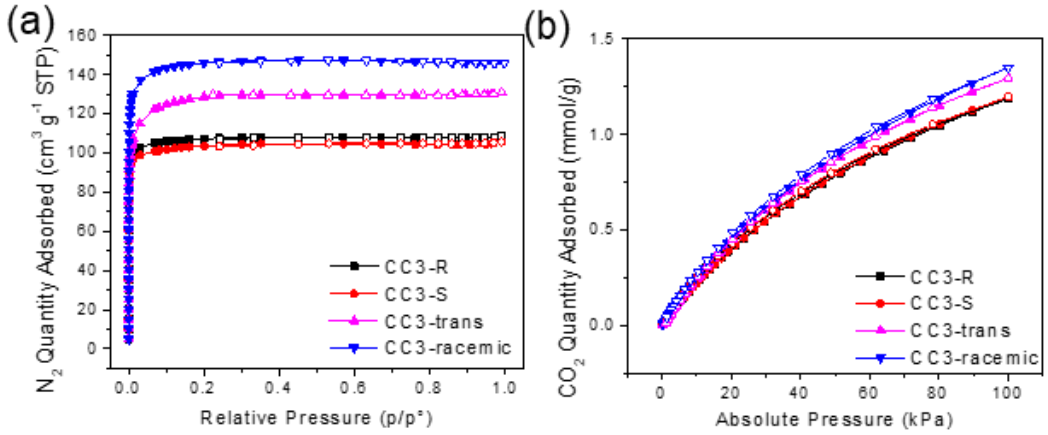

Figure 4.19 (a) N_2 physisorption isotherm at 77 K, and (b) CO_2 physisorption isotherm at 308 K of CC3-R, CC3-S, CC3-trans, and CC3-mix

Although synthesized under the same conditions, CC3-trans and CC3-mix crystals have smaller sizes and smoother crystal surfaces than CC3-R and CC3-S crystals. The difference in the sizes of the crystals likely originates from the faster nucleation rate in the CC3 crystals grown using a mixture of diamine isomers. Racemic cage pair interactions have been noted to be more favorable than homochiral cage pair interactions.[4, 7-8] In the CC3-trans and CC3-mix cases, although each cage contains different chiral linkers, the packing is still more favorable than for enantiopure cages. The lack of strong interactions in CC3-R and CC3-S molecular packing results in more mesoscale defects such as grain boundaries in the crystal, which were visualized by fluorescent confocal microscopy (Figure 4.20). Fluorescein sodium salt was impregnated into the crystal as a dye molecule that is large enough to be excluded from the nanopores in CC3 but can access the space between crystal grains. The images were taken at different depths in the CC3 crystals clearly show grain boundaries in CC3-R and CC3-S crystals, which are filled with the dye solution (green color in the figure). However, no grain boundaries are observed throughout

the CC3-trans and CC3-mix crystals. This difference, we believe, plays a critical role in the distinct interaction behavior of humid SO_2 with the various CC3 crystals.

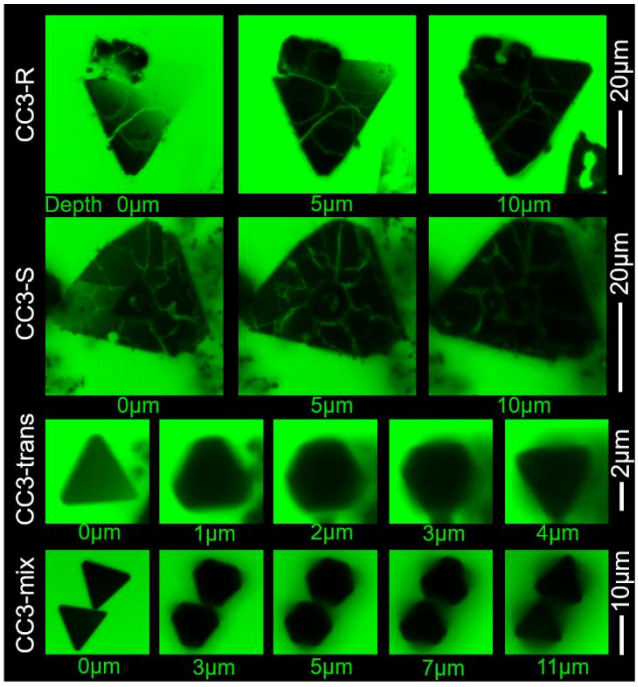

Figure 4.20 Confocal fluorescence microscopy images of fluorescein sodium salt impregnated in the various CC3 samples. The grain boundaries are highlighted in CC3-R and CCR-S, whereas no grain boundaries are observable in the CC3-trans and CC3-mix samples

4.3.5 Humid and Aqueous SO_2 Stability Test in Heterochiral CC3 Crystals

In contrast to the observations of CC3-R and CC3-S, CC3-trans and CC3-mix exhibited only minor surface layer exfoliation (Figure 4.21) in both humid and aqueous SO_2 exposure conditions. Although CC3-mix exhibits some surface morphology changes, the bulk chemical structure has not changed. These observations are consistent with a shrinking core corrosion model, which would be expected with a lack of mesoscale grain boundaries that would permit aqueous acid and liquid-like adsorbed water/acid mixtures to have access throughout the CC3 crystal (Figure 4.22).

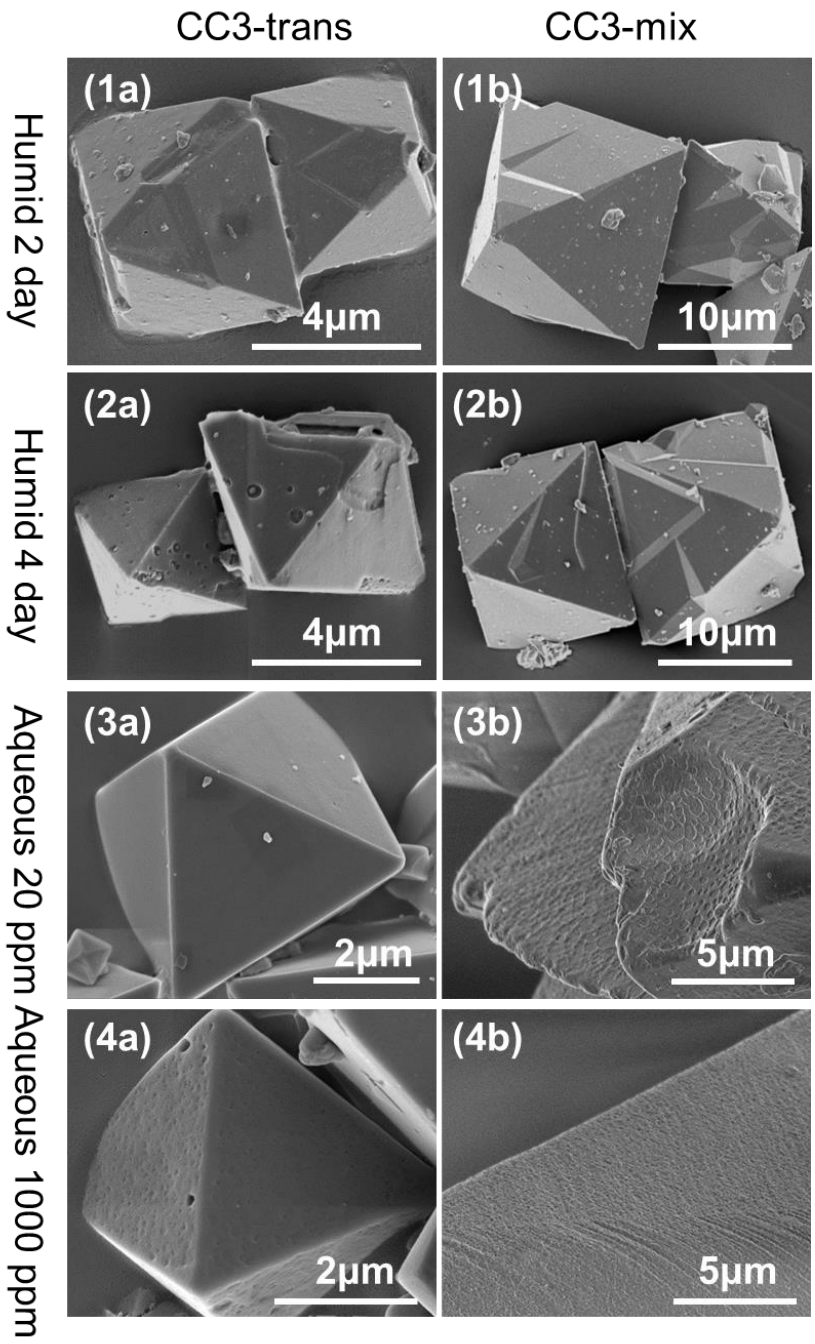

Figure 4.21 Morphological changes of (a) CC3-trans, and (b) CC3-mix after humid SO_2 exposure for 2 and 4 days (rows 1 and 2, respectively) and after aqueous phase SO_2 exposure at 20 and 1000 ppm equivalent (rows 3 and 4, respectively).

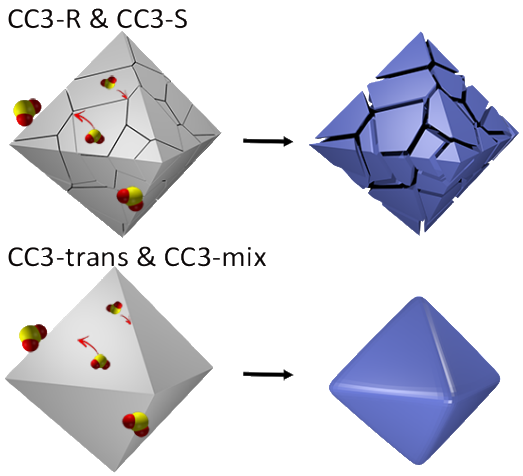

Figure 4.22 Illustration of interaction between different CC3 species with aqueous SO_2.

Compared to the peak intensity changes found in CC3-R, CC3-mix does not show observable changes in the XRD pattern (Figure 4.23).

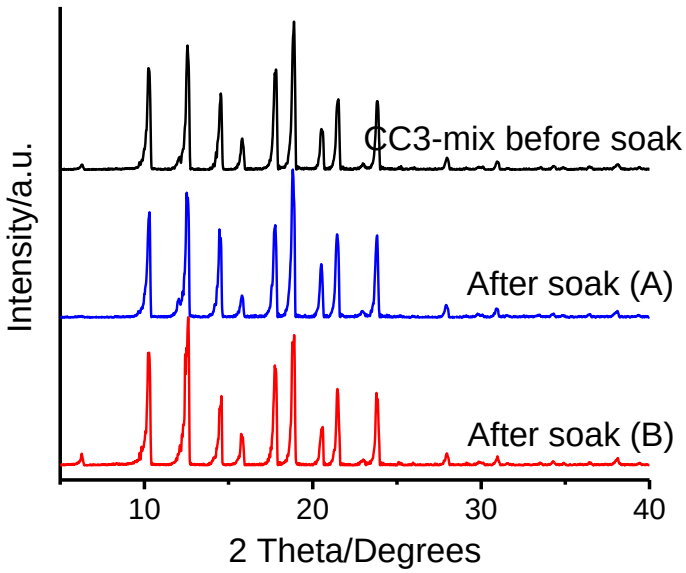

Figure 4.23 XRD of aqueous SO_2 treated CC3-mix

Chemical stability was confirmed by unaltered FTIR spectra in both humid and aqueous SO_2 exposed CC3-trans and CC3-mix samples (Figure 4.24 and Figure 4.25)

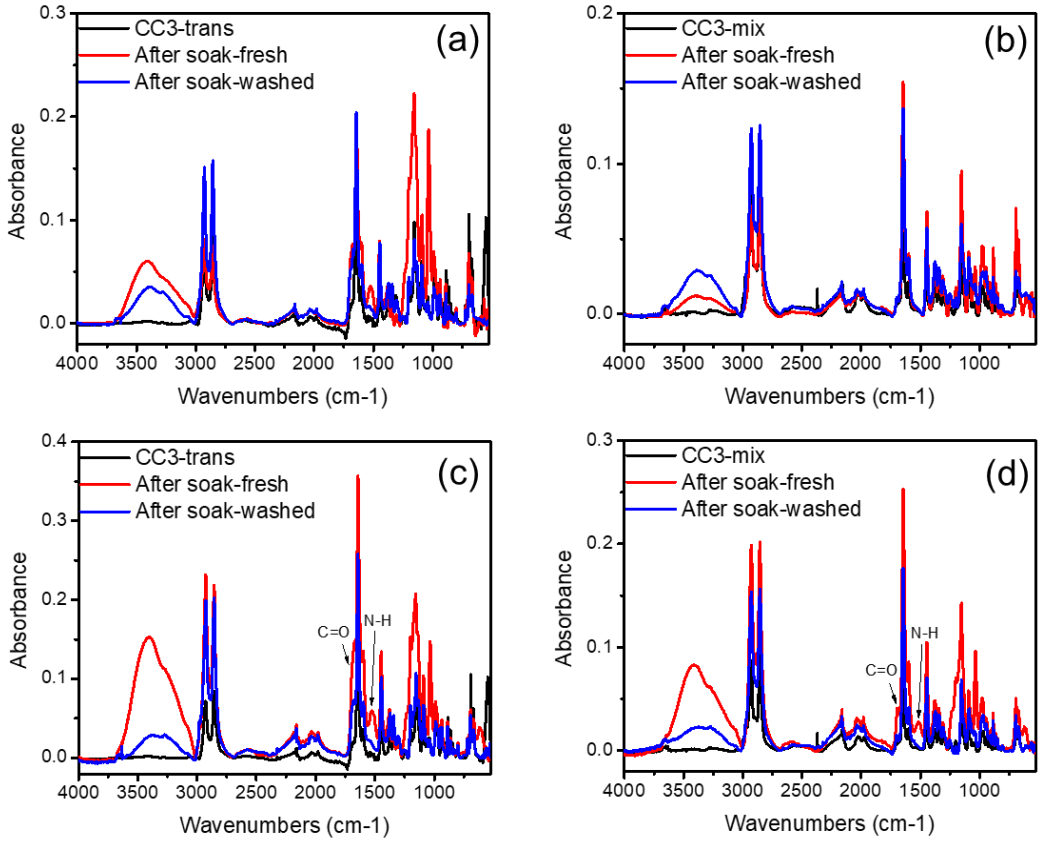

Figure 4.24 FTIR of CC3-trans and CC3-mix after humid SO_2 exposure for 2 days (a) & (b) and 4 days (c) & (d) and after washed with ethanol and dried

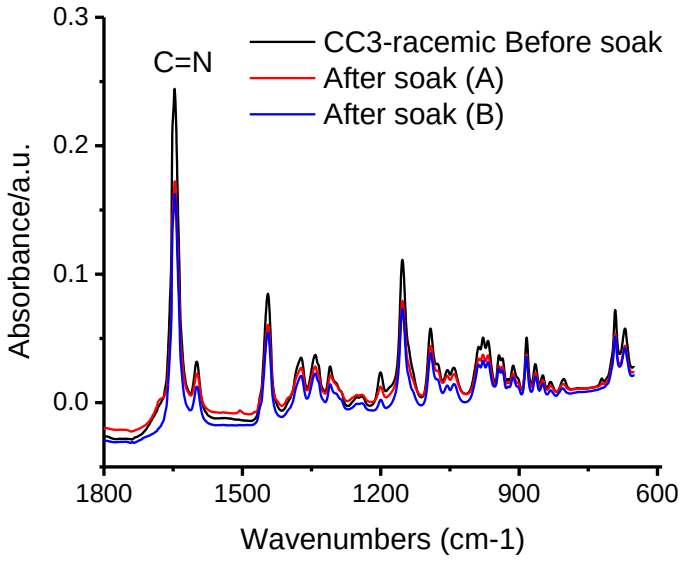

Figure 4.25 FTIR of CC3-mix after aqueous SO_2 exposure for 4 days

The gas sorption properties of the acid-treated samples were compared with the neat materials and summarized in Figure 4.26. The BET surface areas of CC3-R and CC3-S decreased with increasing acid exposure time/concentration. The CO_2 uptake of CC3-R and CC3-S increased after acid gas exposure. This is attributed to the favorable interactions of CO_2 with amines in partially damaged cages in the crystal. For CC3-mix, the surface area and CO_2 uptake were generally unaltered. However, over 50% loss in surface area and CO_2 uptake was observed after 4-day humid exposure for CC3-trans. The different behavior between CC3-trans and CC3-mix was attributed to the integration of *cis*-diaminocyclohexane in the CC3-mix cage. CC3-mix showed an additional peak at 3.9 ppm in ^{1}H NMR and a shoulder at 66.6 ppm in ^{13}C NMR indicating the existence of *cis*-diaminocyclohexane. The cis isomer content was determined to be approximately 30 % according to ^{1}H-NMR and ^{13}C-NMR in Figure 4.27; however, attempts to synthesize CC3 using pure cis isomers yields a glassy polymer. The exact mechanism of the stability conferred by the *cis* stereoisomer is currently not understood.

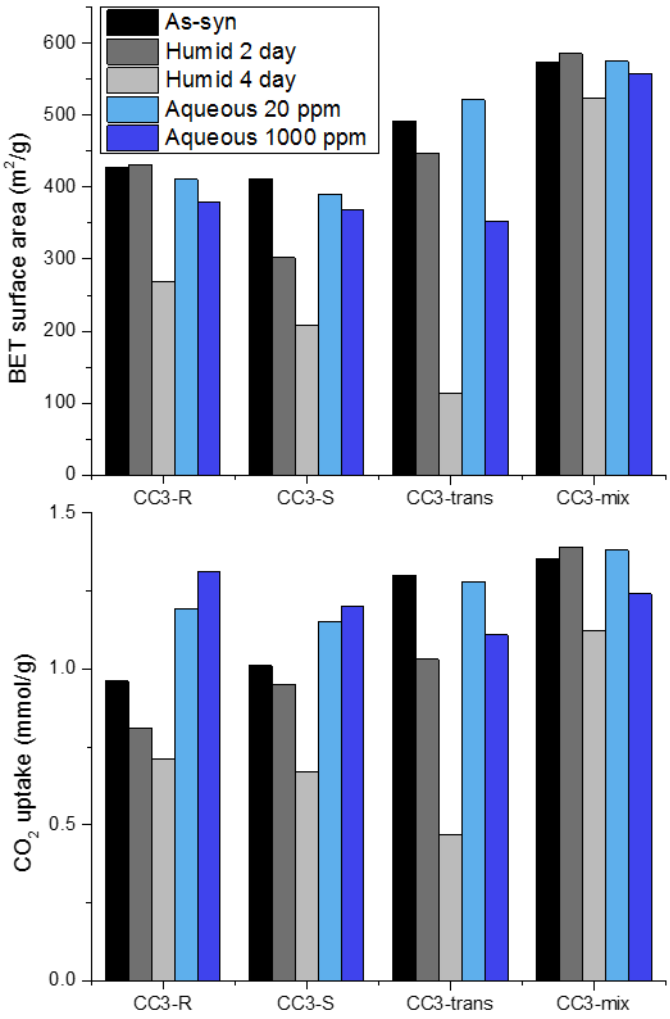

Figure 4.26 Summary of gas adsorption data. BET surface area is calculated from N_2 adsorption-desorption isotherms at 77 K. CO_2 uptake is acquired from CO_2 adsorption-desorption isotherms at 308 K and 1 bar

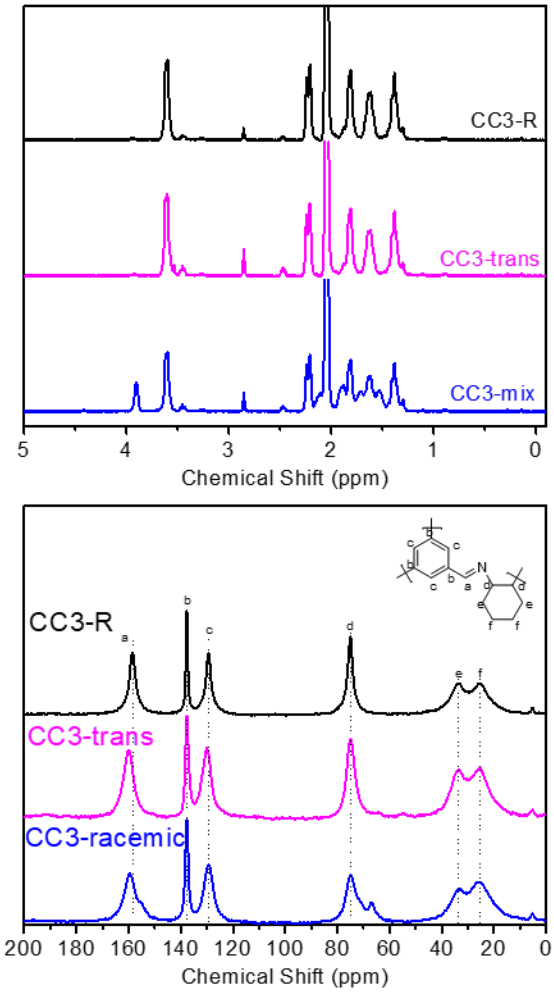

Figure 4.27 ^{1}H solution and ^{13}C solid-state NMR of dissolved cages

The decomposition of CC3 species in the presence of SO_2 and H_2O vapor or liquid happens at the molecular level (i.e., individual cages). The imine bond connecting the two linkers within an individual cage dissociates when challenged with high concentrations of humid acid gas or aqueous acid solutions. Although the total water uptake of CC3-trans and CC3-mix is comparable, the minor difference in the extent of surface erosion is also related to the significant difference in water adsorption at the same relative humidity. Indeed, “liquid-like” water does not occur in CC3-mix and CC3-trans until high relative

humidities (Figure 4.7; 85% RH). The combination of elimination of grain boundaries as well as a decrease in water uptake both contribute to the increase in chemical resistance of CC3-mix relative to CC3-R or CC3-S.

4.4 Conclusions

In summary, the degradation of imine-bond based porous organic cages under SO_2 conditions was studied using *in situ* IR experiments. The synthesis of CC3 variants with mixed linkers at the molecular level is reported. Linkers with opposing chirality increased the stability of the resulting cages packed into the solid state. This is shown from the decreased solubility in common solvents and the increased SO_2 stability, as observed through electron microscopy, textural, spectral, and crystallographic analysis. Samples of CC3-R and CC3-S in both humid vapor and aqueous SO_2 exposure conditions showed severe decomposition while CC3-mix and CC3-trans showed only mild surface changes and no bulk property changes. The morphological differences in the two sample types and their acid-induced degradation were probed by fluorescent confocal microscopy; mesoporous grain boundaries in CC3-R and CC3-S (but not CC3-mix and CC3-trans) were observed. These mesoporous grain boundaries in CC3-R and CC3-S accelerated the corrosion due to reaction with SO_2 and water, as the acid can access surfaces small crystal grains throughout the CC3-R crystals. The good stability and preserved CO_2 uptake reveal CC3-mix as a potential candidate for enhancing membrane separations in aggressive industrial conditions. We also note that the self-synthesized 1,3,5-benzenetricarbaldehyde and racemic diaminocyclohexane used in CC3-trans and CC3-mix reduced the cost to one-tenth of the original expected cost of CC3-R or -S, which makes this material more cost-effective for use in large-scale applications.

4.5 References

(1) Guanghui, Z.; D., H. C.; Yang, L.; Souryadeep, B.; Uma, T.; L., J. M.; Zili, W.; S., S. D.; Sankar, N.; W., J. C.; P., L. R. Engineering Porous Organic Cage Crystals with Increased Acid Gas Resistance. *Chemistry – A European Journal* **2016,** *22*, 10743-10747.

(2) Rezaei, F.; Rownaghi, A. A.; Monjezi, S.; Lively, R. P.; Jones, C. W. SO x/NO x Removal from Flue Gas Streams by Solid Adsorbents: A Review of Current Challenges and Future Directions. *Energy & Fuels* **2015,** *29*, 5467-5486.

(3) Sholl, D. S.; Lively, R. P. Defects in Metal–Organic Frameworks: Challenge or Opportunity? *The journal of physical chemistry letters* **2015,** *6*, 3437-3444.

(4) Hasell, T.; Chong, S. Y.; Jelfs, K. E.; Adams, D. J.; Cooper, A. I. Porous Organic Cage Nanocrystals by Solution Mixing. *Journal of the American Chemical Society* **2012,** *134*, 588-598.

(5) Hasell, T.; Schmidtmann, M.; Stone, C. A.; Smith, M. W.; Cooper, A. I. Reversible water uptake by a stable imine-based porous organic cage. *Chemical Communications* **2012,** *48*, 4689-4691.

(6) Hashimoto, Y.; Tanaka, S. A new method of generation of gases at parts per million levels for preparation of standard gases. *Environmental Science & Technology* **1980,** *14*, 413-416.

(7) Eliel, E. L.; Wilen, S. H. *Stereochemistry of organic compounds*. John Wiley & Sons: 2008.

(8) Jacques, J.; Collet, A.; Wilen, S. H. *Enantiomers, racemates, and resolutions*. Wiley: 1981.

CHAPTER 5. MOLECULAR BLENDS OF METHYLATED-POLY(ETHYLENIMINE) AND AMORPHOUS POROUS ORGANIC CAGES FOR SO_2 ADSORPTION

Porous organic cages (POCs) are emerging porous materials that exhibit intriguing properties in the areas of self-assembly, host-guest interaction, and solution processability. In this Chapter, the applicability of POCs as porous molecular supports for polymeric amines is explored. It is found that primary amines in poly(ethylenimine) (PEI) can undergo metathesis with the imine bonds present in POCs, resulting in non-porous products. This problem can be overcome by transforming the primary amines in PEI to tertiary amines via methylation. The N-methylated PEI (mPEI) forms homogeneous composites with amorphous scrambled porous organic cages (ASPOCs) without undesired reactions or phase separation. These composite materials are evaluated as adsorbents for low concentration SO_2 (200 ppm) adsorption and show good thermal and cyclic stability. This chapter is published as part of a research article.[1]

5.1 Introduction

POC molecules generally pack in the solid state as a crystalline phase as a result of weak van der Waals forces between adjacent POC molecules.[2] However, in some cases, such ordered packing can be disrupted. For example, in POCs made from trialdehydes and mixtures of diamine linkers the solid packing of the cage molecules is disrupted by the asymmetric cage exterior, which derives from the diamine mixture - such POCs are known as amorphous scrambled porous organic cages (ASPOCs).[3-5] Recently Jiang et al. reported

the solution co-processing of functional materials with such organic cage molecules, whereby linear poly(ethylenimine) (PEI) was mixed with ASPOCs, and this mixing has shown positive synergistic effects on CO_2 uptake.[6]

The emission of acid gases such as CO_2, SO_x, and NO_x during fuel combustion poses environmental threats as well as health hazards.[7-12] Current industrial CO_2 removal and SO_2 scrubbing technologies suffer from high energy and material consumption, and can only be effectively applied to large stationary point sources.[13-17] Compared to absorption, adsorption using fixed-bed technologies has the benefit of low energy requirements, safety, and material consumption. Solid-supported amine materials have been recently proposed for various acid gas separations and studied extensively.[18-19] Most of the solid supports investigated are inorganic porous materials such as mesoporous oxides and carbon-based materials.[20-28] Based on the earlier investigation by Jiang et al., in this work, the use of ASPOC materials as supports is explored for acid gas adsorbing moieties, in particular, branched PEI. Branched PEI is commonly used in supported amine adsorbent studies because impregnation is straightforward, and in contrast to the long, straight chain of linear PEI, which mainly contains secondary amines, branched PEI possesses superior oxidation resistance and CO_2 capture performance due to the presence of primary and tertiary amines, as well.[18, 29-30]

Much like the solid supported PEI adsorbents reported in the literature, the reported tertiary amine adsorbents have been mostly limited to use of porous silica as support.[31-32] Importantly, the large pore size in many mesoporous silica materials can lead to the loss of active amine components due to evaporation.[32-33] It is hypothesized that the intimate mixing of porous organic cages with polymer molecules would result in good retention of

the polymer during repeated thermal cycles, while still maintaining or even enhancing the performance of the adsorbing material. Here, ASPOC supported methylated-PEI (mPEI) is employed for SO_2 adsorption as an example to explore the limitations and potential of POC materials in energy and environmental applications. The performance of the composite material for SO_2 adsorption is experimentally evaluated.

5.2 Experimental

5.2.1 Materials

Triformylbenzene was purchased from Manchester Organics. Anhydrous dichloromethane, chloroform, ethylenediamine, (1R,2R)-1,2-cyclohexanediamine, branched PEI (800 M_w), were purchased from Sigma Aldrich. Ethyl acetate and diethyl ether were purchased from BDH Chemicals. Formic acid, 38% formaldehyde solution, potassium hydroxide pellets, and magnesium sulfate were purchased from Alfa Aesar. Ultra-high purity N_2 and CO_2 gas cylinders were purchased from Airgas. Certified standard grade cylinders of 200 ppm SO_2 with a balancing of N_2 were purchased from Matheson Trigas. All chemicals were used as received without any purification.

5.2.2 Synthesis of ASPOC

The synthesis of the ASPOC $CC1_2 3_4$ (the subscripts denote the starting composition of the synthesis solution—2 equivalents of ethylenediamine (the linker for CC1) and 4 equivalents of (1R,2R)-1,2-cyclohexanediamine (the linker for CC3-R)) (Figure 5.1) was carried out following a modified procedure from the literature.[3] To a solution of 500 mg triformylbenzene in 40 mL anhydrous dichloromethane (DCM), a solution of 90 mg

ethylenediamine and 350 mg (1R,2R)-1,2-cyclohexanediamine in 40 mL anhydrous DCM was added. Then the mixture was stirred at room temperature for 3 days. A pale white powder was obtained by rotary evaporation. The product was washed with ethyl acetate to remove unreacted molecules and dried at 80 ºC under vacuum.

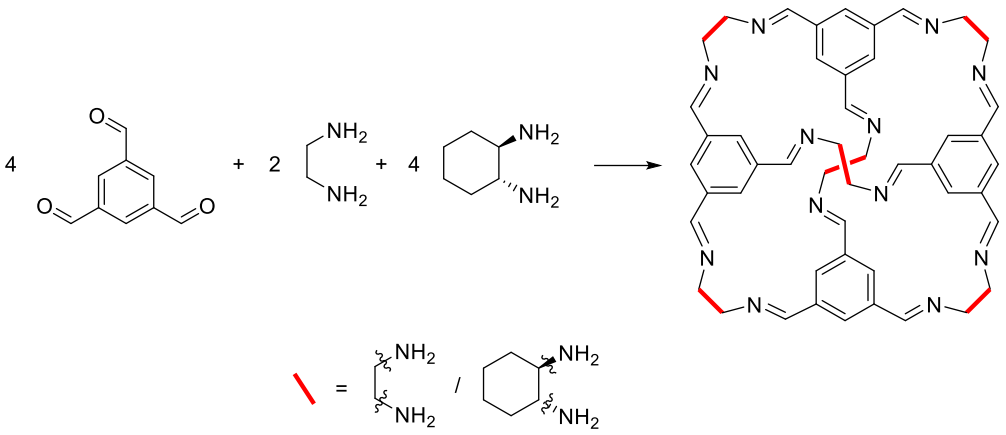

Figure 5.1 Synthesis of ASPOC $CC1_2 3_4$ from 4 equivalents of triformylbenzene, 2 equivalents of ethylenediamine and 4 equivalents of (1R,2R)-1,2-cyclohexanediamine; which results in the formation of a mixture of cages

ASPOC $CC1_x 3_y$ samples with different ethylenediamine to cyclohexanediamine ratio were also synthesized according to the amount of chemicals listed in Table 5.1.

Table 5.1 Synthesis condition of ASPOC $CC1_x 3_y$ samples

Sample	EDA:CHDA	EDA (mg)	CHDA (mg)	TFB (mg)
$CC1_5 3_1$	5:1	231	88	500
$CC1_4 3_2$	4:2	185	176	500
$CC1_3 3_3$	3:3	139	264	500
$CC1_2 3_4$	2:4	90	350	500
$CC1_1 3_5$	1:5	46	440	500

5.2.3 Preparation of PEI/ASPOC Composites

PEI stock solution is prepared by dissolving 100 mg PEI into 10 mL dichloromethane. The $CC1_23_4$ stock solution is prepared by dissolving 100 mg $CC1_23_4$ in 20 mL dichloromethane. Two composite samples were prepared according to Table 5.2. The solvent in the mixed solution was removed by rotary-evaporation, and the solids are collected.

Table 5.2 Preparation of PEI/ASPOC composites

Sample	$CC1_23_4$ stock solution (mL)	PEI stock solution (mL)	$CC1_23_4$ (mg)	PEI (mg)
8 wt% PEI in ASPOC	10	0.43	50	4.3
42 wt% PEI in ASPOC	10	3.62	50	36.2

5.2.4 Methylation of PEI

The N-methylation of PEI was carried out following a modified procedure from the literature.[31] Commercially available branched PEI (800 M_w, 1 g) was added to a round bottom flask equipped with a condenser containing 14 mL formic acid and 12 mL 38% formaldehyde solution. The flask was degassed on a Schlenk line and back-filled with N_2. The mixture was heated at 120 ºC overnight. The resultant solution was cooled to room temperature and transferred to an extraction funnel. Diethyl ether (50 mL) was added to the extraction funnel and KOH pellets were added to the flask until the organic layer turned yellow. The aqueous phase was washed one more time with diethyl ether and additional KOH pellets. The organic layer was dried over $MgSO_4$. The mPEI was obtained as a dark orange oil after rotary evaporation.

5.2.5 Preparation of mPEI/ASPOC Composites

After drying, mPEI and ASPOC powder were dissolved in chloroform as 5 mg/mL stock solution. Different mass ratios of mPEI to ASPOC were prepared as listed in Table 5.3 and denoted as 10-mPEI/ASPOC, 20-mPEI/ASPOC, and 40-mPEI/ASPOC to represent the theoretical weight percent of mPEI in the final composite. The solvent was removed using rotary-evaporation. All samples showed no sign of phase separation and remained in powder form. A sample with 80 wt% mPEI loading was also prepared. However, this sample exhibited sticky surface characteristics and could not be handled as a free-flowing powder. 10-mPEI/ASPOC, 20-mPEI/ASPOC, and 40-mPEI/ASPOC samples were dried under dynamic vacuum at 60 °C to remove residual solvent. Elemental analysis was conducted to calculate the weight loading of mPEI.

Table 5.3 Preparation of mPEI/ASPOC composites

Sample	$CC1_23_4$ stock solution (mL)	mPEI stock solution (mL)	$CC1_23_4$ (mg)	mPEI (mg)
10-mPEI/ASPOC	36	4	180	20
20-mPEI/ASPOC	32	8	160	40
40-mPEI/ASPOC	24	16	120	80
80-mPEI/ASPOC	8	32	40	160

5.2.6 SO_2 Adsorption Measurements

SO_2 adsorption, desorption and cyclic measurements in the composite materials were carried out using a gravimetric method employing a TA Instruments Q500 TGA with a modified furnace chamber. The feed flow rates of both the desorption and adsorption

gases were fixed at 90 mL/min with the internal mass flow controller of the instrument and an external mass flow controller for the N_2 pretreatment gas and sulfur-containing gas, respectively.

The activation temperature was determined with thermogravimetric analysis during the preparation of the mPEI/ASPOC composites. Adsorption of SO_2 was carried out at 25 °C and 35 °C with a cylinder of 200 ppm SO_2 balanced with N_2. Desorption of SO_2 was carried out in flowing N_2 at 60 °C and 90 °C based on the thermostability of the composites. Cyclic studies were carried out between 35 °C and 60 °C using the same time and flow conditions. Samples were cycled between high-temperature inert gas desorption and low-temperature SO_2 adsorption to determine cyclic stability.

5.2.7 Characterization methods

5.2.7.1 Electrospray Ionization – Mass Spectrometry (ESI-MS)

ESI-MS of samples were taken on a Waters Quattro LC system.

5.2.7.2 Thermogravimetric Analysis (TGA)

The thermostability of polymer and composite materials was probed on a TA Instruments Q500 TGA. The samples were heated to the desired temperature at 5 ºC/min under a flow of N_2 and held for 9 h.

5.2.7.3 NMR

Solution ^1H NMR spectra in $CDCl_3$ were recorded at 400.13 MHz using a Bruker Avance III 400 NMR spectrometer.

5.2.7.4 Scanning Electron Microscopy (SEM)

High-resolution imaging of the composite morphology was achieved using a Hitachi SU8230 Cold Field Emission Scanning Electron Microscope (CFE-SEM). The dry samples were attached to aluminum stubs using copper tape. The samples were then coated with a 20 nm layer of gold/palladium using a Hummer 6 Gold/Palladium Sputterer. Imaging was taken at a working distance of 8 mm and a working voltage of 3 kV using a mix of upper and lower secondary electron detectors.

5.2.7.5 Gas Sorption Analysis

The porosity of the materials was assessed via nitrogen physisorption at 77 K using a Micromeritics ASAP2020HD. Surface areas were calculated from the data using the Brunauer–Emmett–Teller (BET) method. CO_2 isotherms were collected from the same equipment at 308 K.

5.2.7.6 Elemental Analysis (EA)

EA of CHN was performed by Atlantic Microlab.

5.3 Results and Discussion

5.3.1 Synthesis and Characterization of ASPOC

The ASPOC samples were synthesized with different ethylenediamine to cyclohexanediamine linker ratios. Note that this synthesis will produce a mixture of cages that have different ethylenediamine and (1R,2R)-1,2-cyclohexanediamine distributions within each cage. The individual cages containing differing amounts of ethylenediamine and (1R,2R)-1,2-cyclohexanediamine are denoted as $CC1^x3^y$ in Figure 5.2, where x is the

number of ethylenediamine molecules in a cage and y is the number of (1R,2R)-1,2-cyclohexanediamine molecules in the same cage.

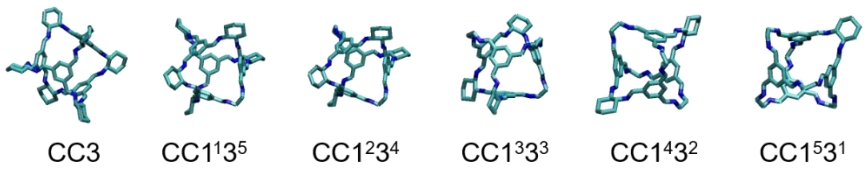

Figure 5.2 CC1^{x}3^{y} denotes a cage having x number of ethylenediamine and y number of diaminocyclohexane vicinal diamines

The mixing of the cages can be observed in ^{1}H NMR spectra of the samples in Figure 5.3. The protons on the alpha-carbon of the imine bond on the aliphatic group have a chemical shift between 3-5 ppm. It can be observed that this peak gradually split and shift from 3.32 ppm to 4.02 ppm, indicating the existence of both CC3 and CC1 cages in the mixture. In addition, there are two peaks at 3.81 ppm and 4.22 ppm that does not belong to pure ethylenediamine cage and cyclohexanediamine cage. These are attributed to scrambled cages bearing both ethylenediamine and cyclohexanediamine linkers.

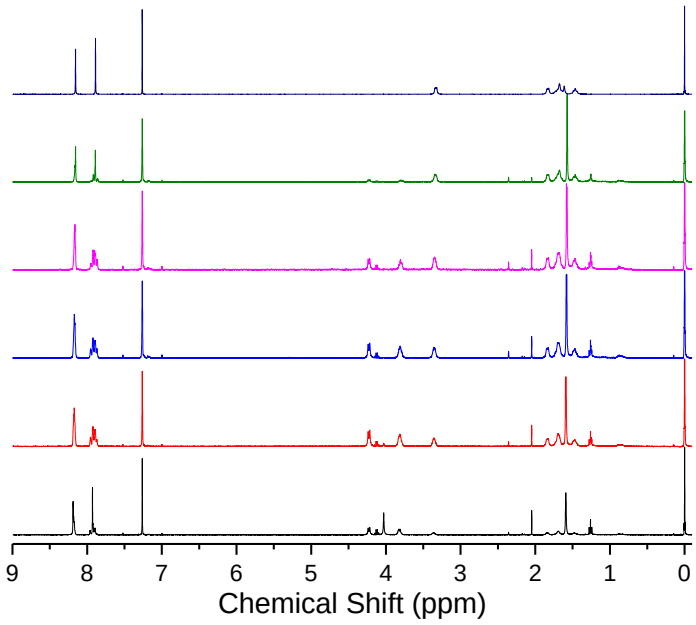

Figure 5.3 ^{1}H NMR spectra of the ASPOC samples. From top to down: CC3-R, $CC1_13_5$, $CC1_23_4$, $CC1_33_3$, $CC1_43_2$, and $CC1_53_1$

Unlike the octahedral crystals seen in earlier chapters for CC3-R, ASPOC samples give different morphologies regarding different diamine linker ratios as seen in SEM images of the samples in Figure 5.4. $CC1_53_1$ exhibited needle crystals mixed with an amorphous phase. $CC1_13_5$ exhibited rod crystals. The samples with closer ratios of diamine linkers ($CC1_43_2$, $CC1_33_3$, and $CC1_23_4$) showed more amorphous characteristics.

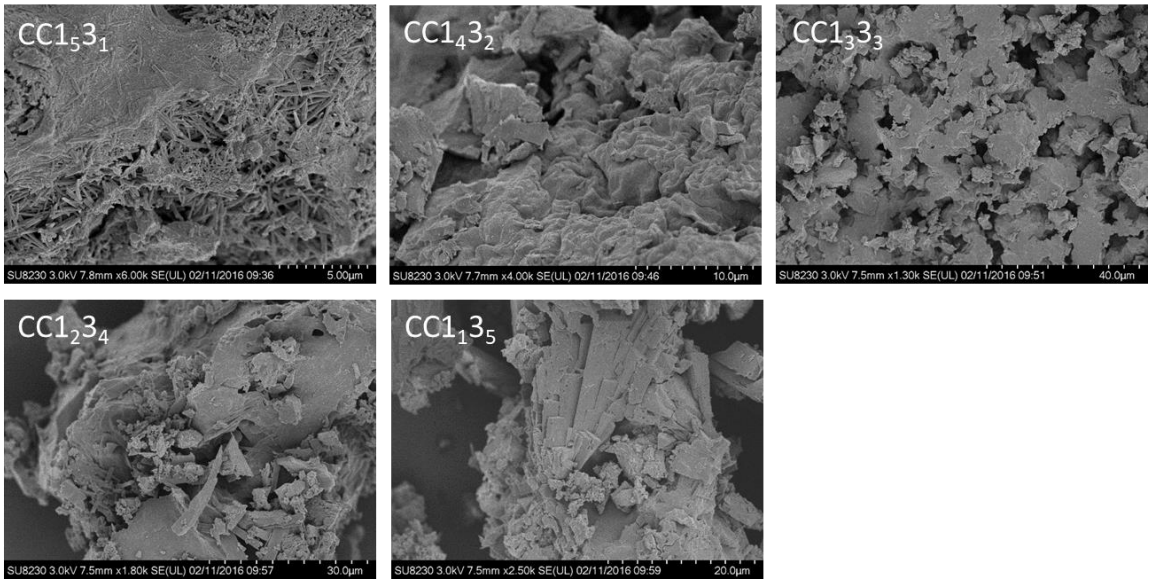

Figure 5.4 SEM images of ASPOC samples with different starting linker ratio

This difference in morphology was also corroborated from powder X-ray diffraction patterns in Figure 5.5. Compared to CC3-R that give sharp crystalline peaks, all the ASPOC samples showed either broadened peaks or amorphous feature. $CC1_53_1$ and $CC1_13_5$ showed broadened peaks that differed from the CC3-R pattern. The samples with closer ratios of diamine linkers showed amorphous feature as a result of a higher level of mixed vertex, which will disturb the packing of the cages.

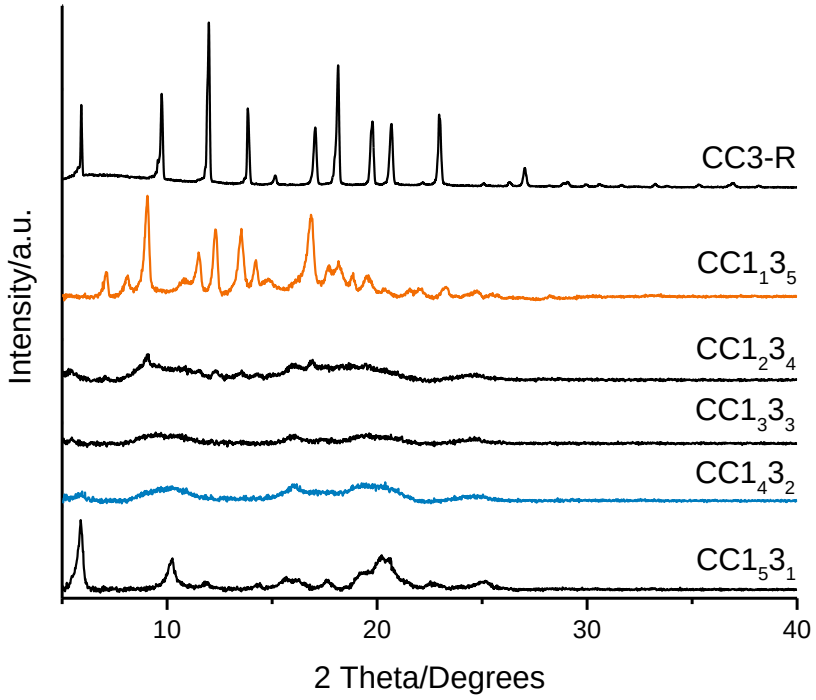

Figure 5.5 XRD patterns of ASPOC samples with different starting linker ratio

Nitrogen physisorption was used to measure the surface area and pore volume of the ASPOC mixtures. The adsorption and desorption isotherms are shown in Figure 5.6. In POC solids, the pore volumes are contributed by both internal and external pores of the cages. While the internal pores of the cages are similar between different cages, the external pore volume depends on the packing efficiency of the cages. In crystalline CC3-R crystals, the external pore volume is minimized as a result of ordered packing directed by cyclohexane moieties around the cage. In amorphous POC solids, the external pore volume is extended as a result of random packing. This is reflected by a larger adsorption volume of N_2 in ASPOCs compared to CC3-R.

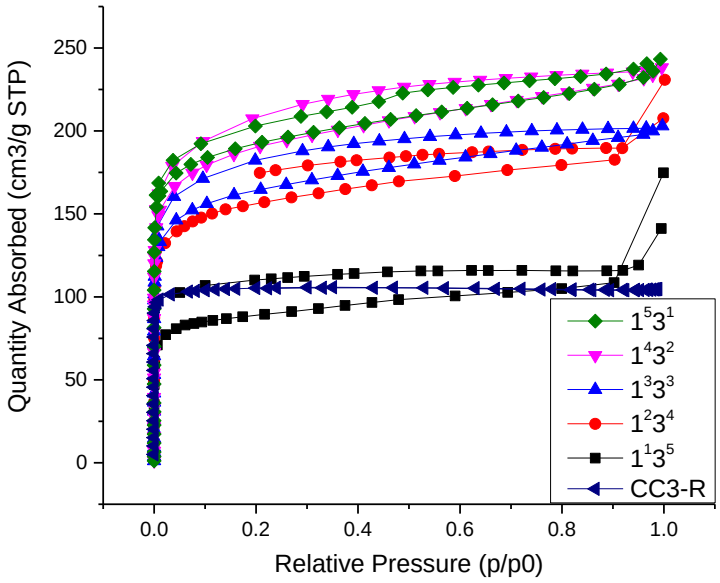

Figure 5.6 Nitrogen physisorption isotherms of CC3-R and ASPOC mixtures

$CC1_2 3_4$ was chosen for further composite studies because of its larger pore volume and disordered packing. I hypothesize that this two properties will lead to faster diffusion and molecular mixing with PEI/mPEI molecules instead of phase separation. This mixture was referred to as ASPOC for clarification in later text.

5.3.2 Synthesis of PEI/ASPOC Composites

I initially impregnated branched PEI (~800 M_w) into ASPOC materials; however, ^{1}H NMR spectra of the resulting composite showed the loss of the characteristic shifts associated with PEI protons (Figure 5.7). This is attributed to a metathesis reaction between the primary amines at the chain ends in the branched PEI molecules and the imine bonds in the ASPOCs, forming new imine and enamine bonds. As a result, no PEI moieties were observed in the resulting composite (MALDI-MS in Figure 5.8). This cage-breaking reaction prevented the use of branched PEI in this type of composite.

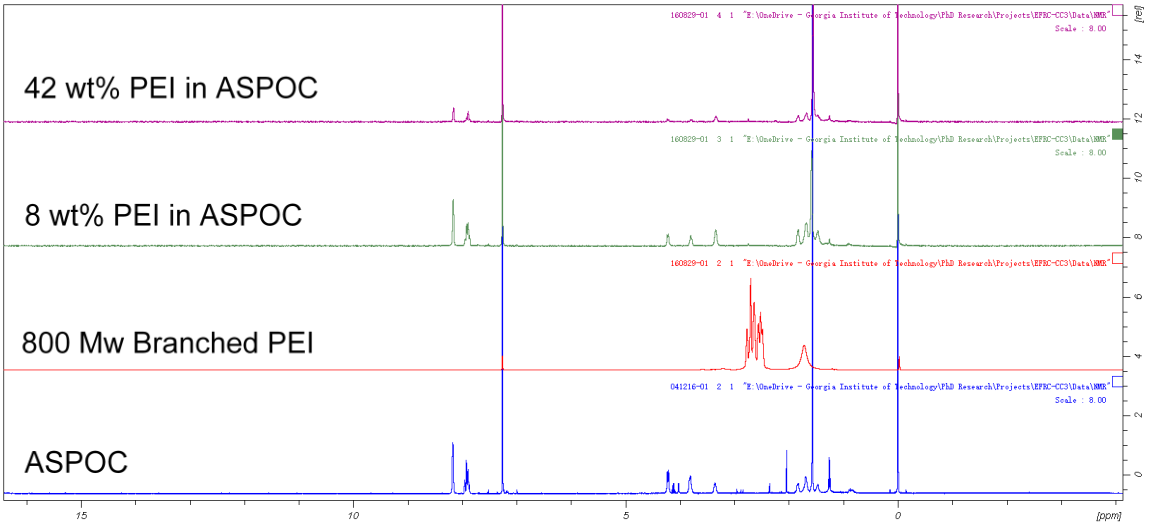

Figure 5.7 ^{1}H NMR spectra of ASPOC, PEI, and two mixtures of ASPOC and PEI

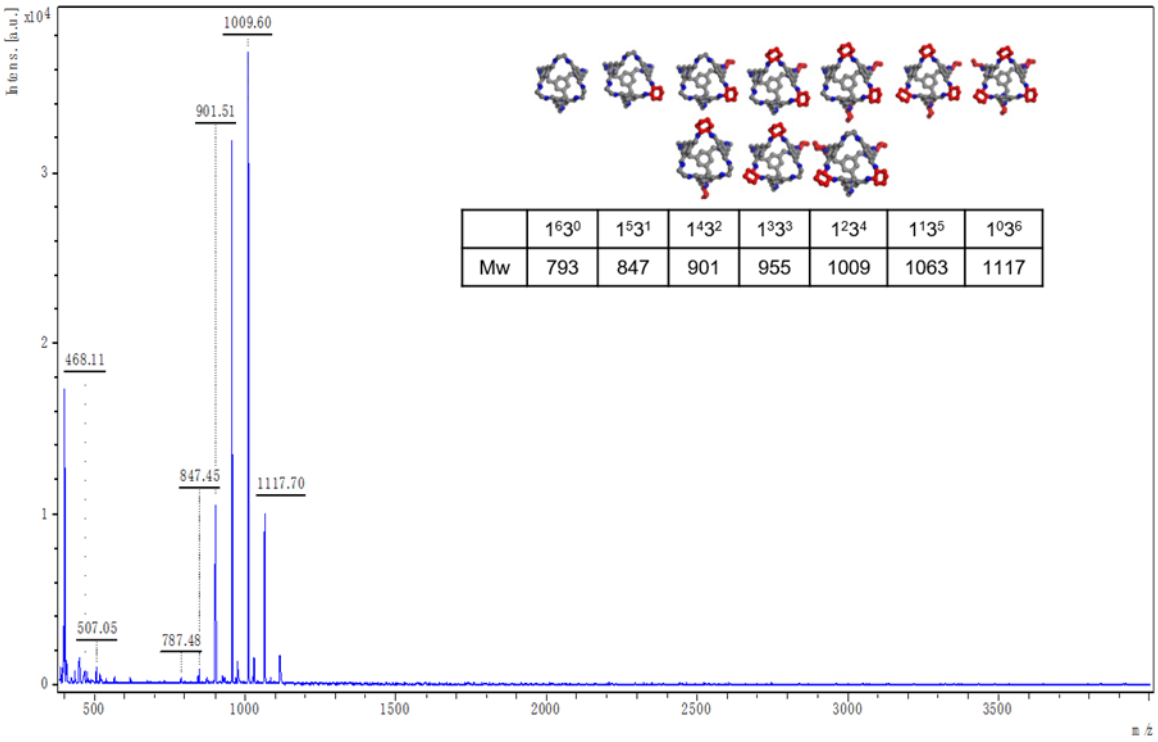

Figure 5.8 MALDI-MS spectrum of 42 wt % PEI in ASPOC

5.3.3 Synthesis of mPEI/ASPOC Composites

To avoid the reaction between polyamines and ASPOCs, one can either change the chemistry of the cage to a platform that is more compatible with amines, or use tertiary

amines that would not react with imine bonds. In this chapter, I adopted the second approach by converting primary and secondary amines in PEI to tertiary amines via methylation. Tertiary amines, including those on a PEI platform, have been previously explored as SO_2 sorbents supported in silica supports[31-32, 34] where they were found to have favorable properties. In contrast, the adsorption of SO_2 on amine-supported solid materials containing primary and secondary amines typically leads to irreversible deactivation of the amines.[35-37] The reaction of SO_2 and tertiary amines forms reversible charge transfer complexes based on FTIR and ^{15}N NMR spectroscopic analysis,[31] but they adsorb little CO_2, which can be advantageous for the selective SO_2 capture from CO_2-containing streams.

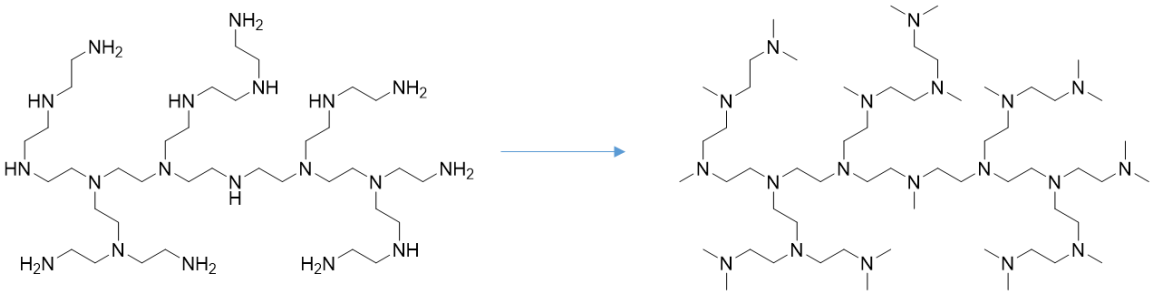

Figure 5.9 Synthesis of mPEI from PEI

All tertiary amine containing PEI (mPEI) was synthesized according to the procedure described in the experimental section.[31] The removal of all primary and secondary amines was confirmed by NMR and MS. Figure 5.10 shows the ^1H NMR spectra of PEI and mPEI. The amine protons (both primary and secondary) in PEI (1.75 ppm) entirely disappeared in the spectrum of mPEI and turned into a sharp peak at 2.23 ppm that was assigned to α-methyl protons, indicating methylation of all amine groups.

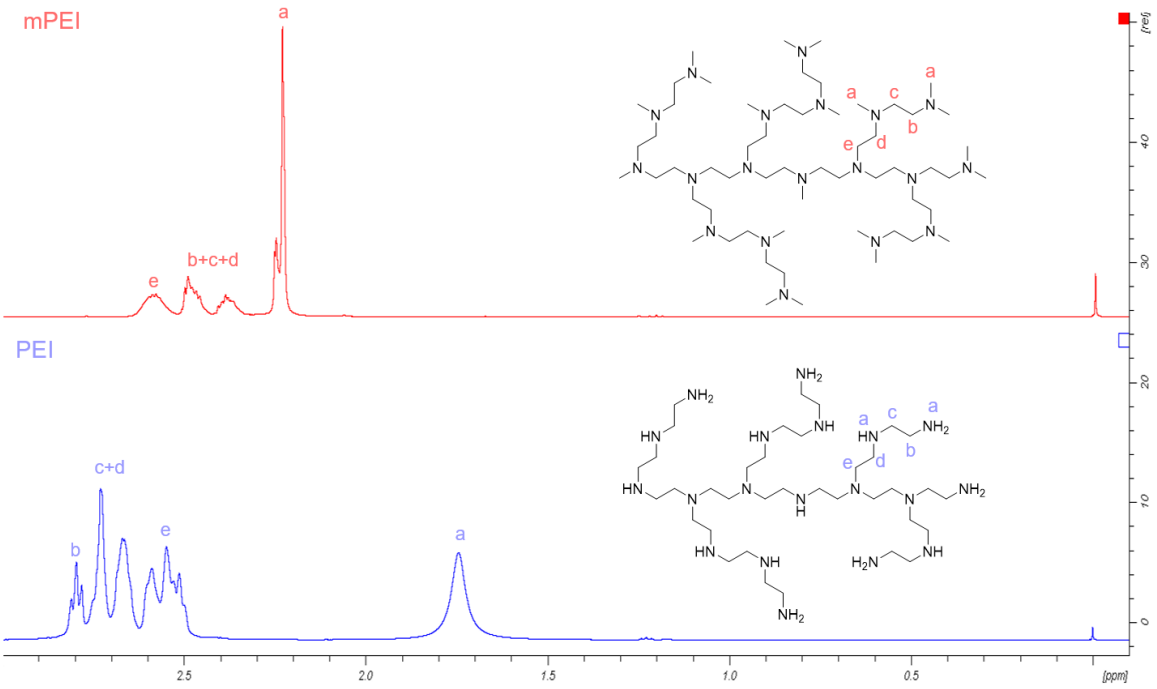

Figure 5.10 ^{1}H NMR spectra of PEI and mPEI

Figure 5.11 shows the ESI-MS spectra of PEI and mPEI, as well as the theoretical molecular weight of the two polymers with increasing nitrogen units. A clear shift of the major peaks to a higher molecular weight corresponding to methylation can be observed.

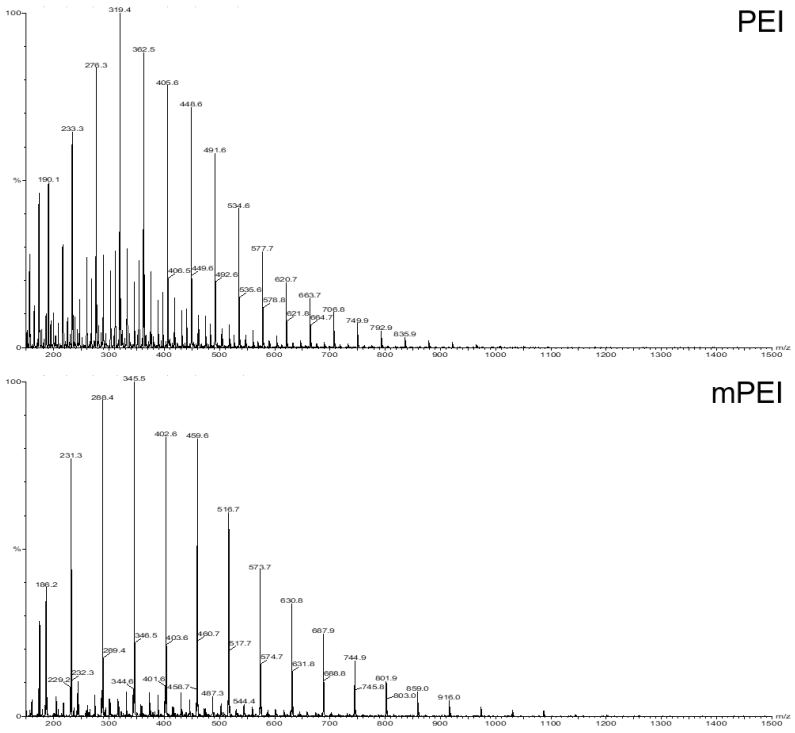

N unit	PEI Mw	mPEI Mw
2	60.07	116.13
3	103.11	173.19
4	146.15	230.25
5	189.2	287.3
6	232.24	344.36
7	275.28	401.42
8	318.32	458.48
9	361.36	515.54
10	404.41	572.59
11	447.45	629.65
12	490.49	686.71
13	533.53	743.77
14	576.58	800.83
15	619.62	857.88
16	662.66	914.94
17	705.7	972
18	748.74	1029.06
19	791.79	1086.11

Figure 5.11 ESI-MS spectra of PEI and mPEI.

The mPEI and ASPOC composite materials were prepared according to the procedure described in the experimental section. The three samples with mPEI weight loading ranging from 10-40 % all appear as free-flowing powders. SEM images of the mPEI/ASPOC composite samples show random particle formation without noticeable aggregation (Figure 5.12). However, as the mPEI loading goes to 80 wt %, the particles became much bigger and showed signs of melting under the electron beam.

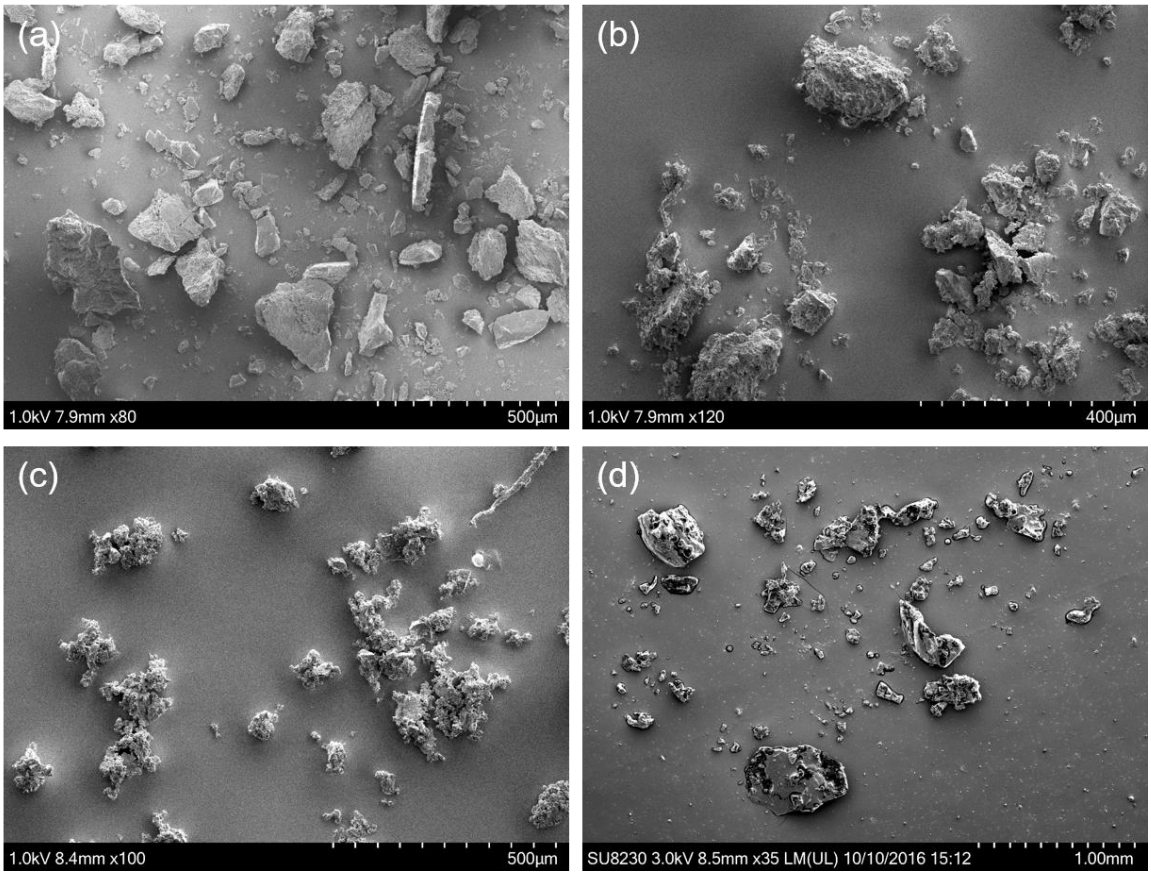

Figure 5.12 SEM of mPEI/ASPOC composite samples with different mPEI loading: (a) 10-mPEI/ASPOC, (b) 20-mPEI/ASPOC, (c) 40-mPEI/ASPOC, and (d) 80-mPEI/ASPOC

The chemical compatibility between the mPEI and the ASPOC molecules was further checked with ^{1}H NMR and ESI-MS. In the ^{1}H NMR spectra (Figure 5.13) of mPEI/ASPOC composites, the proton signals from both the mPEI and ASPOC were retained in the composite materials. ESI-MS (Figure 5.14) spectra also suggest a physical mixture between mPEI and ASPOC molecules was obtained.

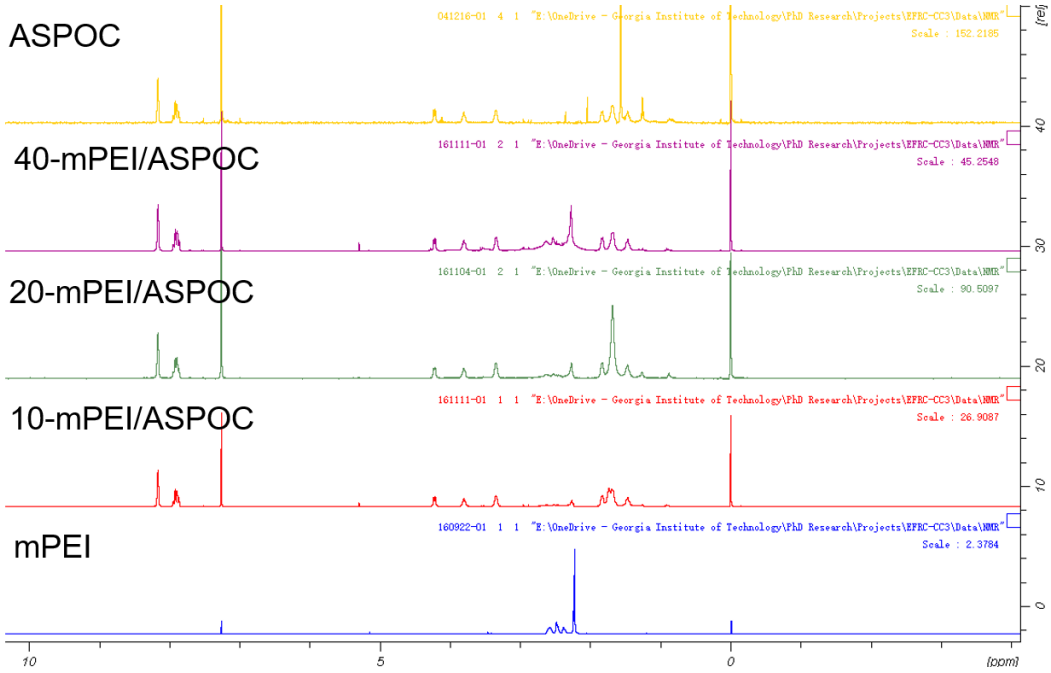

Figure 5.13 ^{1}H NMR of pure ASPOC, mPEI and three composite samples.

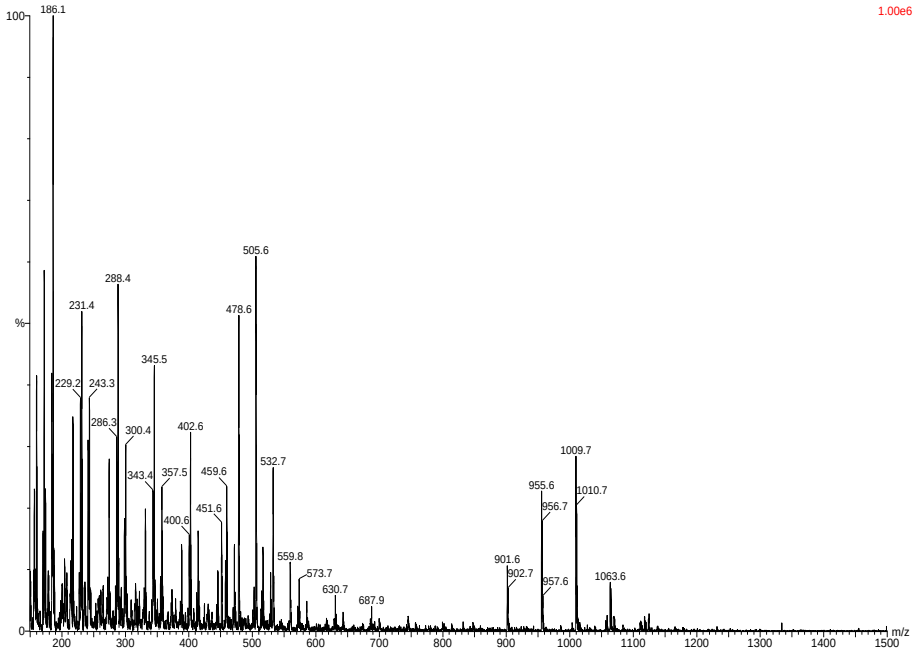

Figure 5.14 ESI-MS spectrum of 20-mPEI/ASPOC sample. Peaks in the left region correspond to mPEI molecules, peaks from 900-1200 m/z correspond to cage molecules

Elemental analysis was carried out for calculating mPEI loading in the dried samples (Table 5.4). The final mPEI loadings were determined by elemental analysis and are listed in Table 5.5. The mPEI loading in the final composite material are all lower than the designed ratio, which might be a result from evaporation of short-chain mPEI during activation. The mPEI loadings and nitrogen content are used in the SO_2 adsorption measurement analysis for calculating amine efficiency.

Table 5.4 Elemental analysis data for ASPOC and composite materials (wt%)

	C	H	N
ASPOC	74.29	7.06	16.6
mPEI	60.56	12.53	23.16
10-mPEI/ASPOC	72.7	7.55	16.61
20-mPEI/ASPOC	70.37	8.08	16.84
40-mPEI/ASPOC	65.69	8.72	17.52

Table 5.5 Theoretical and calculated mPEI loadings in composite materials

	ASPOC	10-mPEI/ASPOC	20-mPEI/ASPOC	40-mPEI/ASPOC	mPEI
Theoretical mPEI loading (wt%)	0	10	20	40	100
mPEI loading from elemental analysis (wt%)	0	6.3	17.2	36.0	100
N from mPEI (mmol/g)	0	1.09	2.96	6.18	17.19

5.3.4 Structural Characterization and Molecular Modeling of mPEI/ASPOC Composites

The textural properties of the composite materials were initially characterized with N_2 physisorption at 77 K. However, in contrast to the gradual pore filling observed in most PEI/silica sorbent materials, the surface area and pore volume of the composite materials were virtually zero under the adsorption temperature of 77 K (Figure 5.15). This is because the mPEI molecules and ASPOC molecules likely form a "mixed matrix" composite rather than the typical, progressive pore filing observed in mesoporous supports. At 77 K, the diffusion of N_2 gas into mPEI was extremely slow and thus could not reach the pores of the ASPOCs.

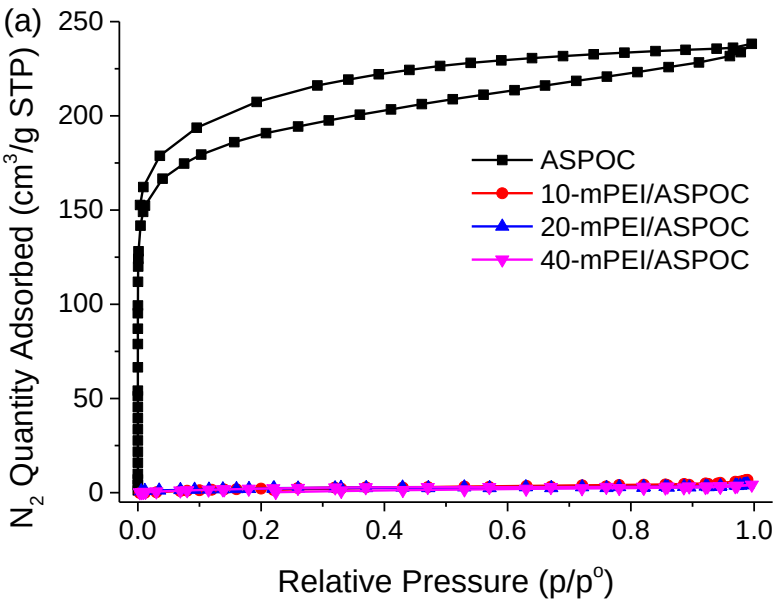

Figure 5.15 N_2 and CO_2 physisorption isotherms measured at 77 K and 308 K, respectively

In contrast, CO_2 physisorption at elevated temperature (308 K) showed decreased uptake for the composite materials relative to the ASPOC materials (Figure 5.16). Since

tertiary amines in mPEI do not adsorb CO_2 under dry conditions, the CO_2 uptakes were also plotted normalized to ASPOC content in Figure 5.17. However, a decreasing trend was still present with increasing mPEI loading. This might be a result of mPEI molecules occupying the external or even internal pore volume of the ASPOC molecules. The external pore volume results from the random packing of the ASPOC molecules, which are responsible for part of the CO_2 uptake of the pure ASPOC. It is apparent that when mPEI molecules mix with ASPOC molecules, part of this volume will be occupied by mPEI. The internal pore volume is the volume held by the pores of the cages.

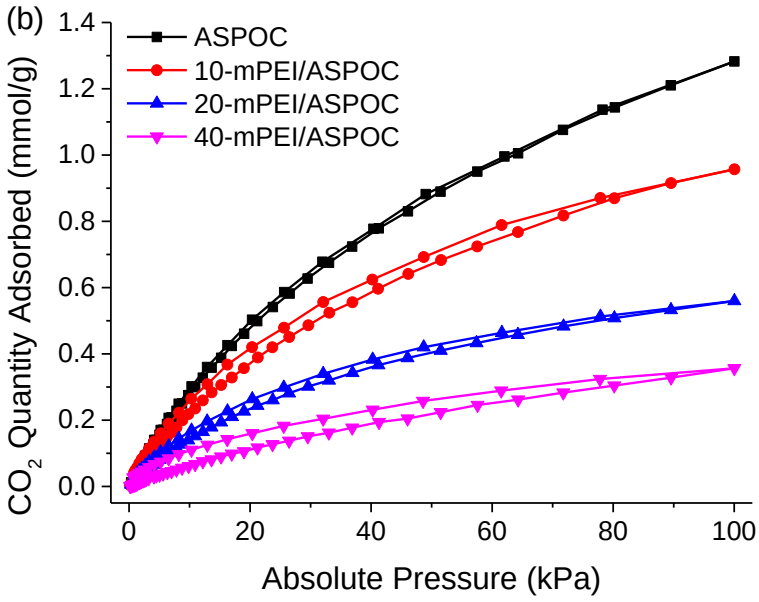

Figure 5.16 CO_2 physisorption isotherms measured at 308 K, respectively

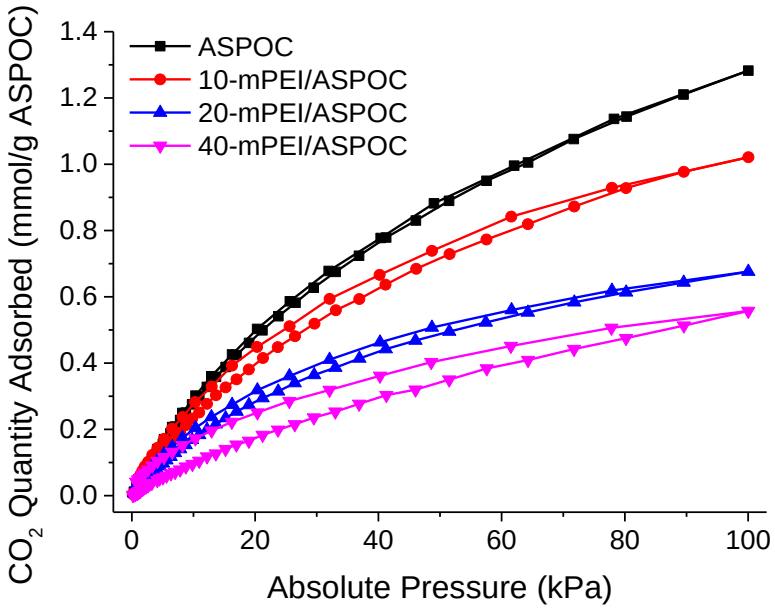

Figure 5.17 CO_2 physisorption isotherms normalized to ASPOC content based on elemental analysis

The NLDFT model was used to calculate the pore size distribution from the CO_2 isotherms as shown in Figure 5.18. As shown in the figure below, ASPOC and the composites have 6Å, 8Å, and 13Å pores. The 6Å pore size corresponds to internal pores of the ASPOC molecules. And the two larger pore sizes correspond to external pores from irregular packing of the cages and mPEI. With increasing mPEI loading, the external pore volume decreases dramatically. At 40 wt%, the 8Å pores are totally filled. The internal pore volume also decreases with increasing mPEI loading.

It needs to be noted that the CO_2 isotherms in this section were collected at 308 K. However, the NLDFT model provided by Micromeritics for CO_2 is designed for isotherms collected at 273 K. Thus, this PSD can only be used as a qualitative comparison between samples.

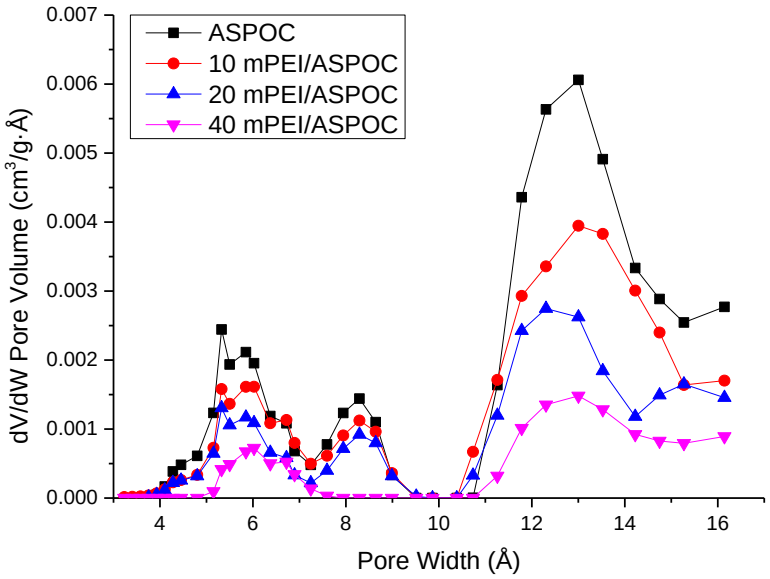

Figure 5.18 Pore size distribution of ASPOC and mPEI/ASPOC mixtures calculated from CO_2 isotherm

The structure of the mPEI/ASPOC that can be summarized as: (1) mPEI molecules are dispersed among ASPOC molecules, the pores in the ASPOCs provide diffusion pathways for gas molecules to interact with tertiary amines in mPEI; (2) mPEI chain ends can penetrate the window of ASPOC molecules, such that at high loadings of mPEI, the pore network in the composite material is partially blocked and will significantly reduce the diffusion rate of gas molecules.

5.3.5 SO_2 Adsorption Measurements

The pseudo-equilibrium SO_2 capacities of the composite materials were determined gravimetrically with 200 ppm SO_2 in N_2 as the feed mixture. The capacities of the composite materials with different mPEI loadings were compared with pure ASPOC and mPEI as benchmarks. As shown in Figure 5.19 (a), the SO_2 capacities of each sample

increased with mPEI loading. Based on the tertiary amine amount calculated from the elemental analysis, the amine efficiency (mole SO_2 per mole amine) of each sample was estimated and is shown in Figure 5.19 (b). The amine efficiency of the composite samples decreased with increasing mPEI loading. This might be caused by steric hindrance, especially by amine moieties in the pores of ASPOC at the higher weight loading of mPEI in the ASPOC support.

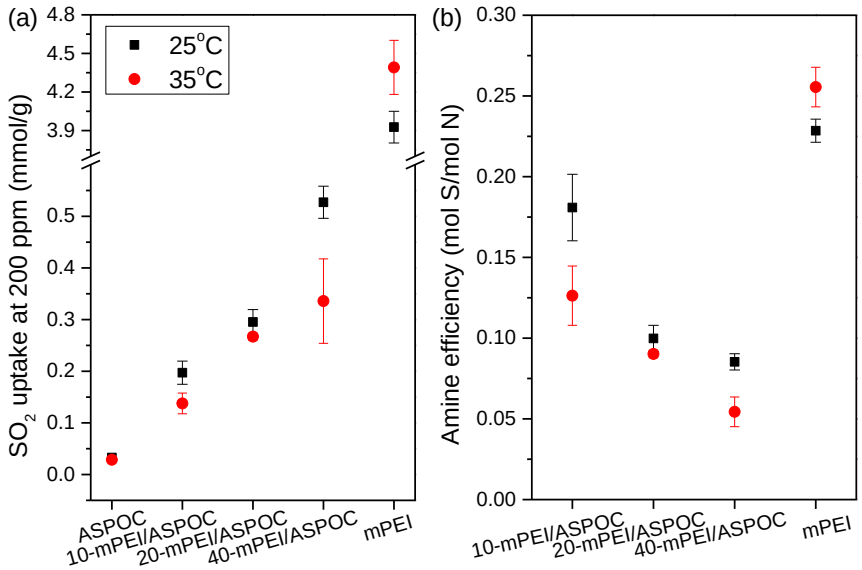

Figure 5.19 (a) SO_2 uptakes of pure ASPOC, mPEI and mPEI/ASPOC composites at 25ºC and 35 ºC; and (b) corresponding amine efficiencies.

*SO_2 uptake capacities for 40-mPEI/ASPOC are determined at 1000 min of adsorption as the uptake is slow and did not reach pseudo-equilibrium.

The adsorption behavior of the mPEI/ASPOC composite at 35 °C was also studied. While pure ASPOC sample showed a minor difference with regards to the adsorption temperature, the composite samples showed a more pronounced decrease in SO_2 uptake. This is expected since the SO_2-tertiary amine interaction occurs exothermically with the

formation of charge transfer complexes. A higher temperature will lead to a lower uptake capacity, which is ideal for regenerating the material after adsorption. On the other hand, the pure mPEI showed an opposite trend from the composite materials, with higher adsorption temperature leading to higher SO_2 uptake. This reversed temperature effect was also observed in PEI/silica adsorbents for CO_2.[20, 38-39] It was elucidated by neutron diffraction studies that the PEI molecules in mesoporous SBA-15 silica supports form liquid phase films or plugs in the pores.[40] A higher adsorption temperature will improve the flexibility of the polymer chains and allow for the system to approach closer to thermodynamic equilibrium. However, the higher temperature leads to a decrease in the thermodynamic equilibrium capacity, which is undesirable. From our molecular dynamics simulations, the mPEI and ASPOC molecules will form a molecular scale mixture instead of separated phases, thus changing the inverse temperature effect observed in the case of PEI/silica adsorbents.

Although the 10-mPEI/ASPOC displayed a much lower SO_2 uptake compared to the pure mPEI at both temperatures, the amine efficiency was only slightly lower, indicating that the performance was maintained in terms of amine utility in the composite materials at low mPEI loadings. More importantly, the uptake kinetics in the composite materials (Figure 5.20) showed an improvement of the SO_2 uptake rate in the composite material. While this holds true for 10-mPEI/ASPOC and 20-mPEI/ASPOC samples, the 40-mPEI/ASPOC material showed a much slower uptake rate compared to the other samples. This is likely because of the impeded gas diffusion from the high degree of chain-end penetration into the ASPOC pores. It can be observed that in this particular experiment mPEI reaches saturation uptake at a time close to 10-mPEI/ASPOC and 20-mPEI/ASPOC.

This is a result of the small amount of mPEI sample used to measure the saturation within a reasonable time duration. If more mPEI is used in the analysis, the time at which mPEI and composite materials reach equilibrium will be different.

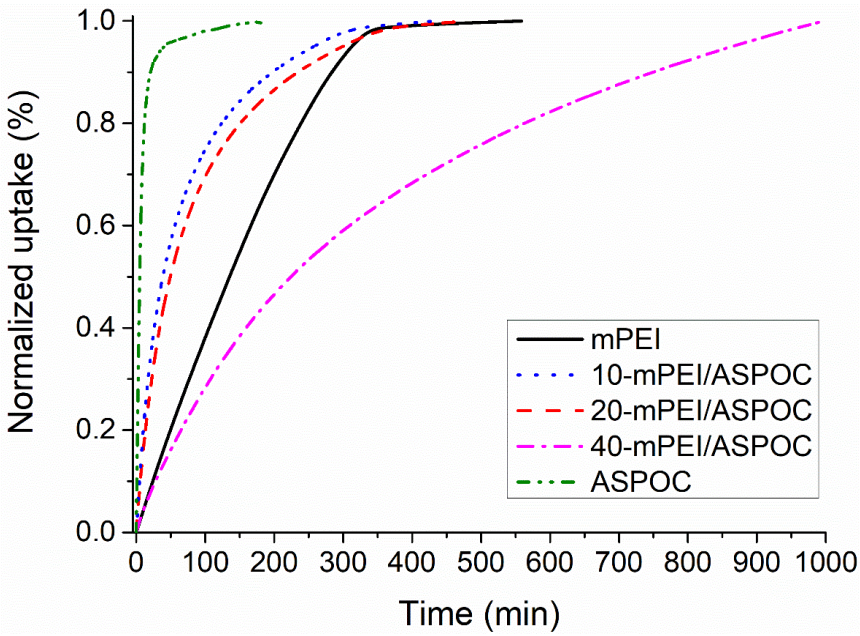

Figure 5.20 SO_2 adsorption kinetics in pure mPEI, ASPOC and mPEI/ASPOC composites at 25°C

5.3.6 Thermostability and Regeneration of Adsorbents

Since the methylation of primary and secondary amines will reduce the number and strength of hydrogen-bond interactions between polymer molecules, the mPEI species are expected to be more volatile than PEI. Figure 5.21 shows the relative volatility of mPEI compared to PEI at 3 different temperatures relevant to desorption conditions. It was observed that the mPEI exhibits higher volatility at all temperatures tested, which might undermine the reusability of the composite material under cyclic operation.

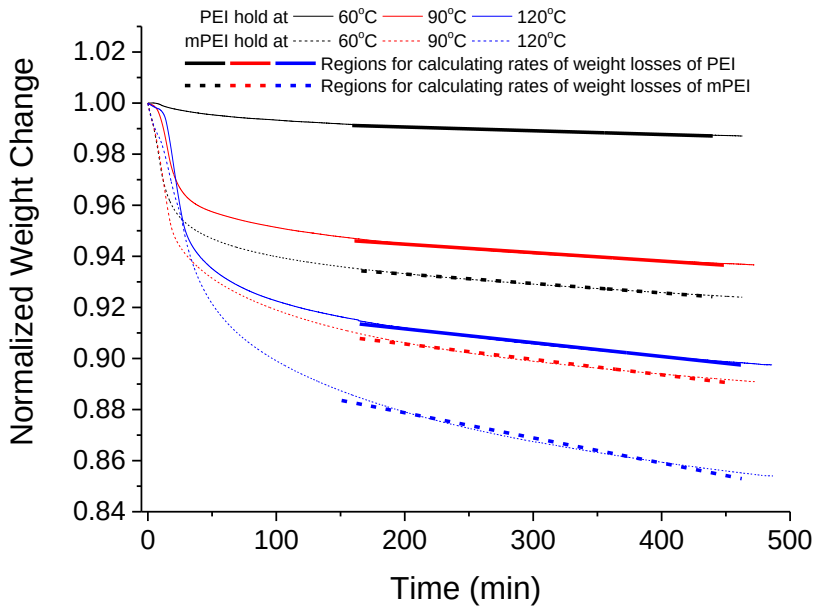

Figure 5.21 Thermal stability of the PEI and mPEI at 60 °C, 90 °C, and 120 °C, and corresponding regions for calculating rates of weight losses

With this in mind, the thermostability of the composite materials was investigated. Figure 5.22 shows the normalized weight loss of the three composite samples being held at different temperatures (60 °C, 90 °C, and 120 °C).

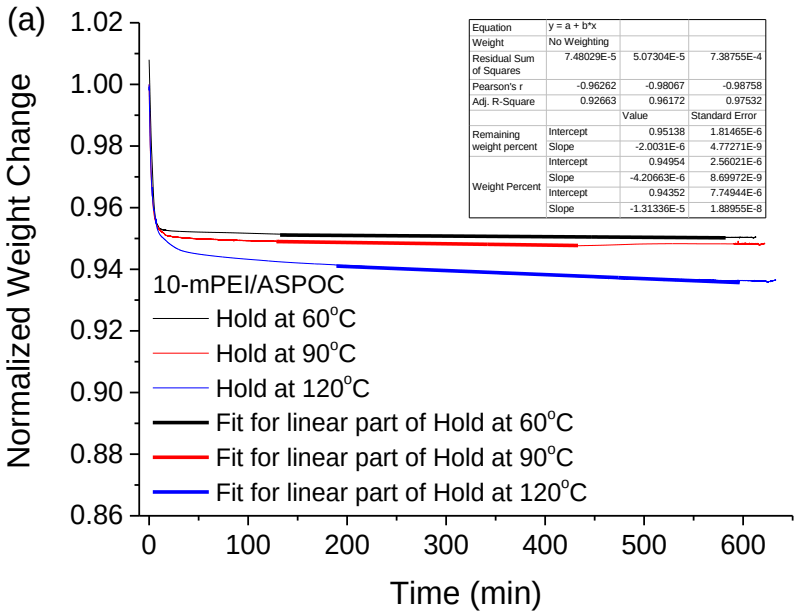

Equation	y = a + b*x		
Weight	No Weighting		
Residual Sum of Squares	7.48029E-5	5.07304E-5	7.38755E-4
Pearson's r	-0.96262	-0.98067	-0.98758
Adj. R-Square	0.92663	0.96172	0.97532
		Value	Standard Error
Remaining weight percent	Intercept	0.95138	1.81465E-6
	Slope	-2.0031E-6	4.77271E-9
Weight Percent	Intercept	0.94954	2.56021E-6
	Slope	-4.20663E-6	8.69972E-9
	Intercept	0.94352	7.74944E-6
	Slope	-1.31336E-5	1.88955E-8

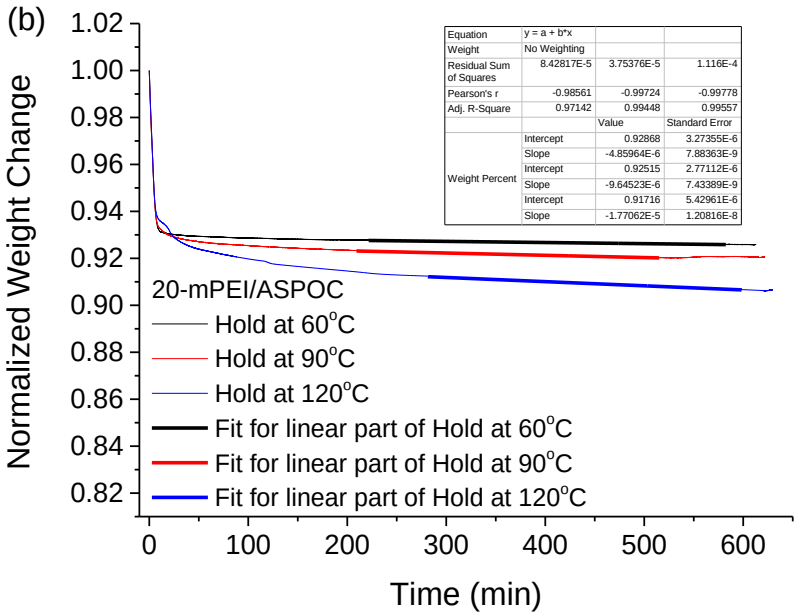

Equation	y = a + b*x		
Weight	No Weighting		
Residual Sum of Squares	8.42817E-5	3.75376E-5	1.116E-4
Pearson's r	-0.98561	-0.99724	-0.99778
Adj. R-Square	0.97142	0.99448	0.99557
		Value	Standard Error
Weight Percent	Intercept	0.92868	3.27355E-6
	Slope	-4.85964E-6	7.88363E-9
	Intercept	0.92515	2.77112E-6
	Slope	-9.64523E-6	7.43389E-9
	Intercept	0.91716	5.42961E-6
	Slope	-1.77062E-5	1.20816E-8

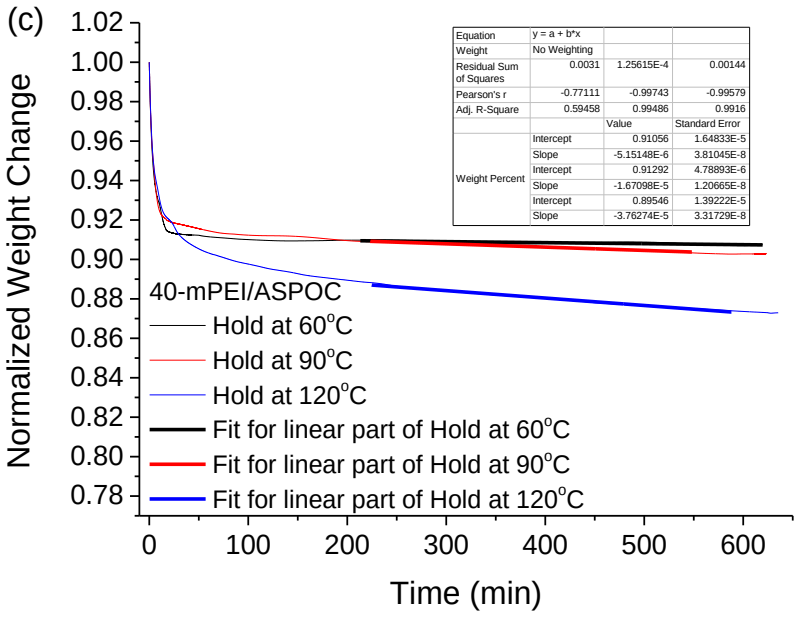

Figure 5.22 Thermal stability of the composite materials, (a) 10-mPEI/ASPOC, b) 20-mPEI/ASPOC and (c) 40-mPEI/ASPOC hold at 60 °C, 90 °C, and 120 °C and the fitting parameters for calculating the rates of weight lose

The initial weight loss is attributed to desorption of moisture, as evidenced by online mass spectrometry analysis of the desorbed species (Figure 5.23 and Figure 5.24). When compared across different samples, a higher mPEI loading resulted in a larger initial weight loss, which is attributed to more adsorbed moisture.

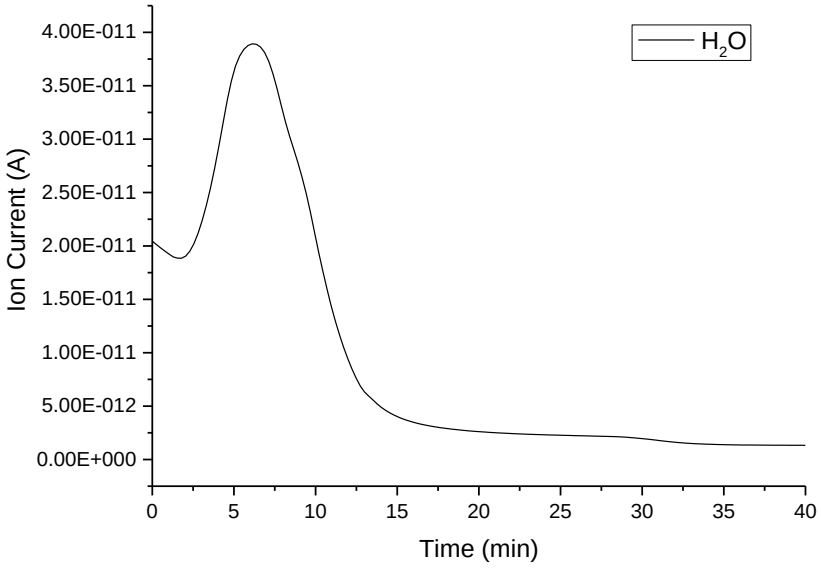

Figure 5.23 Desorption of water from 20-mPEI/ASPOC indicated by online mass spectrometry ion current change during heating to 90ºC with 10 ºC/min and then cooled down to room temperature from 30 min

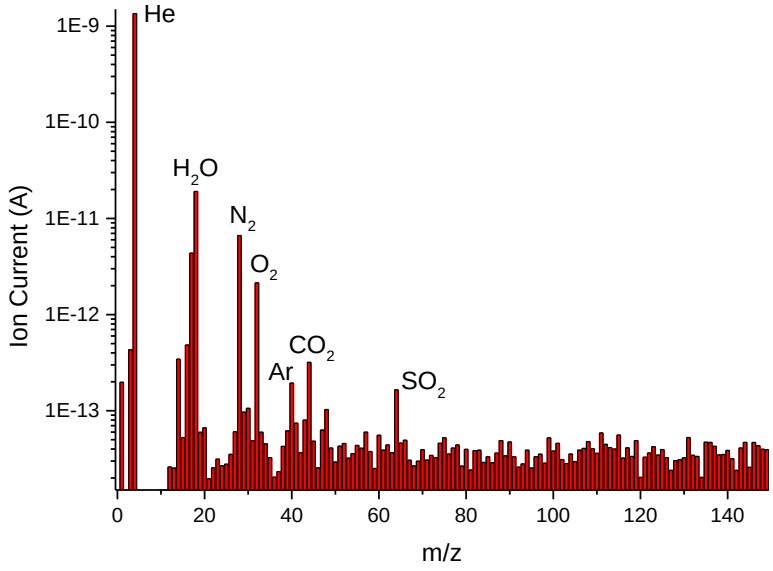

Figure 5.24 Selected mass spectrometry bar-graph during desorption of 20-mPEI/ASPOC between 0-150 m/z

The rates of weight loss are calculated from the slopes shown in Figure 5.25. The incorporation of mPEI into the ASPOC greatly increased its retention during high-temperature exposure as a result of the formation of a solid solution and entanglement of the mPEI with the ASPOC pore structure. It was observed that the composite material was stable to at least 90 °C exposure. At 120 °C, a gradual loss in weight was observed due to slow evaporation of mPEI in the material.

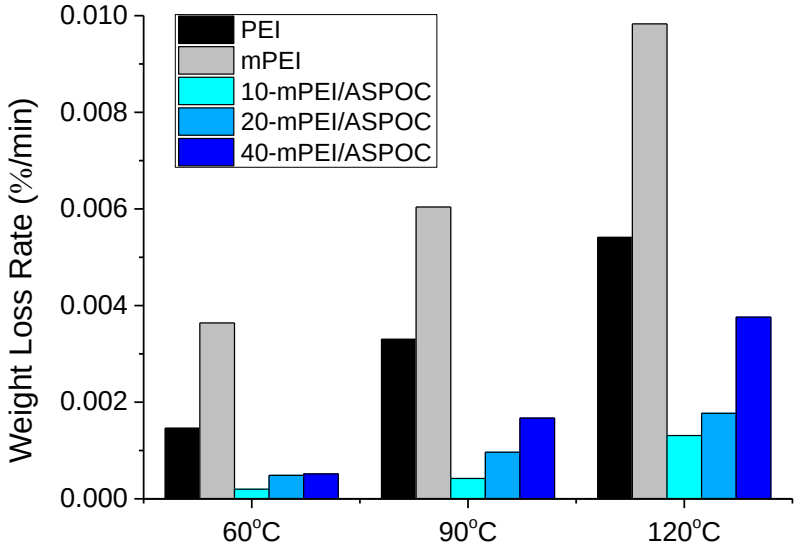

Figure 5.25 Rate of weight loss of the composite samples, PEI and mPEI under 60 °C, 90 °C, and 120 °C

The regeneration of the composite, i.e., desorption of the adsorbed SO_2, was also studied at the three temperatures used above. A fresh sample was used at each temperature. The sample was first activated at either 60 °C, 90 °C, or 120 °C, followed by adsorption of SO_2 at 25 °C for 360 min, and thermal desorption at the same activation temperature. The SO_2 uptake capacities were then compared between each sample. In addition, the regenerability was evaluated by comparing the final sample weight to the activated sample

weight. Figure 5.26 shows the weight change of the 20-mPEI/ASPOC sample under different activation/desorption temperatures. At the desorption temperature of 60 °C, the adsorbed SO_2 did not fully desorb. However, at 90 °C and 120 °C, the weights after desorption were lower than the starting weight, indicating a further loss of polymer and/or moisture from the adsorbents.

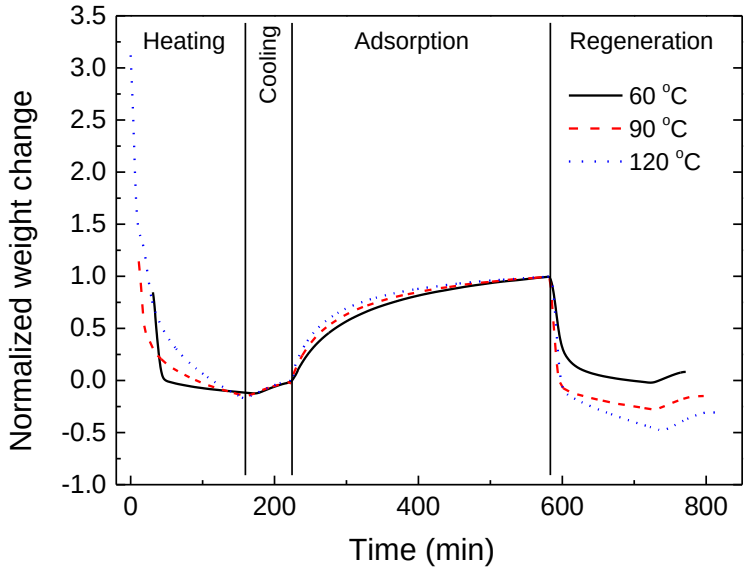

Figure 5.26 Weight change profiles of 20-mPEI/ASPOC during activation-adsorption-regeneration cycle under 60 °C, 90 °C, and 120 °C. The data are normalized by the sample dry weight

5.3.7 Cyclic Adsorption Study

The results from the thermostability and regeneration studies indicate the potential of the mPEI/ASPOC composite materials to be used as stable SO_2 sorbents with a small swing temperature between 25 °C and 60 °C. Thus, the cyclic stability of 20-mPEI/ASPOC was studied in a temperature swing adsorption cycle with adsorption at 25 °C and desorption at 60 °C. The cyclic capacities are shown in Figure 5.27. It can be observed that,

except for the drop in the first cycle, the sample appeared stable after approximately 8 cycles. The amine efficiency of the sample during the 12 total cycles is plotted in Figure 5.28. The capacity drop in the first cycle is probably due to some SO_2 molecules not fully desorbing from the strongest base sites at this low regeneration temperature.

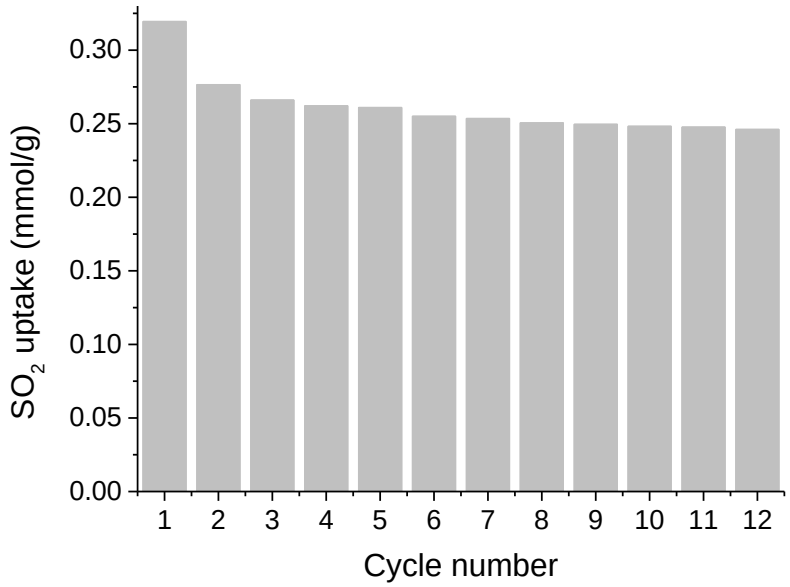

Figure 5.27 Cyclic SO_2 uptake performance of 20-mPEI/ASPOC with a sorption temperature of 25°C and a desorption temperature of 60°C

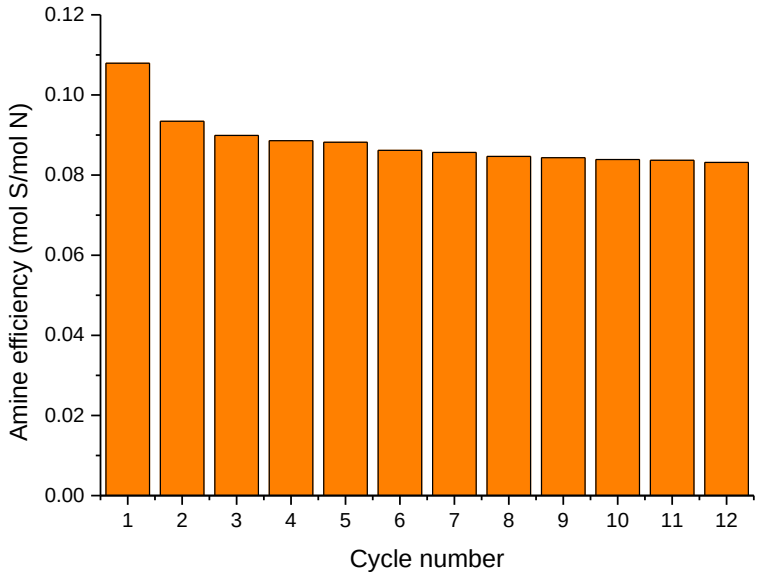

Figure 5.28 Amine efficiency of 20-mPEI/ASPOC for 12 cycles

5.3.8 H_2S Adsorption in mPEI/ASPOC Composite Materials

Although mPEI is not active for chemisorption of H_2S, adsorption of H_2S into the ASPOC as well as the composite materials was tested (Figure 5.29). Similar to CO_2 adsorption in the materials, a general decreasing trend was found with H_2S adsorption determined gravimetrically. Although mPEI did not facilitate the adsorption of H_2S, rapid and stable adsorption of H_2S into the ASPOC was observed. This indicates the potential of ASPOCs as a selective H_2S adsorbent by itself, or it can be used as a stable support for other H_2S sorbents.

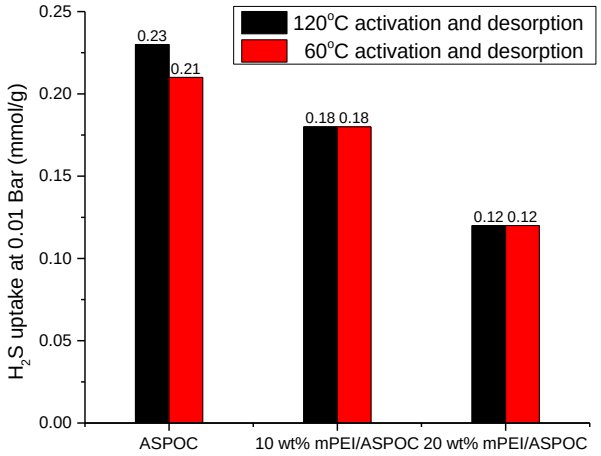

Figure 5.29 H_2S adsorption into ASPOC

5.4 Conclusions

In this work, the applicability of imine-based POCs as potential support for SO_2-sorbing polymers was explored. The imine-based POCs were found to react with primary and secondary amines in branched poly(ethylenediamine). A series of composites with a fully tertiary poly(amine) sample utilizing mPEI as the sorbing phase and ASPOCs as the support/substrate was prepared. It was observed that the mPEI molecules could form a solid solution with the ASPOC molecules. The thermostability and SO_2 capacity of the composite materials were studied as a function of the mPEI loading. The composite materials were found to have improved uptake kinetics and comparable amine efficiencies with the pure mPEI. A representative sample was tested in a simulated temperature swing adsorption-desorption cycle and showed stable cyclic performance at low SO_2 concentration.

Compared to oxide and carbon substrates, POCs can suffer from higher cost and instability. In Chapter 4, it has been shown that more cost-effective feedstocks can be used to reduce the cost of POCs and at the same time, increase their acid gas stability.[41] In this chapter, only impregnated amines were considered, when compared to grafted amines, are less thermally stable but have the advantages of easy preparation and high amine loading.[42] By introducing surface functional groups, grafted amines can also conceptually be applied to POC materials.[43] When choosing POCs as porous substrates, the following points have to be taken into consideration. (1) Compatibility between the POC molecules and the active adsorbent molecule. (2) Stability of POC molecules under the desired operating conditions. For example, in drug delivery applications, the reversibility (instability) of the cage-forming bonds is required. On the other hand, in many catalysis or separation applications, the POCs are expected to be stable. (3) There should be a potential benefit of creating composite materials compared to bare components.

5.5 References

(1) Zhu, G.; Carrillo, J.-M. Y.; Sujan, A.; Okonkwo, C.; Park, S.; Sumpter, B. G.; Jones, C. W.; Lively, R. P. Molecular blends of methylated-poly(ethylenimine) and amorphous porous organic cages for SO2 adsorption. *Journal of Materials Chemistry A* **2018**.

(2) Bojdys, M. J.; Briggs, M. E.; Jones, J. T. A.; Adams, D. J.; Chong, S. Y.; Schmidtmann, M.; Cooper, A. I. Supramolecular Engineering of Intrinsic and Extrinsic Porosity in Covalent Organic Cages. *J. Am. Chem. Soc.* **2011,** *133*, 16566-16571.

(3) Jiang, S.; Jones, J. T. A.; Hasell, T.; Blythe, C. E.; Adams, D. J.; Trewin, A.; Cooper, A. I. Porous organic molecular solids by dynamic covalent scrambling. *Nat. Commun.* **2011,** *2*, 207.

(4) Giri, N.; Davidson, C. E.; Melaugh, G.; Del Popolo, M. G.; Jones, J. T. A.; Hasell, T.; Cooper, A. I.; Horton, P. N.; Hursthouse, M. B.; James, S. L. Alkylated organic cages: from porous crystals to neat liquids. *Chem. Sci.* **2012,** *3*, 2153-2157.

(5) Giri, N.; Del Popolo, M. G.; Melaugh, G.; Greenaway, R. L.; Ratzke, K.; Koschine, T.; Pison, L.; Gomes, M. F. C.; Cooper, A. I.; James, S. L. Liquids with permanent porosity. *Nature* **2015,** *527*, 216-220.

(6) Jiang, S.; Chen, L.; Briggs, M. E.; Hasell, T.; Cooper, A. I. Functional porous composites by blending with solution-processable molecular pores. *Chem. Commun.* **2016,** *52*, 6895-6898.

(7) Houghton, J. T.; Ding, Y.; Griggs, D. J.; Noguer, M.; van der Linden, P. J.; Dai, X.; Maskell, K.; Johnson, C. A. *Climate change 2001: the scientific basis*. The Press Syndicate of the University of Cambridge: 2001.

(8) Jacobson, M. Z. Review of solutions to global warming, air pollution, and energy security. *Energy & Environmental Science* **2009,** *2*, 148-173.

(9) *World health statistics 2017: monitoring health for the SDGs, Sustainable Development Goals*. World Health Organization: 2017.

(10) Seinfeld, J. H.; Pandis, S. N. *Atmospheric chemistry and physics: from air pollution to climate change*. John Wiley & Sons: 2016.

(11) Barea, E.; Montoro, C.; Navarro, J. A. R. Toxic gas removal - metal-organic frameworks for the capture and degradation of toxic gases and vapours. *Chemical Society Reviews* **2014,** *43*, 5419-5430.

(12) Kampa, M.; Castanas, E. Human health effects of air pollution. *Environmental Pollution* **2008,** *151*, 362-367.

(13) Danckwerts, P. V. The reaction of CO2 with ethanolamines. *Chemical Engineering Science* **1979,** *34*, 443-446.

(14) Leung, D. Y. C.; Caramanna, G.; Maroto-Valer, M. M. An overview of current status of carbon dioxide capture and storage technologies. *Renewable Sustainable Energy Rev.* **2014,** *39*, 426-443.

(15) Yeh, J. T.; Resnik, K. P.; Rygle, K.; Pennline, H. W. Semi-batch absorption and regeneration studies for CO2 capture by aqueous ammonia. *Fuel Processing Technology* **2005,** *86*, 1533-1546.

(16) Jung, S.-H.; Jeong, G.-T.; Lee, G.-Y.; Cha, J.-M.; Park, D.-H. Simultaneous removal of SO2, NO and particulate by pilot-scale scrubber system. *Korean Journal of Chemical Engineering* **2007,** *24*, 1064-1069.

(17) Ebrahimi, S.; Picioreanu, C.; Kleerebezem, R.; Heijnen, J. J.; van Loosdrecht, M. C. M. Rate-based modelling of SO2 absorption into aqueous NaHCO3/Na2CO3 solutions accompanied by the desorption of CO2. *Chemical Engineering Science* **2003,** *58*, 3589-3600.

(18) Choi, S.; Drese, J. H.; Jones, C. W. Adsorbent Materials for Carbon Dioxide Capture from Large Anthropogenic Point Sources. *ChemSusChem* **2009,** *2*, 796-854.

(19) Lee, S.-Y.; Park, S.-J. A review on solid adsorbents for carbon dioxide capture. *Journal of Industrial and Engineering Chemistry* **2015,** *23*, 1-11.

(20) Xu, X.; Song, C.; Andresen, J. M.; Miller, B. G.; Scaroni, A. W. Novel Polyethylenimine-Modified Mesoporous Molecular Sieve of MCM-41 Type as High-Capacity Adsorbent for CO2 Capture. *Energy & Fuels* **2002,** *16*, 1463-1469.

(21) Xu, X.; Song, C.; Miller, B. G.; Scaroni, A. W. Influence of Moisture on CO2 Separation from Gas Mixture by a Nanoporous Adsorbent Based on Polyethylenimine-Modified Molecular Sieve MCM-41. *Industrial & Engineering Chemistry Research* **2005,** *44*, 8113-8119.

(22) Xu, X.; Song, C.; Andrésen, J. M.; Miller, B. G.; Scaroni, A. W. Preparation and characterization of novel CO2 "molecular basket" adsorbents based on polymer-modified mesoporous molecular sieve MCM-41. *Microporous and Mesoporous Materials* **2003,** *62*, 29-45.

(23) Xu, X.; Song, C.; Miller, B. G.; Scaroni, A. W. Adsorption separation of carbon dioxide from flue gas of natural gas-fired boiler by a novel nanoporous "molecular basket" adsorbent. *Fuel Processing Technology* **2005,** *86*, 1457-1472.

(24) Huang, K.; Chai, S.-H.; Mayes, R. T.; Veith, G. M.; Browning, K. L.; Sakwa-Novak, M. A.; Potter, M. E.; Jones, C. W.; Wu, Y.-T.; Dai, S. An efficient low-temperature route to nitrogen-doping and activation of mesoporous carbons for CO2 capture. *Chemical Communications* **2015,** *51*, 17261-17264.

(25) Potter, M. E.; Cho, K. M.; Lee, J. J.; Jones, C. W. Role of Alumina Basicity in CO2 Uptake in 3-Aminopropylsilyl-Grafted Alumina Adsorbents. *ChemSusChem* **2017,** *10*, 2192-2201.

(26) Pang, S. H.; Lee, L.-C.; Sakwa-Novak, M. A.; Lively, R. P.; Jones, C. W. Design of Aminopolymer Structure to Enhance Performance and Stability of CO2 Sorbents: Poly(propylenimine) vs Poly(ethylenimine). *Journal of the American Chemical Society* **2017,** *139*, 3627-3630.

(27) Plaza, M. G.; Pevida, C.; Arenillas, A.; Rubiera, F.; Pis, J. J. CO2 capture by adsorption with nitrogen enriched carbons. *Fuel* **2007,** *86*, 2204-2212.

(28) Dillon, E. P.; Crouse, C. A.; Barron, A. R. Synthesis, Characterization, and Carbon Dioxide Adsorption of Covalently Attached Polyethyleneimine-Functionalized Single-Wall Carbon Nanotubes. *ACS Nano* **2008,** *2*, 156-164.

(29) Heydari-Gorji, A.; Belmabkhout, Y.; Sayari, A. Degradation of amine-supported CO2 adsorbents in the presence of oxygen-containing gases. *Microporous and Mesoporous Materials* **2011,** *145*, 146-149.

(30) Bollini, P.; Choi, S.; Drese, J. H.; Jones, C. W. Oxidative Degradation of Aminosilica Adsorbents Relevant to Postcombustion CO2 Capture. *Energy & Fuels* **2011,** *25*, 2416-2425.

(31) Tailor, R.; Abboud, M.; Sayari, A. Supported Polytertiary Amines: Highly Efficient and Selective SO2 Adsorbents. *Environmental Science & Technology* **2014,** *48*, 2025-2034.

(32) Tailor, R.; Ahmadalinezhad, A.; Sayari, A. Selective removal of SO2 over tertiary amine-containing materials. *Chemical Engineering Journal* **2014,** *240*, 462-468.

(33) Zhi, Y.; Zhou, Y.; Su, W.; Sun, Y.; Zhou, L. Selective Adsorption of SO2 from Flue Gas on Triethanolamine-Modified Large Pore SBA-15. *Ind. Eng. Chem. Res.* **2011,** *50*, 8698-8702.

(34) Tailor, R.; Sayari, A. Grafted propyldiethanolamine for selective removal of SO2 in the presence of CO2. *Chemical Engineering Journal* **2016,** *289*, 142-149.

(35) Hallenbeck, A. P.; Kitchin, J. R. Effects of O2 and SO2 on the Capture Capacity of a Primary-Amine Based Polymeric CO2 Sorbent. *Industrial & Engineering Chemistry Research* **2013,** *52*, 10788-10794.

(36) Diaf, A.; Garcia, J. L.; Beckman, E. J. Thermally reversible polymeric sorbents for acid gases: CO2, SO2, and NOx. *Journal of Applied Polymer Science* **1994,** *53*, 857-875.

(37) Bollini, P.; Didas, S. A.; Jones, C. W. Amine-oxide hybrid materials for acid gas separations. *Journal of Materials Chemistry* **2011,** *21*, 15100-15120.

(38) Yue, M. B.; Chun, Y.; Cao, Y.; Dong, X.; Zhu, J. H. CO2 Capture by As-Prepared SBA-15 with an Occluded Organic Template. *Advanced Functional Materials* **2006,** *16*, 1717-1722.

(39) Son, W.-J.; Choi, J.-S.; Ahn, W.-S. Adsorptive removal of carbon dioxide using polyethyleneimine-loaded mesoporous silica materials. *Microporous and Mesoporous Materials* **2008,** *113*, 31-40.

(40) Holewinski, A.; Sakwa-Novak, M. A.; Jones, C. W. Linking CO2 Sorption Performance to Polymer Morphology in Aminopolymer/Silica Composites through Neutron Scattering. *Journal of the American Chemical Society* **2015,** *137*, 11749-11759.

(41) Guanghui, Z.; D., H. C.; Yang, L.; Souryadeep, B.; Uma, T.; L., J. M.; Zili, W.; S., S. D.; Sankar, N.; W., J. C.; P., L. R. Engineering Porous Organic Cage Crystals with Increased Acid Gas Resistance. *Chemistry – A European Journal* **2016,** *22*, 10743-10747.

(42) Didas, S. A.; Choi, S.; Chaikittisilp, W.; Jones, C. W. Amine–Oxide Hybrid Materials for CO2 Capture from Ambient Air. *Accounts of Chemical Research* **2015,** *48*, 2680-2687.

(43) Zhu, G.; Liu, Y.; Flores, L.; Lee, Z. R.; Jones, C. W.; Dixon, D. A.; Sholl, D. S.; Lively, R. P. Formation Mechanisms and Defect Engineering of Imine-Based Porous Organic Cages. *Chemistry of Materials* **2018,** *30*, 262-272.

CHAPTER 6. MOLECULARLY-MIXED COMPOSITE MEMBRANES FOR ADVANCED SEPARATION PROCESSES

Compared to their extended framework counterparts, such as zeolites and metal-organic frameworks (MOFs), POCs offer the distinct advantage of solution processability. Moreover, when fabricated into mixed-matrix membranes (MMMs), the soluble POC molecules have the potential to exhibit intimate molecular-level mixing with the matrix polymer. POCs have only recently been incorporated into mixed matrix membrane materials, but this process has not yet resulted in significant improvements of membrane performance. In this work, we utilize vertex functionalized amorphous scrambled porous organic cages (ASPOCs) as membrane performance enhancers and show that the dispersion of ASPOC mixtures possessing different crystallization tendencies (amorphous and semi-crystalline) within a polymer matrix greatly impacts the molecular mixing within the membranes. Semi-crystalline ASPOC mixtures form particle aggregates within the polymer matrix that resemble traditional MMMs (i.e., a discrete particles dispersed within a matrix phase), whereas the amorphous ASPOC mixtures, on the other hand, are observed to distribute throughout the matrix without any indication of particle formation or agglomeration, creating unique, mixed-matrix membranes with enhanced separation performance. Molecular mixing is evidenced by both glass transition analysis and positron annihilation lifetime spectroscopy. A 340 % permeability increase is observed for N_2, CO_2, and CH_4 in the molecularly-mixed ASPOC membranes compared to the pure polymer membrane.

Moreover, an apparent molecular sieving effect is observed for SF_6, resulting in a 150 % increase in N_2/SF_6 selectivity compared to the pure polymer membrane. Both permeability and selectivity improvement are achieved in industrially-relevant gas separations. On the other hand, the traditional MMMs formed from semi-crystalline ASPOC revealed only a 51 % increase in N_2/SF_6 selectivity improvement relative to the pure polymer membranes. The amorphous ASPOC membranes are also shown to exhibit unprecedented performance in organic solvent nanofiltration separations, with over 95 % rejection of poly(styrene) solutes with molecular weights ranging from 200 to 1800 Dalton. In contrast, the semi-crystalline ASPOC MMMs show only marginal improvement from the pure polymer membrane. Overall, we show that membranes based on non-particle forming ASPOC materials result in homogeneous mixing between the ASPOC molecules and the polymer matrix, which results in significant increases in both membrane permeability and selectivity, offering new avenues for creation of membranes with unique properties in industrially relevant separations.

6.1 Introduction

Membrane separations are promising alternatives for thermally-driven industrial separation processes.[1] Despite being eminently scalable, existing and emerging polymer membranes suffer from a tradeoff between permeability and selectivity, which are among the defining performance metrics for membranes.[2] Inorganic membranes such as zeolites and metal-organic frameworks (MOFs) have surpassed this trade-off and have shown extraordinary separation performances in challenging molecular pairs.[3-5] However, the preparation of large-scale, defect-free inorganic membranes suitable for industrial applications remains a challenge. Mixed matrix membranes (MMM) incorporate inorganic

filler materials (i.e., the "discrete" phase) into a polymer (i.e., the continuous phase or the "matrix") to boost the performance of the membranes while retaining the intrinsic scalability of polymer processing. These materials have long been proposed to address the orthogonal issues associated with polymer membranes and inorganic membranes.[6-7] The area of mixed matrix membranes originated with the study of the addition of zeolite materials to polymer phases before experiencing a resurgence in research interest with the advent of metal-organic frameworks (MOFs)-based MMMs.[8-9]

The purely organic nature of the POC materials suggests that these materials may solve one of the longstanding issues in MMM formation, namely, the propensity for the formation of defect pathways (i.e., "gaps") between the discrete phase and the matrix phase.[10] Doonan et al. have computationally evaluated the use of POC materials as fillers in MMMs using Grand canonical Monte Carlo (GCMC) and molecular dynamics (MD) simulations to estimate guest sorption and diffusion coefficients in the POC and concluded some POC-containing MMMs could exhibit enhanced selectivity and permeability.[11] Experimental explorations of MMMs involving POCs have been reported, where CC3-R (a prototypical POC material) molecules were *in situ* crystallized within the composite membrane from a solution of CC3-R and PIM-1.[12] The incorporation of POCs showed significant permeability increase and better resistance to physical aging, but no enhancements in selectivity. Waterwheel-shaped POC Noria derivatives were reported as a filler in poly(imide) membranes, which resulted in only minor performance increases as a result of the pore size of Noria being larger than most gas molecules.[13]

In addition to only showing limited performance improvement, the existing examples of experimental MMMs involving POCs have so far only demonstrated the

formation of classic MMM structures, i.e., the formation of a discrete particle phase and a continuous matrix phase (likely as a result of the crystallization tendency of traditional POC molecules). However, a potential advantage of the POC material is the promise of achieving truly molecular mixing between polymer chains and individual cage molecules, thus bypassing the issue of interfacial interactions between matrix and particle phases altogether. Addressing the propensity for the POC molecules to crystallize is critical to realizing this unique advantage.

A subset of POCs was recently developed using the concept of mixed-linker synthesis and exchange.[14] The different linker functionalities at the cage vertices were found to reduce the interactions between individual cages, which enabled the cages to pack amorphously in the solid phase—these new types of POC materials were named "amorphous scrambled porous organic cages" (ASPOCs). The decreased inter-cage interactions also increased the solubility of ASPOCs in certain solvents, which is advantageous for fabricating MMMs with high loadings of the ASPOC material. Song et al. utilized a solution-based spin coating technique to fabricate a uniform ASPOC layer on a porous support, which was successfully utilized in proof-of-concept gas separation experiments.[15]

Here, we demonstrate that ASPOCs can form homogeneous composites with polymer materials to form molecularly-mixed composite membranes, which have the potential to be used in a wide range of separation applications including gas separation and organic solvent nanofiltration (OSN) separation modalities. We find that these molecularly-mixed composite membranes dramatically increase gas separation performance (both permeability and selectivity) for gas pairs in which the larger gas cannot

access the ASPOC pore space. Moreover, we find that solvent permeability and solute rejection both increase in OSN separation with alcohol-poly(styrene) solvent-solute systems.

6.2 Experimental

6.2.1 Materials

Triformylbenzene was purchased from Manchester Organics. Anhydrous dichloromethane, chloroform, ethylenediamine, (1R,2R)-1,2-cyclohexanediamine, branched PEI (Mw ~800), poly(styrene) (Mw ~200,000 by GPC) were purchased from Sigma Aldrich. Ethyl acetate and diethyl ether were purchased from BDH Chemicals. Formic acid, 38% formaldehyde solution, potassium hydroxide pellets, and magnesium sulfate were purchased from Alfa Aesar. Ultra-high purity N_2 and CO_2 gas cylinders were purchased from Airgas. Certified standard grade cylinders of 200 ppm SO_2 with a balancing of N_2 were purchased from Matheson Trigas. All chemicals were used as received without any purification.

6.2.2 Synthesis of ASPOC

The synthesis of the ASPOC $CC1_x3_y$ (the subscripts denote the starting composition of the synthesis solution—*x* equivalents of ethylenediamine (the linker for CC1) and *y* equivalents of (1R,2R)-1,2-cyclohexanediamine (the linker for CC3-R)) (Figure 6.1 shows $CC1_43_2$ as an example) was carried out similar to the procedure described in Chapter 5. In this chapter, $CC1_43_2$ and $CC1_13_5$ were synthesized and used as representatives from both amorphous filler and crystalline filler in the membrane fabrication and test.

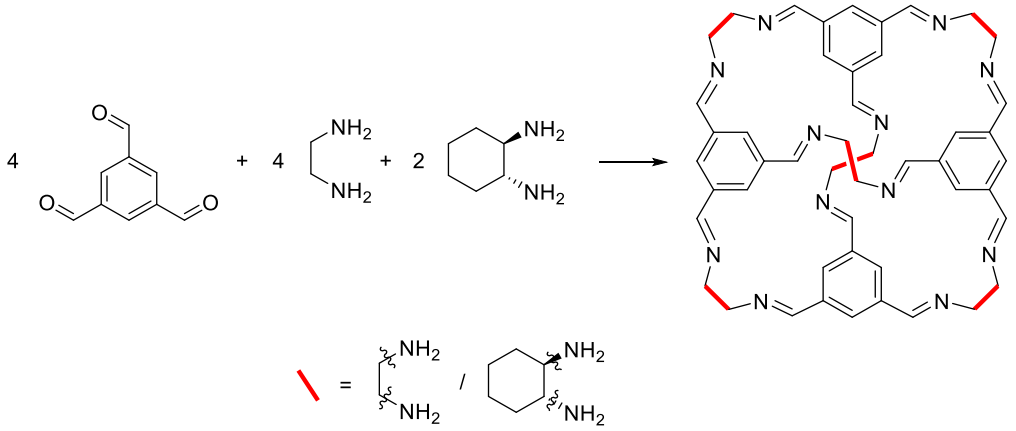

Figure 6.1 Synthesis of ASPOC $CC1_43_2$ from 4 equivalents of triformylbenzene, 2 equivalents of ethylenediamine and 4 equivalents of (1R,2R)-1,2-cyclohexanediamine; which results in the formation of a mixture of cages

6.2.3 Membrane Preparation

The membrane preparation is simplified compared to normal mixed matrix membrane formation as a result of the solubility of the ASPOC molecules (Figure 6.2). In this work, we chose chloroform as it can dissolve both the ASPOC molecules and the polymers (Matrimid® and poly(styrene), Figure 6.3) and resulted in a good-quality membrane. In general, the desired amount of ASPOC and polymer were dissolved in 5 mL anhydrous chloroform. The solutions were passed through a 200 nm syringe filter to remove any insoluble impurities and then poured into PTFE Petri dishes (Dynalon®) in a glove bag pre-saturated with chloroform. After 8 to 12 hours the Petri dishes were taken out from the glove bag, and the membranes were observed to exfoliate from the plate spontaneously. The membranes were dried at 80 ºC under vacuum (29 in.Hg to remove residual solvent and for Matrimid membranes annealed at 200 ºC under vacuum.

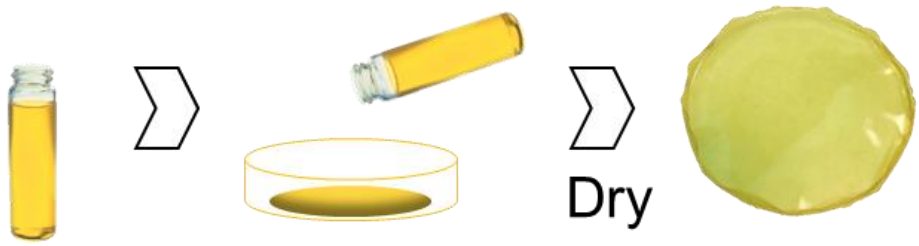

Figure 6.2 Membrane preparation procedure based on casting a pure liquid phase solution

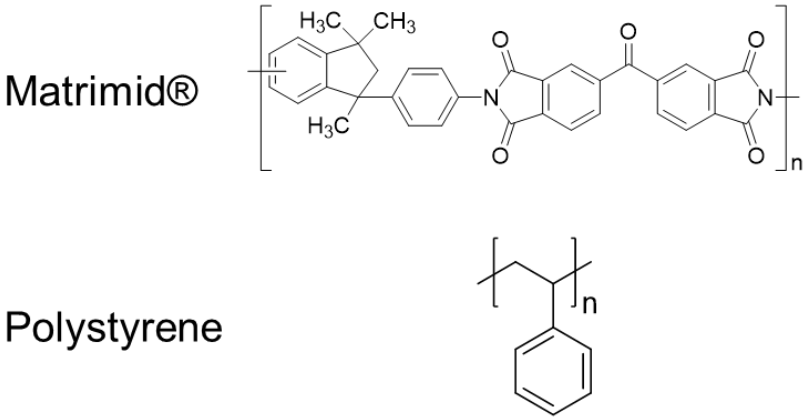

Figure 6.3 Structure of polymers used in the membrane fabrication

6.2.4 Characterization Methods

6.2.4.1 Thermogravimetric Analysis (TGA)

The thermostability of polymer and composite materials was probed on a TA Instruments Q500 TGA. The samples were heated to the desired temperature at 5 ºC/min under a flow of N_2 and held for 9 h.

6.2.4.2 Differential Scanning Calorimetry (DCS)

Polymer glass transitions were measured with a TA Q200 Differential Scanning Calorimeter in a nitrogen atmosphere (50 mL/min) with a heating/cooling rate of 10 ºC/min. For each measurement, 3–5 mg flat membrane was cut into small pieces around

2×4 mm and filled into a DSC pan. Each sample was scanned for three cycles and the second cycle was used for plotting. The onset T_g was calculated from the cross point of the tangent on the initial straight line before baseline shifting and the tangent on the slope. The midpoint T_g was calculated as the maximum of the 1st order derivative of heat flow during glass transition.

6.2.4.3 NMR

Solution ^1H NMR spectra in $CDCl_3$ were recorded at 400.13 MHz using a Bruker Avance III 400 NMR spectrometer.

6.2.4.4 Scanning Electron Microscopy (SEM)

High-resolution imaging of the composite morphology was achieved using a Hitachi SU8230 Cold Field Emission Scanning Electron Microscope (CFE-SEM). The dry samples were attached to aluminum stubs using copper tape. The samples were then coated with a 20 nm layer of gold/palladium using a Hummer 6 Gold/Palladium Sputterer. Imaging was taken at a working distance of 8 mm and a working voltage of 3 kV using a mix of upper and lower secondary electron detectors.

6.2.4.5 Gas Sorption Analysis

The porosity of the materials was assessed via nitrogen physisorption at 77 K using a Micromeritics ASAP2020HD. Surface areas were calculated from the data using the Brunauer–Emmett–Teller (BET) method. CO_2 isotherms were collected from the same equipment at 308 K.

6.2.4.6 Positron Annihilation Lifetime Spectroscopy (PALS)

PALS measurements were performed at room temperature by using a conventional sample-source-sample sandwich geometry at Oak Ridge National Laboratory. The positron source was made from a ^{22}NaCl solution evaporated onto the surface of the samples with a radioactive dose of 20 μCi. The stacked two identical membranes were wrapped by thin Al foil to generate a sample assembly. The characteristic gamma rays were detected by using BaF_2 fast scintillators. Positron lifetime spectrum was collected by using a digital oscilloscope with a system time resolution of 160 ps. Data analysis was performed using PALSfit3.[16]

6.2.4.7 Energy-dispersive X-ray Spectroscopy (EDX)

Carbon and nitrogen elemental mapping of polystyrene membranes was conducted on a Hitachi SU8230 cold field emission (FE)-SEM equipped with an Oxford Instruments 80 mm^2 X-Max energy dispersive X-ray (EDX) detector. The flat membranes were attached to aluminum stubs using copper tape. The samples were then coated with carbon using a Quorum Q-150T ES gold/carbon coater.

6.2.4.8 Raman Mapping

Raman mapping of Matrimid membranes was conducted on a Thermo Nicolet Almega XR Dispersive Raman Spectrometer equipped with an optical microscope. A 488 nm laser was used as the incident. Raman spectra were taken over a membrane area of 100 × 100 μm with a resolution of 5 μm. The Matrimid has a characteristic shift at 1650 cm^{-1}. And ASPOC molecules has various characteristic shifts at 1785 cm^{-1}, 1678 cm^{-1}, 1621 cm^{-1}, and 1378 cm^{-1}. The relative intensity (all spectra normalized to Matrimid peak at 1650 cm^{-1}) of 1678 cm^{-1} was overlayed on the optical image of the membrane surface.

6.2.5 Gas Permeation Tests

Gas permeation performance of the membranes was evaluated on a constant-volume/variable-pressure single gas permeation system (Figure 6.4). The annealed membranes were cut into disks with 3.81 cm diameter and mounted on the sample cell with aluminum tape with 5.08 cm diameter and a 2.54 cm diameter hole in the center. The inner edge was sealed with epoxy (DP100 Plus from McMaster). After the epoxy was cured, the cell was closed with a torque of 45 pound-ft. Membrane upstream, downstream and gas reservoirs were evacuated overnight with an Edwards vacuum pump to less than 0.05 Torr. After evacuation, the upstream and gas reservoir was isolated by closing the gas dosing valve. The gas reservoir was charged to the desired pressure with pure gas and allowed for thermal equilibration for 10 min. The gas dosing valve was then opened, and the downstream pressure was logged with a LabVIEW program. The system leak rate was measured using a closed dosing valve and evacuated downstream for each membrane and was found to be < 2 % of the gas fluxes measured (except a rate of < 40 % for SF_6).

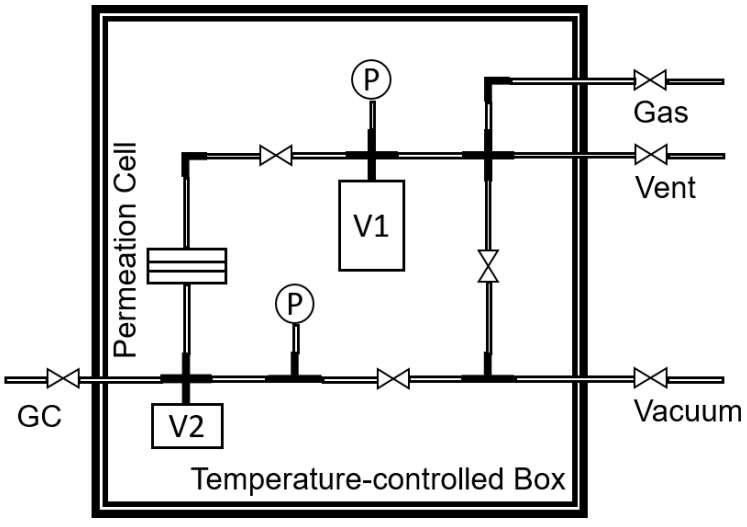

Figure 6.4 Schematic of the permeation system used for the single gas permeability measurements

The permeability of the membrane is calculated according to the following equation:

$$P_i = \frac{(flux)_i \cdot \ell}{\Delta P} = \left[10^{-10} \cdot \frac{cm^3(STP) \cdot cm}{cm^2 \cdot s \cdot cmHg}\right] \quad (6.1)$$

Membrane area A was calculated with ImageJ® on optical images of the membranes. Membrane thicknesses ℓ were measured with a Peacock dial thickness gauge for 10 times.

The ideal selectivity of two gases i and j was calculated as the ratio of the permeabilities of the gases.

$$S_{i/j} = \frac{P_i}{P_j} \quad (6.2)$$

6.2.6 Liquid Permeation Tests

The membrane's performance in organic solvent nanofiltration separations was evaluated according to membrane permeabilities and molecular weight cut off (MWCO) curves. All nanofiltration experiments were carried out at 30 bar using a cross-flow filtration system (Figure 6.5).

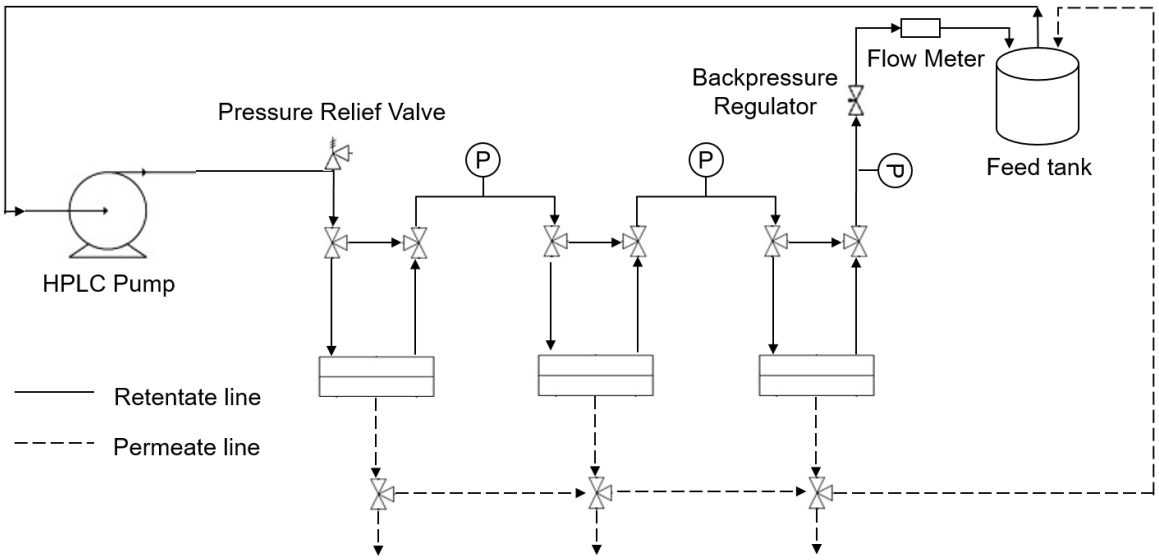

Figure 6.5 Schematic of the cross-flow system used for organic solvent nanofiltration measurement

The effective membrane area was 14 cm^2, and with a feed flow of 0.6 L h^{-1}.(stage cut < 1 %) Permeate samples for flux measurements were collected for around 12 h, and samples for rejection evaluations were taken after steady permeate flux was achieved. The MWCO was determined by interpolating from the plot of rejection against molecular weight of marker compounds and corresponds to the molecular weight for which rejection is 90%. The solute rejection test was carried out using two standard solutions. The first was a standard feed solution comprised of a homologous series of styrene oligomers (PS) dissolved in the selected solvent. The solvents used were MeOH. The styrene oligomer mixture contained 2 g L^{-1} each of PS 580 and PS 1090 (Polymer Labs, UK), and 0.01 g L^{-1} of the α-methylstyrene dimer (Sigma-Aldrich, UK). Analysis of the styrene oligomers was undertaken using an Agilent HPLC system with UV/Vis detector set at a wavelength of 264 nm. Separation was achieved using a reverse phase column (C18–300, 250×4.6 mm). The mobile phase flow rate is 0.5 mL/min. The composition of the mobile phase is a ramp from 35 vol% analytical grade water and 65 vol% tetrahydrofuran with 0.1 vol%

trifluoroacetic acid to 20 vol% analytical grade water and 80 vol% tetrahydrofuran with 0.1 vol% trifluoroacetic acid in 30 min.

Solvent flux (J) was determined by measuring permeate volume (V) per unit area (A) per unit time (t) according to the following equation:

$$J = \frac{V}{A \times t} \tag{6.3}$$

The hydraulic solvent permeability was calculated as follows:

$$P_i = \frac{J \cdot l}{\Delta P} = [L\, m^{-2}\, h^{-1} bar^{-1}\, \mu m] \tag{6.4}$$

The rejection (R_i) of markers was calculated from Eq. (6.5), where $C_{P,i}$ and $C_{F,i}$ correspond to marker concentrations in the permeate and the feed, respectively.

$$R_i = \left(1 - \frac{C_{P,i}}{C_{F,i}}\right) \times 100\% \tag{6.5}$$

6.3 Results and Discussions

6.3.1 Membrane Morphology

A critical step in the formation of molecularly-mixed composite membranes is the creation of homogeneous polymer solutions and membranes during the membrane preparation and fabrication process. The solubility of ASPOCs in solvents typically utilized for membrane fabrication greatly simplifies the preparation of the molecularly-mixed composite membranes relative to traditional mixed-matrix membrane preparation using particle fillers. The dope preparation for the latter usually involves extended sonication to break the aggregation of particles and to aid in the dispersion of the particles within the

polymer solution; moreover, surface functionalization of the particles is sometimes required to promote adhesion between the polymer and the filler in the solid state.[17] In the case of ASPOC-containing mixed-matrix membranes, the dope is a homogeneous solution after mild mixing (for example, sonicate for 1 min). As a result of this unique feature, the preparation of ASPOC-loaded mixed matrix membranes does not deviate from existing, commercial polymer membrane fabrication techniques, which suggests a lower barrier for scale-up of these materials compared to traditional MMMs.

A particular challenge associated with the formation of ASPOC-loaded membranes is the propensity of the ASPOC molecules to interact in solution and precipitate as solid particles. In the polymer-ASPOC solutions utilized to prepare the membranes, polymer-cage interactions and cage-cage interactions compete to affect the microstructure of the resulting ASPOC-loaded membranes. For example, CC3-R/PIM-1 mixed-matrix membranes prepared from homogeneous solutions of polymer and CC3-R molecules resulted in the formation of CC3-R crystals within the PIM-1 matrix, which can be attributed to the CC3-R cage-cage interactions being much stronger than the PIM-1-cage interactions.[12] On the other hand, ASPOCs are mixtures of cages bearing mixed vertex functionality, and differing starting ratios between ethylenediamine and cyclohexanediamine will result in cage mixtures with different cage distribution (Figure 6.6) and crystallinity (Figure 5.5).

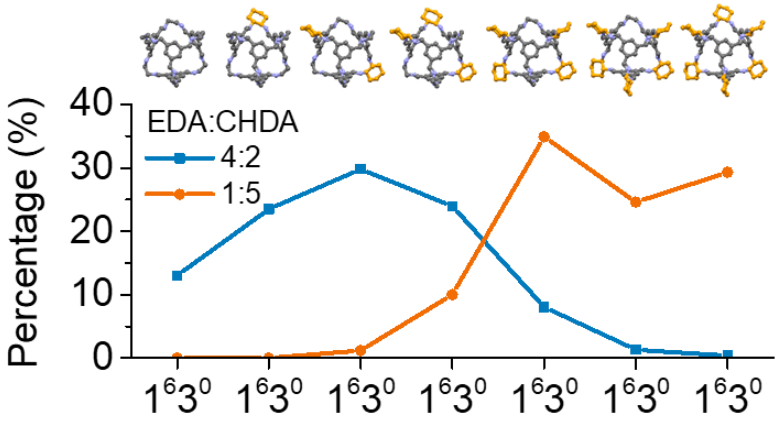

Figure 6.6 ASPOC cage mixtures synthesized from different ratios of ethylenediamine (EDA) and cyclohexanediamine (CHDA).

*Cage ratios are calculated from HPLC peak areas[14]

For example, $CC1_13_5$ mixtures are decorated with an abundance of cyclohexane moieties around each cage. As a result, $CC1_13_5$ cages show higher crystallinity when precipitated from solution when compared against $CC1_43_2$, the former of which forms four-pointed-star-shaped particles within the MMM (Figure 6.7j). By using ASPOC mixtures with low crystallinity—in this case, $CC1_43_2$—the cage-cage interaction can be suppressed during membrane formation. As shown in Figure 6.7, no particle formation or phase separation can be observed for membranes with $CC1_43_2$ loadings up to 20%, and largely resemble the pure Matrimid® membranes (Figure 6.7g) at these magnifications.

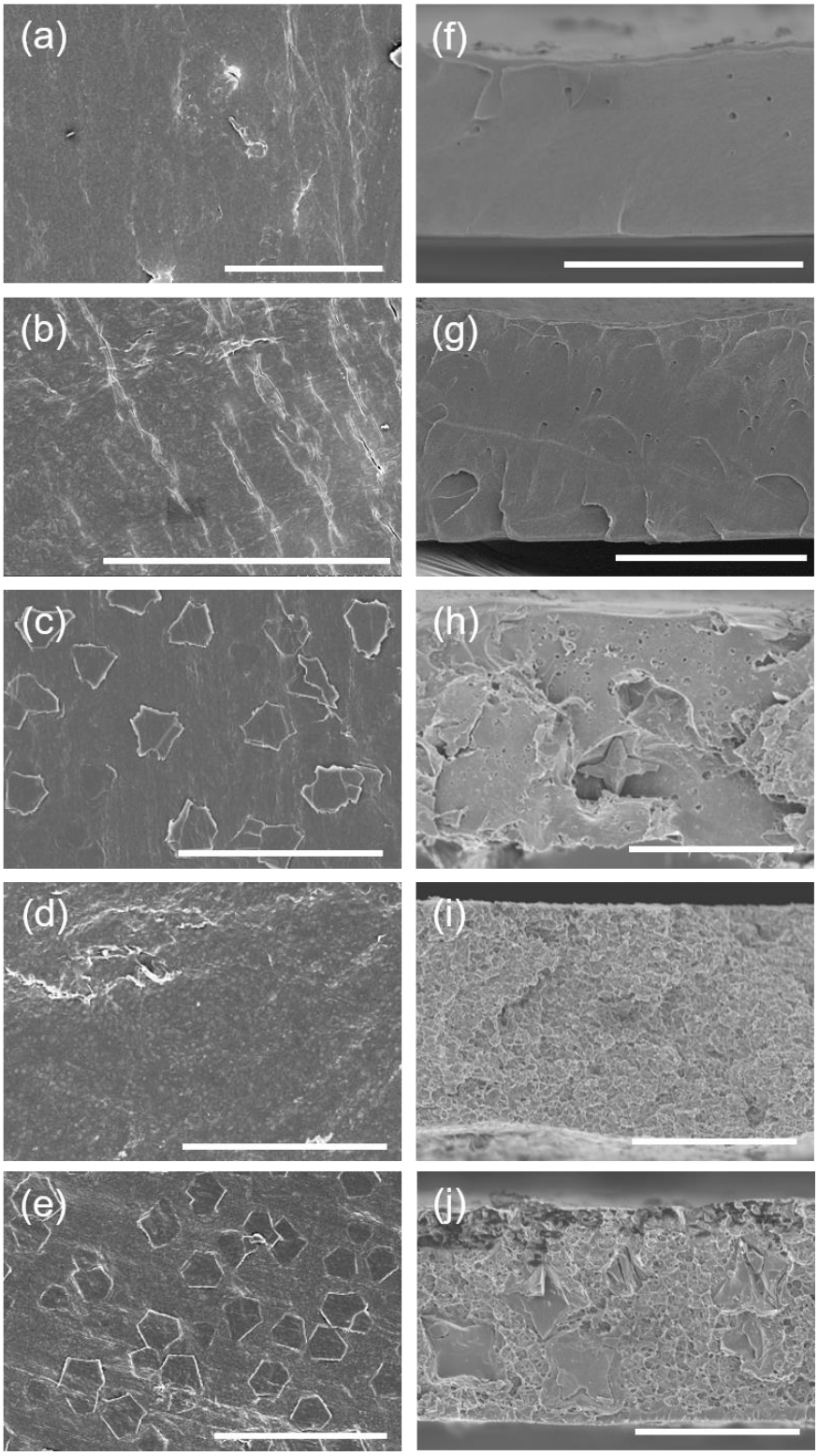

Figure 6.7 Surface (a-e) and cross section (f-J) SEM images of Matrimid (a, f), 10 wt% $CC1_43_2$ (b, g), 10 wt% $CC1_13_5$ (c, h), 20 wt% $CC1_43_2$ (d, i) and 20 wt% $CC1_13_5$ (e, j). Scale bars in all images are 30 µm

6.3.2 Cage Distribution in Membranes

The cage distribution in the Matrimid®-based membranes was initially investigated with EDX. However, Matrimid® and the ASPOC mixtures have the same elemental make-up, i.e., are comprised of carbon, nitrogen, and hydrogen. To probe the distribution of the ASPOC materials within polymer materials, we prepared one set of ad hoc membranes using poly(styrene) as the matrix, which enables EDX mapping of elemental nitrogen that exists only in the ASPOCs (Figure 6.8). For $CC1_4 3_2$-based membranes, elemental nitrogen is distributed throughout the membrane surface evenly. For $CC1_1 3_5$-based membranes, the ASPOC particles in the polymer can be easily seen from the surface image (Figure 6.8e). As can be observed in Figure 6.8 b and d, the elemental nitrogen elements are localized at particle protrusions and also appear throughout the membrane surface. In addition to the morphological information obtained from SEM imaging, EDX mapping provides additional and supporting information to probe the ASPOC distribution. These measurements suggest that the $CC1_4 3_2$ materials are distributed homogeneously throughout the membranes, while the $CC1_1 3_5$ materials form observable particles within the membranes. We hypothesize that this is a result of differences in cage-cage and cage-polymer interactions between the two materials.

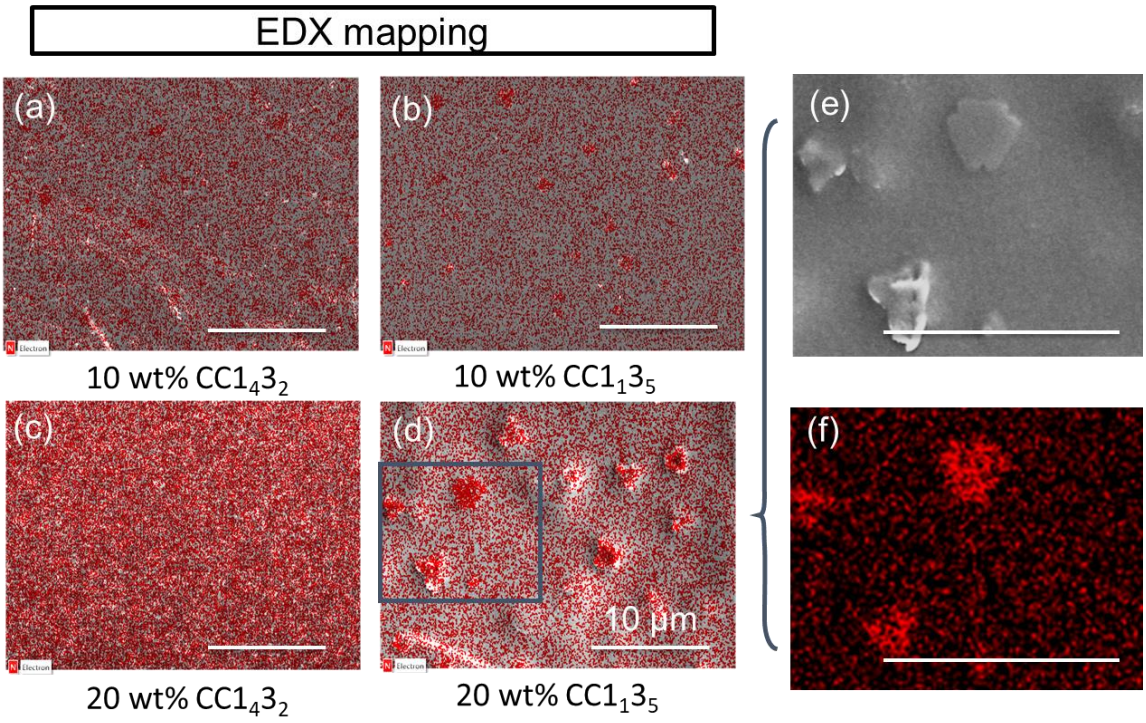

Figure 6.8 (a-d) EDX mapping of elemental nitrogen in mixed-matrix poly(styrene) membranes containing different mass fractions of CC1$_4$3$_2$ and CC1$_1$3$_5$. The red color indicates elemental nitrogen intensity, and these are overlaid on SEM images of the membrane surface. (e) and (f) magnified images of highlighted regions in (d) with separated SEM and elemental mapping signals

The cage distribution was further probed with Raman mapping in as-prepared Matrimid®-based membranes. Matrimid® and the ASPOC materials have different Raman shifts (Figure 6.9), which enables us to map the normalized intensity (relative to the 1621 cm^{-1} Matrimid® peak) of 1651 cm^{-1} ASPOC peak over the membrane surface.

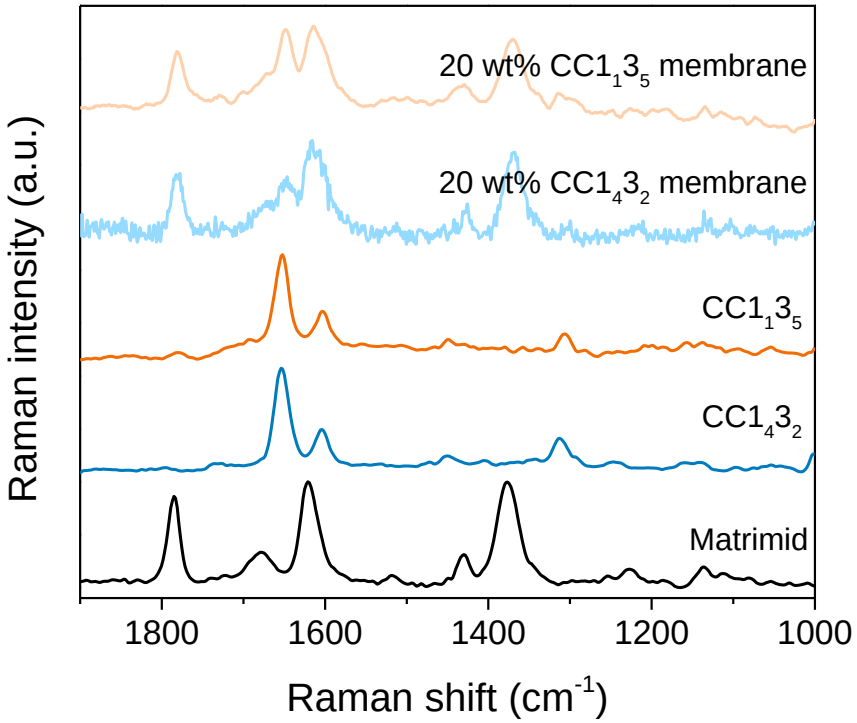

Figure 6.9 Raman shifts of Matrimid®, two types of ASPOCs, and selected high loading membranes

The Raman mapping was carried out on a Raman spectrometer coupled with an optical microscope, allowing the intensity map to be overlaid on the surface optical image. The molecularly-mixed composite membranes (loaded with $CC1_43_2$ molecules) are transparent, which positions Raman mapping as a robust method for assessing the distribution of the ASPOC materials within the polymer matrix. As shown in Figure 6.10 a-f, the 20 wt% $CC1_13_5$ Matrimid® MMMs show good agreement between the local intensity maximums and the crystal location from the optical images. This coherence confirms homogeneous ASPOC distribution in other membranes—$CC1_43_2$ at both loadings and $CC1_13_5$ at low loading. The absence of such intensity localization in Figure 6.10 a-c

suggests that there is no aggregation of the ASPOCs formed in the case of $CC1_43_2$ at both loadings, but aggregation is observed in $CC1_13_5$ at high loading.

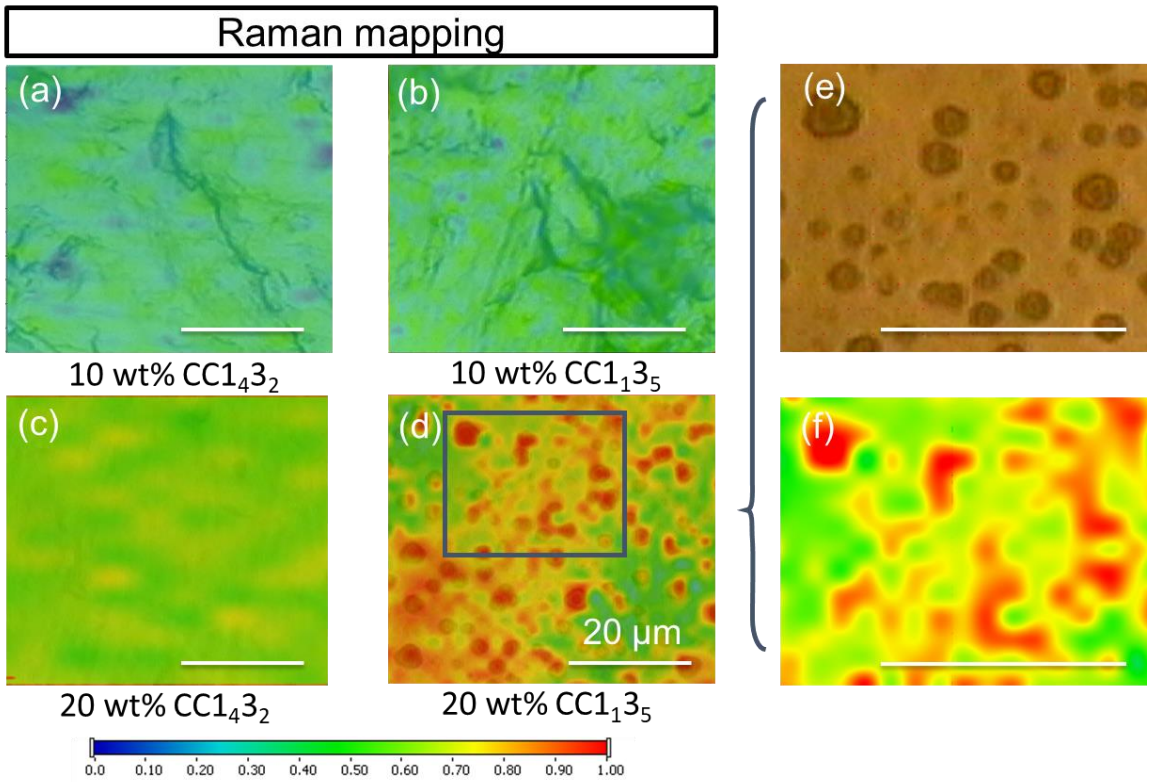

Figure 6.10 (a-d) Raman mapping of the relative intensity of 1384 cm^{-1} peak corresponding to the ASPOC materials at different mass fractions within the membranes. The color mapping is overlaid on the corresponding optical image. (e) and (f) magnified images of highlighted regions in (d) with separated optical and Raman intensity mapping

6.3.3 DSC Evidence for the Formation of "Solid Solutions" Between $CC1_43_2$ and Matrimid®

The miscibility between the ASPOC and the polymer chains was probed by measuring the glass transition temperature (T_g) of the composite membrane using differential scanning calorimetry (DSC). The onset and midpoint T_g are calculated according to the procedure described in the methods section and are shown in Figure 6.11.

The inclusion of crystalline $CC1_13_5$ filler caused a slight increase (~1.6 °C) in the onset and midpoint T_g as well as a broadened glass transition region. This minimal change in the T_g is typical for MMMs with no significant interaction between polymer and filler.[18] In contrast, the $CC1_43_2$ fillers resulted in more significant changes to the observed glass transition behavior of Matrimid®, with an increase of 9~11 °C to both the onset and midpoint T_g. Moreover, a single T_g was observed in all cases. The combination of SEM, EDX, Raman and DSC results provides substantial evidence that the $CC1_43_2$ and Matrimid® form solid solutions and the ASPOC material can be thought of as molecularly-mixed with the Matrimid® chains.

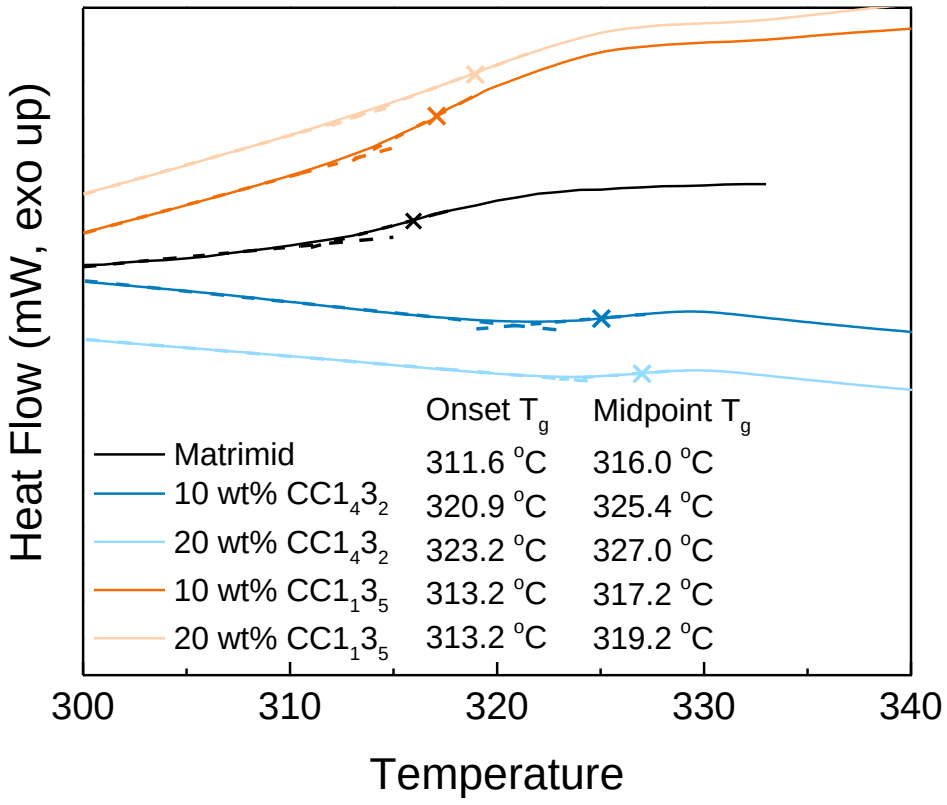

Figure 6.11 DSC curves for neat Matrimid® and ASPOC-loaded composite membranes

6.3.4 *Measurements of Porosity of the Membranes by Physisorption and Positron Annihilation Lifetime Spectroscopy*

The porosity and pore accessibility of the Matrimid® and the MMMs were analyzed using CO_2 physisorption at 35 ºC (Figure 6.12). Pure Matrimid® exhibited a CO_2 uptake of 0.46 mmol/g at 1 bar, while incorporation of the ASPOC molecules increased the CO_2 uptake. Interestingly, the 20 wt% $CC1_13_5$ membrane presented a much higher CO_2 uptake than other samples. We attribute this to the large external volume available in this crystal-containing membrane that resulted from inefficient packing of the cages.[19]

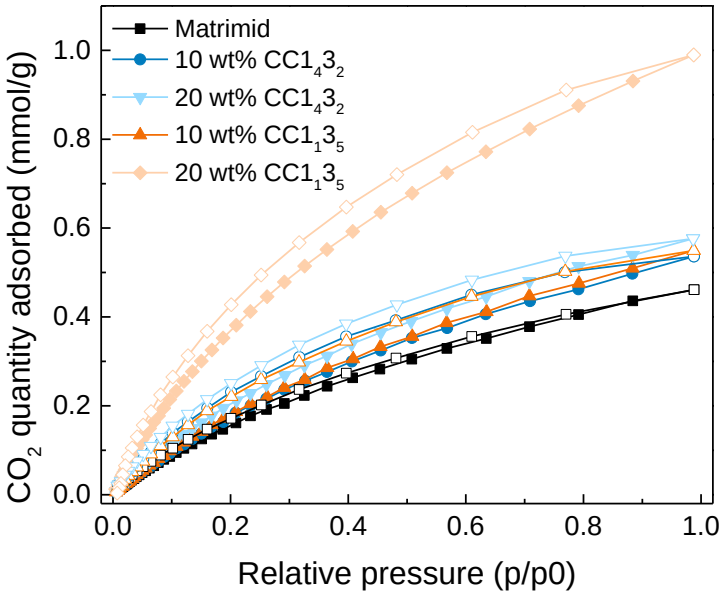

Figure 6.12 CO_2 physisorption isotherms for Matrimid ® and ASPOC-loaded composite membranes at 35 ºC

The pore sizes of the membranes were further analyzed using positron annihilation lifetime spectroscopy (PALS). PALS is a well-established technique to characterize pores in polymers, relying on the fact that ortho-positronium (o-Ps), a parallel spin complex of a

positron and an electron, is generated within low electron density regions (e.g., empty cavities). Positron lifetime is defined as the time interval between the characteristic gamma-ray (1.274 MeV) accompanied with the generation of positrons during the decay process of Na^{22} and the annihilation gamma rays (0.511 MeV). The o-Ps lifetime and its intensity are associated with the size and concentration of the pores, respectively. Compared to pore size distribution calculated from gas physisorption measurements, PALS offers nanoscale detection limits and probe-molecule independent assessments of porosity. Positron lifetimes corresponding to various trapping states were extracted by using 3-component lifetime fitting (Figure 6.13-Figure 6.17).[20]

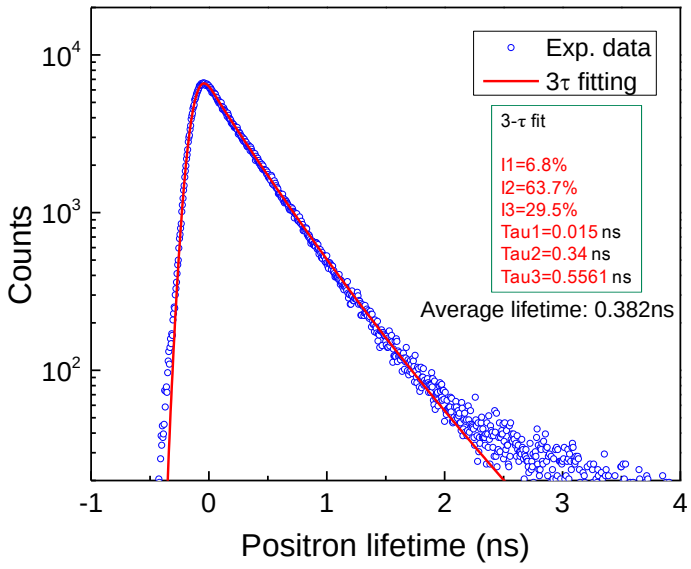

Figure 6.13 3-component lifetime fitting of PALS spectra of Matrimid®

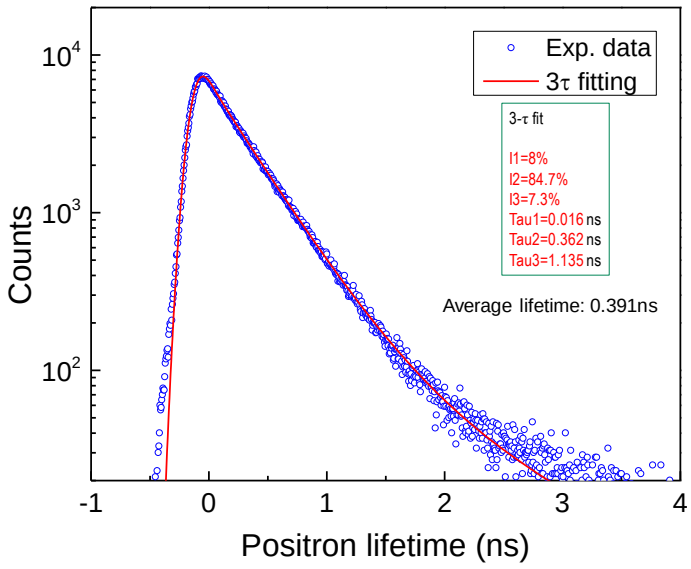

Figure 6.14 3-component lifetime fitting of PALS spectra of 10 wt% $CC1_43_2$ membrane

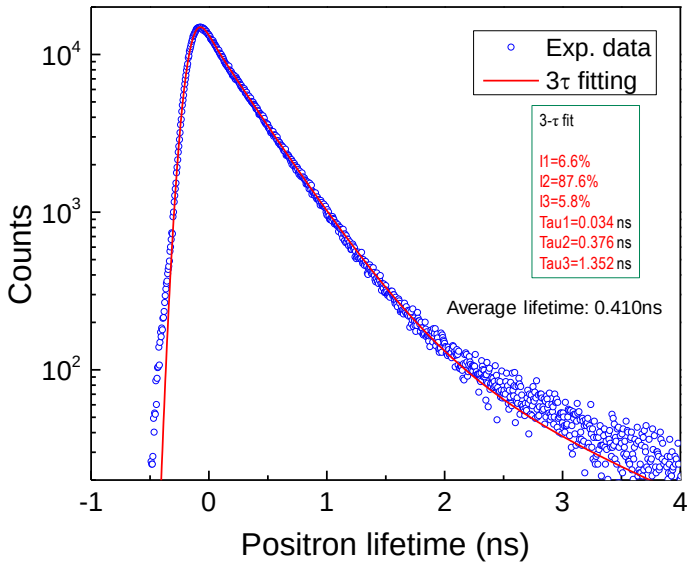

Figure 6.15 3-component lifetime fitting of PALS spectra of 10 wt% $CC1_13_5$ membrane

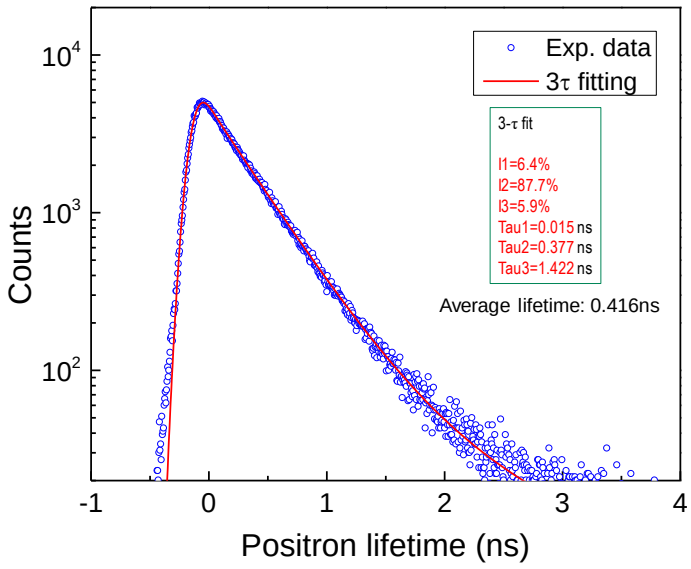

Figure 6.16 3-component lifetime fitting of PALS spectra of 20 wt% $CC1_43_2$ membrane

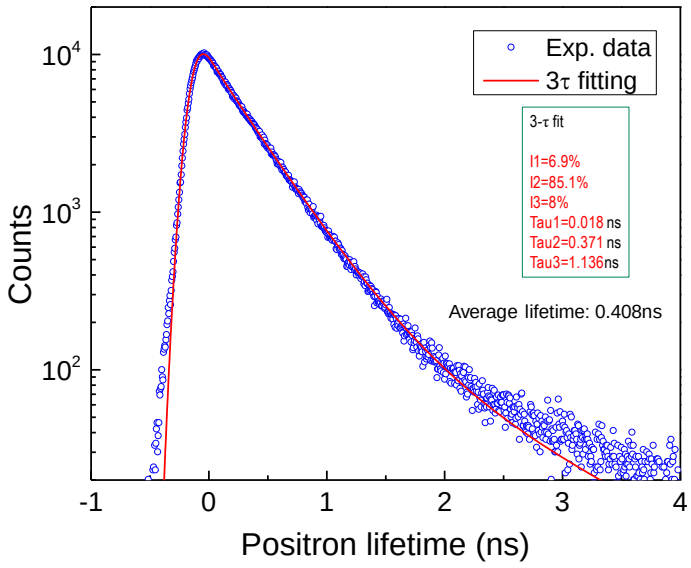

Figure 6.17 3-component lifetime fitting of PALS spectra of 20 wt% $CC1_13_5$ membrane

The o-Ps lifetime is typically related to the average radius of pores present by using the Tao-Eldrup model.[21-22] The results indicated that 3.7 Å to 4.4 Å pores exist in the ASPOC-loaded membranes (Table 6.1), which correspond well with the internal pore sizes of ASPOCs.[14] Compared to the sub-2 Å pores present in the neat Matrimid® membrane, this clearly indicates that ASPOC cages remain shape-persistent and porous when contained within the polymer membrane.

Table 6.1 PALS fitting parameters and average pore size corresponding to Tau3 of Matrimid® and composite membranes

Sample	τ_3 (ns)	Intensity (%)	Average lifetime (ns)	Average size (nm)	Relative concentration
Matrimid®	0.5561	29.5	0.382	n/a	n/a
10 wt% CC1$_4$3$_2$	1.135	7.3	0.391	0.3732	1
10 wt% CC1$_1$3$_5$	1.352	5.8	0.410	0.4320	1.32
20 wt% CC1$_4$3$_2$	1.422	5.9	0.416	0.4492	1.45
20 wt% CC1$_1$3$_5$	1.136	8.0	0.408	0.3735	1.71

6.3.5 Gas Permeation Analysis of ASPOC-loaded Membranes

The gas permeation properties of the ASPOC-loaded membranes were tested using N_2, CO_2, CH_4 and SF_6 as probe gases in a series of constant-volume/variable pressure single gas permeation experiments. We expected that the ASPOC materials would act as permeability enhancers for gases smaller than the window size of the ASPOC (3-4.5 A, Figure 6.18); i.e., N_2, CO_2, and CH_4 in Figure 6.18b. Moreover, since the window of the ASPOC material is larger than all of these gases, we expect minimal-to-negative enhancements in ideal permselectivity between pairs of these small gases. However, the SF_6 probe gas has a kinetic diameter larger than the pore-limiting envelope of the ASPOC materials. Thus we hypothesized that significant selectivity enhancements should be observed for the small gases over the large SF_6.

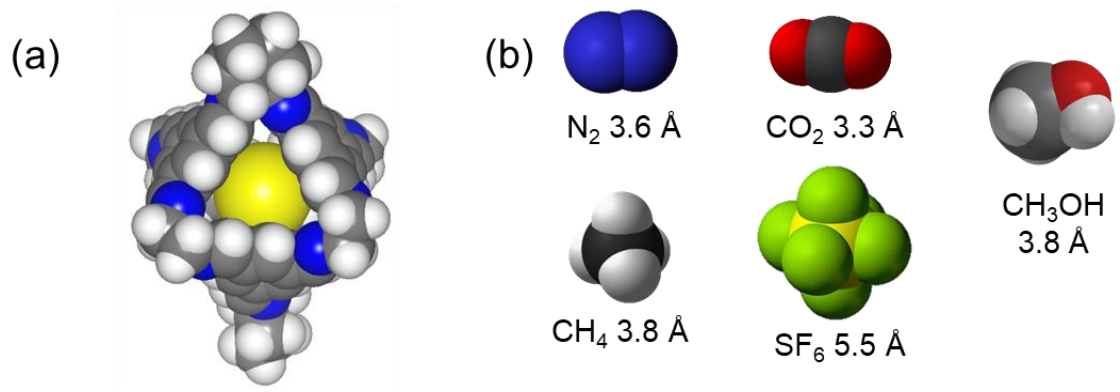

Figure 6.18 (a) Pore limiting envelope of CC1^{4}3^2 (b) gas molecules tested and their kinetic diameters

Figure 6.19 a and b show the permeation performance of the ASPOC-Matrimid® MMMs. The top chart highlights the CO_2 permeability change with respect to pure Matrimid®. A 340 % increase in CO_2 permeability was observed for the 10 wt% CC1$_4$3$_2$ molecularly-mixed composite membranes. The lower chart highlights the ideal permselectivity calculated from the single gas permeabilities for the CO_2/N_2, CO_2/CH_4 and N_2/SF_6 pairs, which are industrially-relevant separations. As expected, the permselectivity for small gas molecules is maintained or only slightly reduced, as the ASPOC does not effectively distinguish these small gases from each other. The N_2/SF_6 selectivity increased from 46±3 for the pure Matrimid® membrane to 115±11 for the 10 wt% CC1$_4$3$_2$ molecularly-mixed composite membranes. This increase is a result of increasing in the N_2 permeability and essentially maintaining the SF_6 permeability at a value similar to that found in the pure Matrimid® case. This result supports our hypothesis that molecular sieving can be achieved from the ASPOC cages in the membranes. The enhancements were not as profound in membranes with higher loadings of ASPOC materials. We speculate that at higher loadings of ASPOC, non-selective pathways may arise as a result of irregular

cage packings (i.e., window-to-arene packing). In addition, cage aggregates may introduce non-ideal interfaces in the membranes that will impair membrane performance.

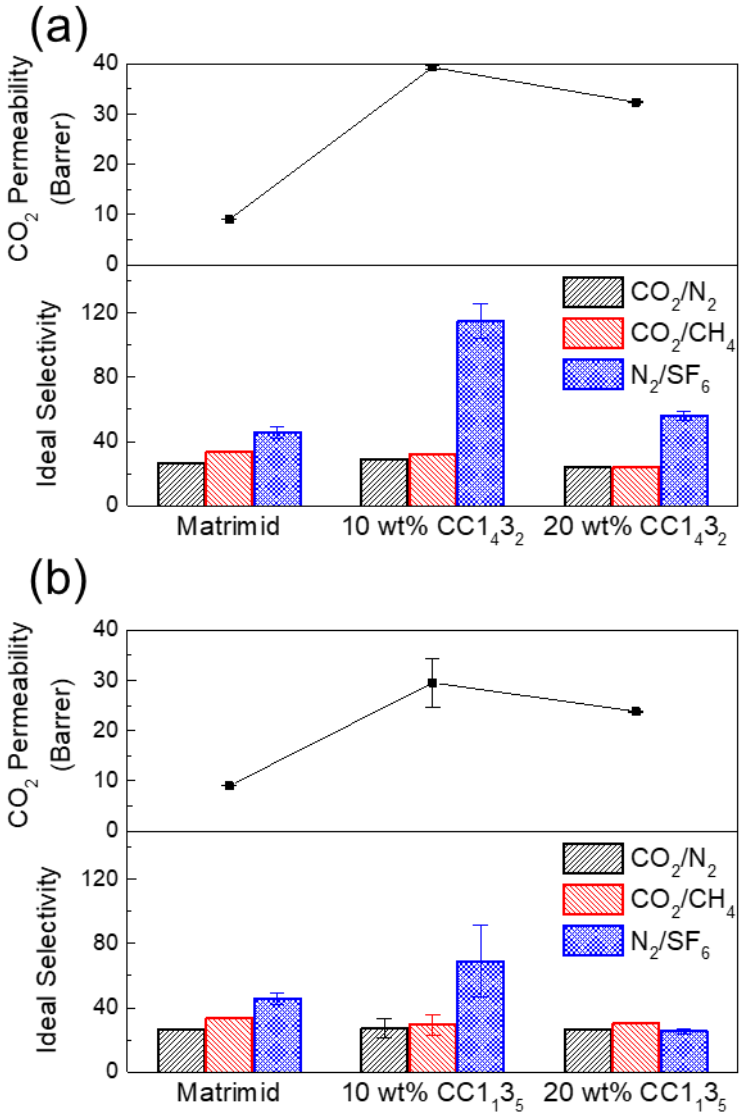

Figure 6.19 (a) and (b) CO_2 permeability results of Matrimid® and molecularly-mixed composite membranes at different ASPOC weight loadings, and ideal permselectivity calculated from the single gas permeabilities for the CO_2/N_2, CO_2/CH_4, and N_2/SF_6 pairs. The error bars are generated from averaging two membranes each with three tests on one gas

Interestingly, the CC1$_1$3$_5$ MMMs do not show a similar increase in the N_2/SF_6 selectivity. It was reported that CC3-R crystals have cooperative sorption behavior for SF_6

via guest-induced structural flexibility.[23] Compared to CC3-R cages, each of which has six cyclohexane groups on the vertices, $CC1_13_5$ mixtures are similar, having the majority of cages heavily functionalized with cyclohexane groups. We hypothesize that this similarity in the cage structure will likely lead to an increased sorption selectivity of SF_6 over N_2 in $CC1_13_5$ MMMs, which undermines the expected permselectivity increase from diffusion selectivity. Additionally, there could be nonselective permeation at the $CC1_13_5$-Matrimid® interface, which is typically found in traditional particle-filler MMMs.

6.3.6 Organic Solvent Permeation

The ASPOC-loaded membranes are also potential candidates for improving organic solvent nanofiltration (OSN) separations due to the relevant pore sizes (Figure 6.20) of the ASPOC molecules, which should allow for small solvent molecule permeation (e.g., methanol) while essentially rejecting solutes larger than ~5.5A. To demonstrate the potential applicability of the molecularly-mixed composite membranes in OSN separations, we tested the as-prepared membranes for their ability to reject model solutes from methanol, a commonly utilized solvent in the pharmaceutical industry.[24] Figure 6.20 shows the methanol permeability after an extended period. The membrane thicknesses for the tested membranes are listed in Table 6.2, which are used in permeability calculation. A slight permeability increase was achieved from the composite membranes.

Table 6.2 Thickness of membranes used in OSN

Membrane number	Thickness (μm)
Matrimid M1	41.6
Matrimid M2	48.0
Matrimid M3	46.9
10 wt% $CC1_43_2$ M1	50.3
10 wt% $CC1_43_2$ M2	55.4
10 wt% $CC1_43_2$ M3	47.3
10 wt% $CC1_43_2$ M4	60.9
10 wt% $CC1_13_5$ M1	42.2
10 wt% $CC1_13_5$ M2	52.3
10 wt% $CC1_13_5$ M3	49.9
10 wt% $CC1_13_5$ M4	45

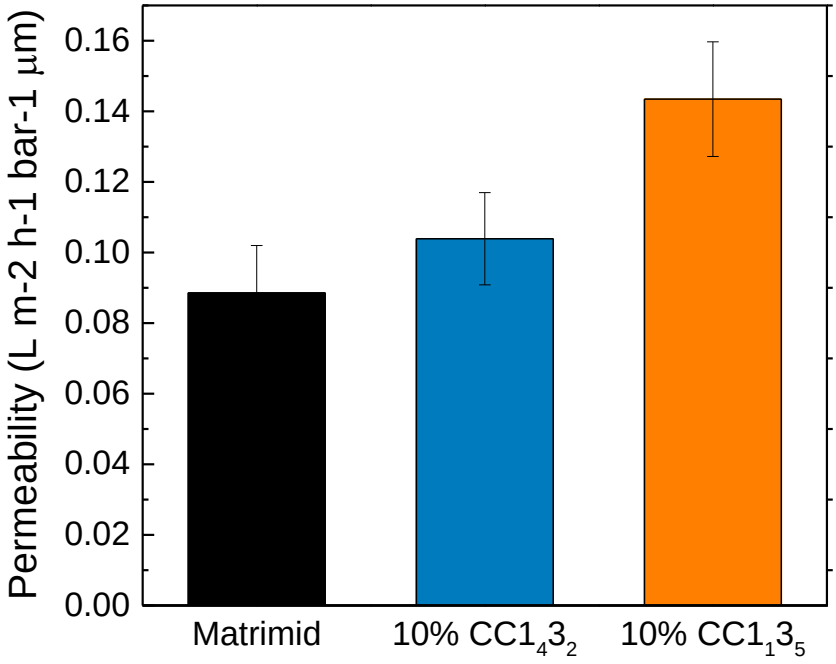

Figure 6.20 Methanol permeability for Matrimid®, 10 wt% $CC1_43_2$ and $CC1_13_5$ composite membranes.

*The error bars are generated from 4 membranes (3 membranes in the case of Matrimid®)

The poly(styrene) rejection performance for pure Matrimid® and the 10 wt% $CC1_43_2$ and $CC1_13_5$ MMCMs is shown in Figure 6.21. The rejection for the MMCMs increased gradually with time (Figure 6.22) and slowly reached steady-state; this is

associated with a concomitant permeability decline and approach towards a steady-state value. These types of changes are often observed as membranes undergo compaction during OSN operation.[25] For 10 wt% CC1$_4$3$_2$ MMM, we observe excellent rejection (>95%) of all poly(styrene) oligomers, demonstrating that these materials are promising for challenging OSN separations with small solutes, which has recently been identified as one of the critical needs in OSN membrane development.[26]

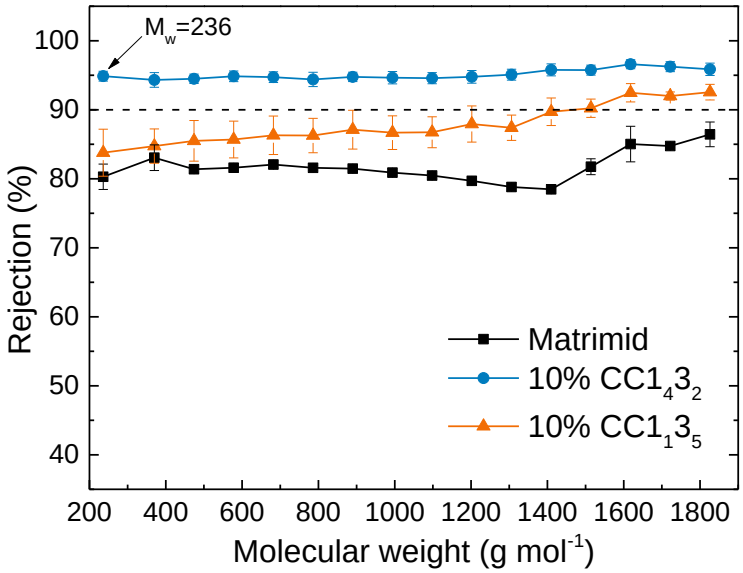

Figure 6.21 (e) Methanol permeability and (f) poly(styrene) rejection for Matrimid®, 10 wt% CC1$_4$3$_2$ and CC1$_1$3$_5$ composite membranes.

*The error bars are generated from 4 membranes (3 membranes in the case of Matrimid®), each permeant is tested three times in the HPLC.

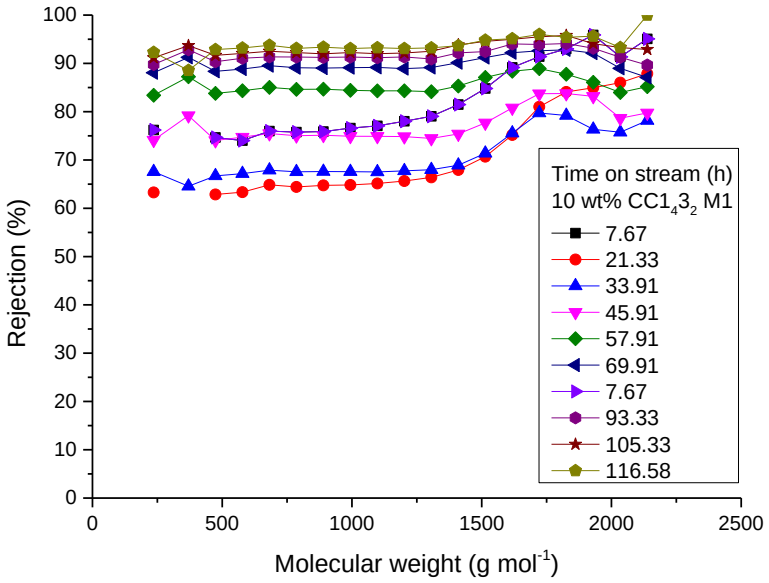

Figure 6.22 Transient rejection rate for 10 wt% $CC1_43_2$ M1

It is important to note that we utilized "dense" membranes in this set of OSN experiments. The thicknesses of the dense membranes are intentionally much larger than asymmetric or thin-film-composite membranes usually reported in the literature (see the comparison of membrane performance in Table 6.3). However, the use of dense membranes allows us to extract intrinsic membrane properties that are more meaningful in membrane materials research and development. Indeed, knowledge of the permeability enables estimates of expected permeance if the MMCM material were fabricated into the typical ISA or TFC architecture. For example, we expect to get 1.2 L m^{-2} h^{-1} bar^{-1} permeance for a 100 nm $CC1_43_2$ MMCM, which is an achievable film thickness in standard membrane fabrication processes. With the high rejections, this combination of permeance and rejection puts our membrane among the best membrane materials reported for poly(styrene) molecular weight cut-off performance (Figure 6.23).

Table 6.3 Comparison of membrane performance from this work to literature reported membranes using methanol as solvent

Membrane material	Permeance at 100 nm ($L\ m^{-2}\ h^{-1}\ bar^{-1}$)	Permeability ($L\ m^{-2}\ h^{-1}\ bar^{-1}\ \mu m$)	Marker	MW (g/mol)	Rejection (% at 236 g/mol)	Ref.
Matrimid M1	0.72	0.072	Poly(styrene)	236-1826	82	This work
Matrimid M2	0.78	0.078	Poly(styrene)	236-1826	81	This work
Matrimid M3	1.15	0.115	Poly(styrene)	236-1826	78	This work
10 wt% $CC1_13_5$ M1	1.87	0.187	Poly(styrene)	236-1826	78	This work
10 wt% $CC1_13_5$ M2	1.49	0.149	Poly(styrene)	236-1826	79	This work
10 wt% $CC1_13_5$ M3	1.19	0.119	Poly(styrene)	236-1826	92	This work
10 wt% $CC1_13_5$ M4	1.18	0.118	Poly(styrene)	236-1826	85	This work
10 wt% $CC1_43_2$ M1	1.30	0.130	Poly(styrene)	236-1826	95	This work
10 wt% $CC1_43_2$ M2	1.17	0.117	Poly(styrene)	236-1826	95	This work
10 wt% $CC1_43_2$ M3	0.83	0.083	Poly(styrene)	236-1826	93	This work
10 wt% $CC1_43_2$ M4	0.79	0.079	Poly(styrene)	236-1826	96	This work
Membrane material	Permeance ($L\ m^{-2}\ h^{-1}\ bar^{-1}$)	Thickness (μm, estimate)	Permeability ($L\ m^{-2}\ h^{-1}\ bar^{-1}\ \mu m$)	Marker	MW (g/mol)	Rejection (%)	Ref.
PIM-1/x-UT	2	0.25	0.5	Poly(styrene)	236-1410	5 (236 g/mol)	[27]
Starmem™122	5.6	-	-	Poly(styrene)	236-1098	82 (236 g/mol)	[28]
rGO	76.0 75.3	0.018	1.368 1.355	Basic fuchsin Methylene blue	323.8 319.9	86.2 100	[29]
HPEI-rGO	74.2 72.5	0.018	1.336 1.305	Brilliant yellow Evans blue	624.6 960.8	88.5 90	[29]
PDD-TFE	0.24 0.16	0.6 1.67	0.144 0.267	Safranin O Brilliant Blue R Safranin O Brilliant Blue R	351 826 351 826	94 97 97 99	[30]
TMC-MPD/polyimide	0.9	0.1	0.09	Ramazol brilliant blue	626.5	99	[31]
sPPSU	44	0.05	2.2	Rose Bengal	1017	100	[32]
rGO-$TMPyP_{0.6}$-44	5.26	0.036	0.189	Evans blue Brilliant yellow Acid fuchsin	960.8 624.6 585.5	100 94.6 92.2	[33]
Polyamide	52.22	0.01	0.52	HNSA Methyl orange Naphthalene brown Acid fuchsin	246.2 327.3 400.3 585.5	98.5 98.9 99.9 99.9	[34]
UiO-66-NH_2@Polyamide	2.8	0.1	0.28	Poly(styrene)	236-1098	97 (236 g/mol)	[35]

Table 6.3 Continued

Membrane material	Permeance (L m^{-2} h^{-1} bar^{-1})	Thickness (µm, estimate)	Permeability (L m^{-2} h^{-1} bar^{-1} µm)	Marker	MW (g/mol)	Rejection (%)	Ref.
Cross-linked PANI	0.8	-	-	Poly(styrene)	236-1098	97 (236 g/mol)	36
PPSf	0.4	-	-	Rose Bengal	1017	88	37
PPSf/PI	2	0.1	0.2	Sudan II	276	95	38
VAPEEK	0.2	-	-	Rose Bengal	1017	90	39
PA/cross-linked P84 PI	1.5	-	-	Poly(styrene)	236-1098	98 (236 g/mol)	40
(PS-b-PEO/PAA)/ alumina	0.1	0.22	0.022	polyethylene glycols	200-900	80 (370 g/mol)	41
(PA/MOFs)/P 84 PI	3.9	0.06	0.234	Poly(styrene)	236-1098	96 (236 g/mol)	42

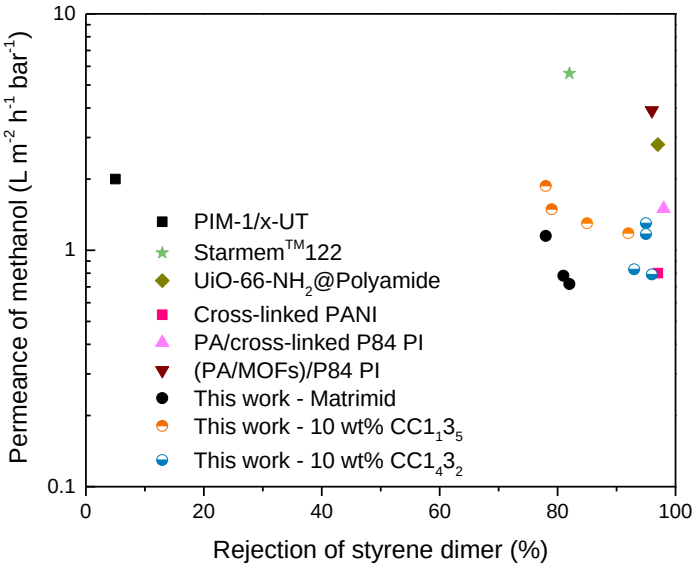

Figure 6.23 The permeance of methanol versus rejection of α-methyl styrene dimer (236 g mol^{-1}) for molecularly-mixed composite membranes.

*Nanofiltration data using poly(styrene) as markers in Table 6.3 have been included. The molecularly-mixed composite membranes assume a selective layer of 100 nm.

6.4 Conclusions

The use of soluble, amorphous, porous molecular fillers enables the fabrication of a series of mixed-matrix membranes that form "solid solutions" with the host polymer. The

distribution of the ASPOC molecules within the MMCMs was probed with EDX and Raman mapping whereby they were found to be uniformly incorporated into the membrane, unlike other POC molecules that tend to form particles and thus segregate into "filler" and "polymer" domains. The MMCMs have shown potential in both gas and liquid separations. A nearly 4-fold increase in gas permeability was observed for N_2, CO_2, and CH_4 compared to the pure polymer membrane. Moreover, a clear molecular sieving effect was observed for SF_6, resulting in 2-3 fold increase in N_2/SF_6 selectivity compared to the pure polymer membrane. The same membranes were tested in model OSN applications without further modification. High rejections (>95%) were observed for all permeate species with MW ranging from 200 to 2000 Da. The collected results suggest great potential for development of ASPOC based mixed-matrix membranes in both gas and liquid phase separations.

6.5 References

(1) Sholl, D. S.; Lively, R. P. Seven chemical separations: to change the world. *Nature* **2016,** *532*, 435-437.

(2) Robeson, L. M. The upper bound revisited. *Journal of Membrane Science* **2008,** *320*, 390-400.

(3) Lai, Z.; Bonilla, G.; Diaz, I.; Nery, J. G.; Sujaoti, K.; Amat, M. A.; Kokkoli, E.; Terasaki, O.; Thompson, R. W.; Tsapatsis, M.; Vlachos, D. G. Microstructural Optimization of a Zeolite Membrane for Organic Vapor Separation. *Science* **2003,** *300*, 456-460.

(4) Jeon, M. Y.; Kim, D.; Kumar, P.; Lee, P. S.; Rangnekar, N.; Bai, P.; Shete, M.; Elyassi, B.; Lee, H. S.; Narasimharao, K.; Basahel, S. N.; Al-Thabaiti, S.; Xu, W.; Cho, H. J.; Fetisov, E. O.; Thyagarajan, R.; DeJaco, R. F.; Fan, W.; Mkhoyan, K. A.; Siepmann, J. I.; Tsapatsis, M. Ultra-selective high-flux membranes from directly synthesized zeolite nanosheets. *Nature* **2017,** *543*, 690.

(5) Brown, A. J.; Brunelli, N. A.; Eum, K.; Rashidi, F.; Johnson, J. R.; Koros, W. J.; Jones, C. W.; Nair, S. Interfacial microfluidic processing of metal-organic framework hollow fiber membranes. *Science* **2014,** *345*, 72-75.

(6) Kulprathipanja, S.; Neuzil, R. W.; Li, N. N. Separation of fluids by means of mixed matrix membranes. US4740219A, 1988.

(7) Chung, T.-S.; Jiang, L. Y.; Li, Y.; Kulprathipanja, S. Mixed matrix membranes (MMMs) comprising organic polymers with dispersed inorganic fillers for gas separation. *Progress in Polymer Science* **2007,** *32*, 483-507.

(8) Zhang, C.; Dai, Y.; Johnson, J. R.; Karvan, O.; Koros, W. J. High performance ZIF-8/6FDA-DAM mixed matrix membrane for propylene/propane separations. *Journal of Membrane Science* **2012,** *389*, 34-42.

(9) Liu, G.; Chernikova, V.; Liu, Y.; Zhang, K.; Belmabkhout, Y.; Shekhah, O.; Zhang, C.; Yi, S.; Eddaoudi, M.; Koros, W. J. Mixed matrix formulations with MOF molecular sieving for key energy-intensive separations. *Nature Materials* **2018,** *17*, 283-289.

(10) Tarabara, E. M. V. H. V. *Encyclopedia of Membrane Science and Technology*. Wiley: 2013.

(11) Evans, J. D.; Huang, D. M.; Hill, M. R.; Sumby, C. J.; Thornton, A. W.; Doonan, C. J. Feasibility of Mixed Matrix Membrane Gas Separations Employing Porous Organic Cages. *The Journal of Physical Chemistry C* **2013,** *118*, 1523-1529.

(12) Bushell, A. F.; Budd, P. M.; Attfield, M. P.; Jones, J. T. A.; Hasell, T.; Cooper, A. I.; Bernardo, P.; Bazzarelli, F.; Clarizia, G.; Jansen, J. C. Nanoporous Organic Polymer/Cage Composite Membranes. *Angewandte Chemie International Edition* **2013,** *52*, 1253-1256.

(13) Mao, H.; Zhang, S. Mixed-matrix membranes incorporated with porous shape-persistent organic cages for gas separation. *Journal of Colloid and Interface Science* **2017,** *490*, 29-36.

(14) Jiang, S.; Jones, J. T. A.; Hasell, T.; Blythe, C. E.; Adams, D. J.; Trewin, A.; Cooper, A. I. Porous organic molecular solids by dynamic covalent scrambling. *Nature Communications* **2011,** *2*.

(15) Song, Q.; Jiang, S.; Hasell, T.; Liu, M.; Sun, S.; Cheetham, A. K.; Sivaniah, E.; Cooper, A. I. Porous Organic Cage Thin Films and Molecular-Sieving Membranes. *Advanced Materials* **2016**, n/a-n/a.

(16) Kirkegaard, P.; Olsen, J. V.; Eldrup, M. M. http://palsfit.dk.

(17) Dechnik, J.; Gascon, J.; Doonan, C. J.; Janiak, C.; Sumby, C. J. Mixed-Matrix Membranes. *Angewandte Chemie International Edition* **2017,** *56*, 9292-9310.

(18) Şen, D.; Kalıpçılar, H.; Yilmaz, L. Development of polycarbonate based zeolite 4A filled mixed matrix gas separation membranes. *Journal of Membrane Science* **2007,** *303*, 194-203.

(19) Bojdys, M. J.; Briggs, M. E.; Jones, J. T. A.; Adams, D. J.; Chong, S. Y.; Schmidtmann, M.; Cooper, A. I. Supramolecular Engineering of Intrinsic and Extrinsic Porosity in Covalent Organic Cages. *Journal of the American Chemical Society* **2011,** *133*, 16566-16571.

(20) Seeger, A. The study of defects in crystals by positron annihilation. *Applied physics* **1974,** *4*, 183-199.

(21) Tao, S. J. Positronium Annihilation in Molecular Substances. *The Journal of Chemical Physics* **1972,** *56*, 5499-5510.

(22) Eldrup, M.; Lightbody, D.; Sherwood, J. N. The temperature dependence of positron lifetimes in solid pivalic acid. *Chemical Physics* **1981,** *63*, 51-58.

(23) Hasell, T.; Miklitz, M.; Stephenson, A.; Little, M. A.; Chong, S. Y.; Clowes, R.; Chen, L. J.; Holden, D.; Tribello, G. A.; Jelfs, K. E.; Cooper, A. I. Porous Organic Cages for Sulfur Hexafluoride Separation. *Journal of the American Chemical Society* **2016,** *138*, 1653-1659.

(24) Marchetti, P.; Jimenez Solomon, M. F.; Szekely, G.; Livingston, A. G. Molecular Separation with Organic Solvent Nanofiltration: A Critical Review. *Chemical Reviews* **2014,** *114*, 10735-10806.

(25) Kim, J. H.; Moon, S. J.; Park, S. H.; Cook, M.; Livingston, A. G.; Lee, Y. M. A robust thin film composite membrane incorporating thermally rearranged polymer support for organic solvent nanofiltration and pressure retarded osmosis. *Journal of Membrane Science* **2018,** *550*, 322-331.

(26) Marchetti, P.; Peeva, L.; Livingston, A. The Selectivity Challenge in Organic Solvent Nanofiltration: Membrane and Process Solutions. *Annual Review of Chemical and Biomolecular Engineering* **2017,** *8*, 473-497.

(27) Cook, M.; Gaffney, P. R. J.; Peeva, L. G.; Livingston, A. G. Roll-to-roll dip coating of three different PIMs for Organic Solvent Nanofiltration. *Journal of Membrane Science* **2018,** *558*, 52-63.

(28) See Toh, Y. H.; Loh, X. X.; Li, K.; Bismarck, A.; Livingston, A. G. In search of a standard method for the characterisation of organic solvent nanofiltration membranes. *Journal of Membrane Science* **2007,** *291*, 120-125.

(29) Huang, L.; Chen, J.; Gao, T.; Zhang, M.; Li, Y.; Dai, L.; Qu, L.; Shi, G. Reduced Graphene Oxide Membranes for Ultrafast Organic Solvent Nanofiltration. *Advanced Materials* **2016,** *28*, 8669-8674.

(30) Chau, J.; Basak, P.; Kaur, J.; Hu, Y.; Sirkar, K. K. Performance of a composite membrane of a perfluorodioxole copolymer in organic solvent nanofiltration. *Separation and Purification Technology* **2018,** *199*, 233-241.

(31) Sun, S.-P.; Chan, S.-Y.; Chung, T.-S. A slow–fast phase separation (SFPS) process to fabricate dual-layer hollow fiber substrates for thin-film composite (TFC) organic solvent nanofiltration (OSN) membranes. *Chemical Engineering Science* **2015,** *129*, 232-242.

(32) Feng, Y.; Weber, M.; Maletzko, C.; Chung, T.-S. Facile fabrication of sulfonated polyphenylenesulfone (sPPSU) membranes with high separation performance for organic solvent nanofiltration. *Journal of Membrane Science* **2018,** *549*, 550-558.

(33) Gao, T.; Huang, L.; Li, C.; Xu, G.; Shi, G. Graphene membranes with tuneable nanochannels by intercalating self-assembled porphyrin molecules for organic solvent nanofiltration. *Carbon* **2017,** *124*, 263-270.

(34) Karan, S.; Jiang, Z.; Livingston, A. G. Sub–10 nm polyamide nanofilms with ultrafast solvent transport for molecular separation. *Science* **2015,** *348*, 1347.

(35) Guo, X.; Liu, D.; Han, T.; Huang, H.; Yang, Q.; Zhong, C. Preparation of thin film nanocomposite membranes with surface modified MOF for high flux organic solvent nanofiltration. *AIChE Journal* **2016,** *63*, 1303-1312.

(36) Loh, X. X.; Sairam, M.; Bismarck, A.; Steinke, J. H. G.; Livingston, A. G.; Li, K. Crosslinked integrally skinned asymmetric polyaniline membranes for use in organic solvents. *Journal of Membrane Science* **2009,** *326*, 635-642.

(37) Darvishmanesh, S.; Tasselli, F.; Jansen, J. C.; Tocci, E.; Bazzarelli, F.; Bernardo, P.; Luis, P.; Degrève, J.; Drioli, E.; Van der Bruggen, B. Preparation of solvent stable polyphenylsulfone hollow fiber nanofiltration membranes. *Journal of Membrane Science* **2011,** *384*, 89-96.

(38) Jansen, J. C.; Darvishmanesh, S.; Tasselli, F.; Bazzarelli, F.; Bernardo, P.; Tocci, E.; Friess, K.; Randova, A.; Drioli, E.; Van der Bruggen, B. Influence of the blend composition on the properties and separation performance of novel solvent resistant polyphenylsulfone/polyimide nanofiltration membranes. *Journal of Membrane Science* **2013,** *447*, 107-118.

(39) Hendrix, K.; Van Eynde, M.; Koeckelberghs, G.; Vankelecom, I. F. J. Crosslinking of modified poly(ether ether ketone) membranes for use in solvent resistant nanofiltration. *Journal of Membrane Science* **2013,** *447*, 212-221.

(40) Jimenez Solomon, M. F.; Bhole, Y.; Livingston, A. G. High flux membranes for organic solvent nanofiltration (OSN)—Interfacial polymerization with solvent activation. *Journal of Membrane Science* **2012,** *423-424*, 371-382.

(41) Li, X.; Fustin, C.-A.; Lefevre, N.; Gohy, J.-F.; Feyter, S. D.; Baerdemaeker, J. D.; Egger, W.; Vankelecom, I. F. J. Ordered nanoporous membranes based on diblock

copolymers with high chemical stability and tunable separation properties. *Journal of Materials Chemistry* **2010,** *20*, 4333-4339.

(42) Sorribas, S.; Gorgojo, P.; Téllez, C.; Coronas, J.; Livingston, A. G. High Flux Thin Film Nanocomposite Membranes Based on Metal–Organic Frameworks for Organic Solvent Nanofiltration. *Journal of the American Chemical Society* **2013,** *135*, 15201-15208.

CHAPTER 7. DISSERTATION CONCLUSIONS AND FUTURE DIRECTIONS

7.1 Dissertation Overview

This thesis presented a systematic study from fundamental to applied aspects of porous organic cages aiming at pushing porous organic cage materials towards designed structure and functionality for targeted applications. The formation mechanism study closed the loop for *in silico* design and prediction for POCs. The properties of POCs are tuned by defect engineering for better CO_2 affinity or acid gas stability, which are first steps towards industrial application. Two proof-of-concept applications in both adsorptive and membrane-based separations are demonstrated with the use of amorphous POCs. The findings of this thesis can be extended in various directions such as computational guided design and synthesis, properties modification, and targeted applications, which will drive the POCs research area forward.

7.2 Summary and Conclusions

7.2.1 Chapter Summaries

Porous organic cages (POCs) are a class of discrete porous molecules with unique properties and potential for various applications. This thesis work focuses on fundamental as well as applied aspects of POCs. This thesis will start with detailed investigation of the formation mechanisms of imine-based POCs and implying new design strategies for POCs (Chapter 2). Then various defect behavior of POC molecules and solids are studied that showed improved physical properties (Chapter 3&4). One particular type of amorphous

POC named amorphous scrambled porous organic cages (ASPOCs) is tested as adsorbent support and membrane additives as proof-of-concept studies of potential applications of POCs (Chapter 5&6).

The syntheses of POCs represent an important synthetic puzzle in dynamic covalent chemistry based self-sorting. Improved understanding of the formation mechanisms of POCs can lead to control and rational design of cages with desired functionality. In the first study (Chapter 2), I explore the formation mechanisms of imine-based POCs using time-resolved electrospray mass spectrometry. Upon mixing of the linkers, localized random assembly immediately occurs between the linkers to form a wide range of intermediates. These intermediates transform into several species with specific metastable geometries in a short time period. The metastable species then act as a reservoir for simultaneous dissolution and assembly towards the desired cages, with a small amount of incomplete cages or undesired byproducts coexisting in the final product. Electronic structure calculations at the density functional theory and correlated molecular orbital theory levels are used to validate the formation mechanism. Based on our observations from both experiments and calculations, we propose a comprehensive method for designing and predicting new POC species.

The observation of stable incomplete cages during CC3-R synthesis inspired us to design intentionally defective cages (Chapter 3). These “missing-linker” type molecular defects are installed into CC3-R via non-solvent induced crystallization. The defective CC3-R materials are found to have enhanced CO_2 interaction and improved CO_2 uptake capacity due to the additional functional groups present within the CC3 crystals. In addition to molecular defects, defect at the crystal level is also studied (Chapter 4). Both known and

new CC3-based porous organic cages are prepared and exposed to acidic SO_2 in vapor and liquid conditions. Distinct differences in the stability of the CC3 cages exist depending on the chirality of the diamine linkers used. The acid catalyzed CC3 degradation mechanism is probed via in-situ IR and a degradation pathway is proposed and supported with computational results. CC3 crystals synthesized with racemic mixtures of diaminocyclohexane exhibited enhanced stability compared to CC3-R and CC3-S. Confocal fluorescent microscope images reveal that the stability difference in CC3 species originates from an abundance of mesoporous grain boundaries in CC3-R and CC3-S, allowing facile access of aqueous SO_2 throughout the crystal, promoting decomposition. These grain boundaries are absent from CC3 crystals made with racemic linkers.

In Chapter 5, I explore the applicability of POCs as molecular porous supports for polymeric amines. I find that primary amines in poly(ethylenimine) (PEI) can undergo metathesis with the imine bonds present in POCs, resulting in non-porous products. This problem can be overcome by transforming the primary amines in PEI to tertiary amines via methylation. The methylated PEI (mPEI) forms homogeneous composites with ASPOCs without undesired reactions or phase separation. The microscopic structure of the composites is studied using molecular dynamics simulations. These composite materials are evaluated as adsorbents for low concentration SO_2 (200 ppm) adsorption and show good thermal and cyclic stability.

Finally, I investigate performance of ASPOC containing mixed-matrix membranes. When fabricated into mixed matrix membranes, the soluble POC molecules have the potential to exhibit molecular-level intimate mixing with matrix polymer. However, the incorporation of POCs into mixed matrix membrane is still in its infancy and lacks

demonstration of comprehensive improvement of membrane performance. In chapter 6, I utilized vertex functionalized amorphous scrambled porous organic cages (ASPOCs) in mixed matrix membranes to study a series of key questions in this field. The dispersion of ASPOC mixtures possessing different crystallization tendencies within a polymer matrix are probed using Raman imaging and Energy Dispersive X-Ray (EDX) mapping. Gas permeation experiments of N_2, CO_2, CH_4 and SF_6 were carried out as a function of ASPOC loading and crystallization tendency. A 4 fold of permeability increase was observed for N_2, CO_2 and CH_4 compared to pure polymer membrane. Moreover, a clear molecular sieving effect was observed for SF_6, resulting in 2-4 fold of increase of N2/SF6 selectivity compared to the pure polymer membrane. The membranes were further examined in organic solvent nanofiltration experiments using a cross-flow permeation approach. The Molecular Weight Cut-off (MWCO) of the membranes were calculated based on the polystyrene permeation tests. Overall, these membranes demonstrated homogeneous mixing between the POC molecules and the polymer matrix, and showed potential to be used in molecular separation processes.

7.2.2 Conclusions and Impacts

The formation mechanisms work presented in Chapter 2 and the derived prediction strategies closed the loop for fully prediction of POC solids. I have demonstrated the application of this prediction method in Chapter 3 for the discovery of defective cages.[1] In addition, my collaborator Yang Liu has recently finished a study in predicting the structure and properties of racemic cage crystals, which is closely related to the cage material discovered in Chapter 4.[2]

The same prediction strategies was recently adopted in a combinatory high-throughput discovery of new POC species that combines computational screening and robotic synthesis.[3] In this work 33 new cages are discovered, which indeed demonstrated the power of computational assist design and synthesis of new materials. In silico design and prediction is also applied for discovering of large-pore imine cages.[4]

The more recently published works in defect engineering and application examples do not have much follow-up works in the literature, except the racemic CC3-R crystal has inspired several related studies.[5-8] However, I believe that the proof-of-concept membrane study reported in Chapter 6 will open up heated research into more versatile filler-polymer combinations and applications.

7.3 Future Directions

7.3.1 Scale-up Synthesis of POC and ASPOC

Due to the mild conditions of imine-based POC syntheses, there is no virtual limit to the size of batch synthesis. The question lies in if we can scale-up the ASPOC synthesis by using continuous flow system. There were two reports of flow synthesis of cages. [9-10] In Briggs' work, the flow synthesis of CC1, CC3, and ASPOC $CC1^{x}3^{y}$ were explored on the lab scale. To produce POCs at a larger scale, a process is designed as illustrated in Figure 7.1.

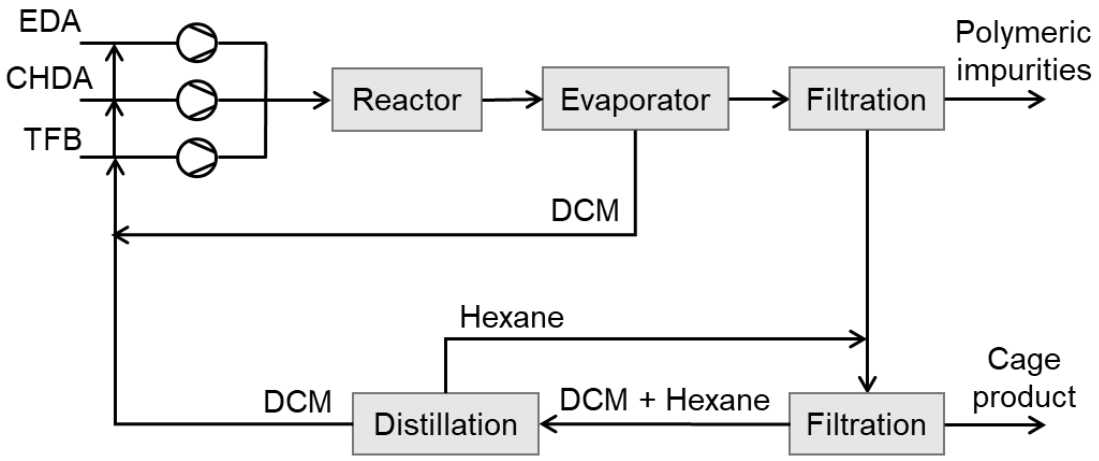

Figure 7.1 ASPOC scale up production process diagram

Ethylenediamine (EDA), cyclohexanediamine (CHDA), and triformylbenzene (TFB) solutions are separately prepared and pumped to a mixer before sending to a PFR reaction consists of heated tubings. A back pressure regulator is used to maintain the pressure in the reactor. The reaction mixture is expanded into a evaporator to flash off DCM to a predetermined solid concentration such that the polymeric species are precipitated out. The polymeric impurities are filtered. To the liquid phase, a stream of hexane is mixed and the cage product are precipitated out. Cage products are collected with filtration as the solid product. The DCM/hexane mixture are sent into a flash distillation column. DCM will be cycled back for preparation of the stock solutions. And hexane are recycled for precipitation of cage product. Note that reaction intermediate will accumulate in the hexane stream and occasional regeneration of the hexane stream is needed and the intermediates can be fed into the reactor.

This process uses knowledge accumulated from the studies carried out in Chapter 2 and Chapter 3, which deals with separating cage product from polymeric impurities and reaction intermediates. And full recycle of the solvent is achieved with the use of a

distillation column that separates DCM and hexane. Several operational related studies need to be carried out, such as the reactor condition, evaporation extent, and hexane/DCM ratio. The feasibility of the process need to be validated via economic analysis before the next step. The formation mechanism information obtained in Chapter 2 can be used in the modelling of the reactor, with solving the reaction network problem.

7.3.2 Tying ASPOC

Based on the knowledge accumulated in the group on imine-based POCs, it is worth well to further explore the chemistry possibilities offered by this class of material for broader applications. One chemistry that is accessible to imine bond is reduce to amine bond and further amide formation with ketones. Liu et al. have demonstrated the modification of CC3-R with reduction and sequential "tying" with acetone and formaldehyde.[11] The resulting cages present higher stability under both acid and base conditions. This feature can be further explored in acid gas stability test and humid CO_2 and SO_2 adsorption. The tying of the cages also reduce the effective pore size of the cages that might have effects on the selectivity over small gas molecules.

7.3.3 Cross-linkable Cage-polymer Composite Membrane for OSN and OSRO

The membrane developed in Chapter 6 are limited to alcohol OSN systems due to the commonly practiced diamine crosslinking towards solvent resistant membranes prohibited by the reaction of diamines with the cages. This reaction will destroy the cages in the membrane and lead to disrupted membrane performance. One way to fabricate cross-linkable composite membranes is to use cages without imine bond. As discussed in 7.3.2, the chemical modification removes the imine bond and resulted in a cage with higher

chemical stability. This cage can be used in composite membranes that reopens the diamine crosslinking route. After the casting of the molecularly mixed composite membrane use the TCCs (tied cage compound), the polyimide polymers can be crosslinked with diamines and used as solvent resistant membranes for OSN or OSRO. The as-casted membrane can also be explored in humid acid gas separations.

7.3.4 Double-cross-linkable Cage-polymer Membrane

One problem the membranes fabricated in Section 7.3.2 is the leaching of POC fillers in liquid systems. For example, the swelling of the polymer will increase the diffusivity of POCs (although mostly negligible); the partial or total solvation of the POCs will be more detrimental in the leaching problem. To solve this problem, the crosslinking between the cage and the polymer chain is necessary. Extra functionality is needed to be introduced to the cage in order to make the crosslinking possible. Click-chemistry is one possible route. Another more-viable route is to use vinyl-substituted diamine that would not affect the cage formation and tying chemistry. The crosslinking can be done in two sequences.

The first sequence is to pre-link the cages to polymer chains. During this process, the cages may also act as crosslinkers between the polymer chains, which will result in gel formation. When this happens, the membrane can be casted during the gel formation. If the crosslinking extent is not sufficient, extra crosslinking agent might be needed on the membranes.

The second sequence is to cast the membrane with the cages and then do the crosslinking between cages and polymer chains. Again the crosslinking extent need to be checked to determine if additional crosslinking is needed.

7.3.5 Alkyl-substituted Linkers for Pore Size Control

As demonstrated in Chapter 6, the relatively small imine cages are still too large for small gas molecule separations. In addition, cages with larger openings do not necessarily to be exact the size for large molecule separation. One way of modifying the cage opening aperture is using alkyl-substituted triformylbenzene, or alkyl-substituted triamine.[3, 12-13] The methyl-substituted triformylbenzene is not commercially available and need to be obtained via synthesis (Figure 7.2). Ethyl substituted triformylbenzene and triamine can also be synthesized via a more complicated route (Figure 7.3).

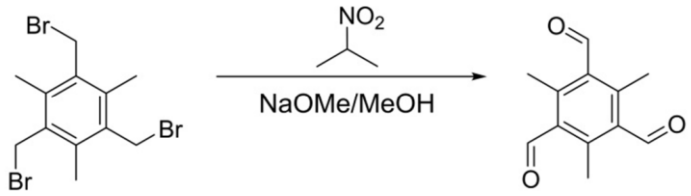

Figure 7.2 Synthesis of 1,3,5-Trimethyl-2,4,6-tris(formyl)benzene[6, 14]

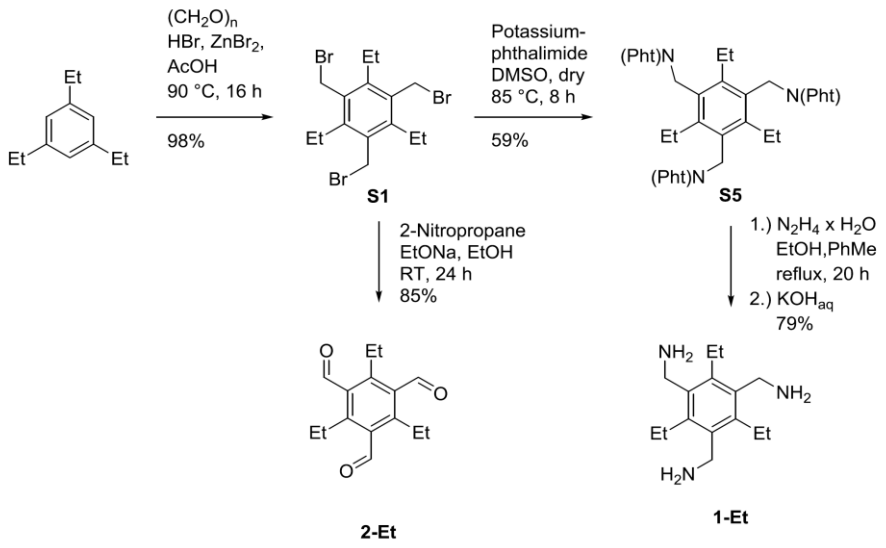

Figure 7.3 Synthesis of 2,4,6-triethylbenzene-1,3,5-tricarbaldehyde and 1,3,5-tris(aminomethyl)-2,4,6-triethylbenzene[5]

The resulting alkyl-substituted linkers can potential be used to synthesize cages with modified pore opening, which will further provide modified sieving properties for different molecular pairs. The problem might be existing in the synthesis of cages containing alkyl-substituted linkers is the steric hindrance, which might prevent *de novo* synthesis the cages in their pure form. Alternatively, scrambled synthesis with unsubstituted linkers or post-synthetic linker exchange might be useful techniques. The resulting cages could be explored in kinetic separations, breakthrough experiments and membranes. The performance of the altered cages can be compared to their parent cages.

7.3.6 Other POC Chemistries

Despite imine cages being the most dominant POCs due to their low synthesis requirement, POCs build on other chemistries offer the potential to be stable under conditions imine-based POCs are not. As introduced in Chapter 1, disulfide exchange, boronic acid condensation, and olefin/alkyne metathesis have all been used in cage

synthesis. It will be interesting from the fundamental point of view to study the acid gas as well as other aggressive conditions (basic, solvents) of the corresponding cages.

Because of the different connecting chemistry, other cage species might find wider application where better chemical stability are needed. For example, cages stable to acid gases and cages stable to membrane crosslinking conditions. There are several questions to be answered before entering this area.

The pore size ranges of the cages built from other chemistry. Usually imine based cages offer smaller pore size due to the use of simple organic linkers. Other cage types in general result in larger pore sizes, which may not be applicable to molecular separation processes. They may still find applications in OSN.

The scalability and yield of the cage synthesis. As discussed in Section 7.3.1, imine-based POCs can be potential scaled up in continuous process with good overall yield. However, other chemistries especially irreversible reactions usually give low yield. This factor need to be considered before claiming commercial potential of the material.

The cages synthesized in the section can also be applied to the membrane fabrication described in Section 7.3.3.

7.3.7 Demonstrate MMM Performance in State-of-the-art Polymers

In this thesis, commercially available polymer Matrimid was used as the proof-of-concept example for permeation performance enhancement. To truly demonstrate the concept and potential of the molecularly mixed composite membranes with ASPOCs, state-of-the-art polymers need to be tested as the matrix. This will provide the information on

how far can we push beyond the polymer upper bound. Some easily migratable complexities can be foreseen. As I have discussed in Chapter 6, the balance of interactions between solvent, filler, and polymer is essential to achieve the desired homogeneous morphology. When the polymer is changed, a new solvent need to be identified that will solvate both ASPOC and polymer. In addition, the ASPOC mixture distribution might need to be turned to find the optimal interaction with the polymer.

7.3.8 Model Development for Guest Transport in Molecularly Mixed Composite Membranes

The available present models for MMMs are adopted from thermal and electrical conductivity models. These models have close relations between electrical and thermal conduction and permeation of species through composite materials. The Maxwell model provides the improvement for the permeability from randomly distributed and non-interacting homogeneous solid spheres in a continuous matrix. This model generally described the permeability accurately when filler volume ratio is less than about 0.2. The Bruggeman model was developed for the estimation of the dielectric constant of particulate composites; this model could be modified for the permeability prediction of MMMs. Additional models can be found in this review of models for conductive polymer composite.[15]

However, our membrane performance have exceeded the prediction of Maxwell model as the homogenous distribution of ASPOCs in the matrix do not satisfy the assumption for above mentioned models. I propose that models for predicting thermal and electrical conductivity of binary metallic systems can be used for the permeability prediction of molecularly mixed composite membranes. For example, Northeim rule and Mott's model.[16]

7.3.9 Molecular Responsive Separation from Phase Change POC Materials

The last proposed direction is largely conceptual and hypothetical. The guest induced flexibility and phase transition have been reported for multiple cage systems.[17-20] This switching between different pore structures and porous network connectivities is potentially useful in "smart" separation processes, where certain trigger molecules in the separation stream can change the performance of the membrane or sorbent material. This trigger molecules can be intentionally added to the stream for function switch between adsorption and desorption or between permeation and rejection. They can also be native species (such as impurities) in the stream that can be detected by the material for "decision making".

7.4 REFERENCES

(1) Zhu, G.; Liu, Y.; Flores, L.; Lee, Z. R.; Jones, C. W.; Dixon, D. A.; Sholl, D. S.; Lively, R. P. Formation Mechanisms and Defect Engineering of Imine-Based Porous Organic Cages. *Chemistry of Materials* **2018,** *30,* 262-272.

(2) Zhu, G.; Hoffman, C. D.; Liu, Y.; Bhattacharyya, S.; Tumuluri, U.; Jue, M. L.; Wu, Z.; Sholl, D. S.; Nair, S.; Jones, C. W.; Lively, R. P. Engineering Porous Organic Cage Crystals with Increased Acid Gas Resistance. *Chemistry – A European Journal* **2016,** *22,* 10743-10747.

(3) Greenaway, R. L.; Santolini, V.; Bennison, M. J.; Alston, B. M.; Pugh, C. J.; Little, M. A.; Miklitz, M.; Eden-Rump, E. G. B.; Clowes, R.; Shakil, A.; Cuthbertson, H. J.; Armstrong, H.; Briggs, M. E.; Jelfs, K. E.; Cooper, A. I. High-throughput discovery of organic cages and catenanes using computational screening fused with robotic synthesis. *Nature Communications* **2018,** *9,* 2849.

(4) Bernabei, M.; Pérez-Soto, R.; Gomez Garcia, I.; Haranczyk, M. In silico design and assembly of cage molecules into porous molecular materials. *Molecular Systems Design & Engineering* **2018**.

(5) Beaudoin, D.; Rominger, F.; Mastalerz, M. Chiral Self-Sorting of [2+ 3] Salicylimine Cage Compounds. *Angewandte Chemie International Edition* **2017,** *56,* 1244-1248.

(6) Slater, A.; Little, M.; Briggs, M.; Jelfs, K.; Cooper, A. A solution-processable dissymmetric porous organic cage. *Molecular Systems Design & Engineering* **2018,** *3*, 223-227.

(7) Wang, X.; Peng, P.; Xuan, W.; Wang, Y.; Zhuang, Y.; Tian, Z.; Cao, X. Narcissistic chiral self-sorting of molecular face-rotating polyhedra. *Organic & biomolecular chemistry* **2018,** *16*, 34-37.

(8) Zhang, F.; He, Y.; Huang, J.; Sumpter, B. G.; Qiao, R. Multicomponent Gas Storage in Organic Cage Molecules. *The Journal of Physical Chemistry C* **2017,** *121*, 12426-12433.

(9) Briggs, M. E.; Slater, A. G.; Lunt, N.; Jiang, S.; Little, M. A.; Greenaway, R. L.; Hasell, T.; Battilocchio, C.; Ley, S. V.; Cooper, A. I. Dynamic flow synthesis of porous organic cages. *Chemical Communications* **2015,** *51*, 17390-17393.

(10) Kitchin, M.; Konstas, K.; Sumby, C. J.; Czyz, M. L.; Valente, P.; Hill, M. R.; Polyzos, A.; Doonan, C. J. Continuous flow synthesis of a carbon-based molecular cage macrocycle via a three-fold homocoupling reaction. *Chemical Communications* **2015,** *51*, 14231-14234.

(11) Liu, M.; Little, M. A.; Jelfs, K. E.; Jones, J. T. A.; Schmidtmann, M.; Chong, S. Y.; Hasell, T.; Cooper, A. I. Acid- and Base-Stable Porous Organic Cages: Shape Persistence and pH Stability via Post-synthetic "Tying" of a Flexible Amine Cage. *Journal of the American Chemical Society* **2014,** *136*, 7583-7586.

(12) Lauer, J. C.; Zhang, W.-S.; Rominger, F.; Schröder, R. R.; Mastalerz, M. Shape-Persistent [4+4] Imine Cages with a Truncated Tetrahedral Geometry. *Chemistry – A European Journal* **2018,** *24*, 1816-1820.

(13) Slater, A. G.; Reiss, P. S.; Pulido, A.; Little, M. A.; Holden, D. L.; Chen, L.; Chong, S. Y.; Alston, B. M.; Clowes, R.; Haranczyk, M.; Briggs, M. E.; Hasell, T.; Day, G. M.; Cooper, A. I. Computationally-Guided Synthetic Control over Pore Size in Isostructural Porous Organic Cages. *ACS Central Science* **2017,** *3*, 734-742.

(14) Hass, H.; Bender, M. ORTHO-TOLUALDEHYDE. *Organic Syntheses* **1950,** *30*, 99-101.

(15) Mohd Radzuan, N. A.; Sulong, A. B.; Sahari, J. A review of electrical conductivity models for conductive polymer composite. *International Journal of Hydrogen Energy* **2017,** *42*, 9262-9273.

(16) Wei, C.; Antolin, N.; Restrepo, O. D.; Windl, W.; Zhao, J.-C. A general model for thermal and electrical conductivity of binary metallic systems. *Acta Materialia* **2017,** *126*, 272-279.

(17) Jones, J. T. A.; Holden, D.; Mitra, T.; Hasell, T.; Adams, D. J.; Jelfs, K. E.; Trewin, A.; Willock, D. J.; Day, G. M.; Bacsa, J.; Steiner, A.; Cooper, A. I. On-Off Porosity

Switching in a Molecular Organic Solid. *Angewandte Chemie-International Edition* **2011,** *50*, 749-753.

(18) Jelfs, K. E.; Schiffmann, F.; Jones, J. T. A.; Slater, B.; Cora, F.; Cooper, A. I. Conformer interconversion in a switchable porous organic cage. *Physical Chemistry Chemical Physics* **2011,** *13*, 20081-20085.

(19) Hasell, T.; Culshaw, J. L.; Chong, S. Y.; Schmidtmann, M.; Little, M. A.; Jelfs, K. E.; Pyzer-Knapp, E. O.; Shepherd, H.; Adams, D. J.; Day, G. M.; Cooper, A. I. Controlling the Crystallization of Porous Organic Cages: Molecular Analogs of Isoreticular Frameworks Using Shape-Specific Directing Solvents. *Journal of the American Chemical Society* **2014,** *136*, 1438-1448.

(20) Hasell, T.; Miklitz, M.; Stephenson, A.; Little, M. A.; Chong, S. Y.; Clowes, R.; Chen, L.; Holden, D.; Tribello, G. A.; Jelfs, K. E. Porous organic cages for sulfur hexafluoride separation. *Journal of the American Chemical Society* **2016,** *138*, 1653-1659.